

UNIVERSITY OF KWAZULU-NATAL



Initial Conditions of the Universe: Signatures in the Cosmic Microwave Background and Baryon Acoustic Oscillations

by

Simon Muya Kasanda

Submitted in fulfillment of the
academic requirements for the degree of
Doctor of Philosophy (Science),
in the
School of Mathematical Sciences,
University of KwaZulu-Natal

Durban
March, 2012

*Now unto him that is able to do exceeding abundantly
above all that we ask or think,
According to the power that worketh in us,
For in him we live, and move, and have our being; ...
Unto him be glory...
By Christ Jesus throughout all ages.
Amen.*

Eph 3:20, Act 17:28

Abstract

In this thesis, we investigate the signatures of isocurvature initial conditions in the cosmic microwave background (CMB) through the temperature and polarization anisotropies, and in the large-scale structure distribution through the baryon acoustic oscillations (BAO).

The first part of this thesis is a brief review of the standard cosmological model with its underlying linear cosmological perturbation theory. We supplement it with a general discussion on the initial conditions of the primordial fluctuations.

In the third chapter, we review the evolution of the perturbations in the adiabatic model. We focus on the evolution of adiabatic perturbations in the photons and baryons from the epoch of initial conditions to the photon-baryon decoupling, as these determine the main features of the primary CMB anisotropies and of the baryon acoustic oscillations.

The fourth chapter recalls the theory of the CMB anisotropies in the adiabatic model. We consider the perturbations from the last scattering surface and evolve them through the line of sight integral to get the adiabatic CMB power spectrum. We review the effect of different cosmological parameters on the adiabatic CMB temperature spectrum.

In the fifth chapter, we investigate the observational signatures of the isocurvature perturbations in the CMB anisotropies. We first derive simple semi-analytic expressions for the evolution of the photon and baryon perturbations prior to decoupling for the four isocurvature regular modes and show that these modes excite different harmonics which couple differently to Silk damping and alter the form and evolution of acoustic waves. We study the impact of different cosmological parameters on the CMB angular power spectrum through the line of sight integral and find that the impact of the physical baryon and matter densities in isocurvature models differ the most from their effect in adiabatic models.

In the last two chapters, we explore in detail the effect of allowing for small amplitude admixtures of general isocurvature perturbations in addition to the dominant adiabatic mode, and their effect on the baryon acoustic oscillations. The sixth chapter focuses on the distortion of the standard ruler distance and the degradation of dark energy constants due to the inclusion of isocurvature perturbations, while the seventh chapter discusses in more detail the sensitivity of BAO dark energy constraints to general isocurvature perturbations. We stress the role played by Silk damping on the BAO peak features in breaking the degeneracy in the peak location for the different isocurvature modes and show how more general initial conditions impact our interpretation of cosmological data in dark energy studies. We find that the inclusion of these additional isocurvature modes leads to a significant increase in the Dark Energy Task Force figure of merit when considered in conjunction with CMB data. We also show that the incorrect assumption of adiabaticity has the potential to substantially bias our estimates of the dark energy parameters. We find that the use of the large scale structure data in conjunction with CMB data significantly improves our ability to measure the contributions of different modes to the initial conditions.

Acknowledgments

The research work for this thesis has been carried out in the School of Mathematical Sciences of the University of KwaZulu-Natal for the last four years. I wish to thank all the numerous people here for creating an enjoyable environment for research.

I wish to thank my supervisor, Prof. Kavilan Moodley for his expert guidance, patience and insight that have always been available throughout the years of my PhD. Words will never be enough to express my gratitude.

I would also like to thank Dr. Caroline Zunckel and Prof. Bruce Bassett for useful input and discussions over the last two years of the completion of this PhD.

It was a pleasure working with all the members of the Astrophysics and Cosmology Research Unit (ACRU) and the members of the School of Mathematical Sciences of the University of KwaZulu-Natal.

I also want to thank Dr. Matadi Maba, Mr. Lucien Nzuzi and Mr. Tony Nsio Nzundu for willingly spending a number of hours proof reading this thesis in spite of their multiple occupations.

I wish to acknowledge the National Research Foundation (NRF), the Square Kilometre Array (SKA) *Human Capital Development* fund and the Meraka Institute via funding for the South African Centre for High Performance Computing (CHPC) for financial support.

I wish to thank my parents, brothers and sisters for being supportive and for their trust.

I would like to greatly thank all my colleagues and friends for their encouragement and various input.

Finally, I wish to express my most sincere gratitude to my children Parfait, Favoured, Perle and my precious wife Princesse. Thank you for always being there for me, with unwavering love, care and support. I owe you this thesis.

Above all, I acknowledge the grace and mercy of the Lord Jesus Christ who, in the end, have made all this possible.

Preface

The work described in this thesis was carried out in the School of Mathematical Sciences, University of KwaZulu-Natal from October 2007 to December 2011. This dissertation was completed under the supervision of Prof. K. Moodley.

This study represents original work by the author and has not been submitted in any form for any degree or diploma to any other tertiary institution. Where use was made of the work of others it has been duly acknowledged in the text.

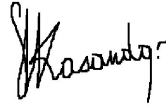
Declaration of Non-Plagiarism

I, **Simon MUYA KASANDA** declare that

1. The research reported in this thesis, except where otherwise indicated, is my original research.
2. This thesis has not been submitted for any degree or examination at any other university.
3. This thesis does not contain other persons' data, pictures, graphs or other information, unless specifically acknowledged as being sourced from other persons.
4. This thesis does not contain other persons' writing, unless specifically acknowledged as being sourced from other researchers. Where other written sources have been quoted, then:
 - (a) Their words have been re-written but the general information attributed to them has been referenced.
 - (b) Where their exact words have been used, then their writing has been placed in italics and inside quotation marks, and referenced.

5. This thesis does not contain text, graphics or tables copied and pasted from the Internet, unless specifically acknowledged, and the source being detailed in the thesis and in the References sections.

Signed in Westville, KwaZulu-Natal:

A handwritten signature in black ink, appearing to read 'S. KwaZulu-Natal'.

Date: **21 March 2012**

Declaration of Publications

Details of contribution to publications that form part and/or include research presented in this thesis:

1. *Fundamental Uncertainty in the BAO Scale from Isocurvature Modes*

Zunckel C., Okouma P., Muya Kasanda S., Moodley K. & Bassett B. A., Physics Letters B **696**, 433 (2011)

For this paper I contributed to section 2 on "the BAO peak with adiabatic and isocurvature initial conditions". The results were analysed jointly between all authors. The form of the publication has been altered slightly to adhere to the formatting requirements of this thesis.

2. *The Sensitivity of BAO Dark Energy Constraints to Isocurvature Perturbations*

Muya Kasanda S., Zunckel C., Okouma P., Moodley K. & Bassett B. A., arXiv:1111.2572 (2011)

Submitted for publication to JCAP.

For this paper I contributed to the phenomenology of the physics of the BAO in isocurvature modes (section 2). For the statistical part (section 3), I contributed to "the impact of

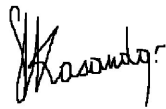
isocurvature modes on dark energy”. I coordinated the paper. The results were analysed jointly between all authors. The form of the publication has been altered slightly to adhere to the formatting requirements of this thesis.

3. *Observational Signatures of Isocurvature Perturbations in the CMB*

Muya Kasanda S. & Moodley K. 2012, in preparation.

I am the sole contributor to this work. I consulted with co-authors during the course of the work.

Signed:

A handwritten signature in black ink, appearing to read 'M. Kasanda S.', written over a horizontal line.

Contents

| | |
|--|-------------|
| Abstract | i |
| Acknowledgments | iii |
| Preface | v |
| Declaration of Non Plagiarism | vi |
| Declaration of Publications | viii |
| 1 Introduction | 1 |
| 2 The Standard Cosmological Model | 6 |
| 2.1 Brief overview | 7 |
| 2.1.1 The expansion of the universe (Hubble’s law) | 7 |
| 2.1.2 Light element abundances | 8 |
| 2.1.3 Cosmic microwave background radiation | 8 |
| 2.1.4 Evolution and distribution of galaxies | 9 |
| 2.2 Age and energy contents of the universe | 10 |

| | | |
|----------|---|-----------|
| 2.3 | Background and perturbed Friedmann-Robertson-Walker models | 11 |
| 2.4 | Einstein equations and energy momentum conservation | 14 |
| 2.5 | Initial conditions | 19 |
| 3 | Evolution of Cosmological Perturbations: Adiabatic case | 22 |
| 3.1 | Cold dark matter evolution | 24 |
| 3.1.1 | Large scales | 24 |
| 3.1.1.1 | Super-horizon solution | 24 |
| 3.1.1.2 | Through horizon crossing | 26 |
| 3.1.2 | Small scales | 27 |
| 3.1.2.1 | Horizon crossing | 28 |
| 3.1.2.2 | Sub-horizon evolution | 30 |
| 3.1.3 | Matter transfer function and Power spectrum | 33 |
| 3.1.4 | Growth function | 34 |
| 3.1.5 | Including other species | 35 |
| 3.2 | Evolution of photons and baryons prior to decoupling | 37 |
| 4 | CMB Anisotropies: Adiabatic case | 42 |
| 4.1 | Sachs-Wolfe derivation | 42 |
| 4.1.1 | The ordinary Sachs-Wolfe effect | 45 |
| 4.1.2 | The Doppler effect | 46 |
| 4.1.3 | The integrated Sachs-Wolfe effect | 47 |
| 4.2 | Boltzmann Hierarchy and the line of sight integral approach | 47 |
| 4.2.1 | Line of sight integral approach | 51 |
| 4.3 | CMB anisotropies | 55 |
| 4.3.1 | Transfer function $\Delta_\ell(k)$ | 55 |
| 4.3.2 | Angular power spectrum C_ℓ | 56 |
| 4.4 | Effect of cosmological parameters on the CMB temperature spectrum: adiabatic case | 57 |
| 4.4.1 | Baryon density $\Omega_b h^2$ | 58 |

| | | |
|----------|--|------------|
| 4.4.2 | Matter density $\Omega_m h^2$ | 59 |
| 4.4.3 | Cosmological constant density Ω_Λ | 60 |
| 4.4.4 | Curvature density Ω_K | 62 |
| 4.4.5 | Optical depth τ_e | 63 |
| 4.4.6 | Spectral index n_s | 64 |
| 5 | Observational Signatures of Isocurvature Perturbations in the CMB | 66 |
| 5.1 | Introduction | 66 |
| 5.2 | Evolution of photon and baryon perturbations | 67 |
| 5.2.1 | Evolution of photons and baryons prior to decoupling | 69 |
| 5.2.1.1 | AD mode | 72 |
| 5.2.1.2 | NID mode | 75 |
| 5.2.1.3 | NIV mode | 80 |
| 5.2.1.4 | CI & BI modes | 84 |
| 5.3 | CMB anisotropies in isocurvature models | 91 |
| 5.4 | Effect of cosmological parameters on the isocurvature CMB temperature power spectrum | 100 |
| 5.4.1 | Baryon density $\Omega_b h^2$ | 101 |
| 5.4.2 | Matter density $\Omega_m h^2$ | 104 |
| 5.4.3 | Cosmological constant density Ω_Λ | 106 |
| 5.4.4 | Curvature density Ω_K | 107 |
| 5.4.5 | Optical depth τ_e | 108 |
| 5.4.6 | Spectral index n_s | 110 |
| 6 | Fundamental Uncertainty in the BAO Scale from Isocurvature Modes | 112 |
| 6.1 | Introduction | 112 |
| 6.2 | The BAO peak with adiabatic and isocurvature initial conditions | 114 |
| 6.3 | Dark energy constraints | 118 |
| 6.4 | Conclusions | 124 |

| | | |
|----------|---|------------|
| 7 | The Sensitivity of BAO Dark Energy Constraints to General Isocurvature Perturbations | 125 |
| 7.1 | Introduction | 125 |
| 7.2 | The BAO peak with adiabatic and isocurvature initial conditions | 127 |
| 7.2.1 | AD mode | 131 |
| 7.2.2 | NID mode | 135 |
| 7.2.3 | NIV mode | 138 |
| 7.2.4 | CI & BI modes | 141 |
| 7.2.4.1 | Time evolution of the BAO peak position | 145 |
| 7.3 | Impact of isocurvature modes on dark energy constraints | 146 |
| 7.3.1 | Statistical Formalism | 146 |
| 7.3.1.1 | Large Scale Structure (LSS) surveys | 148 |
| 7.3.1.2 | Cosmic microwave background (CMB) surveys | 151 |
| 7.3.2 | The impact of isocurvature modes on dark energy | 153 |
| 7.3.2.1 | Constraints on isocurvature modes from the LSS data | 158 |
| 7.4 | Conclusions | 169 |
| 8 | Conclusion | 171 |
| | Bibliography | 175 |
| | Appendix | 185 |
| A | Matter Power Spectrum Derivatives with respect to the Isocurvature Parameters | 185 |

CHAPTER 1

Introduction

Over the last two decades, there has been a dramatic increase in both the quantity and the quality of cosmological data from different observations. These observational data have greatly improved our understanding of the whole universe by testing different theoretical models about the origin, the structure and the evolution of the universe. Among these observations, three main cosmological probes can be highlighted: the measurements of the cosmic microwave background (CMB) anisotropies with the Wilkinson Microwave Anisotropy Probe (WMAP) [127, 125], the discovery of the acceleration of the expansion of the universe using supernovae [144, 133] and the detection of the imprint of baryon acoustic oscillations (BAO) in the early universe on galaxy clustering [46, 37].

The CMB radiation and more precisely its temperature anisotropies, is undeniably the most important and accurate source of data today. The CMB is the residual radiation from decoupling after the epoch of recombination when the universe was only a few hundred thousand years old. It has a perfect thermal black-body spectrum and an isotropic temperature, one part in 10^5 , of 2.7 K today. Having traveled essentially undisturbed ever since, it is a powerful tool to probe of

the early universe. More interestingly, its tiny anisotropies reflect the small perturbations in the energy density of the universe at the time of the initial conditions.

The measurement of the expansion of the universe from the supernovae indicates that the expansion of the universe has begun to gradually accelerate instead of decelerating as one would expect [133]. This acceleration has strengthened the dark energy case. It is not known whether the universe will accelerate indefinitely or whether it will eventually reverse.

Large scale structure (LSS) surveys aim to construct a three dimensional distribution of the galaxies in the universe and measure the matter power spectrum [142, 172]. This dataset is currently expanding rapidly. It comes from a much later period and on smaller scales than the CMB. Although it has not yet reached the same level of accuracy as the CMB data, it is a powerful tool for constraining cosmological models [90]. In this thesis, we use information from both the CMB and the LSS.

From all the available data, we now know much more about the composition and the geometry of the universe. A model of the history and structure of the universe has arisen: The standard cosmological model, also called the concordance model. In this model, we live in a flat or nearly flat universe that is roughly 13.7 Gyr old and made up of slightly less than thirty percent non-relativistic matter, of which only about one sixth is ordinary baryonic matter, the remaining being cold dark matter (CDM), with seventy percent of the energy density in the form of dark energy. The cold dark matter is some non-baryonic matter in the universe which cannot be observed by its electromagnetic radiation while at the same time the particles making up this matter are slowly moving. The existence of the cold dark matter is inferred from the motions of astronomical objects, specifically stellar, galactic, and galaxy cluster observations [36]. It is also required in order to enable gravity to amplify the small fluctuations in the Cosmic Microwave Background enough to form the large-scale structures that we see in the universe today. The dark energy is a hypothetical form of energy that explains observations that the universe appears to be expanding at an accelerating rate. Its nature is still a mystery but is commonly thought to be a residual

vacuum energy density, also referred to as the cosmological constant Λ , or a time varying scalar field such as quintessence [130]. Present data favours a model of dark energy with the equation of state i.e. the ratio of pressure to energy density being close to -1 [163]. Photons and neutrinos constitute a tiny fraction of the total density of the universe today.

Although much progress has been made in understanding the universe, many conceptual and technical problems remain unsolved. For example, the nature of the fluctuations which generated anisotropies in the CMB and the large scale structure remains not well understood. Several different mechanisms of generating the primordial fluctuations have been proposed among which, the cosmological inflation is currently the favourite. There are many variants of inflation, but they all have in common that, during the first few fractions of a second, the energy density of the universe was dominated by one or more scalar fields. The simplest variants use a single field and predict that the primordial fluctuations are adiabatic and drawn from a Gaussian distribution. Although current data does not show evidence of significant non-gaussianity [163], one must wait for the analysis of the Planck data in order to confirm or discard this trend [93].

In addition to the statistics and form of the primordial fluctuations, the initial conditions that the fluctuations satisfy also present a challenge for modern cosmology. Although adiabatic primordial perturbations are generally assumed, there are two fundamental types of perturbations, adiabatic and isocurvature [25, 29, 61, 78]. For adiabatic perturbations, the fractional overdensity in each component (baryons, photons, cold dark matter and neutrinos) is the same up to a constant, which gives rise to a curvature perturbation. Isocurvature perturbations are generated during inflation whenever there is more than one scalar field present [109, 134]. They are predicted by a wide range of scenarios: multifield inflation, topological defects, the decay of particles prior to nucleosynthesis such as a scalar curvaton or axions, etc [29]. For isocurvature perturbations, the fractional overdensities add up to zero, keeping the curvature initially unperturbed, which creates an entropy perturbation. The location of the first acoustic peak in the CMB temperature power spectrum $l \approx 220.7 \pm 0.7$ as measured by WMAP [88, 13, 70], strongly suggests adiabatic initial conditions for the cosmological perturbations [173]. However, there is no a priori

reason to discard more general initial conditions involving isocurvature perturbations as they can be generated by several different mechanisms [111, 109, 87, 120, 137, 147, 148, 96, 131, 10]. While current observations exclude pure isocurvature models [44, 51, 127, 70, 88], they still allow for an admixture of adiabatic and isocurvature contributions [88, 17, 14, 177]. The most general situation is the superposition of the adiabatic, the cold dark matter isocurvature (CI) and the neutrino isocurvature density (NID) and velocity (NIV) modes [29, 121, 173, 32].

Testing the nature of the primordial perturbations requires a good understanding of the different possibilities of the initial conditions [122]. The CI mode have been studied previously [25]. It excites a sine wave rather than a cosine wave, as is the case for adiabatic conditions [78], and produces a first peak in the power spectrum located at $l \approx 330$ [25, 92, 102, 175] with the height of the peak differing from the adiabatic mode. The baryonic isocurvature (BI) mode behaves like the CI mode [25] and can be neglected [65]. The neutrino isocurvature density and velocity modes recently introduced [29, 102] are characterized by a non-zero initial entropy perturbation in the neutrino density with respect to the photon density or by a relative velocity between the photon and the neutrino components with a vanishing total momentum density [29]. In this thesis, we consider a more generic situation where we allow the possibility of several isocurvature modes in addition to the adiabatic one.

In this thesis, we investigate the signatures of isocurvature initial conditions in the CMB through the temperature anisotropies, and in the large-scale structure distribution through the BAO.

The thesis is structured as follows. In the second chapter, we briefly review the standard cosmological model and supplement it with a general discussion on the initial conditions of the primordial fluctuations. In the third and fourth chapters, we review respectively the evolution of the perturbations and the CMB anisotropies in the adiabatic models. The fifth chapter investigates the observational signatures of the isocurvature perturbations in the CMB anisotropies. In the sixth chapter, we explore the distortion of the standard ruler distance and the degradation of dark energy constraints due to the inclusion of isocurvature perturbations. The seventh chapter

discusses in more detail the sensitivity of BAO dark energy constraints to general isocurvature perturbations. In the last chapter of the thesis, we present concluding remarks.

CHAPTER 2

The Standard Cosmological Model

Over the course of past several decades, a huge amount of observational data has greatly improved our understanding of the universe by testing different theoretical models about the origin, the structure and the evolution of the universe. The currently accepted view is that the observed large scale structures of the universe such as galaxies and galaxy clusters, and the CMB anisotropies originated from some small initial fluctuations in the matter and radiation in the early universe and grew under gravitational instability. For such fluctuations, the linear perturbation theory can be used to solve for the growth of the fluctuations. The perturbation theory allows examining the initial conditions of the fluctuations, their evolution and their imprint on the large scale structures and on the CMB. This picture represents the standard cosmological model.

In this chapter, we briefly introduce the standard cosmological model with its underlying linear cosmological perturbation theory that provides a basis for understanding the formation of the large scale structures of the universe and anisotropies in the CMB. We first present the underlying pillars of the model, introduce the unperturbed and the perturbed Friedmann-Robertson-Walker cosmological models and argue for our choice of the gauge. We then introduce the Einstein

equations and the energy momentum conservation principle to derive the differential evolution equations for the four species of the universe. Lastly, we supplement the standard cosmological model with a discussion on the initial conditions of the primordial fluctuations.

2.1 Brief overview

The Big Bang model, based on the homogeneous and isotropic Friedmann-Robertson-Walker (FRW) spacetimes, is undeniably the prevailing cosmological theory describing with unprecedented success the evolution of the universe on large scales. The evidence for angular isotropy on large scales of the CMB as well as the isotropy of deep galaxy and radio source surveys strongly support the assumption of homogeneity and isotropy. This assumption, with the Copernican principle leads to the conclusion that the universe is spatially homogeneous and constitutes the cosmological principle, cornerstone of the standard cosmology. Four main observational pillars support this model: the expansion of the universe, the abundances of the light elements in agreement with the predictions of nucleosynthesis, the thermal spectrum of the CMB radiation and the large-scale structures observed in the universe.

2.1.1 The expansion of the universe (Hubble's law)

Distant galaxy and quasar surveys show that these objects are moving away from us and the further away an object is, the more rapid its recession appears to be. This universal expansion, predicted by Alexander Friedmann in 1922 [55] and Georges Lematre in 1927 [99], and first observed by Edwin Hubble in 1929 [80] constitutes Hubble's law which states that the recessional velocity v of a galaxy is proportional to the its distance d away from us

$$v = Hd,$$

where H is known as the Hubble parameter. WMAP experiment has determined its value today to be $H_0 = 70.4 \pm 1.4 \text{ km sec}^{-1} \text{ Mpc}^{-1}$ [81].

2.1.2 Light element abundances

Prior to about one second after the Big Bang, the universe was very hot and dense. As it expanded and cooled, some nucleons were synthesized into the light elements such as hydrogen (H), deuterium (D), helium-3 (^3He), helium-4 (^4He) and lithium-7 (^7Li). The abundances of these light elements depend only on the ratio of photons to baryons, which itself can be independently calculated from fluctuations in the CMB. The measured abundances all agree with those predicted from the Big Bang Nucleosynthesis (BBN), except for the lithium which presents a discrepancy of a factor of 2.3 – 4.3 from abundances inferred from observations of Population II star due to substantial systematic uncertainties [39].

2.1.3 Cosmic microwave background radiation

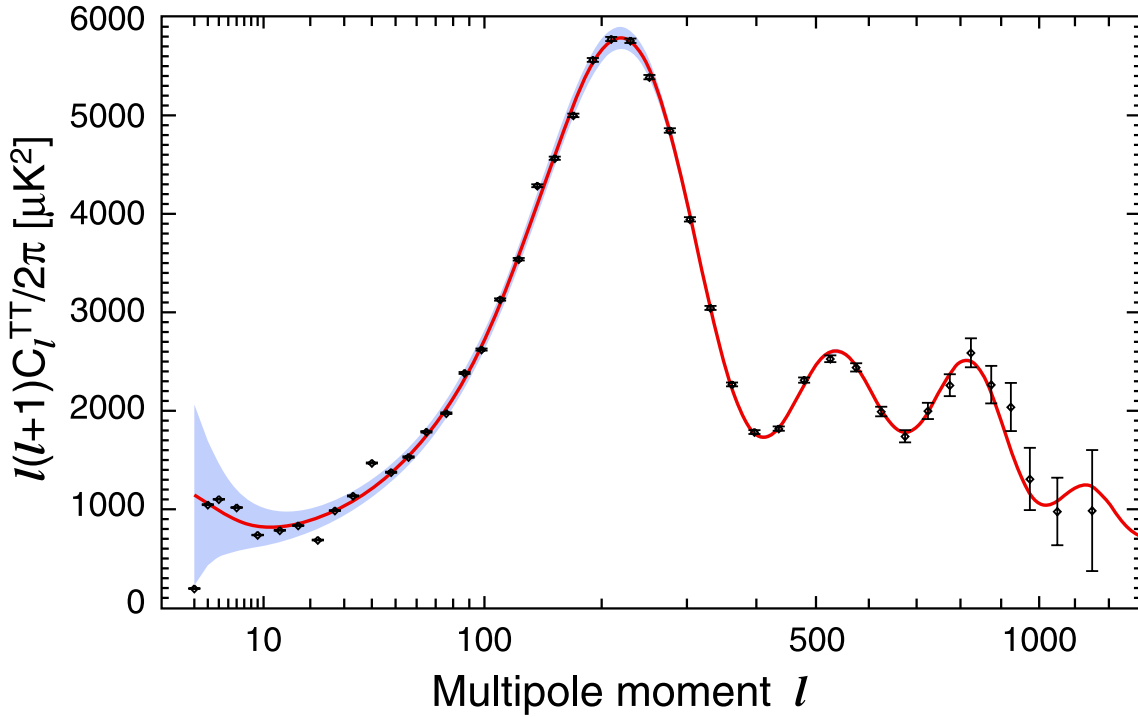


Figure 2.1: CMB temperature anisotropy spectrum. This is from the 7-year WMAP data. The plotted errors include instrument noise, but not the small, correlated contribution due to beam and point source subtraction uncertainty. The blue band represents cosmic variance.

Since its accidental discovery by Arno Penzias and Robert Wilson in 1964 [132], the CMB radiation is considered a landmark of the Big Bang model. It is the radiation left over from the early hot universe that free streams towards us from the epoch of last scattering, approximately 379,000 years after the Big Bang, cooling as the universe expands. Precise measurements by the Far Infrared Absolute Spectrophotometer (FIRAS) instrument on the Cosmic Background Explorer (COBE) satellite revealed perfect black body spectrum of the CMB at a temperature of 2.725 K and detected for the first time the fluctuations in the CMB, at a level of 10^{-5} K [161]. Figure 2.1.3 combines measurements of the CMB anisotropies by various observational experiments. The existence of the CMB and its blackbody spectrum were predicted by Gamow in 1946 and Alpher and Herman in 1948 [59, 6]. Large number of ground-based experiments, balloon experiments and satellite experiments has been since undertaken. More recently, the WMAP experiment has yielded the most accurate values for some of the cosmological parameters [69, 16].

The smoothness of the CMB confirmed that the universe had earlier undergone a brief period of rapid exponential expansion, called inflation. In addition, studies on the effects of the dynamics of distant astrophysical objects on the CMB have provided further evidence for the Copernican principle [164].

2.1.4 Evolution and distribution of galaxies

The large scale structures such as galaxy clusters and superclusters, and the morphology and distribution of galaxies and quasars, as well as observations of star formation are in good agreement with simulations of the structure formation based on the Big Bang model [20]. The morphology of distant galaxies differs from the nearby galaxies due to the star populations that are aging and evolving. In addition, for galaxies situated at comparable distance, recently formed galaxies appear different from galaxies formed shortly after the Big Bang. The large scale structures originated from the primordial fluctuations that were generated during inflation. According to the inflationary paradigm, the expansion of the universe was accelerated during an early epoch of the universe, well before the period of primordial nucleosynthesis. In this period, primordial density

and gravitational wave perturbations were generated from quantum fluctuations redshifted out of the Hubble radius, where they remain frozen until they re-enter the Hubble radius [123, 106].

2.2 Age and energy contents of the universe

According to the standard cosmological model and in view of recent experiments, the universe is believed to be flat with mean energy density (critical density) equal to $\bar{\rho}_{cr} = 9.9 \times 10^{-30} \text{ g cm}^{-3}$, 13.75 ± 0.11 billion years old and composed of relativistic components such as photons and neutrinos, relic of the Big Bang; atoms or ordinary matter called baryon; and of not yet well understood substances such as the dark energy and the dark matter. The baryonic matter (stars, galaxies, clusters, dusts,...) responsible for all visible matter in the universe, represents only about 4.6% of the total contents of the universe [88].

The dark energy which accounts for 72% of the contents of the universe, is a hypothetical form of energy that uniformly permeates all space with anti-gravitational properties tending to increase the rate of expansion of the universe. Its existence was first suggested by observations of Type Ia supernovae in 1998 when, independently, A.G. Riess *et al.* [144] and S. Perlmutter *et al.* [133] noticed that rather than slowing down, the expansion appeared to be speeding up. Since then, different and independent experiments such as the measurement of the CMB anisotropies [88], the gravitational lensing [150], and the large scale structure surveys [142], have corroborated these observations. Two popular forms for dark energy have been proposed: the cosmological constant Ω_Λ , equivalent to the vacuum energy filling space homogeneously, and scalar fields with energy density changing in space and time. The measurement of the equation of state of dark energy is currently one of the most active research areas in cosmology as it parameterizes the evolution of the expansion.

The cold dark matter which represents the remaining 23% of the contents of the universe, first postulated by Fritz Zwicky in 1934 to account for evidence of "missing mass" in the dynamics of galaxies in clusters, is a form of non-radiative and non-relativistic matter but detectable through gravitational interaction with the ordinary matter [186, 187]. The measurements of galaxy ve-

locities, gravitational lensing of background objects by galaxy clusters, and the temperature distribution of hot gas in galaxies and clusters of galaxies all point to the existence of the cold dark matter [145, 53, 178]. The cold dark matter plays a key role in structure formation and galaxy evolution, and has impacts on the CMB anisotropies [69].

2.3 Background and perturbed Friedmann-Robertson-Walker models

To describe a homogeneous and isotropic universe, we consider the FRW metric which describes a homogeneous, isotropic expanding universe. Its metric line element is given by

$$ds^2 = g_{\mu\nu}dx^\mu dx^\nu = a^2(\tau)[-d\tau^2 + \gamma_{ij}(\vec{x})dx^i dx^j], \quad (2.1)$$

where the indices μ and ν range from 0 to 3, a is the scale factor accounting for the expansion of the universe and $g_{\mu\nu}$ is the unperturbed Robertson-Walker metric. The spatial coordinates x^i take the range $1 < i, j < 3$, $\gamma_{ij} = g_{ij}/a^2$ is the symmetric spatial part of the metric for a constant curvature space and τ is the conformal time related to the proper time by $dt = a(\tau)d\tau$. The above metric is usually written using the spherical-like coordinates of a fundamental observer (r, θ, ϕ) as

$$ds^2 = a^2(\tau) \left(-d\tau^2 + \left[\frac{dr^2}{1 - \kappa r^2} + r^2(d\theta^2 + \sin^2 \theta d\phi^2) \right] \right), \quad (2.2)$$

where κ is a constant describing the (constant) curvature of the space. It can take the values 1, 0 or -1 corresponding to a closed (spherical), flat (euclidean) and open (hyperbolic) universe respectively. Units are chosen such that the speed of light is unity. The FRW is a direct consequence of the spatial homogeneity of the universe, independently of whether or not the Einstein equation is valid.

The unperturbed Robertson-Walker metric above describes a smooth homogeneous and isotropic expanding universe. In the presence of perturbations, there is no uniquely preferred coordinate system. However, the coordinates must reduce to those of equation (2.1) in the limit of zero

perturbation. A coordinate system meeting this requirement is called a gauge. To account for the inhomogeneity of the universe, we consider the perturbed Robertson-Walker metric. The most general first-order perturbation to the line element can be written as [106]

$$ds^2 = a^2(\tau)[-d\tau^2 + \gamma_{ij}(\vec{x})dx^i dx^j + h_{\mu\nu}(\vec{x}, \tau)dx^\mu dx^\nu], \quad (2.3)$$

where $h_{\mu\nu}$ is the metric perturbation. Its components can be explicitly written as

$$h_{00} = -2A, \quad h_{0i} = -B_i, \quad h_{ij} = 2(D\gamma_{ij} + E_{ij}), \quad (2.4)$$

where E_{ij} is a traceless 3-metric. The trace of h_{ij} is proportional to D . For a flat universe ($\kappa = 0$), a cartesian coordinate can be chosen such that $\gamma_{ij} = \delta_{ij}$. The term A is called the lapse function and is a perturbation to the conformal time component. It specifies the relation between τ and the proper time along the threading. B_i is the shift function which specifies the relative velocity between the threading and the worldlines orthogonal to the slicing and $2(D\delta_{ij} + E_{ij})$ is the perturbation to the curvature of space.

The components of the metric perturbation are further broken down into scalar, vector and tensor perturbations by decomposing every symmetric tensor and every vector into longitudinal and transverse parts. The “tensor mode” E_{ij}^T represents the part of h_{ij} that cannot be obtained from the gradient of a scalar or vector. It is a gauge-invariant. Physically, it represents gravitational waves and the anisotropic stress that can interact with them. The “vector mode” corresponds to the transverse vector parts of the metric, which are found in B_i^\perp and E_{ij}^\perp . It is a generalization of purely rotational fluid flow with anisotropic stress. Each part has 2 degrees of freedom, but by imposing a gauge condition, it is possible to eliminate two of them. The “scalar mode” is spin-0 under spatial rotation and corresponds physically to Newtonian gravitation with relativistic modifications. It is generally believed that the scalar mode is generated by the vacuum fluctuation of the inflation field. Any two of the scalar parts of the metric A , D , B_i^\parallel and E_{ij}^\parallel can be set to zero by a gauge transformation.

The scalar, vector and tensor modes evolve independently in linear perturbation theory. Therefore each mode can be examined separately. In this thesis, we only consider scalar perturbations and

restrict our study to a spatially flat background spacetime. The line element simplifies to

$$ds^2 = a^2(\tau)\{-(1 + 2A)d\tau^2 - B_i d\tau dx^i + [(1 + 2D)\delta_{ij} + 2E_{ij}]dx^i dx^j\}, \quad (2.5)$$

where A , B_i , D and E_{ij} are fixed according to the choice of gauge.

A variety of gauges have been proposed in the literature. Among them, the conformal Newtonian (or longitudinal) gauge and the synchronous gauge are usually used in cosmology.

The conformal Newtonian gauge is a simple gauge for scalar modes of the metric perturbations, but can be generalized to include vector and tensor modes [19]. It is characterized by two scalar potentials ψ and ϕ with the latter playing the role of the gravitational potential in the Newtonian limit. The four scalar perturbations to the metric are given by $A = \psi$, $D = \phi$ and $B_i = E_{ij} = 0$. Thus the line element in this gauge is written as

$$ds^2 = a^2(\tau)[-(1 + 2\psi)d\tau^2 + (1 + 2\phi)\delta_{ij}dx^i dx^j]. \quad (2.6)$$

Since the metric $g_{\mu\nu}$ is diagonal, calculations in this gauge are simple. In addition, the gauge freedom is completely fixed as there is no gauge modes.

The synchronous gauge is a more general gauge including scalar, vector and tensor modes. Only the space-space component of the metric tensor is perturbed ($h_{00} = h_{0i} = 0$). Thus the line element in this gauge is given by

$$ds^2 = a^2(\tau)[-d\tau^2 + (\delta_{ij} + h_{ij})dx^i dx^j]. \quad (2.7)$$

The threading consists of geodesics and the slicing is orthogonal to the threading. As there is no unique threading, the synchronous description does not fix completely the coordinate system but leaves some residual gauge freedom. A particular threading can be chosen to impose adiabatic or isocurvature initial conditions. The synchronous gauge offers a convenient computational frame and various publicly available Boltzmann codes are written in this gauge.

It is always possible to pass from the longitudinal gauge to the synchronous gauge and vice versa using a gauge transformation.

A gauge transformation is an infinitesimal first-order change in coordinates in the perturbed spacetime, from one coordinate system x^μ to another \hat{x}^μ given by

$$\hat{x}^\mu = x^\mu + d^\mu(x^\nu). \quad (2.8)$$

Thus the conformal Newtonian potentials ϕ and ψ are related to the synchronous potentials h and η in k -space by [114]

$$\psi(k, t) = \dot{\alpha} + \frac{\dot{a}}{a}\alpha, \quad \phi(k, t) = \eta - \frac{\dot{a}}{a}\alpha, \quad (2.9)$$

where α is defined by $\alpha \equiv (\dot{h} + 6\dot{\eta})/2k^2$. The potential η comes from writing the scalar mode of $h_{ij}(x, \tau)$ as a Fourier integral as [114]

$$h_{ij}(\vec{k}, \tau) = \hat{k}_i \hat{k}_j h(\vec{k}, \tau) + (\hat{k}_i \hat{k}_j - \frac{1}{3}\delta_{ij})6\eta(\vec{k}, \tau),$$

where we repeat the use of h for the trace part of the perturbation in Fourier space, $\vec{k} = \hat{k}k$ and \hat{k} is the unit vector pointing in the traveling direction of the wave. In this thesis, we mostly use the synchronous gauge although some few times, the conformal gauge is referred to mainly for physical intuition. The overdot stands for the derivative with respect to the conformal time. Similarly, a species density contrast, δ_x , and its velocity divergence, θ_x , in the conformal and synchronous gauges are related by [114]

$$\delta_x^{\text{Con}} = \delta_x^{\text{Syn}} - 4\alpha\frac{\dot{a}}{a}, \quad (2.10)$$

$$\theta_x^{\text{Con}} = \theta_x^{\text{Syn}} + \alpha k^2. \quad (2.11)$$

2.4 Einstein equations and energy momentum conservation

The Einstein's field equations have undeniably revolutionized the development of the modern cosmology during the last century. They relate the Einstein tensor $G_{\mu\nu}$ describing the geometry to the energy-momentum tensor $T_{\mu\nu}$ describing the matter contents, and are given by

$$G_{\mu\nu} = R_{\mu\nu} - g_{\mu\nu}\frac{R}{2} = 8\pi GT_{\mu\nu}. \quad (2.12)$$

In this relation $R_{\mu\nu}$ and $R \equiv g^{\mu\nu}R_{\mu\nu}$ are the Ricci tensor and scalar respectively. The Ricci tensor depends on the metric and its derivatives, and can be most conveniently written as

$$R_{\mu\nu} = \Gamma_{\mu\nu,\alpha}^{\alpha} - \Gamma_{\mu\alpha,\nu}^{\alpha} + \Gamma_{\beta\alpha}^{\alpha}\Gamma_{\mu\nu}^{\beta} - \Gamma_{\beta\nu}^{\alpha}\Gamma_{\mu\alpha}^{\beta},$$

where the $\Gamma_{\alpha\beta}^{\mu}$ are the Christoffel symbols given by

$$\Gamma_{\alpha\beta}^{\mu} = \frac{g^{\mu\nu}}{2} \left[\frac{\partial g_{\alpha\nu}}{\partial x^{\beta}} + \frac{\partial g_{\beta\nu}}{\partial x^{\alpha}} - \frac{\partial g_{\alpha\beta}}{\partial x^{\nu}} \right],$$

and commas denote derivatives with respect to x , for example $\Gamma_{\mu\nu,\alpha}^{\alpha} \equiv \partial \Gamma_{\mu\nu}^{\alpha} / \partial x^{\alpha}$. We also define the covariant derivative denoted by a semi-colon, that will be used later in this chapter as

$$T_{\nu;\mu}^{\mu} \equiv \frac{\partial T_{\nu}^{\mu}}{\partial x^{\mu}} + \Gamma_{\alpha\mu}^{\mu} T_{\nu}^{\alpha} - \Gamma_{\nu\mu}^{\alpha} T_{\alpha}^{\mu}. \quad (2.13)$$

Thus, Einstein equations relate the perturbations in the metric to the perturbations in matter and radiation [41]. For a homogeneous universe with energy density $\bar{\rho}(\tau)$ and pressure $\bar{P}(\tau)$, the Einstein equations give the following evolution equations [114]:

$$H^2 = \left(\frac{\dot{a}}{a} \right)^2 = \frac{8\pi}{3} G a^2 \bar{\rho} - \kappa, \quad (2.14)$$

$$\frac{d}{d\tau} H = \frac{d}{d\tau} \left(\frac{\dot{a}}{a} \right) = -\frac{4\pi}{3} G a^2 (\bar{\rho} + 3\bar{P}), \quad (2.15)$$

where we have defined the Hubble parameter in conformal time, $H = \dot{a}/a$. The equation (2.14) is nothing else but the Friedmann equation which gives the time evolution of the scale factor $a(\tau)$, and equation (2.15) is the acceleration equation. Equation (2.15) shows that the acceleration of the expansion of the universe is due to the density and pressure filling the universe, with positive acceleration requiring a component with negative pressure $\bar{P} < -\bar{\rho}/3$.

The matter components of the universe (baryons and cold dark matter) can be treated as ideal fluid at all time allowing to be completely described by the energy density contrast δ and the velocity divergence θ while, for the radiation components (neutrinos and photons), a full treatment requires the use of the Boltzmann equation. Nevertheless, in the baryon-photon tight-coupling regime, the single fluid can be treated as perfect fluid without loss of accuracy. Here, we do not consider the case of massive neutrinos. The energy-momentum tensor for such a fluid is given by [114]

$$T_{\nu}^{\mu} = \sum_n P_n g_{\nu}^{\mu} + (\rho_n + P_n) V^{\mu} V_{\nu}, \quad (2.16)$$

where $V^\mu = dx^\mu/\sqrt{-ds^2}$ is the four-velocity of the fluid, $\rho = \bar{\rho} + \delta\rho$ and $P = \bar{P} + \delta P$ are the proper energy density and pressure in the fluid rest frame respectively. The barred quantities refer to the background, and $\delta\rho$ and δP are respectively the density and pressure fluctuations. We are summing over all components in the universe. Explicitly, we can write the components of the perturbed energy-momentum tensor as

$$T_0^0 = -(\bar{\rho} + \delta\rho), \quad (2.17)$$

$$T_i^0 = (\bar{\rho} + \bar{P})v_i = -T_0^i, \quad (2.18)$$

$$T_j^i = (\bar{P} + \delta P)\delta_j^i + \Sigma_j^i, \quad \Sigma_i^i = 0, \quad (2.19)$$

where $v_i \equiv dx^i/d\tau$ is the coordinate velocity of the fluid (assumed non-relativistic), and $\Sigma_j^i \equiv T_j^i - \delta_j^i T_k^k/3$ is the anisotropic shear perturbation which denotes the traceless component of T_j^i . $\bar{\rho}(\tau)$ and $\bar{P}(\tau)$ are respectively the energy (or mass) density and pressure of the FRW background universe.

Let us define new variables θ and σ as

$$(\bar{\rho} + \bar{P})\theta \equiv ik^j \delta T_j^0, \quad (2.20)$$

$$(\bar{\rho} + \bar{P})\sigma \equiv -(\hat{k}_i \hat{k}_j - \frac{1}{3}\delta_{ij})\Sigma_j^i, \quad (2.21)$$

where $\theta = ik^j v_j$ is the divergence of the fluid velocity and σ is related to the shear stress. We also define the density contrast $\delta \equiv \delta\rho/\bar{\rho} = -\delta T_0^0/\bar{\rho}$.

Substituting the metric and the stress-energy tensor in the Einstein equation, we deduce the field equations for the perturbations[114]:

$$k^2\eta - \frac{1}{2}\frac{\dot{a}}{a}\dot{h} = -4\pi Ga^2\delta\rho, \quad (2.22)$$

$$k^2\dot{\eta} = 4\pi Ga^2(\bar{\rho} + \bar{P})\theta, \quad (2.23)$$

$$\ddot{h} + 2\frac{\dot{a}}{a}\dot{h} - 2k^2\eta = -8\pi Ga^2\delta P, \quad (2.24)$$

$$\ddot{h} + 6\ddot{\eta} + 2\frac{\dot{a}}{a}(\dot{h} + 6\dot{\eta}) - 2k^2\eta = -24\pi Ga^2(\bar{\rho} + \bar{P})\sigma. \quad (2.25)$$

The time-time component of the Einstein equation (2.22) looks like the Poisson equation. In the limit of no expansion ($\dot{a} = 0$), it reduces to the ordinary Poisson equation for gravity viz $\nabla^2 \eta = -4\pi a^2 G \delta \rho$. The terms proportional to \dot{a} account for the expansion and are typically important for modes with wavelengths ($\lambda \sim a/k$) comparable to, or larger than the Hubble radius H^{-1} .

We label the different species of the universe with subscript $j = 1, \dots, n$, define the critical density of the universe $\bar{\rho}_{cr}$ as the total density needed for a flat universe ($H^2 = 8\pi G a^2 \bar{\rho}_{cr}/3$) and denote by $\Omega_j \equiv \bar{\rho}_j/\bar{\rho}_{cr}$ the ratio of the density of the j^{th} species to the critical density. The set of equations (2.22)-(2.25) can be written as

$$k^2 \eta - \frac{1}{2} \frac{\dot{a}}{a} \dot{h} = -\frac{3}{2} H^2 \bar{\rho}_{cr} \sum_j \Omega_j \delta_j, \quad (2.26)$$

$$k^2 \dot{\eta} = \frac{3}{2} H^2 \bar{\rho}_{cr} \sum_j \Omega_j (1 + w_j) \theta_j, \quad (2.27)$$

$$\ddot{h} + 2 \frac{\dot{a}}{a} \dot{h} - 2k^2 \eta = -9H^2 \bar{\rho}_{cr} \sum_j \Omega_j c_{sj}^2 \delta_j, \quad (2.28)$$

$$\ddot{h} + 6\ddot{\eta} + 2 \frac{\dot{a}}{a} (\dot{h} + 6\dot{\eta}) - 2k^2 \eta = -9H^2 \bar{\rho}_{cr} (1 + w_j) \Omega_j \sigma_j. \quad (2.29)$$

where $w_j = p_j/\rho_j$ is the equation of state for the j^{th} species and $c_s^2 = \partial p_j/\partial \rho_j$ is its sound speed squared.

Combining equations (2.22) and (2.24) we eliminate η and obtain a useful equation which expresses the metric h in terms of the density perturbations:

$$\ddot{h} + \frac{\dot{a}}{a} \dot{h} = -8\pi G a^2 (\delta \rho + \delta P). \quad (2.30)$$

The energy-momentum conservation principle tells us that

$$T^{\mu\nu}{}_{;\mu} = \partial_\mu T^{\mu\nu} + \Gamma_{\alpha\beta}^\nu T^{\alpha\beta} + \Gamma_{\alpha\beta}^\alpha T^{\nu\beta} = 0, \quad (2.31)$$

and leads to the following time evolution equations for the density perturbations and the diver-

gence of the fluid velocity

$$\dot{\delta} = -(1+w) \left(\theta + \frac{\dot{h}}{2} \right) - 3 \frac{\dot{a}}{a} \left(\frac{\delta P}{\delta \rho} - w \right) \delta, \quad (2.32)$$

$$\dot{\theta} = -\frac{\dot{a}}{a}(1-3w)\theta - \frac{\dot{w}}{1+w}\theta + \frac{\delta P/\delta \rho}{1+w}k^2\delta - k^2\sigma, \quad (2.33)$$

where w is given by the equation of state $w \equiv P/\rho$. If w is constant, as we shall consider, the equations simplify further since $\delta P/\delta \rho \equiv c_s^2 = w$ and $\dot{w} = 0$. The equations (2.32) and (2.33) are valid for the global fluid. They are also valid for a fluid component which does not interact with other components. In the case of interaction we have to add some corrective terms. This is the case for baryons which couple to photons through Thomson scattering before recombination. The full set of time evolution equations for photons, baryons, cold dark matter and massless neutrinos are [114]:

$$\dot{\delta}_\gamma = -\frac{4}{3}\theta_\gamma - \frac{2}{3}\dot{h}, \quad (2.34)$$

$$\dot{\delta}_b = -\theta_b - \frac{1}{2}\dot{h}, \quad (2.35)$$

$$\dot{\delta}_c = -\frac{1}{2}\dot{h}, \quad (2.36)$$

$$\dot{\delta}_\nu = -\frac{4}{3}\theta_\nu - \frac{2}{3}\dot{h}, \quad (2.37)$$

for the density contrasts δ , and

$$\dot{\theta}_\gamma = k^2 \left(\frac{1}{4}\delta_\gamma - \sigma_\gamma \right) + an_e\sigma_T(\theta_b - \theta_\gamma), \quad (2.38)$$

$$\dot{\theta}_b = -\frac{\dot{a}}{a}\theta_b + c_s^2k^2\delta_b + \frac{4\bar{\rho}_\gamma}{3\bar{\rho}_b}an_e\sigma_T(\theta_\gamma - \theta_b), \quad (2.39)$$

$$\theta_c = 0, \quad (2.40)$$

$$\dot{\theta}_\nu = k^2 \left(\frac{1}{4}\delta_\nu - \sigma_\nu \right), \quad (2.41)$$

for the velocity divergences. The indices γ , b , c and ν correspond to photons, baryons, cold dark matter and relativistic neutrinos respectively, σ_T is the Thomson cross section, n_e is the electron number density, and $\bar{\rho}_\gamma$ and $\bar{\rho}_b$ are the density of photons and baryons respectively.

The shear stress of the radiation (photons and neutrinos) is relevant once the radiation component has decoupled from the matter component for a mode within the horizon and must be taken into account. Therefore we supplement two equations for the quadrupole [114]. The photon shear stress is particularly useful for studying the primary CMB polarization.

$$\dot{\sigma}_\gamma = \frac{4}{15}\theta_\gamma - \frac{3}{10}kF_{\gamma 3} + \frac{2}{15}\dot{h} + \frac{4}{5}\dot{\eta} - \frac{9}{10}an_e\sigma_T\sigma_\gamma, \quad (2.42)$$

$$\dot{\sigma}_\nu = \frac{4}{15}\theta_\nu - \frac{3}{10}kF_{\nu 3} + \frac{2}{15}\dot{h} + \frac{4}{5}\dot{\eta}, \quad (2.43)$$

where $F_{\nu 3}$ and $F_{\gamma 3}$ are the third moments of the momentum-averaged phase space densities for neutrinos and photons. A complete treatment requires a hierarchy of multipole moments to describe the full distribution function of the radiation component [41, 152].

2.5 Initial conditions

Although the standard cosmological model is well established, some problems remain. Among them is the nature of the primordial fluctuations that eventually led to the formation of the observed large scale structure. There are two possible approaches. In the first approach, fluctuations were generated during the rapid expansion of the universe and linearly imprinted in the matter and radiation contents early in the radiation dominated era. For the second approach, the fluctuations were generated during the radiation and matter eras through some causal mechanism [29, 61]. In this work we adopt the first option. Different possible regular (finite as τ goes to zero) sets of initial conditions are allowed and grouped in adiabatic and isocurvature modes. The adiabatic mode, by far the most studied to date, is characterized by the requirement that the densities of all species are perturbed in proportion at some initial time i , independently of the wavenumber k such that

$$\delta_{c,i} = \delta_{b,i} = \frac{3}{4}\delta_{\gamma,i} = \frac{3}{4}\delta_{\nu,i}, \quad (2.44)$$

where the subscript i labels the initial time. Or equivalently, using the relative entropy between two species x and y given by $\mathcal{S}_{xy} = \frac{\delta_x}{1+w_x} - \frac{\delta_y}{1+w_y}$, where w_x and w_y are the equation of state parameters of the species x and y respectively, we have that $\mathcal{S}_{xy} = 0$ for all pairs of species at

initial time. In addition, all velocity divergences are initially unperturbed. The adiabatic mode is a prediction of the simplest inflationary model [67]. This is due to the fact that inflatons, quantum fluctuations of the field responsible for inflation, give directly rise to perturbations in the energy density of the inflaton field [50]. Though current datasets show that the initial fluctuations were dominantly adiabatic [88], this does not exclude mixtures of adiabatic and isocurvature modes. Recent works have investigated general admixtures in the initial conditions [13, 14, 31, 121] and found that the current datasets allow admixtures with an isocurvature fraction up to forty percent for the CMB temperature and the LSS datasets combined [13, 29]. The isocurvature fraction is expected to be slightly less than ten percent with CMB polarization from PLANCK [30].

The isocurvature modes, also called entropy perturbations, are characterized by the fact that the abundance ratios of different particle species are not spatially constant initially but vary from place to place. They are predicted by a wide range of scenarios as discussed in [29]. Four regular isocurvature modes are distinguished, namely the cold dark matter isocurvature, the baryon isocurvature, the neutrino isocurvature density and the neutrino isocurvature velocity modes.

In the cold dark matter isocurvature mode first proposed by Bond and Efstathiou [24, 25], the cold dark matter to photon ratio varies spatially. Fluctuations are initially imprinted in the cold dark matter component of the universe while the other components are initially unperturbed.

This can be written at some initial time as

$$\delta_{c,i} = 1, \quad \delta_{b,i} = \delta_{\gamma,i} = \delta_{\nu,i} = 0. \quad (2.45)$$

A pure cold dark matter isocurvature mode gives about 30 times more power in the matter perturbations on large scales and consequently yields excessive anisotropies in the CMB [63, 140].

The baryon isocurvature was introduced by Peebles [129] initially for a universe made of baryons, photons and neutrinos. In this mode the baryon to photon ratio is initially spatially perturbed.

This can be written at some initial time as

$$\delta_{c,i} = 0, \quad \delta_{b,i} = 1, \quad \delta_{\gamma,i} = \delta_{\nu,i} = 0. \quad (2.46)$$

A pure baryonic isocurvature mode lacks a curvature component at early time and causes earlier re-ionization and galaxy and star formation, discrepancies in the peculiar velocities on small scales and in the flow velocities on large scales [166, 165].

The neutrino isocurvature density and velocity modes were first introduced in 1999 by M. Bucher *et al.* [29]. In the neutrino isocurvature density mode, the densities of the matter components (baryon and cold dark matter) are initially unperturbed while the initial perturbation in the neutrino density is balanced by its photon counterpart, keeping the curvature unperturbed. Thus the neutrino to photon ratio is initially spatially perturbed but the total density perturbation vanishes. The species initial perturbations are as follows:

$$\delta_{c,i} = \delta_{b,i} = 0, \quad \delta_{\gamma,i} = -\frac{R_\nu}{R_\gamma} \delta_{\nu,i}, \quad (2.47)$$

where we denote the fractional contributions from neutrinos and photons to the total density at times early in the radiation era by R_ν and R_γ , respectively.

For the neutrino isocurvature velocity mode, contrarily to the other isocurvature modes, there is no relative entropy perturbation in the density field at some initial time. The rest frame of the neutrino and the photon do not coincide. The neutrino velocity divergence is initially perturbed but compensated by the baryon-photon common velocity so that the total momentum density vanishes. The species initial perturbations are given by:

$$\theta_{c,i} = 0, \quad \theta_{b,i} = \theta_{\gamma,i} = -\frac{R_\nu}{R_\gamma} \theta_{\nu,i}. \quad (2.48)$$

In the previous section we have derived the set of equations (2.34)-(2.41) governing the perturbations around a smooth background. For each scale k this system of equations can be solve uniquely given suitable initial conditions during the radiation-dominated era, well before horizon entry of the corresponding mode. In this thesis, “horizon” abusively denotes the Hubble distance $d_H = a\tau$, which is the physical distance that the light has travelled in a given lifetime of the universe. In the next chapter, we briefly review the evolution of the different species under adiabatic initial conditions.

CHAPTER 3

Evolution of Cosmological Perturbations: Adiabatic case

The evolution of cosmological perturbations can be subdivided into three stages. First, at *very early times* where all k -modes are outside the horizon ($k\tau \ll 1$) and the gravitational potential ϕ is constant as we shall show later; then, the *intermediate times* where, progressively, the k -modes enter the horizon, small scale and large scale modes evolving differently as they enter the horizon at different times, and the universe passes from being radiation dominated to matter dominated; and finally the *late times* where all the k -modes evolve identically again. In this chapter, we review the evolution of the perturbations in adiabatic models. We first focus on the evolution of the dark matter as it constitutes the main component of most cosmological models, and review the effect of the other components on the matter perturbation evolution. We then present the photon and baryon evolution in the tight-coupling regime. The evolution of the photons after decoupling requires using a full statistical treatment. This will be done in the next chapter. After decoupling, the baryons follow the evolution of the dark matter. Here, we do not consider the evolution of the neutrinos as these decouple very early and therefore, are not relevant for this study. In this chapter, we closely follow the description in [41].

In the previous chapter, we presented the set of time evolution equations for photons, baryons, cold dark matter and massless neutrinos in the synchronous gauge. However, most studies of the adiabatic case are done in the conformal gauge. This makes simpler the interpretation of the different gauge quantities. In the conformal gauge, these can be respectively written for the photons, baryons, cold dark matter and neutrinos as [114]

$$\dot{\delta}_\gamma = -\frac{4}{3}\theta_\gamma + 4\dot{\phi}, \quad (3.1)$$

$$\dot{\delta}_b = -\theta_b + 3\dot{\phi}, \quad (3.2)$$

$$\dot{\delta}_c = -\theta_c + 3\dot{\phi}, \quad (3.3)$$

$$\dot{\delta}_\nu = -\frac{4}{3}\theta_\nu + 4\dot{\phi}, \quad (3.4)$$

for the density contrasts δ , and

$$\dot{\theta}_\gamma = k^2 \left(\frac{1}{4}\delta_\gamma - \sigma_\gamma \right) + k^2\psi + an_e\sigma_T(\theta_b - \theta_\gamma), \quad (3.5)$$

$$\dot{\theta}_b = -\frac{\dot{a}}{a}\theta_b + c_s^2 k^2 \delta_b + \frac{4\bar{\rho}_\gamma}{3\bar{\rho}_b} an_e\sigma_T(\theta_\gamma - \theta_b) + k^2\psi, \quad (3.6)$$

$$\dot{\theta}_c = -\frac{\dot{a}}{a}\theta_c + k^2\psi, \quad (3.7)$$

$$\dot{\theta}_\nu = k^2 \left(\frac{1}{4}\delta_\nu - \sigma_\nu \right) + k^2\psi, \quad (3.8)$$

for the velocity divergences θ . Here for the gravitational potential ϕ , we have adopted the sign convention in [41]. For this review, we follow closely the work of Hu and Dodelson [41, 75]. For the gravitational potential, we supplement the above set with the field equations (2.22) and (2.23) which, in the conformal gauge, can be written as

$$k^2\phi + 3\frac{\dot{a}}{a} \left(\dot{\phi} + \frac{\dot{a}}{a}\phi \right) = 4\pi G a^2 \delta\rho, \quad (3.9)$$

$$k^2 \left(\dot{\phi} + \frac{\dot{a}}{a}\phi \right) = 4\pi G a^2 (\bar{\rho} + \bar{P})\theta, \quad (3.10)$$

where we have set $\psi = \phi$, in the limit that there is no quadrupole moments. For convenience, equations (3.9) and (3.10) can be combined to eliminate the derivatives of the potential and

remain with an algebraic equation for the gravitational potential given by

$$k^2\phi = 4\pi G a^2 \left(\delta\rho - \frac{3H}{k^2}(\bar{\rho} + \bar{P})\theta \right). \quad (3.11)$$

3.1 Cold dark matter evolution

We would like to study the evolution of the dark matter overdensity. We consider the dark matter evolution equations (3.3) and (3.7) and ignore the baryons as they only represent about 4% of the total energy density. The radiations, both photons and neutrinos, contribute to the gravitational potential which in turn, is closely related to the dark matter in the limit of small baryon density. The collision term in equation (3.5) can be neglected (tight-coupling regime). This allows one to treat the photons and neutrinos as one component and write its evolution equations as

$$\dot{\delta}_r = -\frac{4}{3}\theta_r + 4\dot{\phi}, \quad (3.12)$$

$$\dot{\theta}_r = k^2\frac{1}{4}\delta_r + k^2\dot{\phi}, \quad (3.13)$$

where the subscript r stands for radiation. An analytic solution for the dark matter, valid at all times and on all scales is hard to derive. One looks for solution in certain limits of time and scales. We therefore consider the large and small scale modes separately.

3.1.1 Large scales

On very large scales, analytic solutions for the potential can be obtained through the matter-radiation transition and through horizon crossing.

3.1.1.1 Super-horizon solution

For the super-horizon modes, modes that are far outside the horizon, all terms dependent on the velocity divergence $\theta = ikv$ can be neglected in the density evolution equations. In addition, in this limit, the velocity divergences decouple from the density contrasts. The set of equations (3.12), (3.3) and (3.9) becomes

$$\dot{\delta}_r = 4\dot{\phi}, \quad (3.14)$$

$$\dot{\delta}_c = 3\dot{\phi}, \quad (3.15)$$

$$3\frac{\dot{a}}{a} \left(\dot{\phi} + \frac{\dot{a}}{a}\phi \right) = 4\pi G a^2 \delta \rho. \quad (3.16)$$

Equations (3.14) and (3.15) require $\delta_c - \frac{3}{4}\delta_r$ to be constant, equal to zero in the adiabatic mode.

We then substitute $\delta_r = \frac{4}{3}\delta_c$ in equation (3.16) to get

$$3\frac{\dot{a}}{a} \left(\dot{\phi} + \frac{\dot{a}}{a}\phi \right) = 4\pi G a^2 \rho_c \delta_c \left[1 + \frac{4}{3y} \right], \quad (3.17)$$

where we have defined a new variable y as

$$y \equiv \frac{a}{a_{eq}} = \frac{\rho_c}{\rho_r}. \quad (3.18)$$

The derivatives in equation (3.16) can be written using the variable y . This leads to

$$y\phi' + \phi = \frac{3y+4}{6(y+1)}\delta_c. \quad (3.19)$$

Here, we have used $\frac{d}{d\tau} = Hy\frac{d}{dy}$. Prime denotes derivatives with respect to y . A second order differential equation can be obtained by differentiating equation (3.19) and combining with equation (3.15). Thus we get

$$y\phi'' + \frac{21y^2 + 54y + 32}{2y(y+1)(3y+4)}\phi' + \frac{\phi}{y(y+1)(3y+4)} = 0, \quad (3.20)$$

whose solution, first derived by Kodama and Sasaki [86], is

$$\phi = \frac{\phi(0)}{10y^3} \left[16\sqrt{1+y} + 9y^3 + 2y^2 - 8y - 16 \right] \quad (3.21)$$

Equation (3.21) is the solution for the gravitational potential on super-horizon scales. It tells us that, in the limit of small y , equation (3.21) reduces to $\phi = \phi(0)$. For large y , when the universe is matter dominated, $\phi = \frac{9}{10}\phi(0)$. Thus on large scales, the gravitational potential drops by 10% as the universe passes from being radiation dominated to matter dominated. The

gravitational potential decay is not instantaneous, but occurs in a quite long period, after the matter-radiation equality. For cosmological models with less matter, the matter-radiation equality epoch is closer to decoupling so that the gravitational potential decay is more apparent even at the time of recombination. Figure 3.1 represents the evolution of the gravitational potential on large scales.

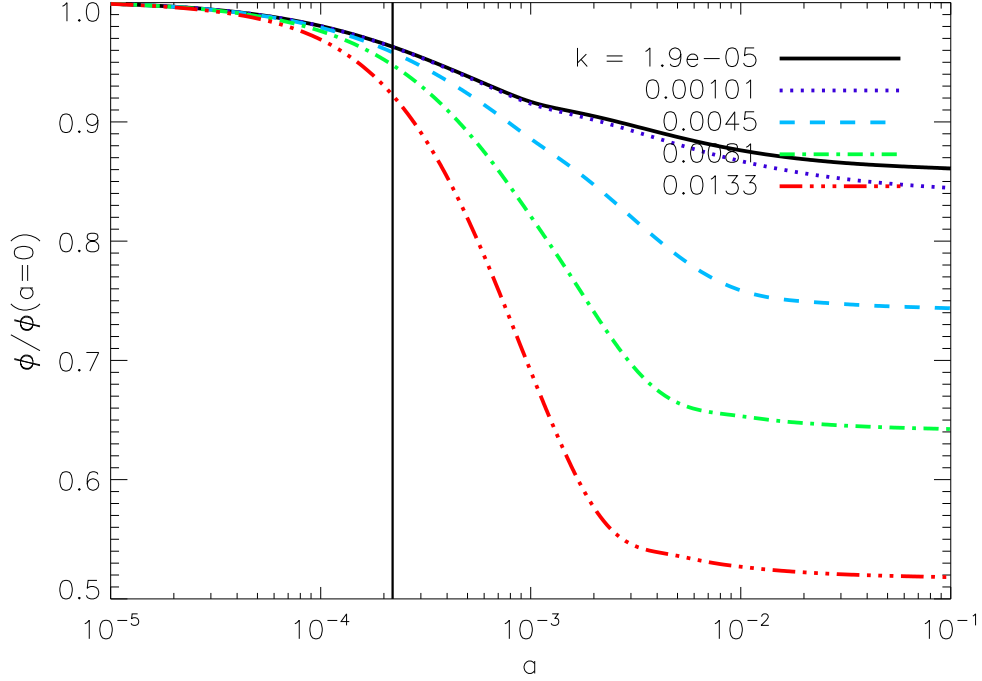


Figure 3.1: Super horizon evolution of the gravitational potential in a flat Λ CDM model with $h = 0.7$, $\Omega_b = 0.0449$, $\Omega_c = 0.245$.

3.1.1.2 Through horizon crossing

In the limit that radiation is not important, that is deep in the matter dominated era, equations (3.12) and (3.13) can be neglected as the gravitational potential depends only on the matter inhomogeneities. From the previous solution, we saw that the gravitational potential is constant deep in the matter dominated era. This allows us to set $\dot{\phi} = 0$ as the initial conditions for this problem. We consider the field equation (3.11) and neglect the radiation components therein to

get the following equation

$$k^2\phi = \frac{3}{2}H^2 \left[\delta_c + \frac{3H}{k^2}\theta_c \right]. \quad (3.22)$$

We use equation (3.22) to eliminate δ_c from equations (3.3) and (3.7), knowing that in the matter dominated era, $H \propto a^{-1/2}$ so that $dH/d\tau = -H^2/2$. Equation (3.3) becomes

$$\frac{2k^2\dot{\phi}}{3H^2} + \frac{2k^2\phi}{3H} - \frac{3H\dot{\theta}_c}{k^2} + \frac{3H^2\theta_c}{2k^2} + \theta_c = 0. \quad (3.23)$$

We would like to get a second order differential equation as for the previous case. To this end, we first eliminate $\dot{\theta}_c$ from equation (3.23) using the velocity divergence equation (3.7). This leads to

$$\frac{2k^2\dot{\phi}}{3H^2} + \left[\frac{\theta_c}{k^2} + \frac{2\phi}{3H} \right] \left(\frac{9H^2}{2} + k^2 \right) = 0. \quad (3.24)$$

Now, if the second order differential equation has no terms proportional to ϕ , then constant gravitational potential is one of the solutions to the differential equation. With this mind, we then differentiate equation (3.24) with respect to the conformal time, dropping all terms proportional to derivatives of the potential and using $\frac{d}{d\tau}H^{-1} = \frac{1}{2}$. Thus we are left with

$$\left[\frac{\dot{\theta}_c}{k^2} + \frac{\phi}{3} \right] \left(\frac{9H^2}{2} + k^2 \right) + \left[\frac{\theta_c}{k^2} + \frac{2\phi}{3H} \right] \frac{d}{d\tau} \frac{9H^2}{2} = - \left[\frac{H\theta_c}{k^2} + \frac{2\phi}{3} \right] (9H^2 + k^2), \quad (3.25)$$

where we have eliminated $\dot{\theta}_c$ by using the velocity divergence equation again. The terms in the square brackets on both left and right hand sides of equation (3.25) can be expressed in terms of $\dot{\phi}$ using equation (3.24). Thus, there are no terms proportional to the gravitational potential in the second order differential equation. Therefore, constant gravitational potential is the solution in the matter dominated era. Thus the gravitational potential remains constant as long as the universe is matter dominated. At later times, when the universe is dark energy dominated, the gravitational potential decays.

3.1.2 Small scales

In the previous sub-section, we solved for the evolution of the perturbations that crossed the horizon well after the epoch of matter radiation equality. In this section, we solve for the evolution

of the perturbations that crossed the horizon deep in the radiation dominated era. We shall separately consider modes in the radiation dominated era crossing the horizon and the sub-horizon modes passing through the matter radiation equality epoch. It is difficult to analytically solve for modes which enter the horizon around the epoch of the matter radiation equality.

3.1.2.1 Horizon crossing

In the radiation dominated era, the gravitational potential is determined by the radiation perturbations. The gravitational potential sources the matter perturbations but the latter do not influence the gravitational potential. Therefore, to solve for the matter perturbations in this case, we first need to solve for the gravitational potential, then finally solve for the matter perturbations using the gravitational potential as an external driving force. We consider the algebraic equation (3.11) and neglect the matter density contrasts therein as they are small compared to the radiation density contrasts deep in the radiation dominated era and get

$$\phi = \frac{6H^2}{k^2} \left[\frac{1}{4}\delta_r + H\theta_r \right], \quad (3.26)$$

since $H^2 = 8\pi a^2 G\rho_r/3$ in the radiation dominated era. Equation (3.26) is used to eliminate δ_r from equations (3.1) and (3.5). These become

$$-\frac{1}{k^2\tau}\dot{\theta}_r + \theta_r \left[1 + \frac{3}{k^2\tau^2} \right] = -\dot{\phi} \left[1 + \frac{k^2\tau^2}{6} \right] - \phi \frac{k^2\tau}{3}, \quad (3.27)$$

$$\dot{\theta}_r + \frac{1}{3}\theta_r = -k^2\phi \left[1 - \frac{k^2\tau^2}{6} \right]. \quad (3.28)$$

We use equation (3.28) to eliminate $\dot{\theta}_r$ from equation (3.27) and differentiate the latter with respect to the conformal time to get the following second order differential equation

$$\ddot{\phi} + \frac{4}{\tau}\dot{\phi} + \frac{k^2}{3}\phi = 0. \quad (3.29)$$

To solve for the gravitational potential ϕ , equation (3.29) can be turned into the spherical Bessel equation of order 1 by defining a variable $u = \phi\tau$. Equation (3.29) becomes

$$\ddot{u} + \frac{2}{\tau}\dot{u} + \left(\frac{k^2}{3} - \frac{2}{\tau^2} \right) u = 0. \quad (3.30)$$

The two solutions of equation (3.30) are the spherical Bessel function $j_1(k\tau/\sqrt{3})$, and the spherical Neumann function $n_1(k\tau/\sqrt{3})$. The latter is discarded on the basis of the initial conditions as it blows up for very small τ . Expressing the spherical Bessel function in terms of trigonometric functions, the gravitational potential can be written as

$$\phi = 3\phi_p \left(\frac{\sin(k\tau/\sqrt{3}) - (k\tau/\sqrt{3}) \cos(k\tau/\sqrt{3})}{(k\tau/\sqrt{3})^3} \right), \quad (3.31)$$

where ϕ_p is the primordial value of ϕ . Equation (3.31) describes the evolution of the gravitational potential for modes crossing the horizon in the radiation dominated era. As the mode enters the horizon, its potential first decays then oscillates. In the limit of large $k\tau$, the gravitational potential oscillates with an amplitude decreasing as τ^{-2} .

With the knowledge of the gravitational potential in the radiation dominated era, let us solve for the matter perturbation evolution. To this end, we consider the matter evolution equations (3.3) and (3.7) and turn them into a second order differential equation, differentiating equation (3.3) and using equation (3.7) to eliminate $\dot{\theta}_c$. We get

$$\ddot{\delta}_c + \left(\frac{\dot{a}}{a} \theta_c - k^2 \phi \right) = -3\ddot{\phi}. \quad (3.32)$$

The term in θ_c can be eliminated using equation (3.3). This leads to

$$\ddot{\delta}_c + \frac{1}{\tau} \dot{\delta}_c = -3\ddot{\phi} + k^2 \phi - \frac{3}{\tau} \dot{\phi}, \quad (3.33)$$

where the right hand side is the source term. We shall denote it by $S(k, \tau)$. The solutions to the homogeneous part of equation (3.33) are $\delta_c = \text{constant}$ and $\delta_c = \ln(a)$. Therefore, the general solution to equation (3.33) can be written as

$$\delta_c(k, \tau) = C_1 + C_2 \ln(\tau) - \int_0^\tau S(k, \tau') \tau' (\ln[k\tau'] - \ln[k\tau]) d\tau', \quad (3.34)$$

where the third term is constructed using the two homogeneous solutions and the source term [74]. The initial conditions, $\delta_c = \text{constant}$ at early times, dictates that $C_2 = 0$ and $C_1 = 3\phi_p/2$. As the source term in the integral, along with the gravitational potential, decays to zero as the mode enters the horizon, the dominant contribution to the integral occurs about $k\tau \approx 1$.

The integral over the first term leads to a constant, while the integral over the second term is proportional to $\ln(k\tau)$. Thus, as the mode enters the horizon, its matter density contrast is given by

$$\delta_c(k, \tau) = A\phi_p \ln(Bk\tau), \quad (3.35)$$

where the constant A and B are given by

$$A\phi_p = \int_0^\infty S(k, \tau') \tau' d\tau', \quad (3.36)$$

$$A\phi_p \ln(B) = \frac{3}{2}\phi_p - \int_0^\infty S(k, \tau') \tau' \ln(k\tau') d\tau'. \quad (3.37)$$

Equation (3.35) gives the matter evolution as the mode crosses the horizon. It tells us that the matter perturbations grow logarithmically during the radiation dominated era, slower than in the matter dominated era. This is due to the pressure of the radiation. As the universe approaches the matter dominated era, the radiation pressure becomes less important and the matter perturbations begin to grow faster. Figure 3.2 shows the evolution of the gravitational potential in the radiation for modes that enter the horizon well before equality.

3.1.2.2 Sub-horizon evolution

As we saw for the horizon crossing, the gravitational potential in the radiation dominated era, is determined by the radiation. However, as the matter perturbations grow, $\rho_c \delta_c$ eventually overtakes $\rho_r \delta_r$, even if ρ_c is still smaller than ρ_r . Once this takes place, the gravitational potential evolves together with the dark matter perturbations, independently of the evolution of the radiation perturbations. To solve for the evolution of the dark matter perturbations in this regime, we consider the matter evolution equations (3.3) and (3.7), and the algebraic field equation (3.11) while neglecting the radiation components therein as they are subdominant. For convenience, we use the variable y introduced in equation (3.18) as we aim to follow the dark matter perturbations through the epoch of the matter radiation equality. This leads to the following set of differential and algebraic equations

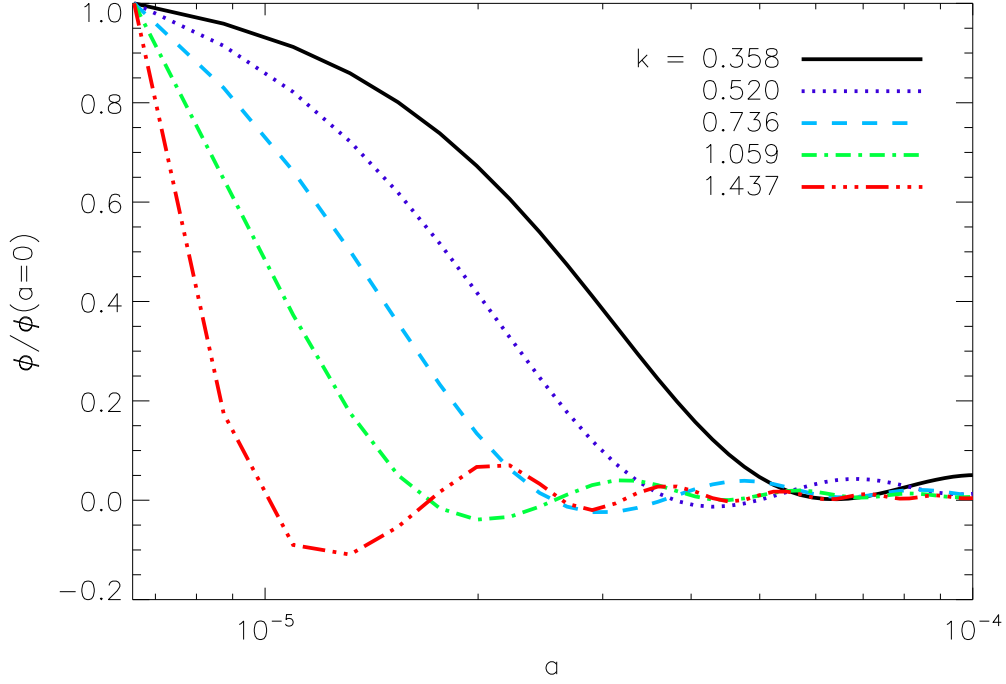


Figure 3.2: Evolution of the potential in the radiation-dominated era. These are small scale modes which enter the horizon well before equality. For a flat Λ CDM model with $h = 0.7$, $\Omega_b = 0.0449$, $\Omega_c = 0.245$.

$$\delta'_c + \frac{\theta_c}{Hy} = -3\phi', \quad (3.38)$$

$$\theta'_c + \frac{\theta_c}{y} = -\frac{k^2\phi}{Hy}, \quad (3.39)$$

$$k^2\phi = \frac{3y}{2(y+1)}H^2\delta_c, \quad (3.40)$$

where the $4\pi G\rho_c a^2$ factor is replaced by $(3/2)H^2 y/(y+1)$ since the universe is far from being dark energy dominated so that the dark energy is negligible. We would like to reduce this set of equation to a second order differential equation. We differentiate equation (3.38), eliminate θ'_c using equation (3.39) and use the fact that $d(1/Hy)/dy = -(1+y)^{-1}(2Hy)-1$ to get the following differential equation

$$\delta_c'' - \frac{(2+3y)\theta_c}{2Hy^2(1+y)} = -3\phi'' + \frac{k^2\phi}{H^2y^2}. \quad (3.41)$$

To eliminate θ_c , ϕ and its derivatives, we recall that for sub-horizon modes, the first term on the right hand side is much smaller than the second and therefore can be neglected since the second term is multiplied by k^2/H^2 . The matter velocity divergence θ_c and the gravitational potential ϕ can be respectively written in terms of δ_c' and δ_c using equations (3.38) and (3.40) and neglecting the gravitational potential which, on sub-horizon scales, is much smaller than δ_c . Thus equation (3.41) becomes

$$\delta_c'' + \frac{2+3y}{2y(y+1)}\delta_c' - \frac{3}{2y(y+1)}\delta_c = 0. \quad (3.42)$$

Equation (3.42) is the *Meszaros* equation. It gives the sub-horizon evolution of the cold dark matter once radiation perturbations have become irrelevant. By inspection, that is if δ_c' is constant, one of the two independent solutions of equation (3.42) is

$$D_1(y) = y + 2/3, \quad (3.43)$$

a first order polynomial in y which corresponds to the growing mode of the matter perturbations. The second solution can be derived knowing that the Meszaros equation tells that $u \equiv \delta_c/D_1$ satisfies

$$(1 + 3y/2)u'' + \frac{u'}{y(y+1)}[(21/4)y^2 + 3y + 1] = 0. \quad (3.44)$$

Integrating twice this equation leads to the second solution, the decaying mode

$$D_2(y) = D_1(y) \ln \left[\frac{\sqrt{1+y} + 1}{\sqrt{1+y} - 1} \right] - 2\sqrt{1+y}. \quad (3.45)$$

In the late time limit, that is $y \ll 1$, the decaying mode falls off as $y^{-3/2}$. Equations (3.43) and (3.45) are both k independent. This implies that at late times, all the modes evolve identically. The general solution to the Meszaros equation is then obtained by a linear combination of the growing and decaying modes as

$$\delta_c = C_1 D_1 + C_2 D_2 \quad \text{for } y \ll y_H, \quad (3.46)$$

where y_H is the ratio of the scale factor when the mode enters the horizon to the scale factor at the matter radiation equality. The constants C_1 and C_2 are determined by matching this solution to the logarithmic solution given by equation (3.35).

3.1.3 Matter transfer function and Power spectrum

The gravitational potential at the late times can be related to the primordial potential in the very early universe as

$$\phi(\vec{k}, a) = \phi_p(\vec{k}) \times T(k) \times D_1(a) \quad (3.47)$$

where $T(k)$ is the matter transfer function which describes the evolution of perturbations through the epochs of horizon crossing and matter radiation equality defined as

$$T(k) \equiv \frac{\phi(k, a_{late})}{\phi_{large-scale}(k, a_{late})}, \quad (3.48)$$

where a_{late} denotes an epoch well after the transfer function regime in the matter dominated era.

If we define the ratio of the gravitational potential at a given time to its value right after the transfer function regime as

$$\frac{\phi(a)}{\phi(a_{late})} \equiv \frac{D_1(a)}{a} \quad (a > a_{late}), \quad (3.49)$$

and for a flat, matter-dominated universe ($D_1(a) = a$), we have

$$\phi(\vec{k}, a) = \frac{9}{10} \phi_p(\vec{k}) T(k) \frac{D_1(a)}{a} \quad (a > a_{late}). \quad (3.50)$$

On the other hand, we can relate the matter over-density to the potential at late times using the Poisson's equation (small scales and no radiation limit of equation (3.11))

$$\phi = \frac{4\pi G \rho_m a^2 \delta_c}{k^2}. \quad (3.51)$$

From equation (3.51) and using the fact that $\rho_m = \Omega \rho_{cr}/a^3$ and $4\pi G \rho_{cr} = (3/2)H_0^2$, the matter density can be written as

$$\delta_c(\vec{k}, a) = \frac{k^2 \phi(\vec{k}, a) a}{(3/2)\Omega_m H_0^2} \quad (a > a_{late}). \quad (3.52)$$

Combining (3.52) and (3.50), we relate the over-density today to the primordial potential

$$\delta_c(\vec{k}, a) = \frac{3}{5} \frac{k^2}{\Omega_m H_0^2} \phi_p(\vec{k}) T(k) D_1(a) \quad (a > a_{late}). \quad (3.53)$$

We define the matter power spectrum $P(k)$ of the primordial perturbation to the metric as [41]

$$\langle \phi(\vec{k}) \phi^*(\vec{k}') \rangle = (2\pi)^3 P_\phi(k) \delta_c^3(\vec{k} - \vec{k}'). \quad (3.54)$$

The power spectrum measures the spread in the distribution of matter throughout the universe. It is large if there much underdense and overdense regions, and small if the distribution is homogeneous. It is shown that the primordial spectrum of density perturbations can be written as $P_i(k) = Ak^n$ where n is the spectral index. Harrison, Zel'dovich and Peebles showed that for the simplest inflationary model, $n = 1$ [66, 184]. The power spectrum of the matter at late times is given by

$$P(k, a) = 2\pi^2 \delta_H^2 \frac{k^n}{H_0^{n+3}} T^2(k) \left(\frac{D_1(a)}{D_1(a=1)} \right)^2. \quad (3.55)$$

This equation relates the power spectrum of the matter distribution to the primordial power spectrum produced during inflation given by $P_\phi = (50\pi^2/9k^3)(k/H_0)^{n-1} \delta_H^2 (\Omega_m/D_1(a=1))^2$, the transfer function and the growth function.

3.1.4 Growth function

We derived the Meszaros equation (3.42) assuming a universe made of matter and radiation only. Here, we generalize the Meszaros equation to account for the dark energy which dominates the universe at late times. Let us consider the set of equations (3.38)-(3.40). At late time, the variable $y \gg 1$ and the radiation density is insignificant. We combine these equations to get a second order differential equation as before, differentiating equation (3.38), setting $4\pi G\rho_c = (3/2)H_0^2\Omega_m a^{-3}$ and using the continuity equation to eliminate the velocity divergence term. This leads to

$$\frac{d^2 \delta_c}{da^2} + \left(\delta d \ln(H) da + \frac{3}{a} \right) \frac{d\delta_c}{da} - \frac{3\Omega_m H_0^2}{2a^5 H^2} \delta_c = 0, \quad (3.56)$$

where we use the scale factor as the variable instead of y . Equation (3.56) has two solutions. The first solution, $\delta_c \propto H \propto a^{-3/2}$, is a decaying mode. The second solution, the one that accounts for the lasting k -modes of the perturbations long after horizon crossing can be obtained by letting $u = \delta_c/H$. We then have

$$\frac{d^2 u}{da^2} + 3 \left[\frac{d \ln(H)}{da} + \frac{1}{a} \right] \frac{du}{da} = 0. \quad (3.57)$$

We integrate twice and substitute back $\delta_c = uH$ to get the expression for the growing mode

$$D_1(a) = AH(a) \int_0^a \frac{da'}{(a'H(a'))^3}, \quad (3.58)$$

where, the proportionality constant A is determined knowing that at late times in the matter dominated era, D_1 should be equal to a . At those time, $H = H_0 \Omega_m^{1/2} a^{-3/2}$. Equation (3.58) becomes

$$D_1(a) = \frac{5\Omega_m}{2} \frac{H(a)}{H_0} \int_0^a \frac{da'}{(a'H(a')/H_0)^3}. \quad (3.59)$$

Equation (3.59) gives the growth of the matter perturbations at late times for a flat universe. In the matter dominated era, it reduces to the scale factor a . For an open universe, a similar equation can be derived. In both cases, open matter dominated universe or flat dark energy dominated universe, the growth is suppressed. Therefore, structures in an open universe or in a dark energy dominated universe develop much earlier than in a flat, matter dominated universe.

3.1.5 Including other species

Besides the cold dark matter, which is the main component in most cosmological models, let us consider the baryons and dark energy. The photon evolution is treated in the next chapter. In this section, we briefly look at how the other species affect the matter perturbations.

As the baryons only represent about 4% of the total energy density of the universe, their effect on the matter power spectrum is small. Nonetheless, two main signatures are worth to notice. First, loading baryons suppresses power on small scales. This is due to the fact that the radiation perturbations undergo a decay when entering the horizon, causing the baryon overdensities to

also decay due to the tight coupling before decoupling. Secondly, baryons imprint ripples on the matter transfer function due to the acoustic oscillations before decoupling. Although this effect is less noticeable, it is important as it relates to the feature of the radiation.

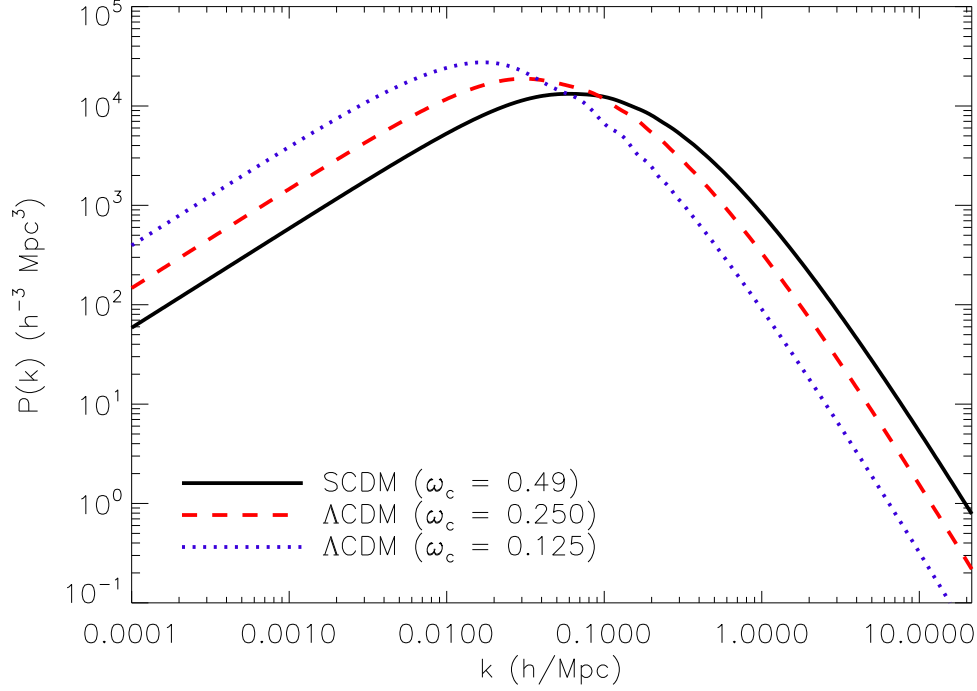


Figure 3.3: Effect of the dark energy on the matter power spectrum.

The dark energy has three main effects on the matter perturbations. First, since introducing the dark energy implies that Ω_m is less than one, the turnover in the matter power spectrum is shifted to small wavenumber as the turnover scale is proportional to the matter density Ω_m . Figure 3.3 show how the matter power spectrum shifts to the left as we introduce the dark energy. Secondly, the dark energy is indirectly related to the small matter density. For a fixed gravitational potential, the Poisson equation (3.52) implies that the overdensities are inversely proportional to the matter density. Consequently, the matter density decreases, the amplitude of the matter power spectrum increases. Thirdly, as we saw in the previous section, introducing the dark matter changes the growth factor at late times. The growth factor in a dark energy dominated era is given by equation

(3.59). As it depends on the Hubble rate, which in turn depends on the model of the dark energy, different models of dark energy will have different growth factors. For a flat universe, the Hubble rate is given by

$$\frac{H(z)}{H_0} = \left[\frac{\Omega_m}{a^3} + \frac{\Omega_{de}}{a^{3[1+w]}} \right]^{1/2}. \quad (3.60)$$

Thus the Hubble rate and therefore the growth factor depends on both the density Ω_{de} and the parameterization of the dark energy.

3.2 Evolution of photons and baryons prior to decoupling

The evolution of the photons and baryons can be separated in two distinct epochs: The period prior to decoupling where photons and baryons evolve together as a single perfect fluid, and the post decoupling period where the photons freestream and the baryons fall into the gravitational potential wells set by the dark matter. Here, we only consider the pre-decoupling period. The tight-coupling approximation of photons and baryons allows us to equate θ_γ and θ_b . Thus combining equations (2.38) and (2.39) leads to

$$(1 + R)\dot{\theta}_{\gamma b} = -\dot{R}\theta_{\gamma b} + k^2\left(\frac{1}{4}\delta_\gamma - \sigma_\gamma\right) + c_s^2 k^2 R \delta_b, \quad (3.61)$$

where $\theta_{\gamma b}$ is the baryon photon common velocity divergence. We differentiate equation (2.34) and make use of equation (3.61) to derive the following second order differential equation for the photon density perturbation

$$\ddot{\delta}_\gamma + \frac{\dot{R}}{1 + R}\dot{\delta}_\gamma + k^2 c_s^2 \delta_\gamma = -\frac{2}{3} \left[\frac{\dot{R}}{1 + R} \dot{h} + \ddot{h} \right], \quad (3.62)$$

where we have neglected the photon shear and the pressure term in δ_b as it remains smaller than the term in δ_γ prior to decoupling. Equation (3.62) represents a driven harmonic oscillator with the competition between gravitational infall and photon pressure giving rise to acoustic waves propagating in the photon-baryon fluid at the speed of sound. For the associated homogeneous equation, we look for solutions of the form $\delta_\gamma \propto \exp[i \int_0^\tau \omega d\tau']$ where $\omega(\tau)$ is some phase function. The two solutions to the homogeneous equation are simply $\sin kr_s$ and $\cos kr_s$ where

$r_s(\tau) = \int_0^\tau c_s d\tau'$ is the sound horizon, and the phase function is $\omega = kc_s$. Here we have made use of the Wentzel-Kramers-Brillouin (WKB) approximation. On large scales, the WKB approximation breaks down, but these modes are irrelevant for the CMB primary anisotropy treatment as they only enter the horizon well after decoupling. The particular solution is constructed by integrating the driving term weighed by the Green's function of the two homogeneous solutions [74]. Thus, the time evolution of the acoustic waves in the photon component prior to decoupling is given by

$$(1+R)^{1/2}\delta_\gamma(k, \tau) = A_S \sin kr_s(\tau) + A_C \cos kr_s(\tau) + \frac{1}{kc_s} \int_0^\tau (1+R(\tau'))^{1/2} \sin [kr_s(\tau) - kr_s(\tau')] F(\tau') d\tau', \quad (3.63)$$

where A_S and A_C are determined by the initial conditions as described in [29], and

$$F(\tau) = -\frac{2}{3} \left(\frac{\dot{R}}{1+R} \dot{h} + \ddot{h} \right), \quad (3.64)$$

is the gravitational driving term which evolves differently for different initial conditions. Equation (3.63) gives the time evolution of the photon density contrast irrespective of initial conditions, in the tight-coupling regime. In this regime, the baryon density contrast is related to its photon counterpart by $\dot{\delta}_b = \frac{3}{4}\dot{\delta}_\gamma$. On small scales, a correction to the tight-coupling approximation must be applied when Silk damping becomes important, as photons leak out of overdense regions, dragging baryons with them. This is done by multiplying the solution above by e^{-k^2/k_D^2} , where the photon diffusion scale k_D^{-1} is given by

$$k_D^{-2} = \frac{1}{6} \int \frac{1}{\dot{\tau}_e} \frac{R^2 + 4(1+R)/5}{(1+R)^2},$$

where $\dot{\tau}_e = an_e\sigma_T$ is the differential optical depth.

For the common photon-baryon velocity divergence, we differentiate equation (3.61) with respect to the conformal time and use $\dot{\delta}_\gamma = -\frac{4}{3}\theta_\gamma - \frac{2}{3}\dot{h}$ to obtain the second order differential equation

$$(1+R)\ddot{\theta}_{\gamma b} + 2\dot{R}\dot{\theta}_{\gamma b} + \left(\frac{k^2}{3} + \ddot{R} \right) \theta_{\gamma b} = -\frac{1}{6}k^2\dot{h}. \quad (3.65)$$

Equation (3.65) represents a forced and damped harmonic oscillator with variable coefficients. Its particular solution, applying the same method as for equation (3.62), is then given by

$$(1 + R)\theta_{\gamma b} = B_C \cos kr_s + B_S \sin kr_s - \frac{k}{6} \int_0^\tau \sqrt{3}(1 + R(\tau'))^{3/2} \sin k(r_s(\tau) - r_s(\tau')) \dot{h}(\tau') d\tau', \quad (3.66)$$

where B_C and B_S are determined by the initial conditions. This solution must be multiplied by $e^{-(k/k_D)^2}$ to correct the tight-coupling approximation.

The adiabatic mode is characterized by the requirement that the densities of all species are perturbed in proportion at some initial time such that

$$\delta_{c,i} = \delta_{b,i} = \frac{3}{4}\delta_{\gamma,i} = \frac{3}{4}\delta_{\nu,i}, \quad (3.67)$$

where the subscript i labels the initial time. Or equivalently, using the relative entropy between two species x and y given by $\mathcal{S}_{xy} = \frac{\delta_x}{1+w_x} - \frac{\delta_y}{1+w_y}$, where w_x and w_y are the equation of state parameters of the species x and y respectively, we have that $\mathcal{S}_{xy} = 0$ for all pairs of species at the initial time. In addition, all velocity divergences are initially unperturbed. Therefore, using the initial conditions for the adiabatic mode [29], the constant A_S and A_C in equation (3.63) are all zero. The photon and baryon density contrasts are respectively given by

$$\delta_\gamma^{AD} = \frac{\sqrt{3}}{k} e^{-k^2/k_D^2} \int_0^\tau (1 + R(\tau'))^{1/2} \sin [kr_s(\tau) - kr_s(\tau')] \times F^{AD}(\tau') d\tau', \quad (3.68)$$

$$\delta_b^{AD} = \frac{3}{4} \frac{\sqrt{3}}{k} e^{-k^2/k_D^2} \int_0^\tau (1 + R(\tau'))^{1/2} \sin [kr_s(\tau) - kr_s(\tau')] \times F^{AD}(\tau') d\tau'. \quad (3.69)$$

Thus, the adiabatic mode is only sourced by the gravitational driving term F^{AD} . This driving term can be approximated by

$$F^{AD}(k, \tau) \approx 2k^2 c_s^2 j_0(kr_s)$$

on small and intermediate scales which reduces to $2k^2 c_s^2$ at early times. On very large scales the above approximation breaks down, however, this does not affect our physical description of the CMB as these large-scale modes are well outside the horizon at decoupling and do not substantially influence the CMB features. The lack of an exact analytic expression for the driving

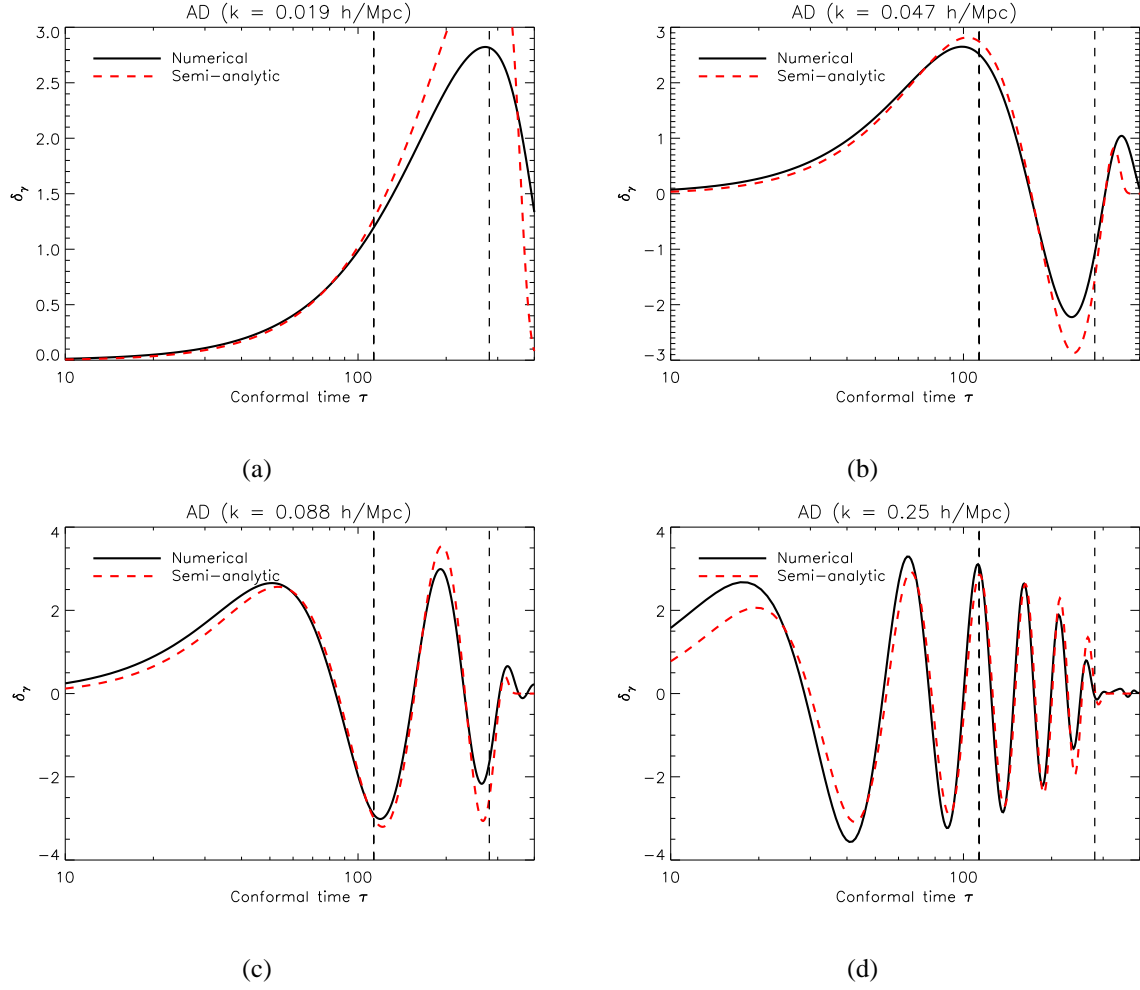


Figure 3.4: Evolution of the photon density contrast prior to decoupling for the AD mode: Comparison of numerical and analytic solutions for some wavenumbers. We consider $k = 0.019 \text{ h Mpc}^{-1}$ for the top-left panel, 0.047 h Mpc^{-1} for the top-right panel, 0.088 h Mpc^{-1} for the bottom-left panel and 0.25 h Mpc^{-1} for the bottom-right panel respectively. The vertical dashed lines mark the matter-radiation equality and decoupling.

term makes it difficult to derive exact analytic solutions for the time evolution of the photon and baryon density contrasts. Nevertheless, good approximations for the photon and baryon density contrasts are given by

$$\delta_\gamma = \frac{4}{3}\delta_b \approx 2kr_s j_1(kr_s) \times e^{-k^2/k_D^2}. \quad (3.70)$$

Therefore, at early times ($kr_s(\tau) \ll 1$) the density contrasts for the adiabatic mode, $\delta_\gamma \propto \delta_b \propto$

$(1 - \cos kr_s)$ couple to a $\cos kr_s$ harmonic [74]. Thus, the acoustic oscillation for the AD mode can be regarded as a forced oscillation with a cosine type phase.

CHAPTER 4

CMB Anisotropies: Adiabatic case

The main features of the CMB are determined by the fluctuations on the last scattering surface. At that time, the universe was nearly an homogeneous plasma with small fluctuations in the density and velocity fields of the particles, and in the gravitational potential. In this chapter, we recall how fluctuations on the last scattering surface translate into the CMB power spectrum as observed today. We first present a simpler calculation that highlights different contributions to the observed CMB anisotropy. For a formal and more detailed study of the photon evolution, which can no longer be treated as a perfect fluid after decoupling, we make use of a perturbed Bose-Einstein distribution function and introduce the line of sight integral approach for the computation of the CMB anisotropies and review the effect of the cosmological parameters on the CMB temperature power spectrum in the AD mode.

4.1 Sachs-Wolfe derivation

Before decoupling, the baryons and photons are coupled through Thomson scattering. The baryons are clustered in gravitational potential wells and since the photons are coupled to the

baryons, they are confined in potential wells created by the dark matter. Therefore, at the last scattering surface when the baryons and photons decouple, the photons have to climb out of the potential wells. In addition, the geodesics of the photons leaving the surface of last scattering are sensitive to the degree of homogeneity of the universe after matter-radiation equality. A photon traveling to us from decoupling will experience a shift in its energy. Thus, the primary anisotropies of the CMB can be considered as being generated in two distinct phases: before and after recombination. Although this description is only a qualitative approximation, it allows a clear and simpler understanding of the CMB physics. In this section we closely follow the derivation of the Sachs-Wolfe effect by Giovannini [61], Dodelson [41] and, Hu and Sugiyama [72].

The photon energy ε as measured in the frame of reference of the fluid, is given by

$$\varepsilon = g_{\mu\nu} u^\mu P^\nu = g_{00} u^0 P^0 + g_{ij} u^i P^j, \quad (4.1)$$

where u^μ is the four-velocity of the fluid and P^ν is the photon four-momentum. The four momentum of a photon can be written as

$$P^\nu = P^0 \frac{dx^\nu}{d\lambda} = \frac{P^0}{a^2} \frac{dx^\nu}{d\tau} = \frac{E}{a^2} \left[n^\nu + \frac{d}{d\tau} \delta x^\nu \right], \quad (4.2)$$

where E is a parameter defining the redshift in the photon energy, δ denotes the scalar perturbation to a variable and $n^\nu = (1, n^i)$ is the four-vector describing the direction of the photon.

Introducing the affine parameter s , the perturbed photon geodesic can be written as

$$\frac{d^2 \delta x^\mu}{d\tau^2} + \delta_s \Gamma_{\alpha\beta}^\mu \frac{dx^\alpha}{d\tau} \frac{dx^\beta}{d\tau} = 0, \quad (4.3)$$

where $\delta_s \Gamma_{\alpha\beta}^\mu$ are the perturbed Christoffel symbols of the metric $g_{\mu\nu}/a^2$. For $\mu = 0$ in equation (4.3) and integrating, we derive that

$$\frac{d\delta x^0}{d\tau} = \int_{\tau_i}^{\tau_0} (\dot{\phi} + \dot{\psi}) d\tau - 2\psi. \quad (4.4)$$

In order to obtain this equation, we have used the time Christoffel symbols $\delta_s \Gamma_{00}^0 = \dot{\psi}$, $\delta_s \Gamma_{ij}^0 = -\dot{\phi} \delta_{ij}$ and $\delta_s \Gamma_{0i}^0 = -\partial_i \psi$. As the four-velocity satisfies the normalization condition $g_{\mu\nu} u^\mu u^\nu = 1$, the first order in the fluctuations gives us [61, 2]

$$u^0 = \frac{1}{a}(1 - \psi). \quad (4.5)$$

In addition since an electron emits and absorbs a photon, the components of the four-velocity are related to the baryonic peculiar velocity v_b^i by

$$\delta_s u^i = \frac{v_b^i}{a} \equiv \frac{1}{a} \partial^i v_b. \quad (4.6)$$

Thus, substituting the four-velocity and the four-momentum (4.2) into the equation (4.1) and using equations (4.4) and (4.6), we can write

$$\varepsilon = \frac{E}{a} \left[1 - \psi - n_i v_b^i + \int_{\tau_i}^{\tau_0} (\dot{\phi} + \dot{\psi}) d\tau \right]. \quad (4.7)$$

The photon temperature fluctuation $\frac{\Delta T}{T}$ can be related to the difference between the final and the initial energies of the photon. If the initial photon energy is given by $E_{init} = E_0[1 + (\delta T/T)] \equiv E_0[1 + \delta_\gamma/4]$, the temperature fluctuation $\frac{\Delta T}{T}$ can be written, after integration, as

$$\left(\frac{\Delta T}{T} \right) = \frac{\delta_\gamma}{4} - [\psi]_{\tau_i}^{\tau_0} - [n_i v_b^i]_{\tau_i}^{\tau_0} + \int_{\tau_i}^{\tau_0} (\dot{\phi} + \dot{\psi}) d\tau. \quad (4.8)$$

Equation (4.8) gives the different contributions to the change in the photon temperature. The first contribution comes from the first two terms of the right hand side and constitute the so-called Sachs-Wolfe (SW) effect [146]. The second contribution, due to the baryon peculiar velocity is the Doppler effect, and the last term is the Integrated Sachs-Wolfe (ISW) effect which depends on the change in the potentials and photons travel [61, 78, 2, 181]. Figure 4.1 gives a qualitative representation of the different contributions to the CMB power spectrum.

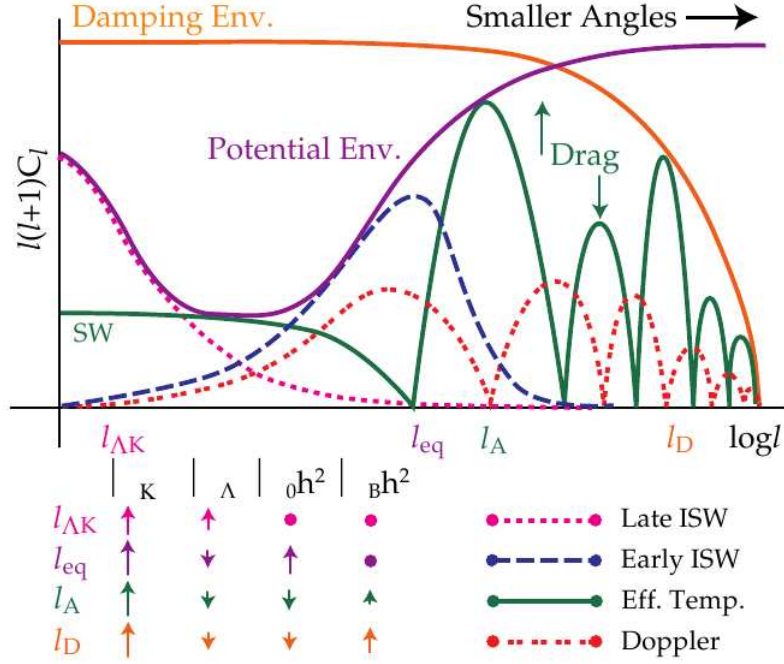


Figure 4.1: Different contributions to the CMB power spectrum. Source: Hu *et al.*, arXiv:astro-ph/9604166v1 (1996).

4.1.1 The ordinary Sachs-Wolfe effect

On large scales, the potentials ϕ and ψ are constant in time after the last scattering. Therefore, the only non-zero terms in equation (4.8) are the intrinsic density contrast of photons at the last scattering surface and the gravitational Newtonian potential. A photon from a dense region at the last scattering surface will be blueshifted. The factor $1/4$ is due to the fact that $\rho_\gamma \propto T^4$. In addition a photon loses energy from climbing out of a gravitational potential well. This corresponds to a redshift in temperature. This effect is the predominant source of fluctuations in the CMB for angular scales above about ten degrees (large angular scales i.e. $\ell \lesssim 20$). The change in the photon temperature on large scales is therefore

$$\left(\frac{\Delta T}{T}\right)_{SW} = \frac{\delta_\gamma}{4} - [\psi] = \frac{1}{3}\psi, \quad (4.9)$$

where we have expressed the density contrast in terms of the potential using equation (3.1) and the adiabatic initial conditions.

4.1.2 The Doppler effect

As the baryons oscillate being tightly coupled to the photons, their motion relative to the observer causes a Doppler shift. The two opposite directions of the baryons with respect to the observer provoke a spatial temperature variation on the last scattering surface. The contribution of this effect is important on small scales ($l \sim 200$) and is subleading on large scales.

In the tight coupling approximation, the photons and baryons are described by the set of equations (3.1), (3.2), (3.5) and (3.6). We substitute the baryon velocity divergence θ_b from equation (3.6) into equation (3.5) and differentiate with respect to the conformal time to get the second order differential equation

$$\left[\frac{d^2}{d\tau^2} + \frac{\dot{R}}{1+R} \frac{d}{d\tau} + k^2 c_s^2 \right] \left(\frac{\delta_\gamma}{4} + \phi \right) = \frac{k^2}{3} \left(\frac{1}{1+R} \phi - \psi \right). \quad (4.10)$$

Before recombination, $\dot{\phi} = \dot{c}_s^2 = \dot{R} = 0$ and $\phi = -\psi$. Therefore, equation (4.10) reduces to

$$\ddot{\delta}_\gamma + c_s^2 k^2 \delta_\gamma = \text{constant}, \quad (4.11)$$

which represents a harmonic oscillator that causes the Doppler peaks of the CMB anisotropy spectrum. The acoustic oscillations are caused by the competition between the photons pressure and the gravitational attraction. Using the WKB approximation, Hu and Sugiyama derived a general solution to equation (4.10) given by

$$\begin{aligned} \frac{\delta_\gamma(\tau)}{4} + \phi(\tau) &= \left[\frac{\delta_\gamma(0)}{4} + \phi(0) \right] \cos(kr_s) \\ &+ \frac{k}{\sqrt{3}} \int_0^\tau d\tau' [\phi(\tau') - \psi(\tau')] \sin[k(r_s(\tau) - r_s(\tau'))], \end{aligned} \quad (4.12)$$

for the photon density contrast, and

$$\begin{aligned} \theta_\gamma &= \sqrt{3} \left[\frac{\delta_\gamma(0)}{4} + \phi(0) \right] \sin(kr_s) \\ &- \frac{k}{3} \int_0^\tau d\tau' [\phi(\tau') - \psi(\tau')] \cos[k(r_s(\tau) - r_s(\tau'))], \end{aligned} \quad (4.13)$$

for the photon velocity divergence with adiabatic initial conditions. From equations (4.12) and (4.13), we see that the density contrast and the velocity divergence are in opposite phase, with

the implication that, the adiabatic spectrum is not zero anywhere. The acoustic peaks are located at $k_n = n\pi/r_s(\tau_*)$, or, in the angular space, $\ell_n = n\pi d_{A*}/r_s(\tau_*)$.

4.1.3 The integrated Sachs-Wolfe effect

The integrated Sachs-Wolfe effect is given by

$$\frac{\Delta T}{T} = \int_{\tau_i}^{\tau_0} (\dot{\phi} + \dot{\psi}) d\tau. \quad (4.14)$$

It is caused by a gravitational redshift occurring between the last scattering surface and us, and is only important on large scales if the potentials ϕ and ψ change in time. There are two main contributions: The first, called *the early ISW*, occurs when the universe passes from being radiation-dominated to matter-dominated. The second, termed *the late ISW*, arises much later as the universe passes from being matter-dominated to cosmological constant dominated. For the early ISW effect, at the matter-radiation transition, the horizon size was much smaller than today. Therefore, these secondary anisotropies will be produced on higher multipoles, around the first peak ($\ell \simeq 200$). Its main contribution occurs at recombination and is in phase with the monopole [41]. The late ISW effect arises at late times, as the universe undergoes a transition from being matter dominated to a curvature or dark energy dominated. At the matter-dark energy equality, the horizon size is much comparable to its current size. Therefore, this effect affects larger scales than the early ISW ($\ell < 100$).

4.2 Boltzmann Hierarchy and the line of sight integral approach

In the present section we derive a formal solution of the CMB anisotropy and introduce the line of sight integral approach for an efficient computation. After leaving the last scattering surface, photons can no longer be treated as a perfect fluid as the shear and higher order moments develop rapidly and become not negligible. One needs to use the Bose-Einstein distribution function for a photon full description [106, 114]. Here, we follow the works of Liddle and Lyth [106], and

Giovannini [61].

We consider a perturbed Bose-Einstein distribution function f in a phase space. The phase space is described by positions, x^i , and conjugate momenta $P_i \equiv mV_i$ where the velocity V_i is given by $dx_i/\sqrt{-ds^2}$. Conjugate momentum is related to the proper momentum p_i by $P_i = a(1 - \phi)p_i$. For convenience, we define the comoving 3-momentum $q_j \equiv ap_j$ which can be written in terms of its magnitude q and direction n_j . It follows that the distribution function can be written as

$$f(x^i, P_j, \tau) = f_0(q)[1 + f^{(1)}(x^i, q, n_j, \tau)], \quad (4.15)$$

where $f^{(1)}$ is a small perturbation to the zero-order phase space distribution f_0 which is the Bose-Einstein distribution for bosons given by:

$$f_0(\epsilon) = \frac{g_s}{h_P^3} \frac{1}{e^{\epsilon/k_B T_0} - 1}, \quad (4.16)$$

where $\epsilon = a(p^2 + m^2)^{1/2} = (q^2 + a^2 m^2)^{1/2}$ is the energy, $T_0 = aT$ is the temperature of the particles today assuming that the scale factor today $a_0 = 1$ and g_s is the number of spin degrees of freedom. The terms h_P and k_B are the Planck and Boltzmann constants.

In terms of the distribution function and of the four-momentum, the energy-momentum tensor is [114]

$$T_{\mu\nu} = \int dP_1 dP_2 dP_3 (-g)^{-1/2} \frac{P_\mu P_\nu}{P_0} f(x^i, P_j, \tau), \quad (4.17)$$

where g is the determinant of $g_{\mu\nu}$. Since $(-g)^{-1/2} = a^{-4}(1 - \psi + 3\phi)$, $dP_1 dP_2 dP_3 = (1 - 3\phi)q^2 dq d\Omega$, $\int d\Omega n_i n_j = 4\pi\delta_{ij}/3$ and $\int d\Omega n_i = \int d\Omega n_i n_j n_k = 0$, the components of the energy-momentum tensor to linear order in the perturbations can be written as [114]:

$$T_0^0 = -a^{-4} \int q^2 dq d\Omega \sqrt{q^2 + m^2 a^2} f_0(q)(1 + f^{(1)}), \quad (4.18)$$

$$T_i^0 = -a^{-4} \int q^2 dq d\Omega n_i f_0(q) f^{(1)}, \quad (4.19)$$

$$T_j^i = -a^{-4} \int q^2 dq d\Omega \frac{q^2 n_i n_j}{\sqrt{q^2 + m^2 a^2}} f_0(q)(1 + f^{(1)}), \quad (4.20)$$

where $d\Omega$ is the solid angle associated with direction n_i . The equations (4.18), (4.19) and (4.20) are general, and hold for massive relativistic particles as well. The rate of change in the phase space distribution can be written as

$$\frac{df}{d\tau} = \frac{\partial f}{\partial \tau} + \frac{dx^i}{d\tau} \frac{\partial f}{\partial x^i} + \frac{dq}{d\tau} \frac{\partial f}{\partial q} + \frac{dn_i}{d\tau} \frac{\partial f}{\partial n_i} = \mathcal{C}_{coll}. \quad (4.21)$$

The term \mathcal{C}_{coll} represents all terms due to collisions. Their form depends on the type of particle interaction. Using the geodesic equation $P^0 \frac{dP^\mu}{d\tau} + \Gamma_{\alpha\beta}^\mu P^\alpha P^\beta = 0$ we deduce a relation for $\frac{dq}{d\tau}$

$$\frac{dq}{d\tau} = q\dot{\phi} - \epsilon(q, \tau) n_i \partial_i \psi. \quad (4.22)$$

To first order approximation, we can neglect the term $\frac{dn_i}{d\tau} \frac{\partial f}{\partial n_i}$ in the Boltzmann equation and therefore write

$$\frac{\partial f^{(1)}}{\partial \tau} + i(\vec{k} \cdot \hat{n}) f^{(1)} + \frac{d \ln f_0}{d \ln q} \left[\dot{\phi} - i \frac{\epsilon}{q} (\vec{k} \cdot \hat{n}) \psi \right] = \frac{1}{f_0} \mathcal{C}_{coll}. \quad (4.23)$$

The equation (4.23) above is a more general equation, valid for all matter and radiation components of the universe. By setting the right-hand side equal to zero (the collision-less Boltzmann equation), one can recover the expression for a perfect fluid model when shear and higher order moments are negligible. Let us notice that the terms in this equation depend on the direction of the momentum \hat{n} only through its angle with \vec{k} .

Though photons travel almost freely after recombination, occasional Thomson scattering continues to transfer energy and momentum between photons and matter. If we define the momentum-average phase space density as [62, 114]

$$F_\gamma(\vec{k}, \hat{n}, \tau) = \frac{\int q^3 dq f_0(q) f^{(1)}}{\int q^3 dq f_0(q)} \equiv \sum_{l=0}^{\infty} (-i)^l F_{\gamma l}(\vec{k}, \tau) \mathcal{P}_l(\hat{k} \cdot \hat{n}), \quad (4.24)$$

where we have expanded F_γ in a series of Legendre polynomials $\mathcal{P}_l(\hat{k} \cdot \hat{n})$ as it depends on the cosine of the angle between \hat{k} and \hat{n} , the photon perturbations δ_γ , θ_γ and σ_γ can be written using

the new variable F_γ and the equation of state $\rho_\gamma = 3P_\gamma = a^{-4} \int q^3 dq d\Omega f_0(q)$ as

$$\delta_\gamma = \frac{1}{4\pi} \int d\Omega F_\gamma(\vec{k}, \hat{n}, \tau) = F_{\gamma 0}, \quad (4.25)$$

$$\theta_\gamma = \frac{3i}{16\pi} \int d\Omega (\hat{k} \cdot \hat{n}) F_\gamma(\vec{k}, \hat{n}, \tau) = \frac{3}{4} k F_{\gamma 1}, \quad (4.26)$$

$$\sigma_\gamma = -\frac{3}{16\pi} \int d\Omega \left[(\hat{k} \cdot \hat{n})^2 - \frac{1}{3} \right] F_\gamma(\vec{k}, \hat{n}, \tau) = \frac{1}{2} F_{\gamma 2}. \quad (4.27)$$

The right hand sides of the above equations (4.25)-(4.27) are derived using the orthogonality of the Legendre polynomials. The zero moment ($\ell = 0$) of the multipole expansion is the monopole δ_γ , the first moment ($\ell = 1$) is proportional to the dipole θ_γ and so on.

Bond and Efstathiou have shown that the linearized collision operator for Thomson scattering is given by [25]

$$\mathcal{C}_{coll} = an_e x_e \sigma_T \left[-F_\gamma(\vec{k}, \hat{n}, \tau) + F_{\gamma 0}(\vec{k}, \tau) + 4\hat{n} \cdot \vec{v}_e - \frac{1}{8} F_{\gamma 2} \mathcal{P}_2(\hat{k} \cdot \hat{n}) \right], \quad (4.28)$$

where σ_T is the Thomson cross-section, n_e and \vec{v}_e are the proper mean density and velocity of the electrons and x_e is the ionization fraction. In order to understand equation (4.28), let us suppose that there is no collision effect. Then the change in the momentum-average phase space density is exactly the sum of contributions due to the photon density perturbations and the scattering terms accounted for by the Doppler effect and an angular dependency. Therefore the collision effect is different from zero if one term dominates. The last term $\frac{1}{8} F_{\gamma 2} \mathcal{P}_2(\hat{k} \cdot \hat{n})$ is proportional to the Legendre polynomial $\mathcal{P}_2(x) = (3x^2 - 1)/2$. It accounts for the angular dependency of Thomson scattering, which has a cross-section $\sim 1 + \cos^2 \varphi$, where φ is the polar angle giving the direction of the scattering.

Now let us define the *brightness perturbation* Θ for the fluctuation of the total density of the radiation field as

$$f(x^i, q, n_j, \tau) = \left(\frac{q}{1 + \Theta} \right) f_0. \quad (4.29)$$

Comparing equations (4.15) and (4.29) to first order, we deduce that the brightness function is related to the perturbation $f^{(1)}$ by

$$\Theta = -f^{(1)} \left(\frac{\partial \ln f_0}{\partial \ln q} \right)^{-1}, \quad \text{and} \quad F_\gamma = -\Theta \frac{\int q^3 dq f_0 \frac{\partial \ln f_0}{\partial \ln q}}{\int q^3 dq f_0} = 4\Theta. \quad (4.30)$$

Then, the Boltzmann equation for perturbation of the brightness becomes

$$\dot{\Theta} + ik\mu(\Theta + \psi) = \dot{\phi} + an_e x_e \sigma_T \left[-\Theta + \Theta_0 + \mu v_b - \frac{1}{2} \mathcal{P}_2(\mu) \Pi \right], \quad (4.31)$$

where v_b is the baryon velocity given by $v_b = \frac{\theta_b}{ik}$ and $\mu = \hat{k} \cdot \hat{n}$. The function $\Pi \equiv \Theta_2 + \Delta_{P2} + \Delta_{P0}$ where Δ_{P0} and Δ_{P2} take into account the polarization of the photons after Thomson scattering. Expanding the temperature anisotropy in multipole moments

$$\Theta(\mu) = \sum_{\ell} (2\ell + 1) (-i)^{\ell} \Theta_{\ell} \mathcal{P}_{\ell}(\mu), \quad (4.32)$$

one finds the following hierarchy of the coupled differential equations

$$\dot{\Theta}_0 = -k\Theta_1 + \dot{\phi}, \quad (4.33)$$

$$\dot{\Theta}_1 = \frac{k}{3} [\Theta_0 - 2\Theta_2 + \psi] + an_e x_e \sigma_T \left(\frac{v_b}{3} - \Theta_1 \right), \quad (4.34)$$

$$\dot{\Theta}_2 = \frac{k}{5} [2\Theta_1 - 3\Theta_3] + an_e x_e \sigma_T \left[\frac{\Pi}{10} - \Theta_2 \right], \quad (4.35)$$

$$\dot{\Theta}_{\ell} = \frac{k}{2\ell + 1} [\ell\Theta_{\ell-1} - (\ell + 1)\Theta_{\ell+1}] - an_e x_e \sigma_T \Theta_{\ell}. \quad \ell > 2 \quad (4.36)$$

Now as we show later (see equation (4.59)), the multipole moments Θ_{ℓ} are related to the CMB power spectrum by

$$C_{\ell} = \frac{2}{\pi} \int \frac{dk}{k} k^3 \frac{|\Theta_{\ell}(\tau, k)|^2}{(2\ell + 1)^2}.$$

Thus, as the set of coupled differential equations (4.33)-(4.36) cannot be solved analytically, one needs to numerically compute iteratively several thousand higher order moments in order to find the CMB power spectrum. In 1996, Seljak and Zaldarriaga presented a method by far more efficient which revolutionised the computation of the CMB power spectrum [152].

4.2.1 Line of sight integral approach

The line of sight integral approach is based on a split of the CMB temperature anisotropy in a time integral over the product of a geometrical term and a source term. The geometrical term given by radial eigenfunctions, does not depend on the cosmological model. The source term is expressed in terms of photon, baryon and metric perturbations. These perturbations can be

computed using a small number of differential equations, thus significantly reducing the computational time.

The starting point of this approach is to integrate equation (4.31) along the line of sight. This leads to

$$\Theta = \int_0^{\tau_0} d\tau e^{ik\mu(\tau-\tau_0)} e^{-\tau_e} \{ \dot{\tau}_e [\Theta_0 + i\mu v_b + \frac{1}{2} \mathcal{P}_2(\mu) \Pi] + \dot{\phi} - ik\mu\psi \}. \quad (4.37)$$

This equation could be immediately turned into an equation for each of the moments Θ_ℓ if the integrand did not depend on μ . But, as the integral is multiplied by $e^{ik\mu(\tau-\tau_0)}$, we can write $\frac{d}{d\tau} e^{ik\mu(\tau-\tau_0)} = ik\mu e^{ik\mu(\tau-\tau_0)}$. Thus as the whole integrand is multiplied by $e^{ik\mu(\tau-\tau_0)}$, each time that a given term in the integrand is multiplied by a μ , we can replace μ with a time derivative [41]

$$\mu \rightarrow \frac{1}{ik} \frac{d}{d\tau}. \quad (4.38)$$

Thus having eliminated the angle μ in the integrand through integration by parts, and noticing that the boundary terms are either damped at $\tau = 0$ by the factor $e^{-\tau_e(0)}$ or irrelevant at $\tau = \tau_0$ since they have no angular dependence, they can be dropped. This alters the monopole but is unobservable. Therefore we can write equation (4.37) as

$$\Theta = \int_0^{\tau_0} d\tau e^{ik\mu(\tau-\tau_0)} S(k, \tau), \quad (4.39)$$

with

$$\begin{aligned} S(k, \tau) = & g \left(\Theta_0 + \psi - \frac{v_b}{k} - \frac{\Pi}{4} - \frac{3\ddot{\Pi}}{4k^2} \right) \\ & + e^{-\tau_e} (\dot{\phi} + \dot{\psi}) - \dot{g} \left(\frac{v_b}{k} + \frac{3\dot{\Pi}}{4k^2} \right) - \frac{3\ddot{g}\Pi}{4k^2}, \end{aligned} \quad (4.40)$$

where the function $S(k, \tau)$ is called the *source function* and $g(\tau) = \dot{\tau}_e e^{-\tau_e}$ is the visibility function. The visibility function gives the probability that a photon last scattered between τ and $\tau + d\tau$. It therefore peaks strongly around the epoch of recombination, when the dominant contribution to the CMB anisotropies arises and can be approximated by a Dirac delta function evaluated at $\tau = \tau_{rec}$.

In terms of the source function, the multipole moments $\Theta_\ell(k, \tau)$ are given by

$$\Theta_\ell(k, \tau_0) = \int_0^{\tau_0} S(k, \tau) j_\ell[k(\tau - \tau_0)] d\tau. \quad (4.41)$$

Equation (4.41) also shows that the anisotropy that we measure today can be seen as a spherical projection through the spherical Bessel function of the fluctuations on the last scattering surface towards us. It is obtained substituting equation (4.39) into equation (4.32), expanding the plane wave $e^{-i\mu k(\tau - \tau_0)}$ in a series of Legendre polynomials as

$$e^{-i\mu k(\tau - \tau_0)} = \sum_\ell (-i)^\ell (2\ell + 1) j_\ell[k(\tau - \tau_0)] \mathcal{P}_\ell(\mu), \quad (4.42)$$

and using the orthogonality property of the Legendre polynomials. This approach of expressing the moments Θ_ℓ as an integral along the line of sight was first derived by Seljak and Zaldarriaga [152]. In this approach, the anisotropy is decomposed into a source term which does not depend on the higher multipole moments, but only on Θ_0 , Θ_1 and Θ_2 , and a spherical Bessel function independent of the cosmological model.

The expression of the source function in the synchronous gauge, that corresponds to the expression in conformal Newtonian gauge given in equation (4.40), can be easily derived knowing that the conformal Newtonian potentials ϕ and ψ are related to the synchronous potentials h and η in k -space by the set of equations (2.9), and the photon density contrasts, δ_γ and the baryon velocity divergences θ_b in both conformal and synchronous gauge are related by equations (2.10) and (2.11). The higher moments ($\Theta_2, \Theta_3, \dots$) of the photon distribution function are gauge invariant as argued in [114]. Thus the source function in the synchronous gauge can be written as:

$$S^{Syn} = e^{-\tau_e} (\dot{\eta} + \ddot{\alpha}) + g(\tau) \left[\frac{\delta_\gamma}{4} + \frac{\dot{\theta}_b}{k^2} + 2\dot{\alpha} + \frac{\Pi}{16} + \frac{3\ddot{\Pi}}{16k^2} \right] + \dot{g}(\tau) \left[\frac{\theta_b}{k^2} + \alpha + \frac{3\dot{\Pi}}{8k^2} \right] + \ddot{g}(\tau) \left[\frac{3\Pi}{16k^2} \right].$$

As we show in the following section, the photon polarization contribution to the source function is small and can be neglected for the primary anisotropy. Thus the source function simplifies to the expression

$$S^{Syn} = e^{-\tau_e} (\dot{\eta} + \ddot{\alpha}) + g(\tau) \left[\frac{\delta_\gamma}{4} + \frac{\dot{\theta}_b}{k^2} + 2\dot{\alpha} \right] + \dot{g}(\tau) \left[\frac{\theta_b}{k^2} + \alpha \right], \quad (4.43)$$

where the contribution due to the intrinsic fluctuation of photon density perturbations, the gravity, the baryon velocity and the integrated Sachs-Wolfe effect in the synchronous gauge are respectively given by

$$g(\tau) \left(\frac{\delta_\gamma}{4} - \frac{\dot{a}}{a} \alpha \right), \quad (4.44)$$

$$g(\tau) \left(\dot{\alpha} + \frac{\dot{a}}{a} \alpha \right), \quad (4.45)$$

$$g(\tau) \left(\frac{\dot{\theta}_b}{k^2} + \dot{\alpha} \right) + \dot{g}(\tau) \left(\frac{\theta_b}{k^2} + \alpha \right), \quad (4.46)$$

$$e^{-\tau_e} (\dot{\eta} + \ddot{\alpha}). \quad (4.47)$$

Now, the brightness can be expanded in spherical harmonics $Y_{\ell m}$ as

$$\Theta(\hat{n}, \tau) = \sum_{\ell=0}^{\infty} \sum_{m=-\ell}^{\ell} a_{\ell m} Y_{\ell m}(\hat{n}) = \frac{1}{(2\pi)^{3/2}} \int d^3 k \Theta(\vec{k}, \hat{n}, \tau), \quad (4.48)$$

where the coefficients $a_{\ell m}$ have to be determined. Considering the expansion (4.32) and using the theorem of addition of spherical harmonics, which stipulates that

$$\mathcal{P}_\ell(\hat{k} \cdot \hat{n}) = \frac{4\pi}{2\ell+1} \sum_{m=-\ell}^{\ell} Y_{\ell m}^*(\hat{k}) Y_{\ell m}(\hat{n}), \quad (4.49)$$

one can compute the coefficients $a_{\ell m}$ and finds

$$a_{\ell m} = \frac{(4\pi)}{(2\pi)^{3/2}} (-i)^\ell \int d^3 k Y_{\ell m}^*(\hat{k}) \Theta_\ell(\vec{k}, \tau). \quad (4.50)$$

Considering two different directions on the sky denoted by \hat{n}_1 and \hat{n}_2 with $\hat{n}_1 \cdot \hat{n}_2 = \cos \vartheta$, the two-point correlation function $C(\vartheta)$ is the ensemble average of the brightness function given by $C(\vartheta) = \langle \Theta(\hat{n}_1, \tau_0), \Theta(\hat{n}_2, \tau_0) \rangle$. Since the background is isotropic, this average depends only on ℓ . Therefore we define the angular power spectrum C_ℓ as

$$\langle a_{\ell m} a_{\ell' m'}^* \rangle = C_\ell \delta_{\ell \ell'} \delta_{m m'}. \quad (4.51)$$

For a given ℓ , C_ℓ is the variance of the $a_{\ell m}$. It tells us about the power of temperature anisotropies on a given angular scale $\propto 1/\ell$ and can be written as

$$\left(\frac{\Delta T_\ell}{T_0} \right)^2 = \frac{\ell(\ell+1)}{2\pi} C_\ell, \quad (4.52)$$

where T_0 is the background temperature and ΔT_ℓ the temperature anisotropy for a given ℓ .

4.3 CMB anisotropies

As introduced earlier, the CMB power spectrum measures of the temperature anisotropies for a given angular scale. It depends on several cosmological parameters and on the mode of the primordial fluctuations. In this section we investigate how the initial conditions affect the CMB power spectrum today. To this end, we first evaluate the different contributions to the source function at the last scattering surface, then evolve them using the CMB transfer function to get the CMB power spectrum today.

4.3.1 Transfer function $\Delta_\ell(k)$

In linear perturbation theory, each Fourier mode evolves independently of the others. We may define a linear transfer function $\Delta(k)$ relating the fluctuations that we measure today to some initial entropy perturbation $\mathcal{S}(k, \tau_i)$ by [45]

$$\Theta(\tau_0, k, n) = \Delta(k, \mu) \mathcal{S}(k, \tau_i), \quad (4.53)$$

where, τ_i is the initial conformal time. If we assume the initial entropy perturbation $\mathcal{S} = 1$, and expand the transfer function in Legendre polynomials $\Delta(k, \mu) = \sum_\ell (-1)^\ell (2\ell + 1) \Delta_\ell(k) \mathcal{P}_\ell(\mu)$, then the transfer function $\Delta_\ell(k)$ is just the multipole moment $\Theta_\ell(k, \tau_0)$ evaluated at present time. The orthogonality of the Legendre polynomials insures that the ℓ modes are all independent.

We have already seen (see equation (4.41)) that the transfer function can be obtained by multiplying the source function by the spherical Bessel function and integrating along the line of sight [152]. For sufficiently large scales, Hu showed [78] that the slowly varying quantities contained in the source function in equation (4.41) can be taken out of the integral and evaluated at photon-baryon decoupling, leading for $\ell \geq 2$ to

$$\begin{aligned} \Theta_\ell(\tau_0) &\simeq [\Theta_0 + \psi](\tau_*) \mathcal{D}(k) (2\ell + 1) j_\ell(k \Delta \tau_*) + \Theta_1(\tau_*) \mathcal{D}(k) [\ell j_{\ell-1}(k \Delta \tau_*) - (\ell + 1) j_{\ell+1}(k \Delta \tau_*)] \\ &+ (2\ell + 1) \int_{\tau_*}^{\tau_0} [\dot{\phi} + \dot{\psi}] j_\ell(k \Delta \tau) d\tau, \end{aligned} \quad (4.54)$$

where τ_* is the conformal time at decoupling, $\Delta \tau_* = \tau_0 - \tau_*$, $\Delta \tau = \tau_0 - \tau$ and $\mathcal{D}(k)$ accounts

for the diffusion damping. This diffusion damping factor is given by

$$\mathcal{D}(k) = \int_0^{\tau_0} g(\tau) e^{[-k/k_D(\tau)]^2} d\tau, \quad (4.55)$$

with the damping length $k_D^{-2} = \frac{1}{6} \int_0^{\tau} \frac{1}{\tau_e} \frac{R^2 + 4(1+R)/5}{(1+R)^2} d\tau$. The damping effect is more effective for scale smaller than the damping length. This is a correction to the tight-coupling approximation around decoupling as photons random walk through baryons with some finite mean distance λ_D . Any perturbation on scales smaller than λ_D is suppressed.

Thus in this approximation (equation (4.54)), the evaluation of the multipole moments requires only the knowledge of the fluctuations at photon-baryon decoupling, and the time evolution of the potentials from the last scattering surface to us today. The Bessel function $j_\ell(k)$ tells us how much anisotropy on large scales is contributed by a plane wave with wavenumber k . As the limit of the Bessel function for very large ℓ (very small angular scales) vanishes, the transfer function $\Delta_\ell(k) \approx 0$ for $\ell \gg k\tau_0$. For a Λ CDM universe, the time dependence of the potentials can be neglected.

4.3.2 Angular power spectrum C_ℓ

The photon transfer function opens the way of computing the CMB angular power spectrum. Here, we make use of the dominant contributions to the transfer function to understand the main features of the CMB power spectrum. We first recall how the transfer function relates to the angular power spectrum.

A complete description of the photon distribution should take into account both spatial and angular distributions of the brightness function Θ . But we only have information on the angular distribution as we can only measure the CMB from one location. We expand the brightness function of photon in spherical harmonics as

$$\Theta(x, \hat{p}, \tau) = \sum_{\ell=1}^{\infty} \sum_{m=-\ell}^{\ell} a_{\ell m}(x, \tau) Y_{\ell m}(\hat{p}), \quad (4.56)$$

where the coefficient $a_{\ell m}$ are given in Fourier space by

$$a_{\ell m}(x, \tau) = \int \frac{d^3 k}{(2\pi)^3} e^{i\vec{k}\vec{x}} \int d\Omega Y_{\ell m}(\hat{p}) \Theta(\vec{k}, \hat{p}, \tau), \quad (4.57)$$

where Ω is the solid angle spanned by \hat{p} . The coefficients $a_{\ell m}$ are usually taken to have a Gaussian probability distribution with a mean value of zero. As the $a_{\ell m}$ are symmetric for a given ℓ , the variance depends on ℓ .

Substituting equation (4.57) into (4.51) and knowing that

$$\langle \Theta^* \Theta \rangle = \frac{1}{2\pi^2} \int \sum_{\ell} \frac{1}{2\ell + 1} k^3 |\Theta_{\ell}(\tau, k)|^2 \mathcal{P}_{\ell}(\hat{p}' \cdot \hat{p}), \quad (4.58)$$

leads to

$$C_{\ell} = \frac{2}{\pi} \int \frac{dk}{k} k^3 \frac{|\Theta_{\ell}(\tau, k)|^2}{(2\ell + 1)^2}, \quad (4.59)$$

where \mathcal{P}_{ℓ} is a Legendre polynomial.

4.4 Effect of cosmological parameters on the CMB temperature spectrum: adiabatic case

In the previous section we reviewed how, from the fluctuations at the last scattering surface, one can derive the observed CMB anisotropy and investigated the features of the CMB power spectrum for isocurvature modes. The CMB anisotropy spectrum depends on several cosmological parameters among which the baryon density ω_b , the matter density ω_m , the dark energy density Ω_X , the optical depth τ_e , the spectral index n_s and the scalar amplitude A_s . Each parameter has a particular effect on the spectrum. A change in the cosmological parameters affects the CMB spectrum shifting different peaks to the left or to the right, raising or lowering their heights, or moving the entire spectrum up or down. In this section, we review the effect of the cosmological parameters on the CMB power spectrum in adiabatic mode in order to compare it, in the next chapter, to the case of isocurvature modes. We particularly focus on the physical baryon density

and the physical matter density as they differently affect the CMB spectrum in different models.

The baryon density, matter density, and cosmological constant each induce a shift in the location of peaks and troughs in the CMB spectrum. For a flat universe, the peaks are located at $\ell_n \simeq n\pi\tau_0/r_s(\tau_*)$. Thus peak location depends on the sound horizon r_s and on the age of the universe τ_0 . An increase in the matter density $\Omega_m h^2$ reduces the age of the universe but does not affect the sound horizon. A change in the baryon density affects the sound horizon. More importantly, the physical densities in matter $\Omega_m h^2$ and baryons $\Omega_b h^2$ fix the heights of acoustic peaks in the CMB spectrum. As we show in a following section, the peaks in the CMB spectrum are lowered and shifted to higher ℓ as the matter density $\Omega_m h^2$ increases.

A dark energy model with cosmological constant Ω_Λ or quintessence, and curvature have no significant effect on the pre-recombination universe and only affect the CMB spectrum through the angular diameter distance d_A and the late-time ISW effect [98]. The optical depth τ_e tells us how much the universe was reionized at late times. The reionization of the universe reintroduces Thomson scattering of photons by free electrons. If the optical depth is large enough, the anisotropies are washed out. The spectral index n_s has an effect different from all of the previous parameters. An increase in the spectral index lowers the anisotropy on large scales and enhances it on small scales, thus tilting the spectrum about a pivot scale. We now study these effects in neutrino isocurvature models using our semi-analytical approximations.

4.4.1 Baryon density $\Omega_b h^2$

The baryon density is the cosmological parameter which most affects the heights and locations of peaks in the CMB power spectrum. Loading the single fluid with more baryons reduces the sound speed and therefore changes the heights and positions of peaks in the CMB power spectrum. Odd peaks are enhanced while even peaks are lowered as the baryon density increases. This is a direct consequence of the lower frequency of the oscillations. The baryon density effect on the CMB spectrum is a unique signature, making the baryon density one of the easiest parameters to extract

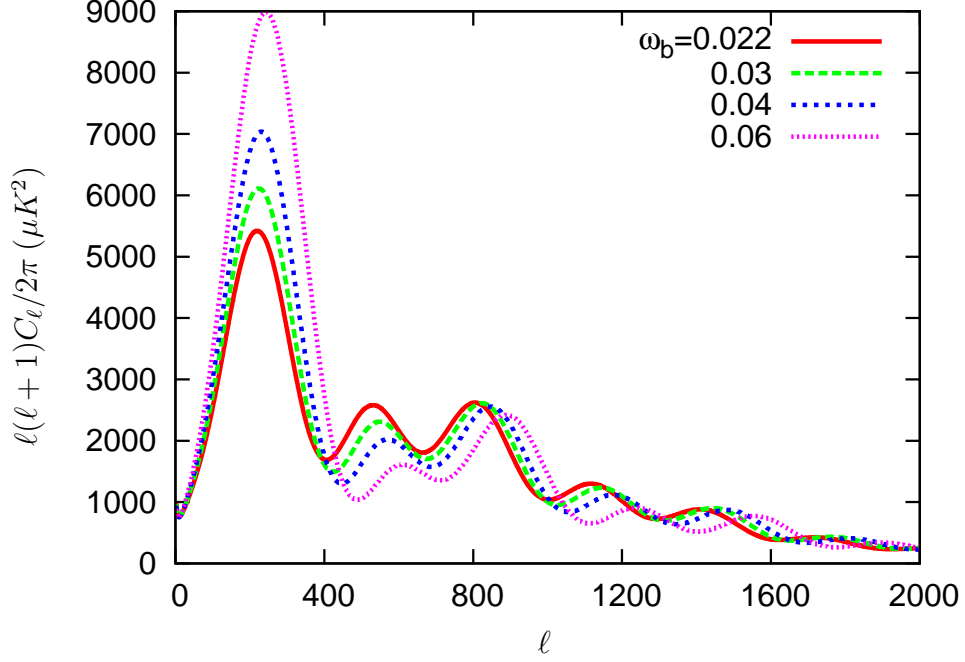


Figure 4.2: $\Omega_b h^2$ dependence of the CMB power spectrum in the adiabatic mode. This is for a flat Λ CDM model with $h = 0.7$ and $\Omega_c h^2 = 0.125$.

from the CMB. Figure 4.2 shows how the CMB spectrum changes with the baryon density.

4.4.2 Matter density $\Omega_m h^2$

To see the imprint of the matter density on the CMB power spectrum, we consider a Λ CDM universe, keep the physical baryon density $\Omega_b h^2$ and h constant, and modify only the dark matter density $\Omega_c h^2$. The change in the matter density is compensated by Ω_Λ . Changing Ω_Λ affects the CMB spectrum but its effect can be neglected compared to the effect of matter density itself.

For a universe with a low matter density $\Omega_m h^2$, the epoch of matter-radiation equality τ_{eq} occurs closer to recombination. The gravitational potential still decays at recombination providing a strong driving force for the oscillations. Therefore the photon density perturbation, δ_γ , is larger compared to high matter density universes. In addition, since the potential is not constant after recombination, the integrated Sachs Wolfe effect contribution is not negligible and should be taken into account. Figure (4.3) shows how all the CMB peaks are enhanced when the matter

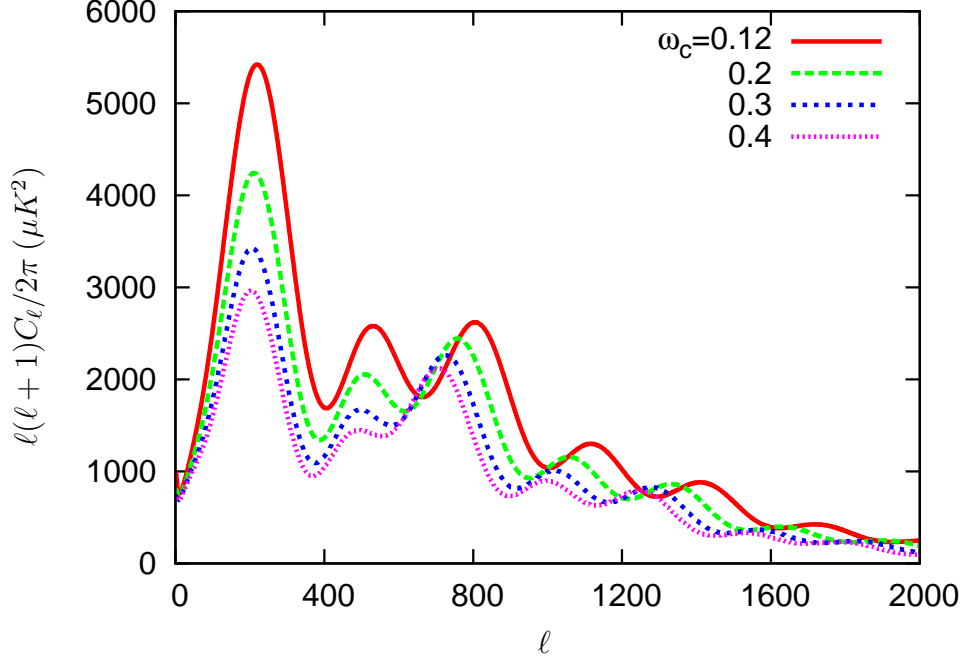


Figure 4.3: $\Omega_m h^2$ dependence of the CMB power spectrum in the adiabatic mode. This is for a flat Λ CDM model with $h = 0.7$ and $\Omega_b h^2 = 0.022$.

density decreases.

4.4.3 Cosmological constant density Ω_Λ

Different models of the dark energy affect differently the CMB power spectrum. Here, we restrict ourselves to the case of the dark energy being the cosmological constant. At the last scattering surface, where the main contributions to the anisotropies that we observe today were formed, the universe was still radiation-dominated and the cosmological constant was negligible and could not affect the perturbations. Therefore the effect of the cosmological constant on the CMB power spectrum is only through the freestreaming of photons from last scattering surface towards us. For a fixed baryon and matter density, the cosmological constant does not affect the sound horizon but change the angular diameter distance d_A which in turn modifies the peak location. The angular diameter distance $d_A = d/\varphi$ is a classic way to measure distances by measuring the angle φ subtended by an object of known physical size d . The effect of the equation of

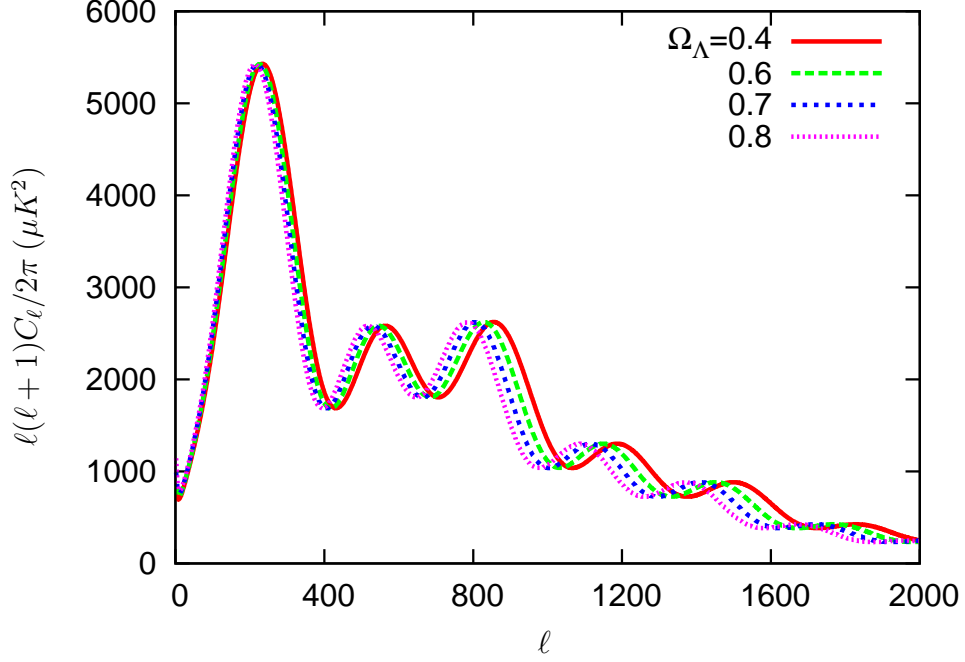


Figure 4.4: Ω_Λ dependence of the CMB power spectrum in the adiabatic mode. This is for a flat Λ CDM model with $\Omega_b h^2 = 0.022$ and $\Omega_c h^2 = 0.125$.

state parameter w on the CMB power spectrum is the same similar to the effect of Ω_Λ . In a flat universe $\Omega_K \equiv 1 - \Omega_\Lambda - \Omega_m = 0$, $\varphi = (d/a)/\Delta\tau$ so that the angular diameter distance is given by [41]

$$d_A^{flat} = a\Delta\tau = \frac{\Delta\tau}{1+z}, \quad a_0 = 1 \quad (4.60)$$

where $\Delta\tau$ is the comoving distance. At low redshift, the angular diameter distance is equal to the comoving distance. Increasing the cosmological constant density, Ω_Λ , shifts the location of peaks to lower values of ℓ . Thus the entire CMB spectrum shifts to lower multipoles ℓ as Ω_Λ increases. Figure (4.4) shows how the CMB power spectrum is shifted to larger scales as we increase the cosmological constant.

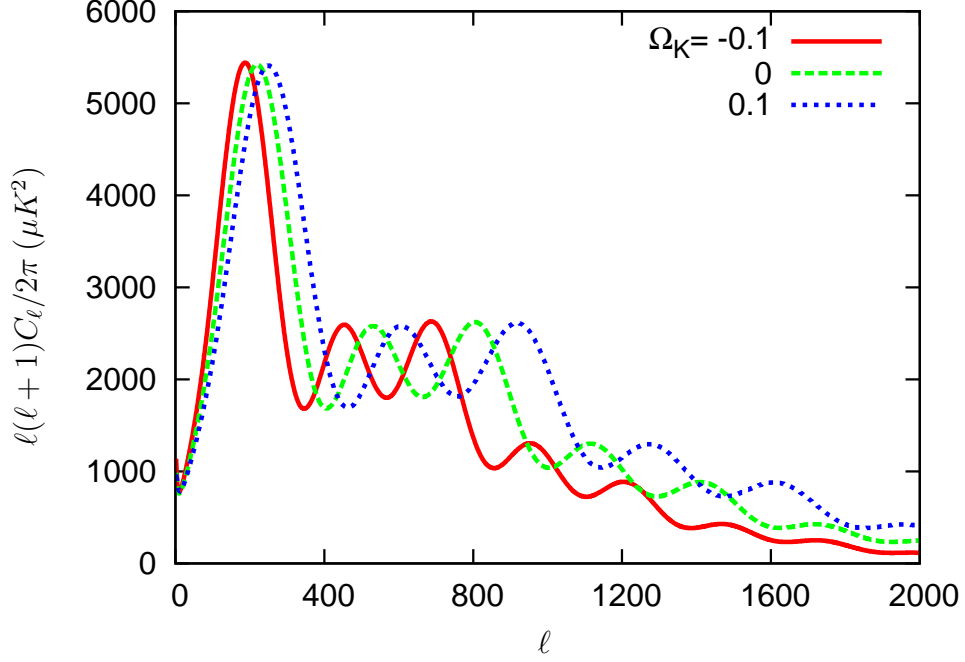


Figure 4.5: Curvature Ω_K dependence of the CMB power spectrum in isocurvature models. As we increase the curvature density, the anisotropy spectrum shifts to small scales. For closed, flat and open Λ CDM universe with $\Omega_b h^2 = 0.022$, $\Omega_c h^2 = 0.125$, $h = 0.7$.

4.4.4 Curvature density Ω_K

Among all the cosmological parameters that we are considering, the curvature density by far causes the largest shift in the location of the peaks [41]. The photon geodesics depend on the geometry of the universe. In an open universe, the geodesics of massless particles start out parallel to each other and then slowly diverge. The physical scale corresponding to the first peak gets projected onto a smaller angular scale in a flat universe compared to an open universe. Therefore we expect that the peaks should be shifted to higher values of ℓ in an open universe. For the closed universe, the peaks are shifted to lower values of ℓ . The magnitude of this shift is determined by the comoving angular diameter distance to the last scattering surface [77]. Equation (4.60) in the previous subsection gives the angular diameter distance in a flat universe.

For a non flat universe, the angular diameter distance generalizes to

$$d_A = \frac{a}{H_0 \sqrt{|\Omega_K|}} \begin{cases} \sinh[\sqrt{\Omega_K} H_0 \Delta\tau] & \Omega_K > 0 \\ \sin[\sqrt{-\Omega_K} H_0 \Delta\tau] & \Omega_K < 0 \end{cases} \quad (4.61)$$

Thus changing the curvature of the universe affects the angular diameter distance and subsequently the peak location. In Figure (4.5) we see how the whole CMB spectrum is shifted to the higher ℓ as we go from a closed universe ($\Omega_K < 0$) to an open universe ($\Omega_K > 0$).

4.4.5 Optical depth τ_e

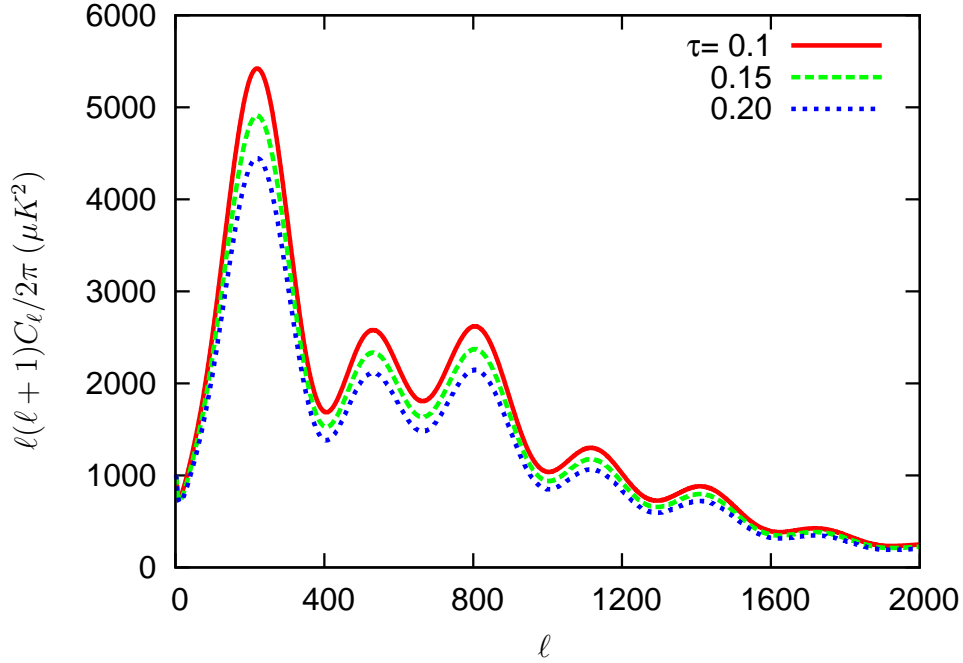


Figure 4.6: Reionization dependence of the CMB power spectrum. As the optical depth from reionization to the last scattering surface increases, anisotropies are washed out for scales inside the horizon at the reionization epoch. For a flat Λ CDM universe with $\Omega_b h^2 = 0.022$, $\Omega_c h^2 = 0.125$, $h = 0.7$.

After leaving the last scattering surface, photons freestream towards us today preserving the anisotropy. This is true if we ignore the reionization of the universe at late time. In fact, as the

first luminous objects form their UV emission reionizes the universe. This brings photons back into contact with free electrons which erases anisotropies through Thomson scattering. Taking into account the reionization of the universe a second peak appears in the visibility function at low redshift. The CMB photons are affected by the temperature, potential, and velocity of the scattering electrons [60]. If we assume that photons have a temperature $T(1 + \Theta)$ where T is the background temperature and Θ the temperature perturbation before reionization, at reionization, only a fraction of photons given by $e^{-\tau_e}$, will emerge without scattering. The remaining fraction $(1 - e^{-\tau_e})$ is re-emitted by the ionized region. Thus the photon temperature after reionization is

$$T(1 + \Theta)e^{-\tau_e} + T(1 - e^{-\tau_e}) = T(1 + \Theta e^{-\tau_e}). \quad (4.62)$$

This means that the CMB anisotropy after reionization is lowered by a factor $e^{-\tau_e}$ and consequently the power spectrum C_ℓ is reduced by $e^{-2\tau_e}$. Hence, all modes within the horizon ($\ell > \tau_0/\tau_{reion}$) at reionization will be affected by this process and the modes outside the horizon remain unchanged. Figure (4.6) shows the effect of reionisation on the CMB power spectrum.

4.4.6 Spectral index n_s

The CMB angular power spectrum can be written as

$$C_\ell = \frac{2}{\pi} \int_0^\infty k^2 P_I(k) |\Theta_\ell(k)|^2 dk, \quad (4.63)$$

where $P_I(k)$ is the primordial power spectrum. The primordial power spectrum is proportional to k^{n_s} where k is the wavenumber and n_s the spectral density [41]. This can be written as

$$P_I(k) \propto \left(\frac{k}{k_p} \right)^{n_s}, \quad (4.64)$$

where k_p is a constant. For a wavenumber $k = k_p$, $(\frac{k}{k_p})^{n_s}$ is independent of the spectral index. For other wavenumbers, n_s will modify the slope of the CMB power spectrum, pivoting around some multipole $\ell_p \simeq k_p \tau_0$. This effect on the CMB spectrum is clearly seen in Figure (4.7). A value of $n_s < 1$ lowers the small scale anisotropy and boosts the large scale anisotropy with the opposite effect for $n_s > 1$.

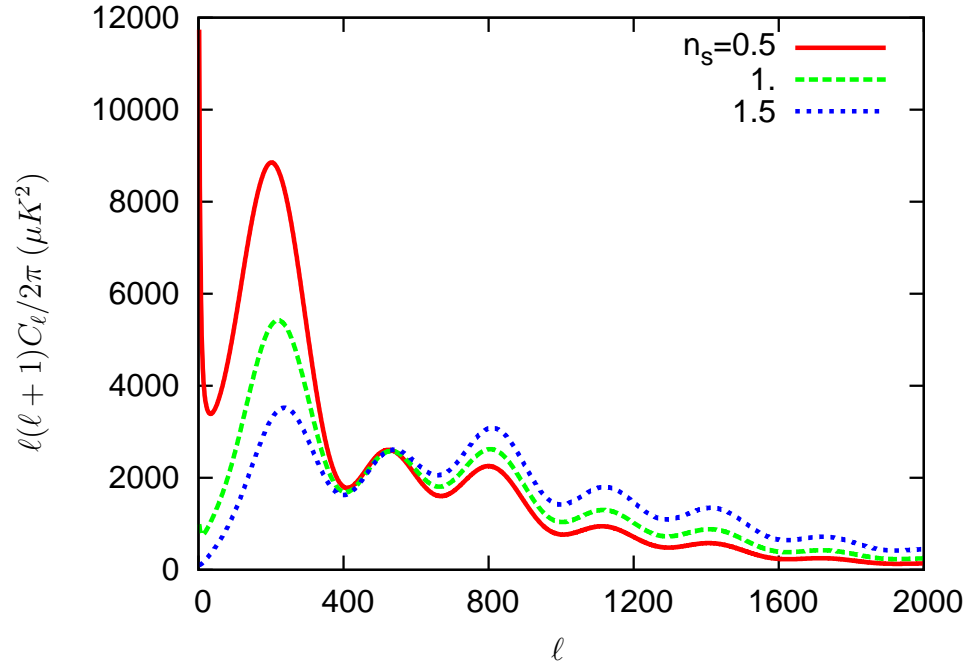


Figure 4.7: Spectral index dependence of the CMB power spectrum for adiabatic models. For a flat Λ CDM universe with $\Omega_b h^2 = 0.022$, $\Omega_c h^2 = 0.125$, $h = 0.7$, pivot scale $k_p = 0.05 \text{Mpc}^{-1}$.

Observational Signatures of Isocurvature Perturbations in the CMB

5.1 Introduction

In the previous chapters (3 & 4), we reviewed the evolution of cosmological perturbations and showed how these perturbations translate into the CMB anisotropies in the case of adiabatic initial conditions. In this chapter, we consider isocurvature initial conditions and study the evolution of the perturbations. We develop a semi-analytic treatment for the perturbations and the CMB spectrum that allows us to understand the dependence of isocurvature CMB spectra on cosmological parameters. The semi-analytic solutions for the perturbations are accurate to about 10%. Finally, we investigate the features of the isocurvature CMB power spectra and study the impact of different cosmological parameters on the isocurvature CMB power spectra.

5.2 Evolution of photon and baryon perturbations

In this section, we only consider the photon and baryon evolution as these, with the gravitational potential, are the only quantities that are involved in the computation of the CMB spectrum through the line of sight integral. We derive semi-analytic solutions for the evolution of the photon density contrast and velocity divergence. For the gravitational potential, we only give large and small scale solutions as a complete solution requires the knowledge of the density and velocity evolution for all species. However, the small– and large–scale solutions are sufficient to understand the CMB features.

Prior to decoupling, the energy-momentum conservation principle leads to the following set of time evolution equations for the photon, baryon, cold dark matter and neutrino density contrasts δ and velocity divergences θ in the synchronous gauge [114]:

$$\dot{\delta}_\gamma = -\frac{4}{3}\theta_\gamma - \frac{2}{3}\dot{h}, \quad (5.1)$$

$$\dot{\delta}_b = -\theta_b - \frac{1}{2}\dot{h}, \quad (5.2)$$

$$\dot{\delta}_c = -\frac{1}{2}\dot{h}, \quad (5.3)$$

$$\dot{\delta}_\nu = -\frac{4}{3}\theta_\nu - \frac{2}{3}\dot{h}, \quad (5.4)$$

for the density contrasts, and

$$\dot{\theta}_\gamma = k^2 \left(\frac{1}{4}\delta_\gamma - \sigma_\gamma \right) + an_e\sigma_T(\theta_b - \theta_\gamma), \quad (5.5)$$

$$\dot{\theta}_b = -\frac{\dot{a}}{a}\theta_b + c_s^2 k^2 \delta_b + \frac{4\bar{\rho}_\gamma}{3\bar{\rho}_b} an_e\sigma_T(\theta_\gamma - \theta_b), \quad (5.6)$$

$$\theta_c = 0, \quad (5.7)$$

$$\dot{\theta}_\nu = k^2 \left(\frac{1}{4}\delta_\nu - \sigma_\nu \right), \quad (5.8)$$

for the velocity divergences. The subscripts γ , b , c and ν label respectively the photons, the baryons, the cold dark matter and the neutrinos, σ_T is the Thomson cross section, n_e is the electron number density, $\bar{\rho}_\gamma$ and $\bar{\rho}_b$ are respectively the photon and baryon background densities,

$c_s = 1/\sqrt{3(1+R)}$ is the sound speed in the photon-baryon single fluid, σ_γ and σ_ν represent respectively the photon and neutrino shear. The shear stress of the radiation (photons and neutrinos) is relevant once the radiation component has decoupled from the matter component for a mode within the horizon and must be taken into account. Therefore we supplement the above set of equations with two equations for the quadrupole [114]

$$\dot{\sigma}_\gamma = \frac{\dot{F}_{\gamma 2}}{2} = \frac{4}{15}\theta_\gamma - \frac{3}{10}kF_{\gamma 3} + \frac{2}{15}\dot{h} + \frac{4}{5}\dot{\eta} - \frac{9}{10}an_e\sigma_T\sigma_\gamma, \quad (5.9)$$

$$\dot{\sigma}_\nu = \frac{\dot{F}_{\nu 2}}{2} = \frac{4}{15}\theta_\nu - \frac{3}{10}kF_{\nu 3} + \frac{2}{15}\dot{h} + \frac{4}{5}\dot{\eta}, \quad (5.10)$$

where $F_{\gamma 2}$, $F_{\nu 2}$, $F_{\gamma 3}$ and $F_{\nu 3}$ are respectively the second and the third moments of the momentum-averaged phase space densities for photons and neutrinos. A complete treatment requires a hierarchy of multipole moments to describe the full distribution function of the radiation component [41, 152]. The synchronous gauge metric field h evolves as [114]

$$\ddot{h} + \frac{\dot{a}}{a}h = -3\left(\frac{\dot{a}}{a}\right)^2 \bar{\rho}_{cr} \sum_j \Omega_j \delta_j (1 + 3c_{sj}^2), \quad (5.11)$$

where $j \in \{\nu, \gamma, b, c\}$ labels the different species of the universe, $\bar{\rho}_{cr}$ is the critical density of the universe and $\Omega_j \equiv \bar{\rho}_j/\bar{\rho}_{cr}$ is the ratio of the density of the j^{th} species to the critical density. The overdot refers to the derivative with respect to the conformal time τ . Hereafter, we study the evolution of the photons and baryons prior to and after decoupling. We focus mostly on the pre-decoupling period as it sets the main features of the primary anisotropies of the CMB.

Moreover, as the gravitational potential ϕ is a conformal gauge quantity, we consider the set of field equations in the conformal gauge. These are given by [114]

$$k^2\phi + 3\frac{\dot{a}}{a}\left(\dot{\phi} + \frac{\dot{a}}{a}\psi\right) = -\frac{3}{2}H^2\bar{\rho}_{cr}\sum_j\Omega_j\delta_j, \quad (5.12)$$

$$k^2\left(\dot{\phi} + \frac{\dot{a}}{a}\psi\right) = \frac{3}{2}H^2\bar{\rho}_{cr}\sum_j\Omega_j(1+w_j)\theta_j, \quad (5.13)$$

$$\ddot{\phi} + \frac{\dot{a}}{a}\left(\dot{\psi} + 2\dot{\phi}\right) + \left(2\frac{\ddot{a}}{a} - \frac{\dot{a}^2}{a^2}\right)\psi + \frac{k^2}{3}(\phi - \psi) = 9H^2\bar{\rho}_{cr}\sum_j\Omega_j c_{sj}^2\delta_j, \quad (5.14)$$

$$k^2(\phi - \psi) = \frac{9}{2}H^2\bar{\rho}_{cr}(1+w_j)\Omega_j\sigma_j, \quad (5.15)$$

where the fluid variables are evaluated in the Newtonian gauge and differ from their counterparts in the synchronous gauge by the gauge transformations as

$$\delta_\gamma^{\text{Con}} = \delta_\gamma^{\text{Syn}} - 4\alpha\frac{\dot{a}}{a}, \quad (5.16)$$

$$\theta_b^{\text{Con}} = \theta_b^{\text{Syn}} + \alpha k^2. \quad (5.17)$$

where α is defined by $\alpha \equiv \frac{1}{2k^2}(\dot{h} + 6\dot{\eta})$ and the potential η comes from writing the scalar mode of $h_{ij}(x, \tau)$, $1 \leq i, j \leq 3$, as a Fourier integral [114].

5.2.1 Evolution of photons and baryons prior to decoupling

We consider the time evolution of the photon-baryon fluid in the tight-coupling regime. Photons and baryons are treated as perfect fluids. The tight-coupling approximation of photons and baryons allows us to equate θ_γ and θ_b . Thus combining equations (5.5) and (5.6) leads to

$$(1+R)\dot{\theta}_{\gamma b} = -\dot{R}\theta_{\gamma b} + k^2\left(\frac{1}{4}\delta_\gamma - \sigma_\gamma\right) + c_s^2 k^2 R\delta_b, \quad (5.18)$$

where $\theta_{\gamma b}$ is the baryon photon common velocity divergence. We differentiate equation (5.1) and make use of equation (5.18) to derive the following second order differential equation for the photon density perturbation

$$\ddot{\delta}_\gamma + \frac{\dot{R}}{1+R}\dot{\delta}_\gamma + k^2 c_s^2 \delta_\gamma = -\frac{2}{3}\left[\frac{\dot{R}}{1+R}\dot{h} + \ddot{h}\right], \quad (5.19)$$

where we have neglected the photon shear (tight-coupling regime) and the pressure term in δ_b as it remains smaller than the term in δ_γ prior to decoupling. Equation (5.19) represents a driven harmonic oscillator with the competition between gravitational infall and photon pressure giving rise to acoustic waves propagating in the photon-baryon fluid at the speed of sound. For the associated homogeneous equation, we look for solutions of the form $\delta_\gamma \propto \exp [i \int_0^\tau \omega d\tau']$ where $\omega(\tau)$ is some phase function. The two solutions to the homogeneous equation are simply $\sin kr_s$ and $\cos kr_s$ where $r_s(\tau) = \int_0^\tau c_s d\tau'$ is the sound horizon, and the phase function is $\omega = kc_s$. Here we have made use of the WKB approximation. On large scales, the WKB approximation breaks down, but these modes are irrelevant for the CMB primary anisotropy treatment as they only enter the horizon well after decoupling. The particular solution is constructed by integrating the driving term weighted by the Green's function of the two homogeneous solutions [74]. Thus, the time evolution of the acoustic waves in the photon component prior to decoupling is given by

$$(1+R)^{1/2}\delta_\gamma(k, \tau) = A_S \sin kr_s(\tau) + A_C \cos kr_s(\tau) + \frac{1}{kc_s} \int_0^\tau (1+R(\tau'))^{1/2} \sin [kr_s(\tau) - kr_s(\tau')] F(\tau') d\tau', \quad (5.20)$$

where A_S and A_C are determined by the initial conditions as described in [29], and

$$F(\tau) = -\frac{2}{3} \left(\frac{\dot{R}}{1+R} \dot{h} + \ddot{h} \right), \quad (5.21)$$

is the gravitational driving term which evolves differently for different initial conditions. Equation (5.20) gives the time evolution of the photon density contrast irrespective of initial conditions, in the tight-coupling regime. In this regime, the baryon density contrast is related to its photon counterpart by $\dot{\delta}_b = \frac{3}{4} \dot{\delta}_\gamma$. On small scales, a correction to the tight-coupling approximation must be applied when Silk damping becomes important, as photons leak out of overdense regions, dragging baryons with them. This is done by multiplying the solution above by e^{-k^2/k_D^2} , where the photon diffusion scale k_D^{-1} is given by

$$k_D^{-2} = \frac{1}{6} \int \frac{1}{\dot{\tau}_e} \frac{R^2 + 4(1+R)/5}{(1+R)^2},$$

where $\dot{\tau}_e = an_e\sigma_T$ is the differential optical depth.

For the evolution of the common photon-baryon velocity divergence, we differentiate equation (5.18) with respect to the conformal time and use $\dot{\delta}_\gamma = -\frac{4}{3}\theta_\gamma - \frac{2}{3}\dot{h}$ to obtain the second order differential equation

$$(1 + R)\ddot{\theta}_{\gamma b} + 2\dot{R}\dot{\theta}_{\gamma b} + \left(\frac{k^2}{3} + \ddot{R}\right)\theta_{\gamma b} = -\frac{1}{6}k^2\dot{h}. \quad (5.22)$$

Equation (5.22) represents a forced and damped harmonic oscillator with variable coefficients. Its particular solution, applying the same method as for equation (5.19), is then given by

$$(1 + R)\theta_{\gamma b} = B_C \cos kr_s + B_S \sin kr_s - \frac{k}{6} \int_0^\tau \sqrt{3}(1 + R(\tau'))^{3/2} \sin k(r_s(\tau) - r_s(\tau')) \dot{h}(\tau') d\tau', \quad (5.23)$$

where B_C and B_S are determined by the initial conditions. This solution must be multiplied by $e^{-(k/k_D)^2}$ to correct the tight-coupling approximation. As we would expect, loading more baryons slows down the frequency of oscillations and decreases their oscillation amplitude.

After decoupling, the photons and baryons evolve separately. There is no pressure to resist the gravitational collapse. The baryons feel the attraction of the cold dark matter and fall into their potential wells. Thus the baryons slow down.

Equations (5.20) and (5.23) are our main solutions for the time evolution of the photon density contrast and velocity divergence prior to decoupling. They both depend on the metric field h related to the gravitational potential ϕ . The coefficients A_S , A_C , B_S and B_C are independently determined by the initial conditions of the perturbations. Hereafter, we study the time evolution of the the photon and baryon perturbations for each mode in turn. We review, using this semi-analytic approach, the well studied adiabatic case, then move onto the isocurvature modes.

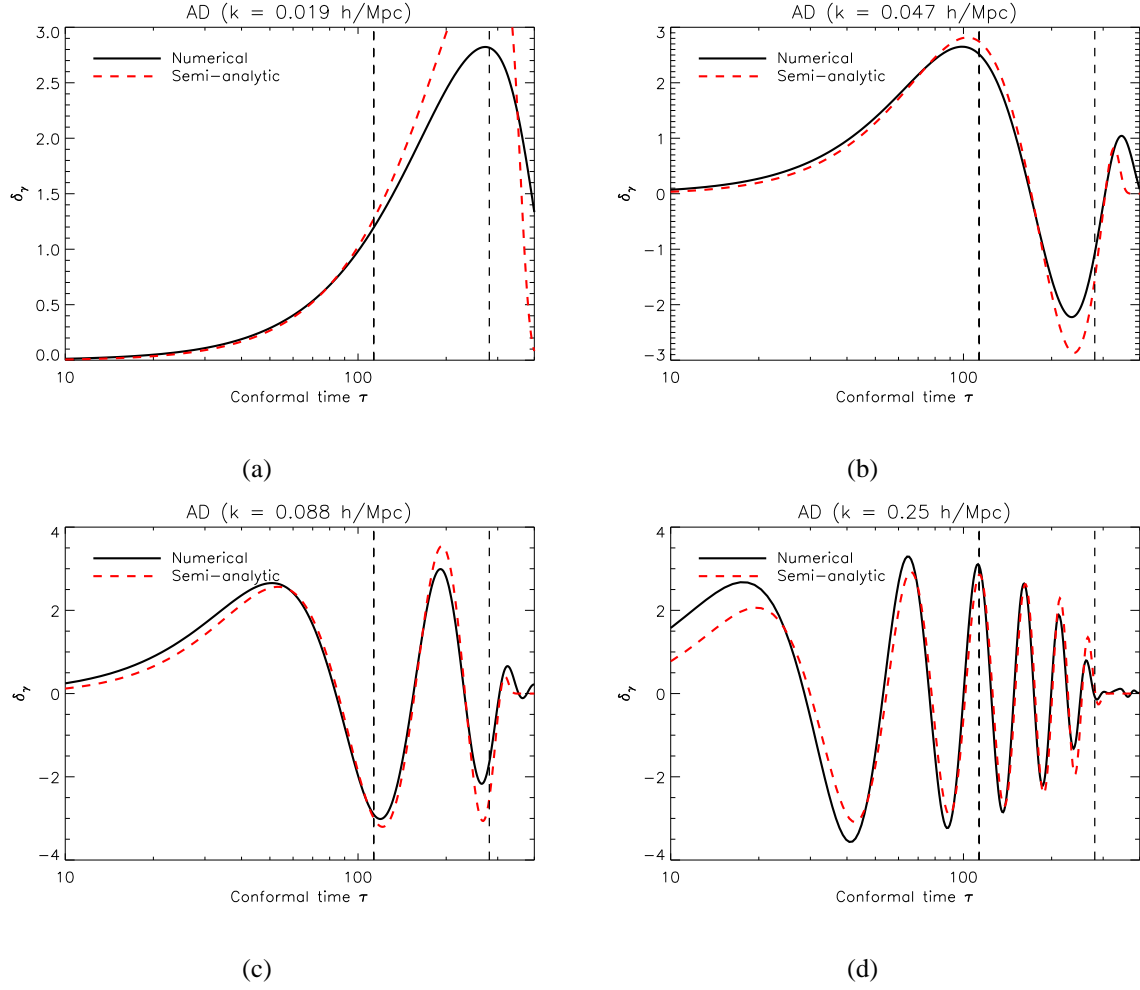


Figure 5.1: Evolution of the photon density contrast prior to decoupling for the AD mode: Comparison of numerical and analytic solutions for some wavenumbers. We consider $k = 0.019 \text{ h Mpc}^{-1}$ for the top-left panel, 0.047 h Mpc^{-1} for the top-right panel, 0.088 h Mpc^{-1} for the bottom-left panel and 0.25 h Mpc^{-1} for the bottom-right panel respectively. The vertical dashed lines mark the matter-radiation equality and decoupling.

5.2.1.1 AD mode

The adiabatic mode is characterized by the requirement that the densities of all species are perturbed in proportion at some initial time such that

$$\delta_{c,i} = \delta_{b,i} = \frac{3}{4}\delta_{\gamma,i} = \frac{3}{4}\delta_{\nu,i}, \quad (5.24)$$

where the subscript i labels the initial time. Or equivalently, using the relative entropy between two species x and y given by $\mathcal{S}_{xy} = \frac{\delta_x}{1+w_x} - \frac{\delta_y}{1+w_y}$, where w_x and w_y are the equation of state parameters of the species x and y respectively, we have that $\mathcal{S}_{xy} = 0$ for all pairs of species at the initial time. In addition, all velocity divergences are initially unperturbed. Therefore, using the initial conditions for the adiabatic mode [29], the constant A_S , A_C , B_S and B_C in equations (5.20) and (5.23) are all zero. The photon and baryon density contrasts are respectively given by

$$\delta_\gamma^{AD} = \frac{\sqrt{3}}{k} e^{-k^2/k_D^2} \int_0^\tau (1 + R(\tau'))^{1/2} \sin[kr_s(\tau) - kr_s(\tau')] \times F^{AD}(\tau') d\tau', \quad (5.25)$$

$$\delta_b^{AD} = \frac{3\sqrt{3}}{4k} e^{-k^2/k_D^2} \int_0^\tau (1 + R(\tau'))^{1/2} \sin[kr_s(\tau) - kr_s(\tau')] \times F^{AD}(\tau') d\tau'. \quad (5.26)$$

Thus, the adiabatic mode is only sourced by the gravitational driving term F^{AD} . This driving term can be approximated by

$$F^{AD}(k, \tau) \approx 2k^2 c_s^2 j_0(kr_s)$$

on small and intermediate scales which reduces to $2k^2 c_s^2$ at early times. On very large scales the above approximation breaks down, however, this does not affect our physical description of the CMB as these large-scale modes are well outside the horizon at decoupling and do not substantially influence the CMB features. The lack of an exact analytic expression for the driving term makes it difficult to derive exact analytic solutions for the time evolution of the photon and baryon density contrasts. Nevertheless, good approximations for the photon and baryon density contrasts are given by

$$\delta_\gamma = \frac{4}{3} \delta_b \approx 2kr_s j_1(kr_s) \times e^{-k^2/k_D^2}. \quad (5.27)$$

Therefore, at early times ($kr_s(\tau) \ll 1$) the density contrasts for the adiabatic mode, $\delta_\gamma \propto \delta_b \propto (1 - \cos kr_s)$ couple to a $\cos kr_s$ harmonic [74]. Thus, the acoustic oscillation for the AD mode can be regarded as a forced oscillation with a cosine type phase.

For the velocity divergence, the adiabatic initial conditions dictate that $B_S = B_C = 0$. The common baryon-photon velocity divergence is then given by

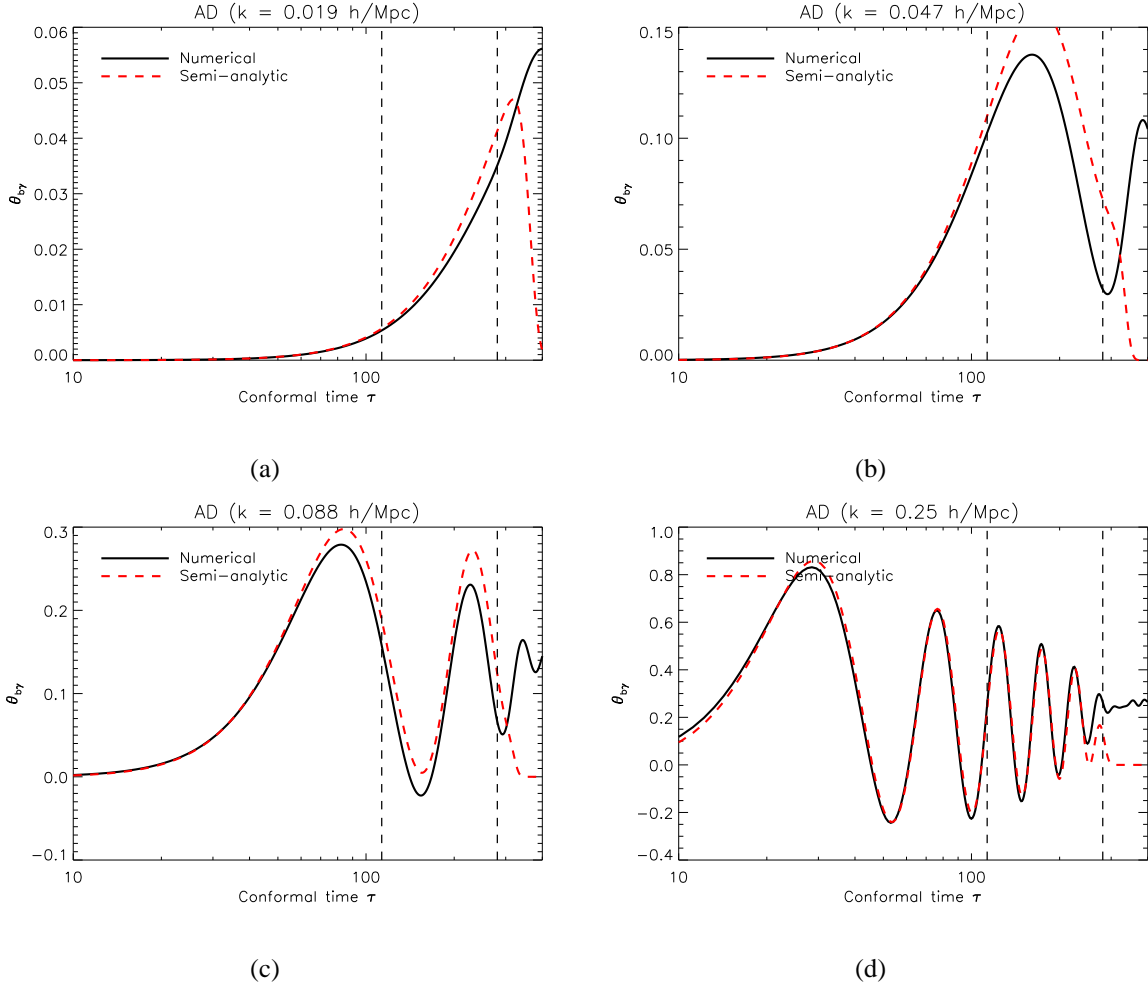


Figure 5.2: Evolution of the photon velocity divergence prior to decoupling for the AD mode: Comparison of numerical and semi-analytic solutions for some wavenumbers. We consider $k = 0.019 \text{ h Mpc}^{-1}$ for the top-left panel, 0.047 h Mpc^{-1} for the top-right panel, 0.088 h Mpc^{-1} for the bottom-left panel and 0.25 h Mpc^{-1} for the bottom-right panel respectively. The vertical dashed lines mark the matter-radiation equality and decoupling.

$$\theta_{b\gamma}^{AD} = -\frac{k}{6(1+R)} e^{-k^2/k_D^2} \int_0^\tau \sqrt{3}(1+R(\tau'))^{3/2} \sin k(r_s(\tau) - r_s(\tau')) \dot{h}(\tau') d\tau'. \quad (5.28)$$

We note that solutions given by equations (5.25) and (5.28) require a perfect knowledge of the metric field h . In Figures 5.1 and 5.2, we compare these semi-analytic solutions for the photons to the numerical solutions outputted by CAMB [100] for some wavenumbers for the AD mode.

Throughout the thesis, 'semi-analytic solution' refers to a solution for the perturbation evolution which requires a prior knowledge of the gravitational potential ϕ evolution for the conformal gauge or, equivalently the metric field h evolution for the synchronous gauge. The gravitational potential and the metric field evolution can be obtained using CAMB. On intermediate scales, the semi-analytic solution agrees considerably well with the numerical solution given by CAMB. On small and large scales, the approximation loses accuracy. However at decoupling, which is the time of our interest, the analytic solution is a good approximation to the numerical solution. As we will see later, in order to compute the primary CMB power spectrum to about 10% accuracy, one only needs to evaluate the perturbations at decoupling.

5.2.1.2 NID mode

The NID mode arises when the densities of the matter components are initially unperturbed while the initial perturbation in the neutrino density is balanced by its photon counterpart, keeping the curvature unperturbed. The initial perturbations are as follows:

$$\delta_{c,i} = \delta_{b,i} = 0, \quad \delta_{\gamma,i} = -\frac{R_\nu}{R_\gamma} \delta_{\nu,i}. \quad (5.29)$$

These initial conditions imply that $A_S = 0$ and $A_C = -\sqrt{3}c_s R_\nu / R_\gamma$ thus exciting the $\cos kr_s$ harmonic. The gravitational driving term contribution for this mode, in contrast to the AD mode, can be neglected without loss of accuracy, as the gravitational potential (related to \dot{h}), is initially unperturbed and only grows inside the horizon. This can also be understood by considering the right-hand side of equation (5.11). In the radiation dominated era, the photon and the neutrino density contrasts roughly cancel while the baryon and the CDM density contrasts remain small until the matter dominated era when they grow. The time evolution of the photon and baryon density contrasts for the NID mode are given by

$$\delta_\gamma^{NID} = -\frac{R_\nu}{R_\gamma} \sqrt{3}c_s \cos kr_s \times e^{-k^2/k_D^2}, \quad (5.30)$$

$$\delta_b^{NID} = \frac{3}{4} \frac{R_\nu}{R_\gamma} \left(1 - \sqrt{3}c_s \cos kr_s\right) \times e^{-k^2/k_D^2}, \quad (5.31)$$

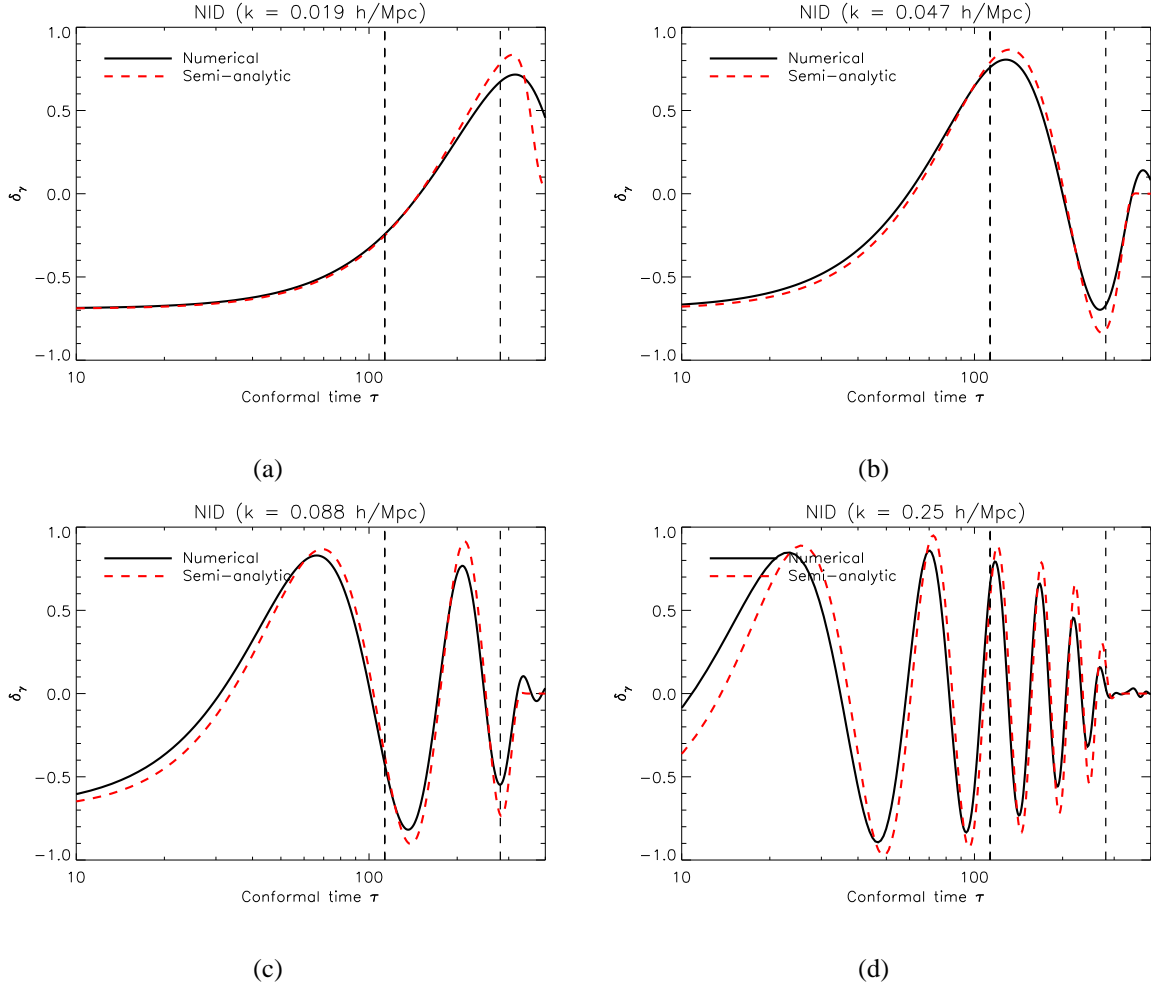


Figure 5.3: Evolution of the photon density contrast prior to decoupling for the NID mode: Comparison of numerical and analytic solutions for some wavenumbers. We consider $k = 0.019 \text{ h Mpc}^{-1}$ for the top-left panel, 0.047 h Mpc^{-1} for the top-right panel, 0.088 h Mpc^{-1} for the bottom-left panel and 0.25 h Mpc^{-1} for the bottom-right panel respectively. The vertical dashed lines mark the matter-radiation equality and decoupling.

where $R_\nu = \Omega_\nu/\Omega_{rad}$ and $R_\gamma = \Omega_\gamma/\Omega_{rad}$ are respectively the fractional energy densities of neutrinos and photons at early times. The smallness of the gravitational potential, hence its decay, affects the evolution of photons even after recombination lowering the early Integrated Sachs Wolfe (ISW) effect. Thus, the NID mode can be regarded as a free oscillation with a cosine type phase.

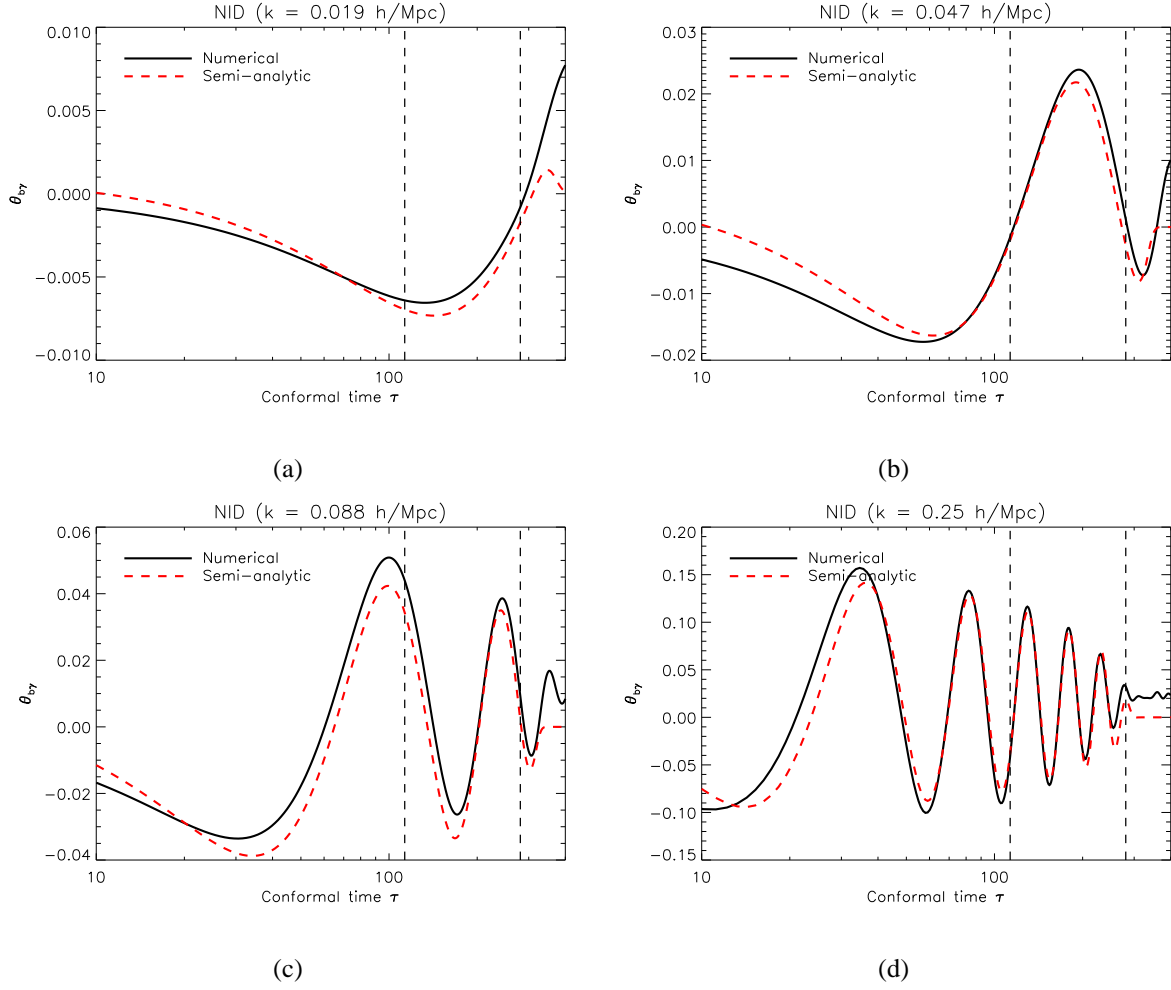


Figure 5.4: Evolution of the photon velocity divergence prior to decoupling for the NID mode: Comparison of numerical and analytic solutions for some wavenumbers. We consider $k = 0.019 \text{ h Mpc}^{-1}$ for the top-left panel, 0.047 h Mpc^{-1} for the top-right panel, 0.088 h Mpc^{-1} for the bottom-left panel and 0.25 h Mpc^{-1} for the bottom-right panel respectively. The vertical dashed lines mark the matter-radiation equality and decoupling.

For the photon-baryon velocity divergence, the initial conditions dictate that $B_C = 0$ and $B_S = -3kc_s A_C/4$ in equation (5.23), and the sourcing term is irrelevant. Therefore the photon-baryon velocity divergence is given by

$$\theta_{\gamma b}^{NID} = \sqrt{3} \frac{3 R_\nu}{4 R_\gamma} k c_s^2 \sin k r_s \times e^{-k^2/k_D^2}. \quad (5.32)$$

For the NID mode, the semi-analytic solutions do not require knowledge of the gravitational

potential. In Figures 5.3 and 5.4, we compare the numerical and analytical solutions for the evolution of the photon density contrast and velocity divergence for some wavenumbers in the NID mode. For the photon density contrast, the semi-analytic solution is in good agreement with the numerical, as it does not require the evolution of the gravitational potential. For the photon velocity divergence, the approximation improves as $k\tau$ increases. Nevertheless it is a good approximation around decoupling.

Equation (5.12) suffices to give us a good approximation to the behaviour of the gravitational potential ϕ for modes still outside the horizon. For those modes, $k\tau \ll 1$. We therefore neglect the term proportional to k^2 . The conformal gauge perturbation in the time component of the energy-momentum tensor δT_0^0 is given in the synchronous gauge by $\delta\rho^{Con} = \delta\rho^{Syn} + \alpha\dot{\rho}^{Syn}$. In the case of the NID mode, α is given to leading order by

$$\alpha = -\frac{R_\nu}{15 + 4R_\nu}\tau. \quad (5.33)$$

Using the fact that $\dot{\rho} = -3H\rho(1 + w)$ with $H = 1/\tau$ in the radiation-dominated era together with the Friedmann equation, equation (5.12) becomes

$$\tau\dot{\phi} + \phi = -\frac{2R_\nu}{15 + 4R_\nu}, \quad (5.34)$$

which admits the general solution

$$\phi = A\tau^{-1} - \frac{2R_\nu}{15 + 4R_\nu}, \quad (5.35)$$

where A is some constant. The first term of this solution represents a decaying mode which vanishes rapidly with time and the second term is constant. Thus we can omit the decaying mode and write the solution as

$$\phi = \frac{-2R_\nu}{15 + 4R_\nu}. \quad (5.36)$$

Thus outside the horizon, in the radiation-dominated era, the potential ϕ is constant and does not even depend on the wavenumber of the considered mode, but depends only on the ratio of neutrino density to radiation density, R_ν . This behaviour is seen in Figure 5.5(a) where we have

represented the time evolution of the gravitational potential for different wavenumbers using CAMB [100]. The gravitational potential starts off constant at early times, then decays at the matter-radiation transition.

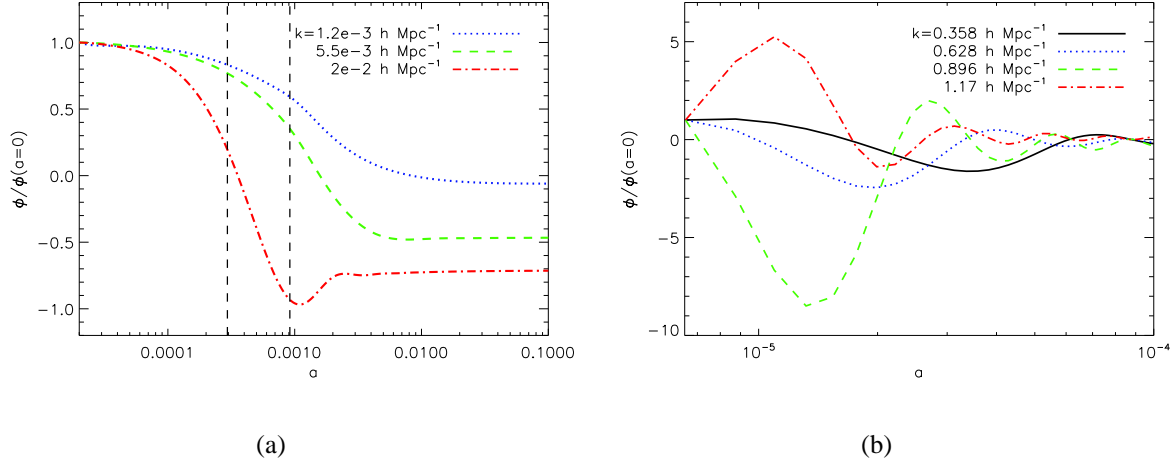


Figure 5.5: Evolution of the gravitational potential ϕ in the NID mode. **(a)**: Super horizon evolution; **(b)**: Sub-horizon evolution in the radiation era. These curves are obtained using CAMB. The vertical dashed lines mark the matter-radiation equality and decoupling.

It is difficult to solve for the potential ϕ exactly through horizon crossing. However, for the NID mode, the potential ϕ does not play a dominant role in determining the CMB anisotropies and finding an analytical solution for ϕ is not so crucial. We obtain asymptotic solutions for ϕ , firstly at early times when radiation dominates, and then at late times when matter dominates.

Inside the horizon and for small scales, $k\tau \gg 1$, so we neglect the terms in $1/\tau$ with respect to those in k . Prior to matter-radiation equality, equation (5.12) can be written as

$$\phi = -\frac{3}{2} \frac{H^2}{k^2} (\Omega_\gamma \delta_\gamma^{Syn} + \Omega_\nu \delta_\nu^{Syn} + \alpha \frac{\dot{\rho}}{\rho}), \quad (5.37)$$

where H is given by $1/\tau$ and the term $\alpha \frac{\dot{\rho}}{\rho}$ is constant and arises from gauge transformation from the synchronous to the conformal gauge using equation (5.16) and $\dot{\rho}/\rho = -3H(1+w)$ [29], since ϕ is a conformal gauge quantity and the density contrasts are in synchronous gauge. Since

neutrinos decoupled early on, they freestream toward us today and their density perturbations can be neglected in the above equation. The baryons and photons are still coupled and oscillate due to pressure and gravity. Thus the behaviour of the potential is mainly determined by the photon density perturbations. The potential ϕ thus oscillates with decreasing amplitude (due to the H^2 term in equation (5.37)), which matches the behaviour of the small scale mode shown in Figure 5.5(b).

In the matter-dominated era and well after decoupling, the photons and neutrino densities can be neglected. We bear in mind that $H = 2/\tau$ in the matter-dominated era. Equation (5.12) becomes

$$\phi = -\frac{6}{k^2\tau^2}(\Omega_c\delta_c^{Syn} + \Omega_b\delta_b^{Syn} + \alpha\frac{\dot{\rho}}{\rho}). \quad (5.38)$$

Well after decoupling, the baryons feel the potential well set up by the cold dark matter. Thus equating δ_c and δ_b is a good approximation. As the matter perturbation grows like τ^2 , we can neglect the constant gauge transformation term. We then have

$$\phi \propto -\frac{6}{k^2\tau^2}\delta_c^{Syn}. \quad (5.39)$$

As the dark matter perturbation grows inside the horizon as τ^2 , we can easily see that the potential ϕ is therefore constant in the matter-dominated era. The features described above can easily be seen in Figure 5.5(b) in which the time evolution of the potential ϕ is represented for four different wavenumbers corresponding to different epochs of horizon crossing.

5.2.1.3 NIV mode

Unlike the other isocurvature modes, the NIV mode, like the AD mode, shows no relative entropy perturbation in the density field at some initial time. All the density perturbations are zero initially. The main difference with the AD mode is in the velocity field where the neutrino velocity divergence starts perturbed, being compensated by the photon-baryon velocity. The initial perturbations are given by:

$$\theta_{c,i} = 0, \quad \theta_{b,i} = \theta_{\gamma,i} = -\frac{R_\nu}{R_\gamma}\theta_{\nu,i}. \quad (5.40)$$

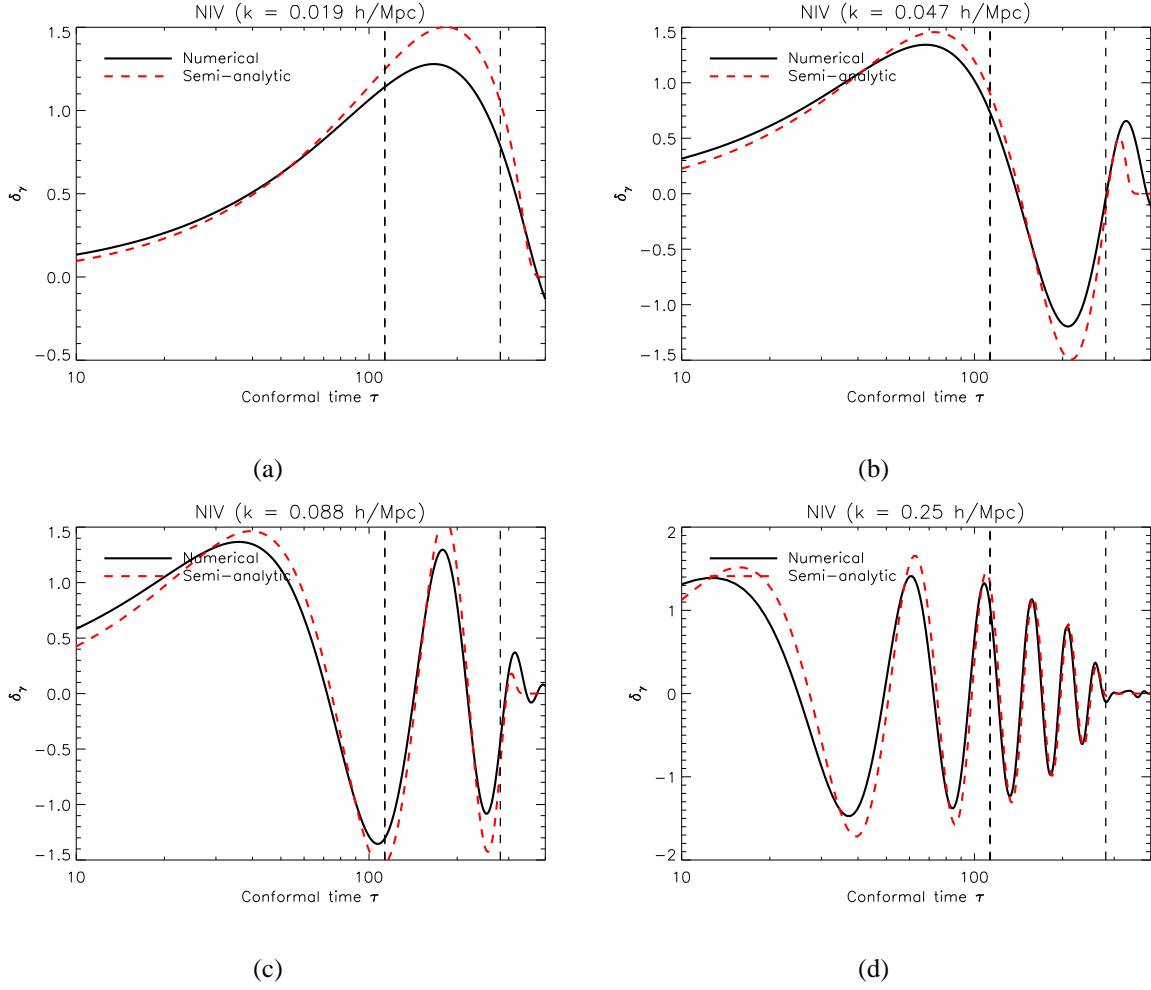


Figure 5.6: Evolution of the photon density contrast prior to decoupling for the NIV mode: Comparison of numerical and analytic solutions for some wavenumbers. We consider $k = 0.019 \text{ h Mpc}^{-1}$ for the top-left panel, 0.047 h Mpc^{-1} for the top-right panel, 0.088 h Mpc^{-1} for the bottom-left panel and 0.25 h Mpc^{-1} for the bottom-right panel respectively. The vertical dashed lines mark the matter-radiation equality and decoupling.

The NIV mode excites the $\sin kr_s$ harmonic, so that we can set $A_C = 0$ and $A_S = 4R_\nu/\sqrt{3}R_\gamma$ in equation (5.20). As in the case of the NID mode, the gravitational driving term contribution remains irrelevant at all times as all the densities start unperturbed and the perturbations only grow in the matter dominated era. Therefore, the NIV mode can be regarded as a free oscillation with a sine type phase. The photon velocity divergence is initially perturbed. This sets $B_S = 0$

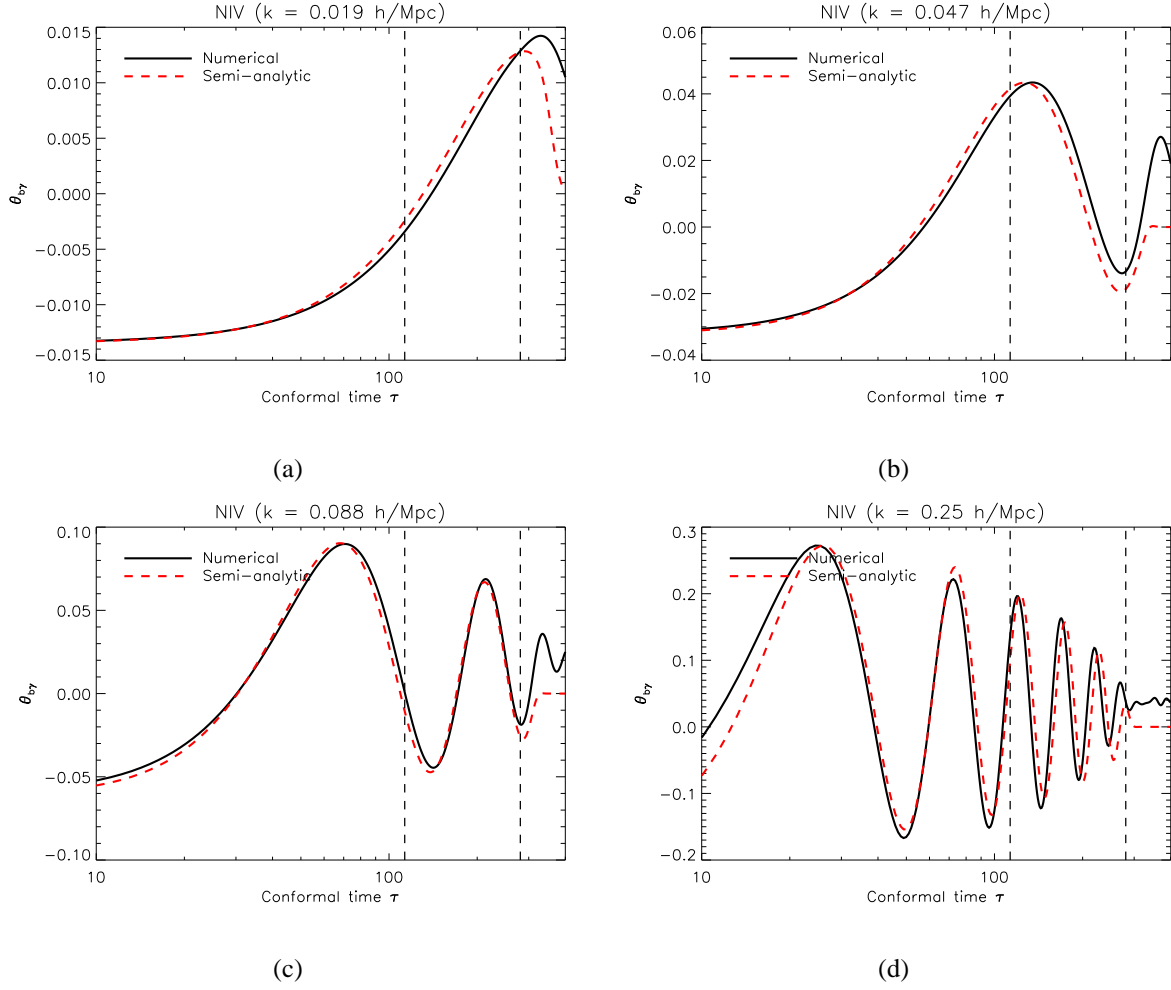


Figure 5.7: Evolution of the photon velocity divergence prior to decoupling for the NIV mode: Comparison of numerical and analytic solutions for some wavenumbers. We consider $k = 0.019 \text{ h Mpc}^{-1}$ for the top-left panel, 0.047 h Mpc^{-1} for the top-right panel, 0.088 h Mpc^{-1} for the bottom-left panel and 0.25 h Mpc^{-1} for the bottom-right panel respectively. The vertical dashed lines mark the matter-radiation equality and decoupling.

and $B_C = -3 \frac{R_\nu}{R_\gamma} k c_s^2$ in equation (5.23). The time evolution of the photon and baryon density contrasts and the baryon-photon common velocity divergence for the NIV mode are given by

$$\delta_\gamma^{NIV} = \frac{R_\nu}{R_\gamma} \sqrt{3} \sin kr_s(\tau) \times e^{-k^2/k_D^2}, \quad (5.41)$$

$$\delta_b^{NIV} = \frac{3}{4} \frac{R_\nu}{R_\gamma} \sqrt{3} \sin kr_s(\tau) \times e^{-k^2/k_D^2}, \quad (5.42)$$

$$\theta_{\gamma b}^{NIV} = -3 \frac{R_\nu}{R_\gamma} k c_s^2 \cos kr_s \times e^{-k^2/k_D^2}. \quad (5.43)$$

In Figures 5.6 and 5.7, we compare the numerical and analytical solutions for the evolution of the photon density contrast and velocity divergence for some wavenumbers for the NIV mode. The semi-analytic density contrast and velocity divergence for photons are in good agreement with their numerical counterparts.

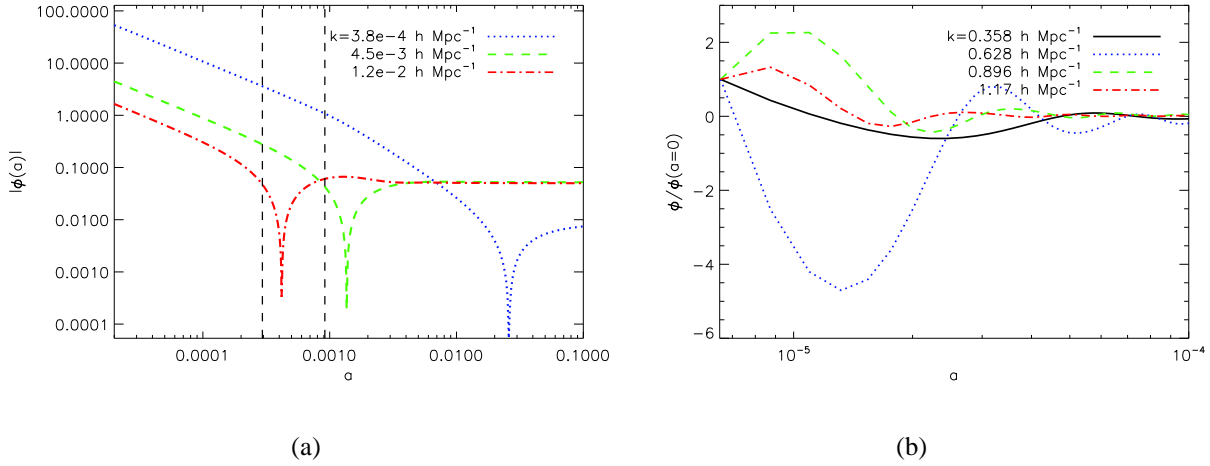


Figure 5.8: Evolution of the gravitational potential ϕ in the NIV mode. **(a)**: Super horizon evolution; **(b)**: Sub-horizon evolution in the radiation era. These curves are obtained using CAMB. The vertical dashed lines mark the matter-radiation equality and decoupling.

For the asymptotic behaviour of the gravitational potential for the NIV mode, let us consider equation (5.13). The velocity divergence in the Newtonian gauge is related to the velocity in the synchronous gauge by equation (5.17) with $\alpha = -\frac{4R_\nu}{5 + 4R_\nu} \frac{1}{k}$ for the NIV mode. Bearing in mind that $H = 1/\tau$ in the radiation-dominated era, we can rewrite equation (5.13) as

$$\dot{\phi} + \frac{1}{\tau} \phi = \frac{3}{2} \frac{1}{k^2 \tau^2} \sum_j (1 + w_j) \Omega_j \left(\theta_j^{syn} - \frac{4R_\nu}{5 + 4R_\nu} k \right), \quad (5.44)$$

where ψ has been replaced by ϕ since there is no shear in the tight-coupling regime (see equation (5.15)). The solution of equation (5.44) up to leading order is given by

$$\phi = -\frac{4R_\nu}{5 + 4R_\nu} \frac{1}{k\tau}. \quad (5.45)$$

The potential ϕ decreases with time outside the horizon in the radiation-dominated era. This is shown in Figure 5.8(a) for different k -modes.

Through horizon crossing, as we emphasized for the neutrino isocurvature density model, it is difficult to obtain the potential ϕ exactly. A similar treatment to that for the neutrino isocurvature density model can be applied here. The equations (5.37) and (5.38) that we found for the neutrino isocurvature density model are still valid and applicable for we did not make any restrictive assumption related to the nature of the primordial perturbations for their derivation. Therefore prior to matter-radiation equality, the potential oscillates and is sourced by the photons. After matter-radiation equality, it becomes constant. These features are shown in Figure 5.8(b) where the time evolution of the potential ϕ is shown for four different wavenumbers corresponding to different epochs of horizon crossing.

5.2.1.4 CI & BI modes

The CI and the BI modes have been well studied in the literature [25, 35, 76]. The CI and BI modes are similar in that the perturbation starts in the CDM density contrast and the baryon density contrast respectively while the other species are initially unperturbed. This can be written at some initial time as

$$\delta_{c,i} = 1, \quad \delta_{b,i} = \delta_{\gamma,i} = \delta_{\nu,i} = 0, \quad (5.46)$$

for the CI mode, and as

$$\delta_{c,i} = 0, \quad \delta_{b,i} = 1, \quad \delta_{\gamma,i} = \delta_{\nu,i} = 0, \quad (5.47)$$

for the BI mode. The CI and BI initial conditions dictate that $A_S = -\frac{8}{\sqrt{3}k}\Omega_{c,0}$ for the CI mode and $A_S = -\frac{8}{\sqrt{3}k}\Omega_{b,0}$ for the BI mode, while $A_c = 0$ in both cases, thus exciting the $\sin kr_s$ harmonic [85, 29]. The constants $\Omega_{c,0}$ and $\Omega_{b,0}$ are respectively the CDM and the baryon densities

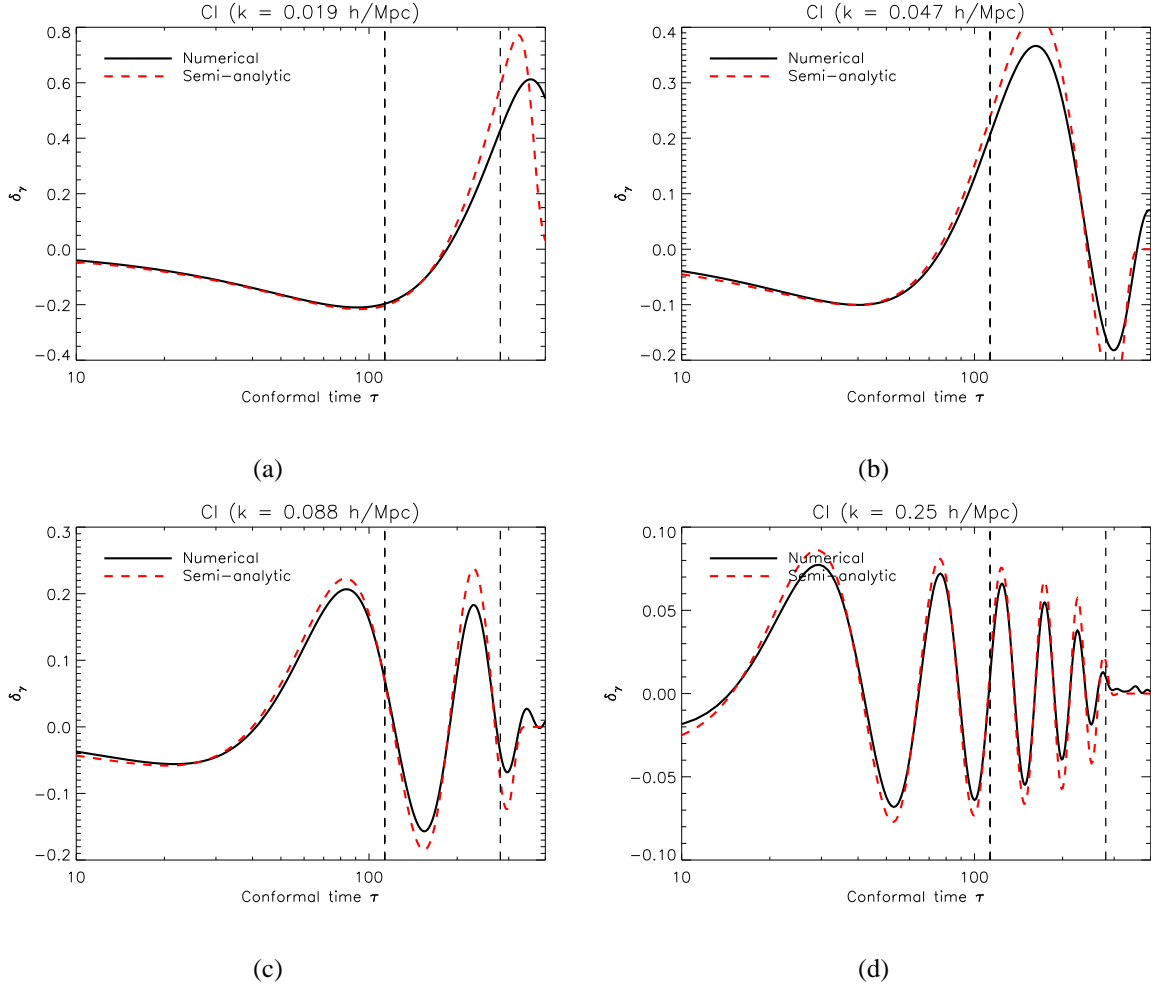


Figure 5.9: Evolution of the photon density contrast prior to decoupling for the CI mode: Comparison of numerical and semi-analytic solutions for some wavenumbers. We consider $k = 0.019 \text{ h Mpc}^{-1}$ for the top-left panel, 0.047 h Mpc^{-1} for the top-right panel, 0.088 h Mpc^{-1} for the bottom-left panel and 0.25 h Mpc^{-1} for the bottom-right panel respectively. The vertical dashed lines mark the matter-radiation equality and decoupling.

today. The driving term is small in the radiation domination era as the photon and the neutrino densities are initially unperturbed but becomes important in the matter domination era as the matter perturbation sources the gravitational potential [73].

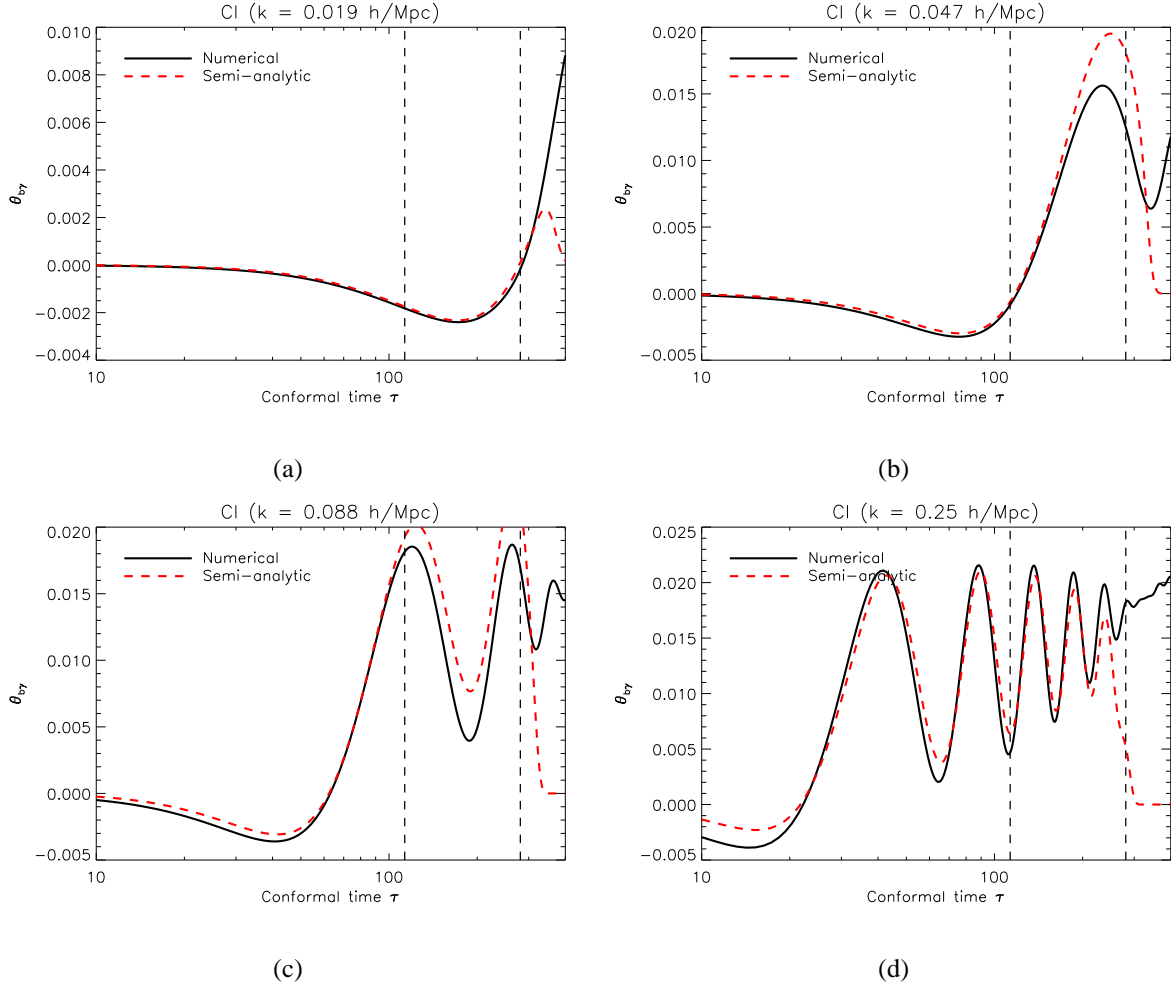


Figure 5.10: Evolution of the photon velocity divergence prior to decoupling for the CI mode: Comparison of numerical and semi-analytic solutions for some wavenumbers. We consider $k = 0.019 \text{ h Mpc}^{-1}$ for the top-left panel, 0.047 h Mpc^{-1} for the top-right panel, 0.088 h Mpc^{-1} for the bottom-left panel and 0.25 h Mpc^{-1} for the bottom-right panel respectively. The vertical dashed lines mark the matter-radiation equality and decoupling.

The time evolution of the photon and baryon density contrasts for the CI and BI modes are given

by [73]

$$\begin{aligned}\delta_\gamma^{CI} = & -\frac{8}{3}\Omega_{c,0}\frac{\sqrt{3}}{k}\sin kr_s(\tau) \times e^{-k^2/k_D^2} \\ & + \frac{\sqrt{3}}{k} \int_0^\tau (1+R(\tau'))^{1/2} \sin[kr_s(\tau) - kr_s(\tau')] \times F^{CI}(\tau') d\tau',\end{aligned}\quad (5.48)$$

$$\begin{aligned}\delta_b^{CI} = & -2\Omega_{c,0}\frac{\sqrt{3}}{k}\sin kr_s(\tau) \times e^{-k^2/k_D^2} \\ & + \frac{3}{4}\frac{\sqrt{3}}{k} \int_0^\tau (1+R(\tau'))^{1/2} \sin[kr_s(\tau) - kr_s(\tau')] \times F^{CI}(\tau') d\tau',\end{aligned}\quad (5.49)$$

for the CI mode, and by

$$\begin{aligned}\delta_\gamma^{BI} = & -\frac{8}{3}\Omega_{b,0}\frac{\sqrt{3}}{k}\sin kr_s(\tau) \times e^{-k^2/k_D^2} \\ & + \frac{\sqrt{3}}{k} \int_0^\tau (1+R(\tau'))^{1/2} \sin[kr_s(\tau) - kr_s(\tau')] \times F^{BI}(\tau') d\tau',\end{aligned}\quad (5.50)$$

$$\begin{aligned}\delta_b^{BI} = & 1 - 2\Omega_{b,0}\frac{\sqrt{3}}{k}\sin kr_s(\tau) \times e^{-k^2/k_D^2} \\ & + \frac{3}{4}\frac{\sqrt{3}}{k} \int_0^\tau (1+R(\tau'))^{1/2} \sin[kr_s(\tau) - kr_s(\tau')] \times F^{BI}(\tau') d\tau',\end{aligned}\quad (5.51)$$

for the BI mode. Equations (5.48-5.51) are exact but require a perfect knowledge of the gravitational driving term. One thing to notice is the k^{-1} dependence of the photon density contrast for the CI and BI modes that washes out perturbations on small scales while amplifying them on large scales. As we show in the next section, this redistribution of power boosts the ISW effect of the CMB temperature power spectrum (large scales) and suppresses anisotropies on small scales, for these modes. On small scales, the effect of the k^{-1} factor can be compared to Silk damping as they both suppress perturbations on these scales. However there are two main differences. Firstly, Silk damping does not act on large scales while the k^{-1} factor amplifies large scale perturbations. Secondly, Silk damping only becomes significant around recombination while the k^{-1} factor redistributes the power at all times.

For the photon-baryon velocity divergence, $B_S = B_C = 0$ for both CI and BI modes. The velocity is solely determined by the driving term of equation (5.23). The photon-baryon velocity

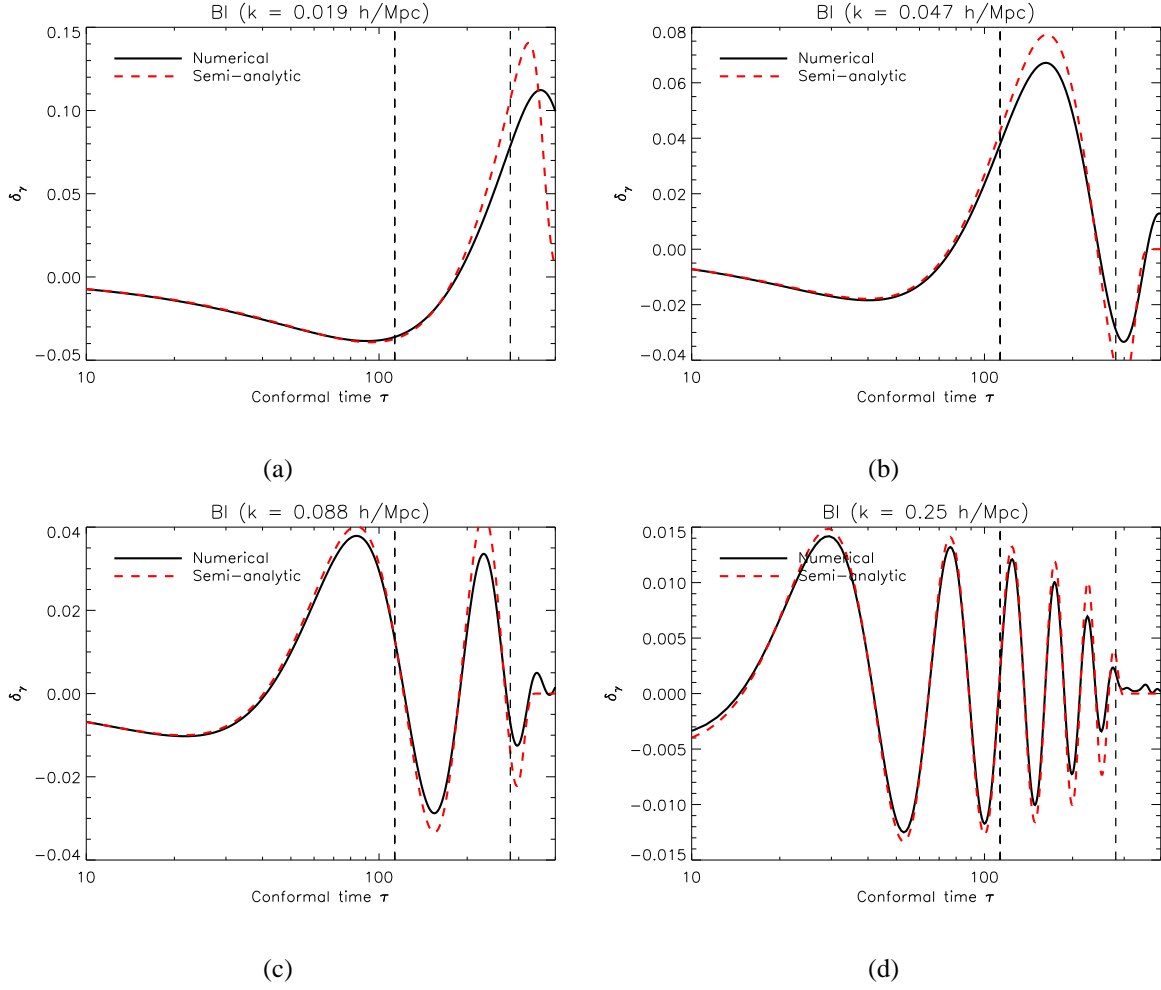


Figure 5.11: Evolution of the photon density contrast prior to decoupling for the BI mode: Comparison of numerical and semi-analytic solutions for some wavenumbers. We consider $k = 0.019 \text{ h Mpc}^{-1}$ for the top-left panel, 0.047 h Mpc^{-1} for the top-right panel, 0.088 h Mpc^{-1} for the bottom-left panel and 0.25 h Mpc^{-1} for the bottom-right panel respectively. The vertical dashed lines mark the matter-radiation equality and decoupling.

divergence for the CI and BI modes is given by

$$\theta_{b\gamma}^{CI,BI} = -\frac{k}{6(1+R)} \int_0^\tau \sqrt{3}(1+R(\tau'))^{3/2} \sin k(r_s(\tau) - r_s(\tau')) \dot{h}(\tau') d\tau', \quad (5.52)$$

as for the adiabatic mode. However, the metric field in the CI and BI modes differs from the metric field in the adiabatic mode. Figures 5.9-5.10 and 5.11-5.12 compare the semi-analytic and the numerical solution for the evolution of the photon density contrast and velocity divergence

for the CI and BI modes respectively.

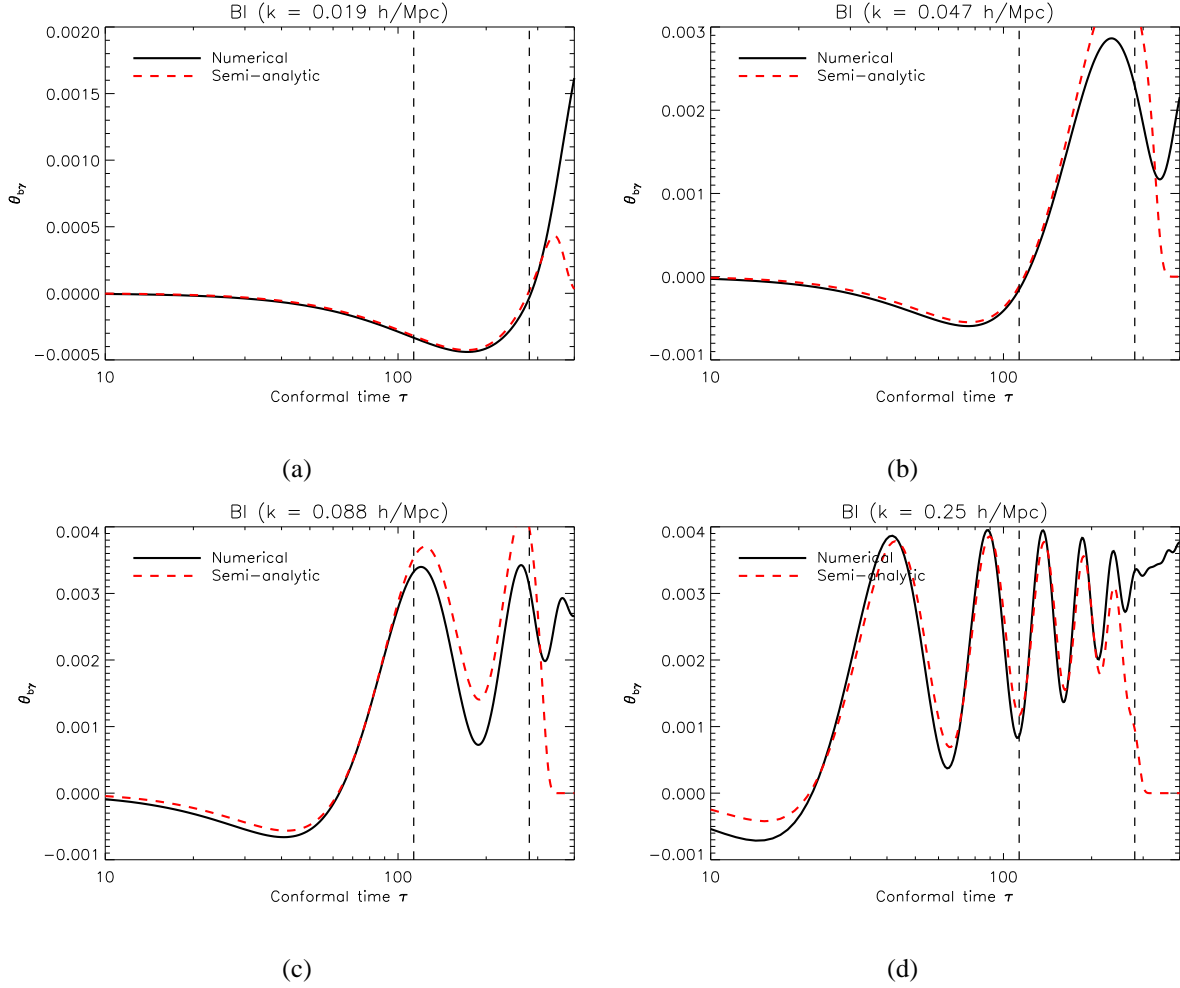


Figure 5.12: Evolution of the photon velocity divergence prior to decoupling for the BI mode: Comparison of numerical and semi-analytic solutions for some wavenumbers. We consider $k = 0.019 \text{ h Mpc}^{-1}$ for the top-left panel, 0.047 h Mpc^{-1} for the top-right panel, 0.088 h Mpc^{-1} for the bottom-left panel and 0.25 h Mpc^{-1} for the bottom-right panel respectively. The vertical dashed lines mark the matter-radiation equality and decoupling.

For the super horizon evolution of the gravitational potential in CI and BI models, we proceed as previously in the NID mode. One should note that for these modes, $\alpha = 0$ to leading order, causing the synchronous gauge densities to be equal to their conformal gauge counterparts. Equation

(5.12) simplifies for the CI and BI modes respectively as

$$\tau\dot{\phi} + \phi = \frac{4}{3}\Omega_{c,0}\tau, \quad (5.53)$$

$$\tau\dot{\phi} + \phi = \frac{4}{3}\Omega_{b,0}\tau, \quad (5.54)$$

which admit the general solutions

$$\phi^{CI} = B\tau^{-1} - \frac{4}{3}\Omega_{c,0}\tau, \quad (5.55)$$

$$\phi^{BI} = C\tau^{-1} - \frac{4}{3}\Omega_{b,0}\tau, \quad (5.56)$$

where B and C are some constants. As for the NID mode, the first terms of these solutions represent decaying modes which vanishes rapidly with time. The second terms, proportional to τ , are the growing modes. Thus we can omit the decaying modes and write the solutions as

$$\phi^{CI} = -\frac{4}{3}\Omega_{c,0}\tau, \quad (5.57)$$

$$\phi^{BI} = -\frac{4}{3}\Omega_{b,0}\tau. \quad (5.58)$$

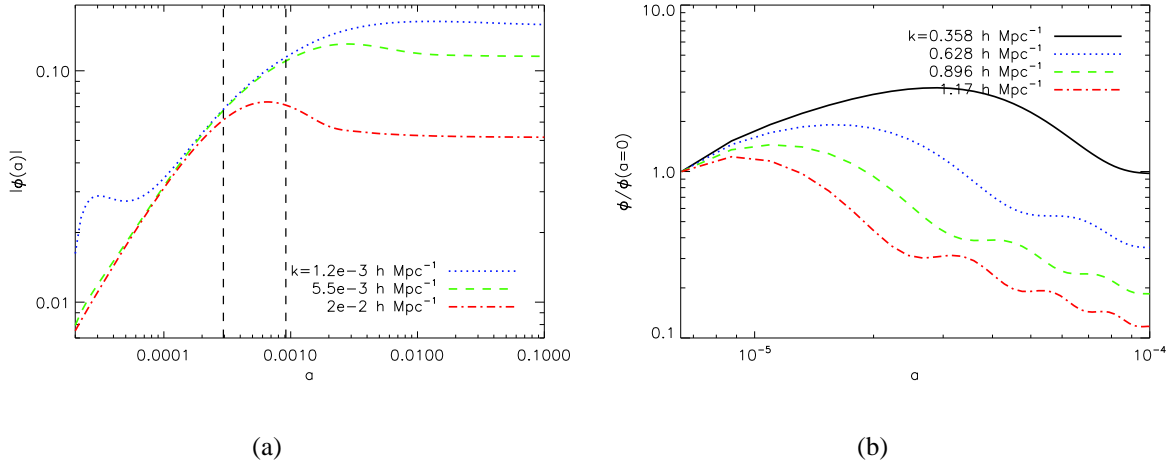


Figure 5.13: Evolution of the gravitational potential ϕ in the CI mode. **(a)**: Super horizon evolution; **(b)**: Sub-horizon evolution in the radiation era. These curves are obtained using CAMB. The vertical dashed lines mark the matter-radiation equality and decoupling.

Thus outside the horizon, in the radiation-dominated era, the gravitational potential ϕ in the CI and BI modes grows linearly with time in magnitude, and does not even depend on the wavenum-

ber of the considered mode, but depends only on the dark matter and baryon densities. This behaviour is shown in Figures 5.13(a) and 5.14(a) where we have respectively represented the super horizon evolution of the gravitational potential in CI and BI models for different wavenumbers. For the sub-horizon evolution, the derivation done in the case of the NID mode holds.

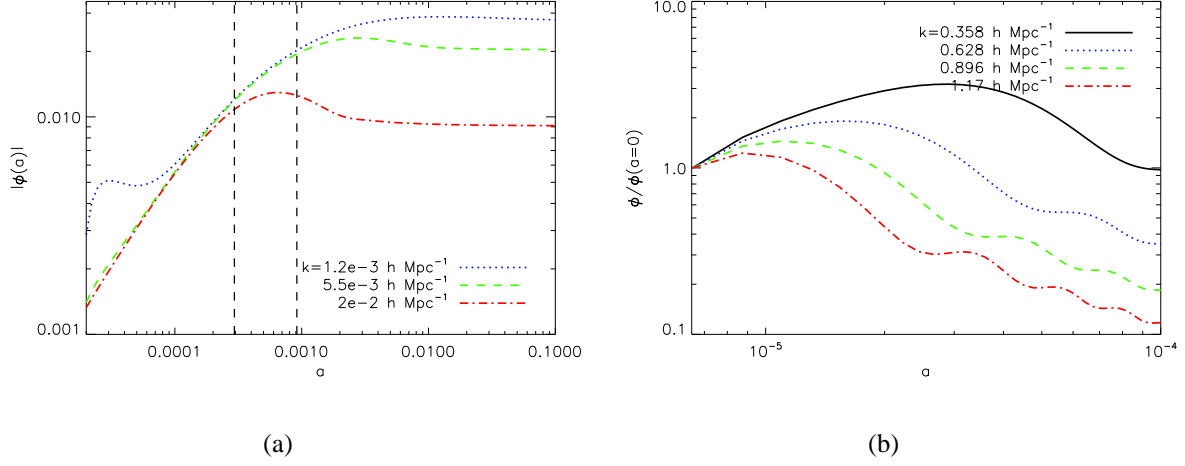


Figure 5.14: Evolution of the gravitational potential ϕ in the BI mode. **(a)**: Super horizon evolution; **(b)**: Sub-horizon evolution in the radiation era. These curves are obtained using CAMB. The vertical dashed lines mark the matter-radiation equality and decoupling.

Therefore prior to matter-radiation equality, the potential oscillates and is sourced by the photons. After matter-radiation equality, it becomes constant. These features are shown in Figures 5.13(b) and 5.14(b) where the sub-horizon evolution of the potential ϕ is shown for four different wavenumbers.

5.3 CMB anisotropies in isocurvature models

In the previous section, we followed the time-evolution of the photon density contrast, δ_γ , the common photon-baryon velocity divergence, $\theta_{b\gamma}$, and the gravitational potential, ϕ , for different initial conditions, from some initial time to the last scattering surface where the photons and

baryons decouple. After decoupling, photons freestream towards us today and baryons, through gravitational attraction, fall into the dark matter potential wells. The three quantities δ_γ , $\theta_{b\gamma}$ and ϕ above-mentioned allow us to compute the primary CMB angular power spectrum C_ℓ using the line of sight integral approach.

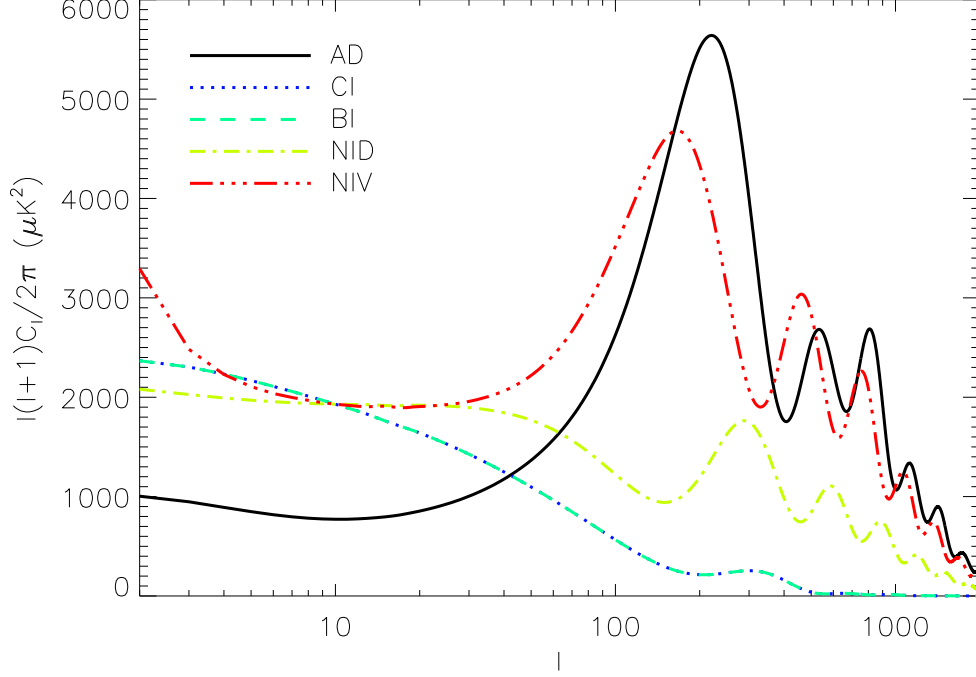


Figure 5.15: Comparison of CMB temperature power spectra for AD, CI, BI, NID and NIV modes for the same cosmological model. This is for a flat Λ CDM universe with $\Omega_b h^2 = 0.022$, $\Omega_c h^2 = 0.125$ and $h = 0.7$. The isocurvature spectra are normalized to have same $C_{10}^{ISO} = 2.5C_{10}^{AD}$ for clarity. These spectra are obtained using CAMB.

We recall that the CMB angular power spectrum is given by

$$C_\ell = \frac{2}{\pi} \int \frac{dk}{k} k^3 \frac{|\Theta_\ell(\tau, k)|^2}{(2\ell + 1)^2}, \quad (5.59)$$

where the multipole moments $\Theta_\ell(\tau, k)$ are given, using the line of sight integral approach, by

$$\Theta_\ell(k, \tau_0) = \int_0^{\tau_0} S(k, \tau) j_\ell[k(\tau - \tau_0)] d\tau, \quad (5.60)$$

with $S(k, \tau)$ being the source function. In the synchronous gauge, the source function is given by

$$S = e^{-\tau_e} (\dot{\eta} + \ddot{\alpha}) + g(\tau) \left[\frac{\delta_\gamma}{4} + \frac{\dot{\theta}_b}{k^2} + 2\dot{\alpha} + \frac{\Pi}{16} + \frac{3\ddot{\Pi}}{16k^2} \right] + \dot{g}(\tau) \left[\frac{\theta_b}{k^2} + \alpha + \frac{3\dot{\Pi}}{8k^2} \right] + \ddot{g}(\tau) \left[\frac{3\Pi}{16k^2} \right],$$

where $g(\tau)$ is the visibility function. For the primary anisotropies, the contribution to the source function due to the photon polarization is small compared to the other terms in the source function and can be neglected. Thus the source function further simplifies to the expression

$$S = e^{-\tau_e} (\dot{\eta} + \ddot{\alpha}) + g(\tau) \left[\frac{\delta_\gamma}{4} + \frac{\dot{\theta}_b}{k^2} + 2\dot{\alpha} \right] + \dot{g}(\tau) \left[\frac{\theta_b}{k^2} + \alpha \right]. \quad (5.61)$$

Figure 5.15 shows the CMB temperature power spectra for the CI, BI, NID and NIV modes for the same cosmological model. The AD mode is shown here only for reference purposes. Here, the isocurvature spectra are normalized to have the same power at $\ell = 10$. Except for the CI and BI modes that have the same spectrum, these spectra show different features from the fact that the evolution of photon density contrast and velocity divergence, and the evolution of the gravitational potential differ from one mode to another. Among these distinctive features are, the positions and the amplitude of the acoustic peaks, the height of the Sachs-Wolfe plateau and the steepness of the spectrum on small scales. Hereafter, we first show that CMB power spectrum can be obtained to about 10% accuracy, using only the photon density contrast and velocity divergence evaluated at decoupling, and the evolution of the gravitational potential. We then consider each isocurvature mode in turn and compare it to the adiabatic and other isocurvature modes. We group the NIV and NID modes as these are free oscillations and have some similarities with regard to the acoustic peak positions and the integrated Sachs-Wolfe effect, then consider the CI and BI modes which have the same CMB temperature power spectrum.

The multipole moments can be further simplified knowing that the visibility function is approximately a Dirac delta function that peaks at decoupling (ignoring reionization for now). Thus, to a good accuracy, the multipole moments can be computed using the photon density contrast and the baryon velocity divergence evaluated at decoupling, and the evolution of the gravitational potential [78]. In this approximation, the multipole moments are given by

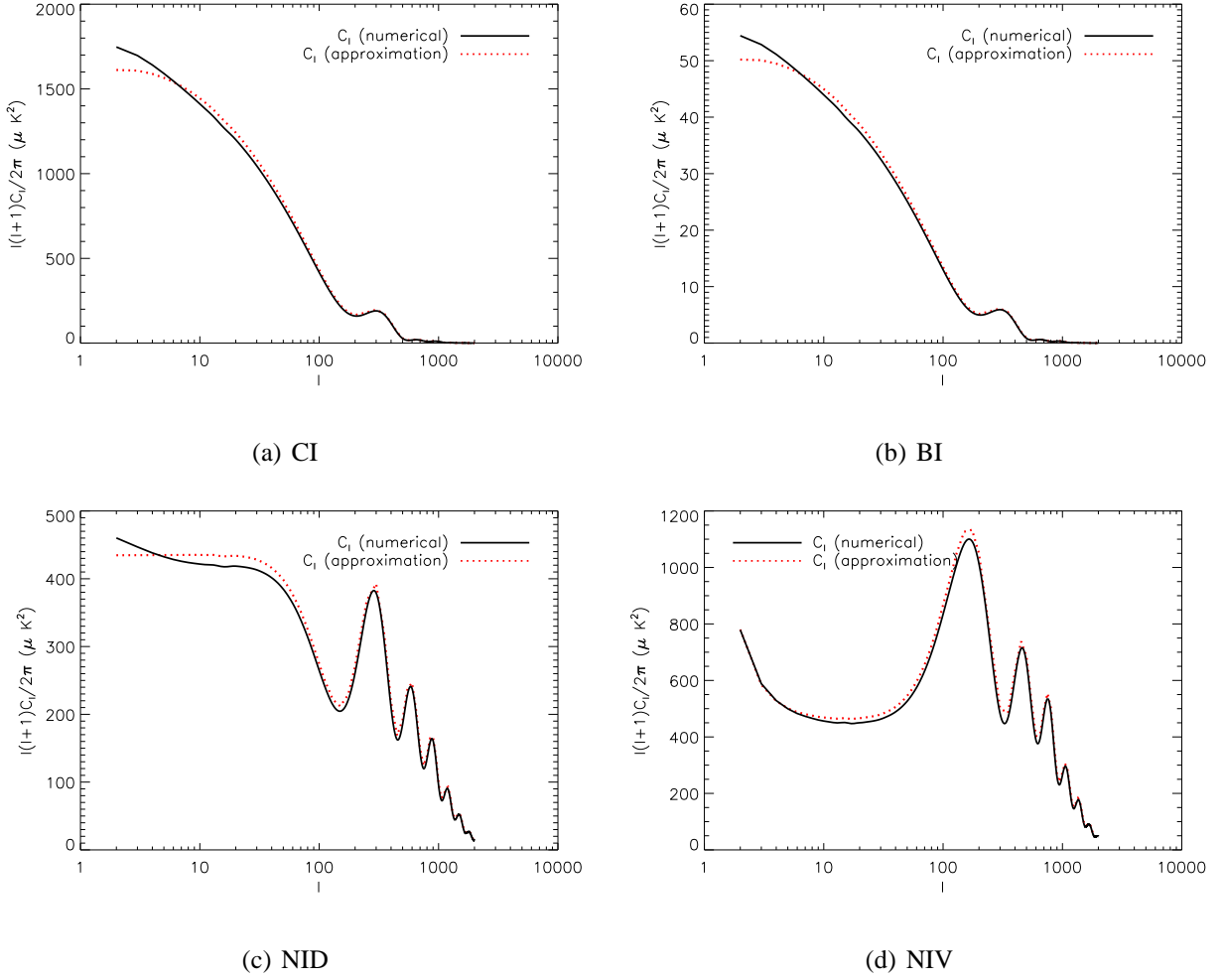


Figure 5.16: CMB angular power spectrum for **(a):** CI, **(b):** BI, **(c):** NID and **(d):** NIV modes. The dotted line represents the C_ℓ obtained using only the three main contributions to the source function, and the solid line is the C_ℓ obtained using the full source function. The solid line is obtained using CAMB. The dotted line is computed with a code written in IDL.

$$\begin{aligned}
\Theta_\ell(\tau_0) \simeq & [\Theta_0 + \psi](\tau_*)\mathcal{D}(k)(2\ell + 1)j_\ell(k\Delta\tau_*) + \Theta_1(\tau_*)\mathcal{D}(k)[\ell j_{\ell-1}(k\Delta\tau_*) - (\ell + 1)j_{\ell+1}(k\Delta\tau_*)] \\
& + (2\ell + 1) \int_{\tau_*}^{\tau_0} [\dot{\phi} + \dot{\psi}]j_\ell(k\Delta\tau)d\tau,
\end{aligned} \tag{5.62}$$

where τ_* is the conformal time at decoupling, $\Delta\tau_* = \tau_0 - \tau_*$, $\Delta\tau = \tau_0 - \tau$ and $\mathcal{D}(k)$ accounts

for the diffusion damping. This diffusion damping factor is given by

$$\mathcal{D}(k) = \int_0^{\tau_0} g(\tau) e^{[-k/k_D(\tau)]^2} d\tau. \quad (5.63)$$

Figure (5.16) represents the CMB power spectrum computed using the full transfer function compared to the one using only the main three contributions to the transfer function for the CI, BI, NID and NIV modes. These are respectively obtained by integration of the exact (see equation (5.60)) and the approximated (see equation (5.62)) transfer functions through equation (5.59). One can see that the approximation reproduces the main features of the CMB power spectrum.

Thus, the evolution of the photon density contrast and velocity divergence and the evolution of the gravitational potential, themselves depending on the mode of the primordial fluctuations, give a good approximation to the total CMB angular power spectrum. Hereafter, we study the main features of the CMB temperature power spectrum in isocurvature models, for each mode in turn.

By studying Figure 5.15 we observe that, of all the isocurvature CMB power spectra, the NIV CMB power spectrum is the most similar to the AD CMB power spectrum with regard to its overall shape. The Sachs-Wolfe plateau and the ISW effect are similar for both modes, and at higher ℓ 's, the NIV and AD CMB spectra show the same behaviour in the damping of anisotropies on small scales. However, the acoustic peaks are shifted to lower ℓ 's compared to the adiabatic model as the NIV excites a pure $\sin kr_s$ harmonic instead of the driven cosine like harmonic for the AD mode, but the peak positions still follow the (1:2:3:4) series as for the AD mode. The ISW effect contribution around the first peak in the NIV mode is not as important as in the AD mode due to the smallness of the gravitational potential and its time derivative. At the horizon crossing, the gravitational potential decays but this weakly affects the height of the first acoustic peak. As a result, the first peak in the NIV mode is not as high as in the AD mode. In addition, on very large scales ($\ell \lesssim 10$), the Sachs-Wolfe plateau is boosted by the velocity divergence contribution as in this mode, the photon velocity divergence is initially perturbed. In Figure 5.17, we represent the different contributions to the CMB power spectrum for the NIV mode. For this mode, the CMB spectrum is essentially dominated by the baryon velocity on large scales and

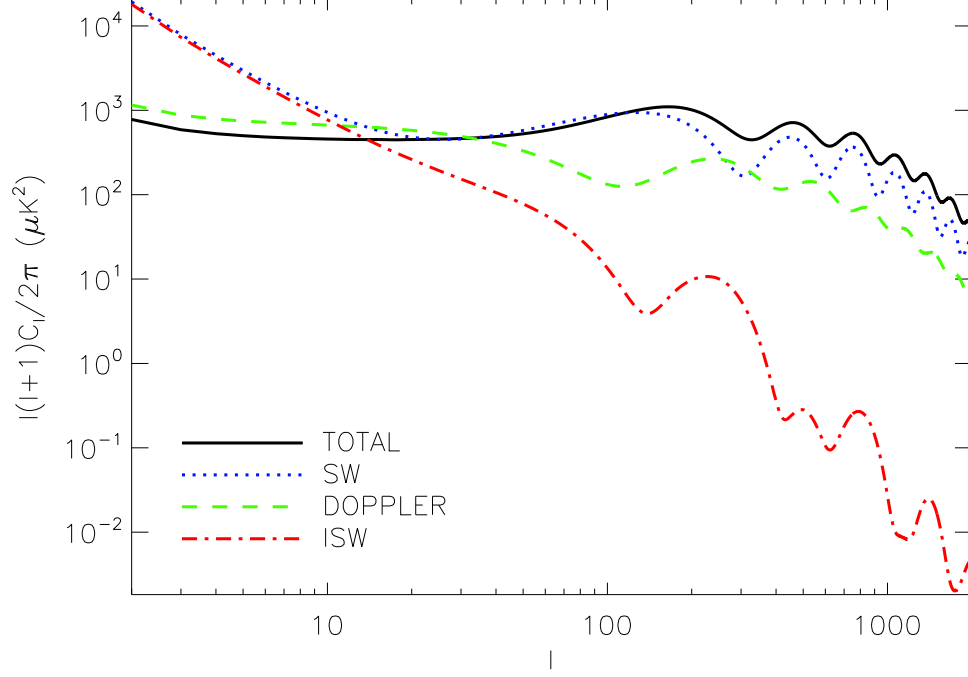


Figure 5.17: Different contributions to the CMB power spectrum for the NIV mode. These contributions are obtained using CAMB. This is for a flat Λ CDM universe with $\Omega_b h^2 = 0.022$, $\Omega_c h^2 = 0.125$ and $h = 0.7$.

the gravitational potential is proportional to $1/k\tau$ on large scales (see equation (5.45)), boosting both the ordinary and integrated SW contributions at low ℓ 's as also explained in [121]. However, the ordinary and the integrated SW contributions roughly cancel each other as they are opposite in sign. As ℓ increases, the contribution due to the change in the gravitational potential decreases and the ordinary SW contribution becomes dominant in the transfer function. Note that the velocity divergence contribution in the source function is weighted by k^{-2} thus reducing its significance on intermediate and small scales. Let us also note that the phase difference between the gravitational potential and the photon density contrast is not constant but changes with ℓ .

For the NID mode, the acoustic peaks are located roughly at the NIV trough positions, due to the fact that the NID and NIV modes, are both free oscillations with respectively a cosine and

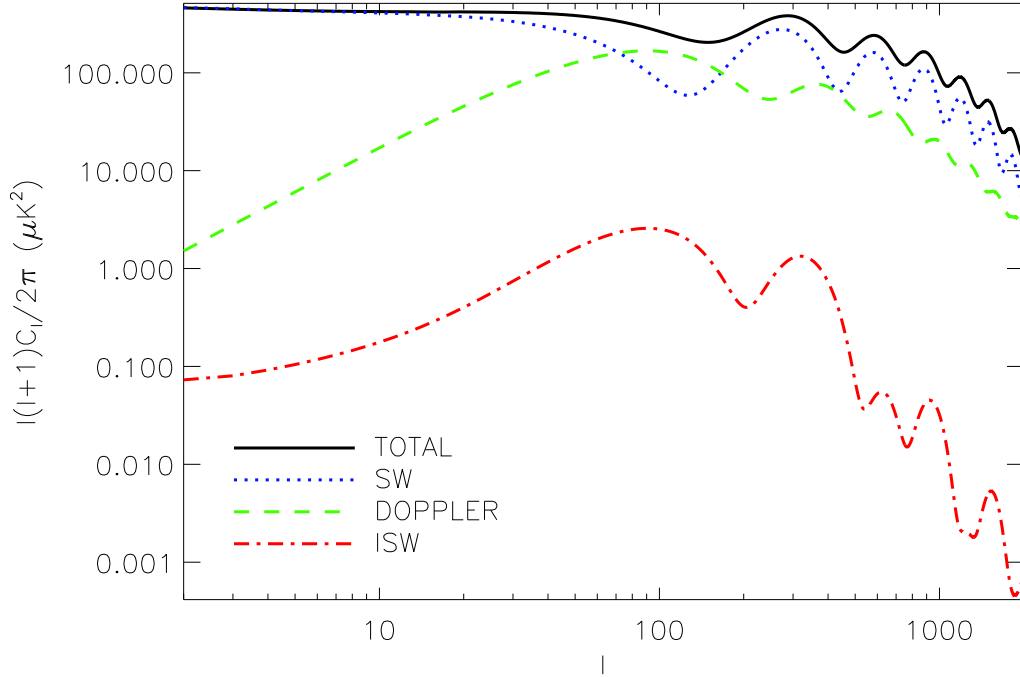


Figure 5.18: Different contributions to the CMB power spectrum for the NID mode. These contributions are obtained using CAMB. This is for a flat Λ CDM universe with $\Omega_b h^2 = 0.022$, $\Omega_c h^2 = 0.125$ and $h = 0.7$.

sine type phases. The NID CMB angular power spectrum contains more power on large scales, compared to the anisotropies on intermediate and small scales. The first acoustic peak and the SW plateau have almost the same height. One should bear in mind that the NID CMB spectrum has a trough before the first peak. Figure 5.18 shows the different contributions to the spectrum. The Doppler effect, though not important as in the NIV mode, reduces the depth of the first trough. As for the NIV mode, the gravitational potential, initially not significant, decays at the horizon crossing. But this decay does not significantly boost the anisotropy temperature before and after recombination due to the smallness of the gravitational potential. The velocity divergence contribution to the spectrum remains subdominant on all scales in this mode, while the ISW contribution to the spectrum is of no significance.

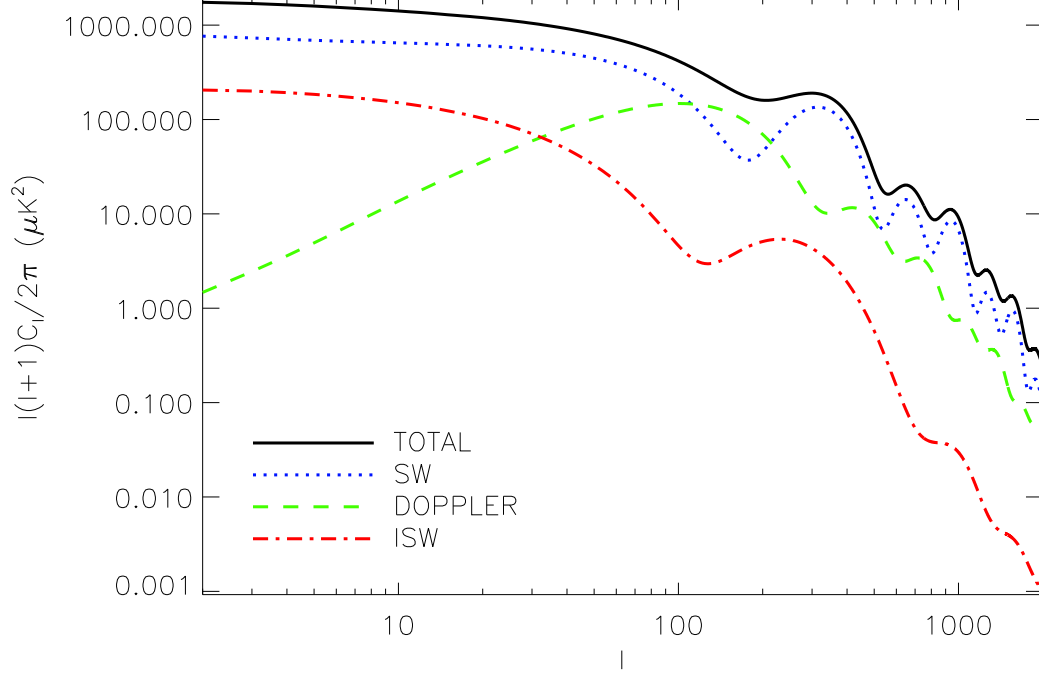


Figure 5.19: Different contributions to the CMB power spectrum for the CI mode. These contributions are obtained using CAMB. This is for a flat Λ CDM universe with $\Omega_b h^2 = 0.022$, $\Omega_c h^2 = 0.125$ and $h = 0.7$.

The CI and BI modes have the same CMB power spectrum as their photon evolution equations are similar. They both represent a driven oscillation and excite a $\sin kr_s$ like harmonic, setting the ℓ peak positions in the CI and BI modes roughly at the trough positions in the AD CMB power spectrum. Most importantly, though the gravitational potential in the CI and BI modes is as important as in the AD mode, in contrast to the NID and NIV modes where it is negligible, the CMB power spectrum in the CI and BI modes completely differs for the AD spectrum: At low ℓ 's, the CMB power spectrum in the CI and BI modes do not show the Sachs-Wolfe plateau as in the AD case but instead decreases as ℓ increases. This is due to the k^{-1} factor in the evolution equation of the photon density contrast which boosts anisotropies on large scales (low ℓ 's) and suppresses them on small scales. The k^{-1} factor also dictates the steep overall shape of the BI and CI CMB power spectra and tends to hide the fact that the CMB power spectrum has a

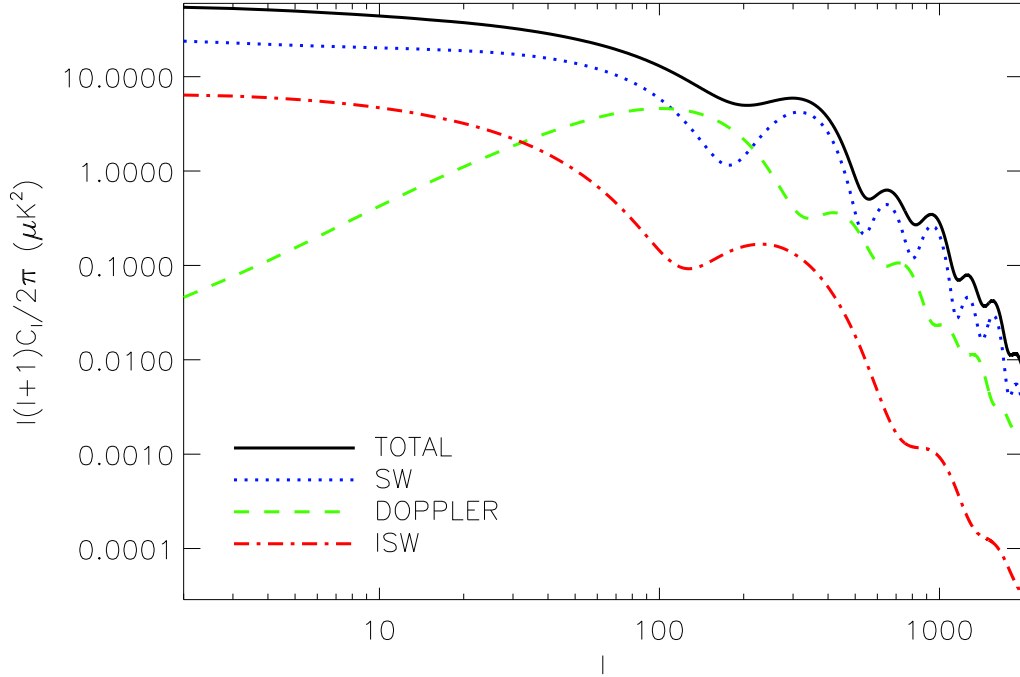


Figure 5.20: Different contributions to the CMB power spectrum for the BI mode. These contributions are obtained using CAMB. This is for a flat Λ CDM universe with $\Omega_b h^2 = 0.022$, $\Omega_c h^2 = 0.125$ and $h = 0.7$.

trough before the first acoustic peak in these modes as in the NID mode. For the same reason, the ISW effect in these modes, though as relevant as in the AD mode (since the gravitational potential is relatively large at the horizon crossing time), does not noticeably increase the height of the first peak as for the AD case. Figures 5.19 and 5.20 show the contributions to the CMB spectrum in these modes. It turns out that the CI, BI and NID modes, for which the first peak of the CMB power spectrum is preceded by a trough have their acoustic peak positions following the (1:3:5) series in contrast to the AD and NIV modes (where the first acoustic peak comes right after the Sachs-Wolfe plateau) which have the CMB spectrum following the (1:2:3:4) series.

5.4 Effect of cosmological parameters on the isocurvature CMB temperature power spectrum

In the previous section we reviewed how, from the fluctuations at the last scattering surface, one derives the observed CMB anisotropy, and subsequently studied the features of the CMB power spectrum for isocurvature modes. The CMB anisotropy spectrum depends not only on the mode of the initial fluctuations but also on several cosmological parameters including the baryon density $\omega_b = \Omega_b h^2$, the matter density $\omega_m = \Omega_m h^2$, the dark energy density Ω_Λ , the optical depth τ_e , the spectral index n_s and the scalar amplitude A_s . Each parameter has a distinct effect on the spectrum. In a previous chapter, we studied how a change in the cosmological parameters affects the CMB spectrum in the adiabatic case. The baryon density, matter density, and cosmological constant each induce a shift in the location of the acoustic peaks and troughs in the CMB spectrum. For a flat universe, the peak location depends on the sound horizon r_s and on the age of the universe τ_0 . An increase in the matter density $\Omega_m h^2$ reduces the age of the universe but does not affect the sound horizon. A change in the baryon density affects the sound horizon. More importantly, the physical densities in matter $\Omega_m h^2$ and baryons $\Omega_b h^2$ fix the heights of acoustic peaks in the CMB spectrum. The peaks in the CMB spectrum are lowered and shifted to higher ℓ as the matter density $\Omega_m h^2$ increases.

A dark energy model with cosmological constant Ω_Λ or quintessence, and curvature have no significant effect on the pre-recombination universe and only affect the CMB spectrum through the angular diameter distance d_A and the late-time ISW effect [98]. The optical depth τ_e tells us how much the universe was reionized at late times. The reionization of the universe reintroduces Thomson scattering of photons by free electrons. If the optical depth is large enough, the anisotropies are washed out. The spectral index n_s has an effect different from all of the previous parameters. An increase in the spectral index lowers the anisotropy on large scales and enhances it on small scales, by tilting the spectrum about a pivot scale.

In this section, we study the effect of each of the above-mentioned cosmological parameters on the CMB power spectrum in isocurvature modes. We particularly focus on the physical baryon density and the physical matter density as they affect the CMB spectrum for adiabatic and isocurvature modes differently. The effect of the other cosmological parameters on the CMB spectrum in isocurvature models is similar to the AD case.

5.4.1 Baryon density $\Omega_b h^2$

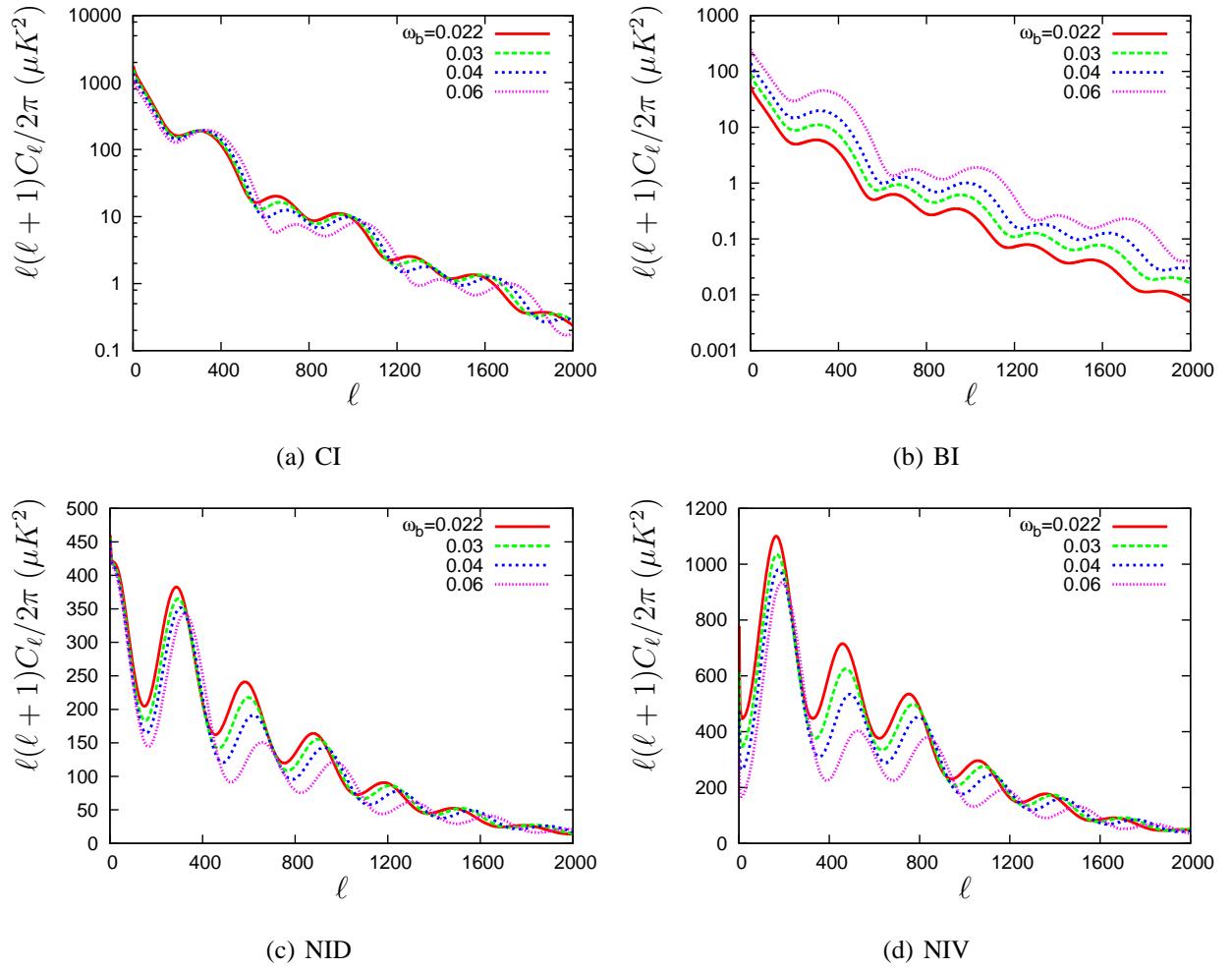


Figure 5.21: $\Omega_b h^2$ dependence of the CMB power spectrum in isocurvature models. This is for a flat Λ CDM universe with $\Omega_b h^2 = 0.022, 0.03, 0.04$ and 0.06 , $\Omega_c h^2 = 0.125$ and $h = 0.7$.

Figure 5.21 represents the baryon density dependence of the CMB temperature power spectrum for different isocurvature modes. The baryon density is the cosmological parameter which most affects the heights and locations of peaks in the CMB power spectrum. Except for the NIV mode, the effect of a change in the baryon density on the CMB power spectrum is essentially determined by the change in the photon density contrast. Prior to decoupling, the baryons and photons are coupled and form a single fluid whose squared sound speed is given by $c_s^2 = \frac{1}{3(1+R)}$ where $R = \frac{3\bar{\rho}_b}{4\bar{\rho}_\gamma}$. The oscillation phase depends on the sound horizon r_s . Thus loading more baryon reduces the sound speed, shifting the acoustic peaks to higher ℓ 's. This effect is also seen in the AD mode. However, the lowering and enhancement of the acoustic peaks differ from mode to mode.

In the NID mode, as, the baryon density increases, all the acoustic peaks are significantly lowered. This differs from the AD mode, where the odd peaks are enhanced while even peaks are lowered, due to a gravitational potential shift. As we showed for the NID mode, the gravitational potential contribution is negligible and the amplitude of the oscillations for the photon density contrast and velocity divergence (see equations (5.30) and (5.32)) depends on the sound speed. The lowering of the acoustic peaks is strongest about the first three peaks where the Doppler effect contribution, related to $\theta_{b\gamma}$ and $\dot{\theta}_{b\gamma}$, becomes as important as the monopole contribution. We recall that $\theta_{b\gamma}$ is proportional to c_s^2 while δ_γ is proportional to c_s . Figure 5.22(c) shows the effect of a change in the baryon density on the contributions to the NID CMB spectrum.

The NIV mode shows the strongest height reduction of the acoustic peaks. The first three peaks are strongly reduced as the baryon density increases, while the other peaks slightly decrease as in the NID mode. However, the effect of the change in the baryon density is noticeable even on very large scales in contrast to the NID case. Here, the monopole contribution and the Doppler effect contribution are in phase. At lower ℓ 's the velocity divergence, with its amplitude proportional to the square of the sound speed (see equation (5.43)), contributes most to the transfer function, while for higher ℓ 's the photon density contrast (see equation (5.41)), proportional to the sound

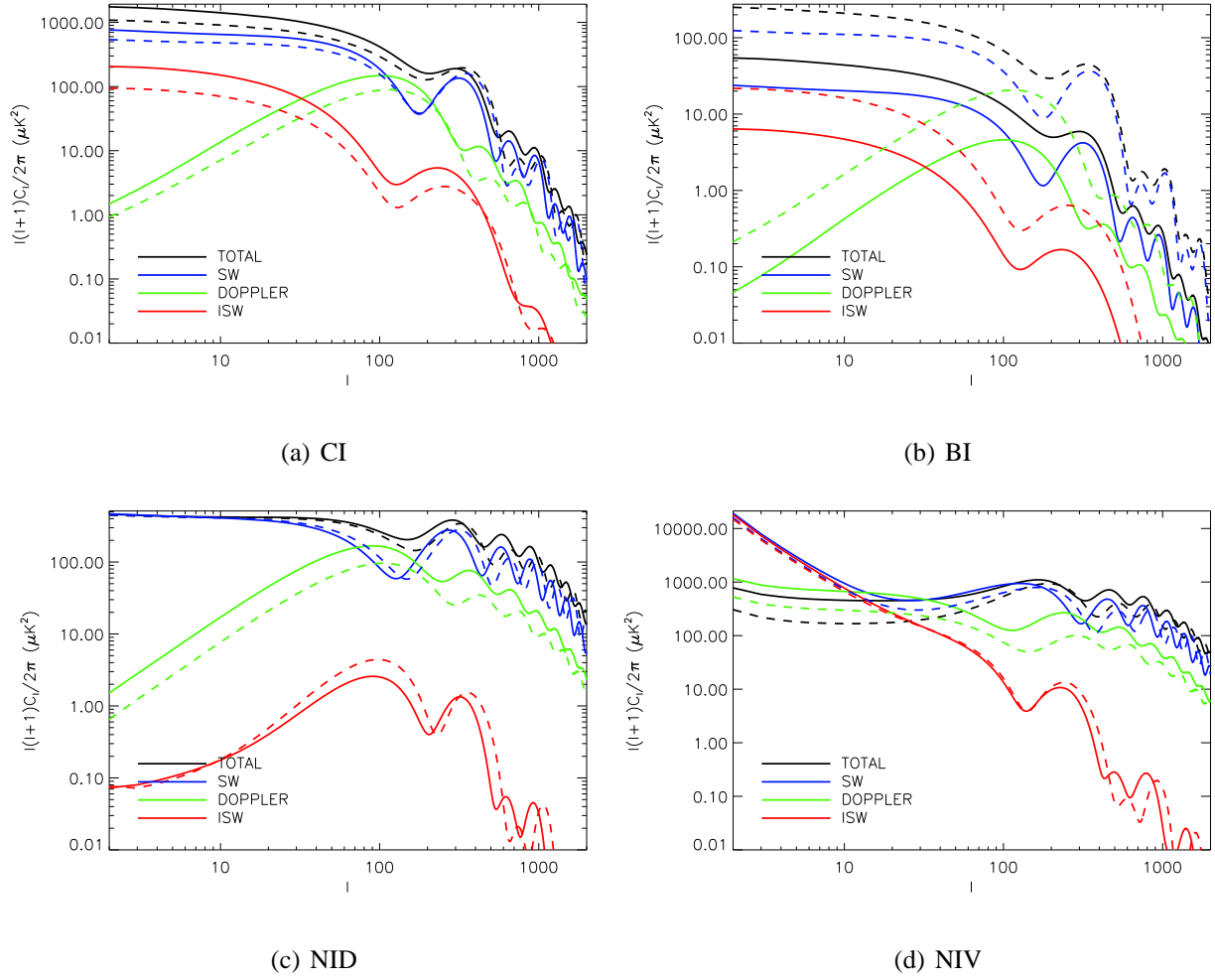


Figure 5.22: Baryon density effect on the contributions to the CMB power spectrum for the isocurvature modes. The baryon density increases from $\Omega_b h^2 = 0.022$ (solid lines) to 0.06 (dashed lines). This is for a flat Λ CDM universe with $\Omega_c h^2 = 0.12$ and $h = 0.7$.

speed, dominates in the transfer function. This is shown in Figure 5.22(d) where we represent the changes in the contributions to the CMB power spectrum.

The CI and BI modes react differently to an increase in the baryon density. In the CI mode, acoustic peaks are lowered. However, the baryon density dependence of the CMB power spectrum is weaker in the CI mode than in the NID and NIV modes. This is due to the fact that the photon density contrast amplitude (see equation (5.48)) depends on the photon-to-baryon ratio

R only through the forcing term. The amplitude of the sine harmonic is constant. Figure 5.22(a) shows that there is no significant change in the monopole contribution as the baryon density increases. For the BI mode, the amplitude of the sine harmonic (see equation (5.50)) is directly proportional to the baryon density. Thus in contrast to the other modes, loading more baryons in BI models enhances significantly the acoustic peaks. Figure 5.22(b) shows that all the contributions are boosted as the baryon density increases.

5.4.2 Matter density $\Omega_m h^2$

To see the imprint of the matter density on the CMB power spectrum, we consider a Λ CDM universe, keep the physical baryon density $\Omega_b h^2$ and h constant, and modify only the dark matter density $\Omega_c h^2$. The change in the matter density is compensated by Ω_Λ . Changing Ω_Λ affects the CMB spectrum but its effect can be neglected compared to the effect of the matter density itself.

For a universe with a low matter density $\Omega_m h^2$, the epoch of matter-radiation equality τ_{eq} occurs closer to recombination. The gravitational potential still decays at recombination providing a strong driving force for the oscillations. Therefore the photon density perturbation, δ_γ , is larger compared to high matter density universes. In addition, since the potential is not constant after recombination, the integrated Sachs Wolfe effect contribution is not negligible and should be taken into account. Figure 5.23 shows the effect of a change in the matter density on the CMB acoustic peaks in isocurvature modes. In contrast to the baryon dependence, an increase in the matter density shifts the CMB acoustic peaks to lower ℓ 's. The location of the acoustic peaks, ℓ_p , in the CMB spectrum is proportional to $\ell_p \propto \pi \tau_0 / r_s(\tau_*)$ where τ_0 is the age of the universe in conformal time. Increasing the matter density decreases the age of the universe pushing the peaks to lower ℓ .

The effect of an increase in the matter density on the height of the CMB temperature acoustic peaks in the BI, NID and NIV modes is similar to the AD case. For a low matter density,

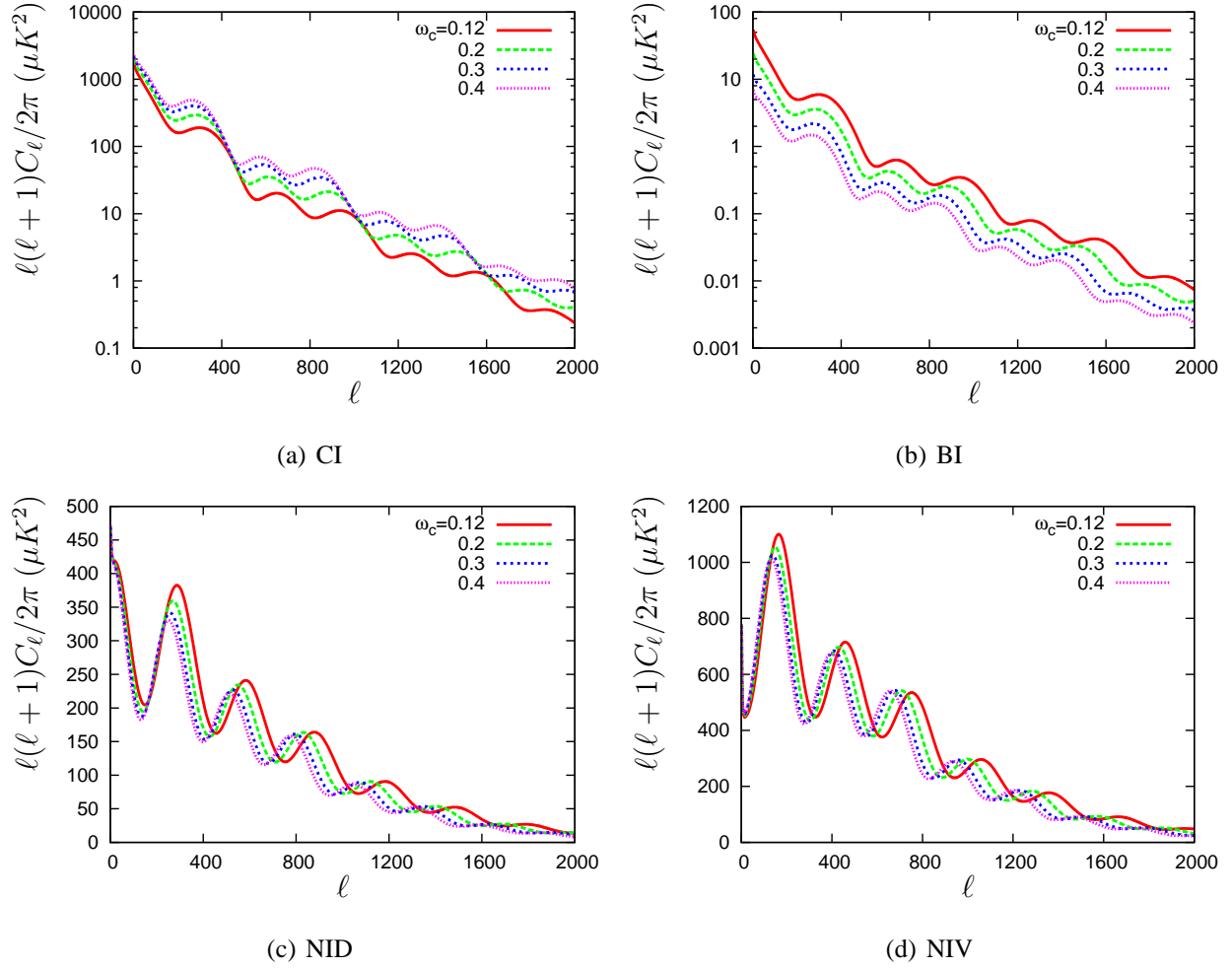


Figure 5.23: $\Omega_c h^2$ dependence of the CMB power spectrum in isocurvature models. This is for a flat Λ CDM universe with $\Omega_b h^2 = 0.022$, $\Omega_c h^2 = 0.125, 0.2, 0.3$ and 0.4 , and $h = 0.7$.

the matter-radiation equality happens closer to recombination. Therefore, the photon density contrast at recombination is larger than in a purely matter dominated universe. In addition, an increase in the matter density increases the gravitational potential which in turn, causes the ISW effect to significantly affect the anisotropies around the first and second peaks as it decays. In the CI mode, an increase in the matter density enhances the acoustic peaks as the photon density contrast is directly proportional to the matter density as shown in equation (5.48).

5.4.3 Cosmological constant density Ω_Λ

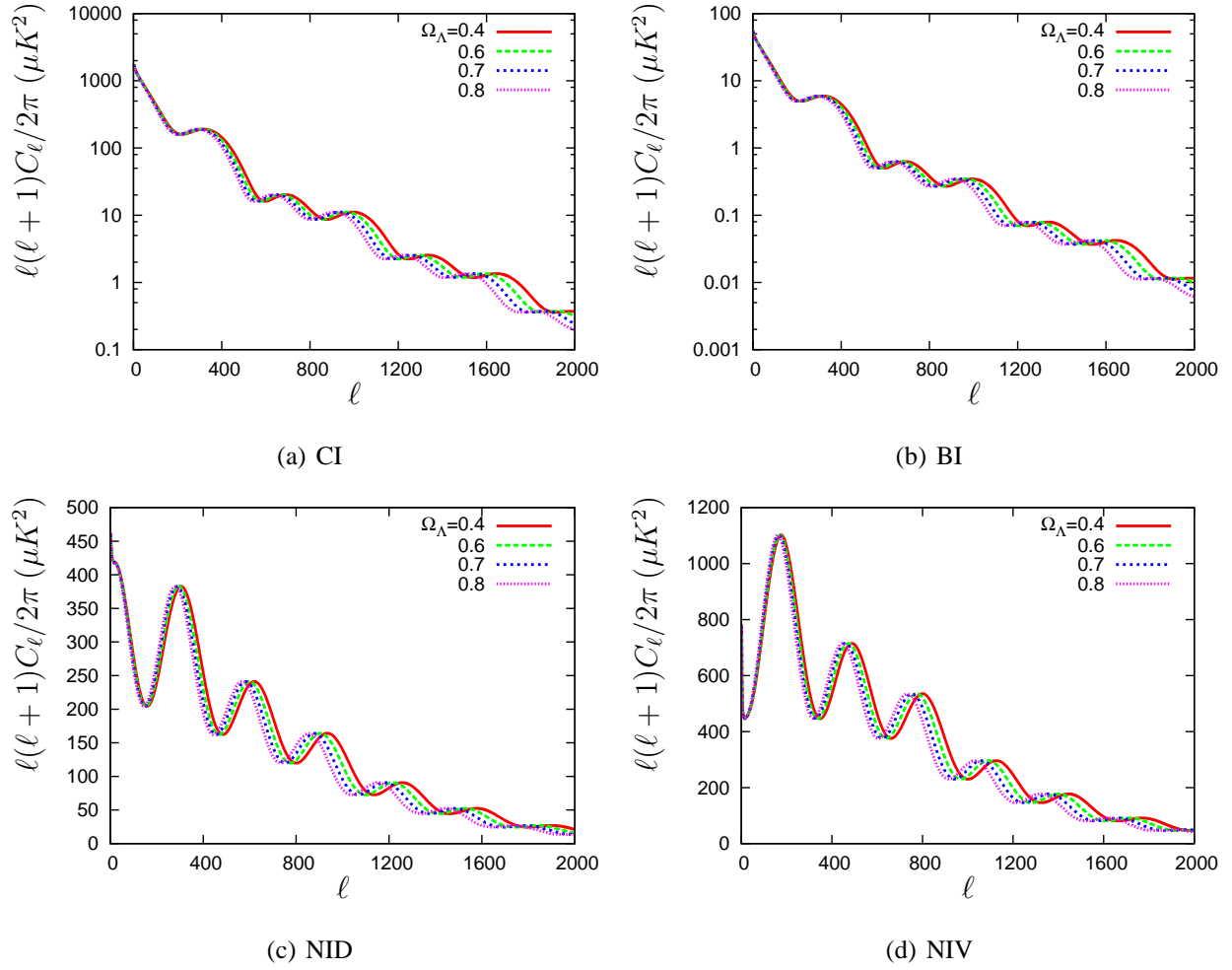


Figure 5.24: Ω_Λ dependence of the CMB power spectrum in isocurvature models. This is for a flat Λ CDM universe with $\Omega_b h^2 = 0.022$, $\Omega_c h^2 = 0.125$ and $\Omega_\Lambda = 0.4, 0.6, 0.7$ and 0.8 .

The effect of a change in the cosmological constant density on the CMB temperature power spectrum in isocurvature modes is similar to the AD case. At the last scattering surface, where the main contributions to the anisotropies that we observe today were formed, the universe was still radiation-dominated and the cosmological constant was negligible and could not affect the perturbations. Therefore the effect of the cosmological constant on the CMB power spectrum is only through the freestreaming of photons from last scattering surface towards us. For a fixed baryon and matter density, the cosmological constant affects the angular diameter distance d_A

which in turn modifies the peak location in the CMB power spectrum. The angular diameter distance $d_A = d/\varphi$ is a classic way to measure distances by measuring the angle φ subtended by an object of known physical size d . In a flat universe $\Omega_K \equiv 1 - \Omega_\Lambda - \Omega_m = 0$, $\varphi = (d/a)/\Delta\tau$ so that the angular diameter distance is given by [41]

$$d_A^{flat} = a\Delta\tau = \frac{\Delta\tau}{1+z}, \quad a_0 = 1 \quad (5.64)$$

where $\Delta\tau$ is the comoving distance. At low redshift, the angular diameter distance is equal to the comoving distance. Thus the entire CMB spectrum shifts to lower multipoles ℓ as Ω_Λ increases. However the shift in the peak location due to the Ω_Λ is weaker, compared to the shift due to a change in the matter and baryon densities. Figure 5.24 shows how the CMB power spectrum for both isocurvature modes is shifted to larger scales as the cosmological constant increases.

5.4.4 Curvature density Ω_K

Among all the cosmological parameters that we are considering, the curvature density by far causes the largest shift in the location of the peaks [41]. The photon geodesics depend on the geometry of the universe. In an open universe, the geodesics of massless particles start out parallel to each other and then slowly diverge. The physical scale corresponding to the first peak gets projected onto a smaller angular scale in a flat universe compared to an open universe. Therefore we expect that the peaks should be shifted to higher values of ℓ in an open universe. For the closed universe, the peaks are shifted to lower values of ℓ . The magnitude of this shift is determined by the comoving angular diameter distance to the last scattering surface [77]. Equation (5.64) in the previous subsection gives the angular diameter distance in a flat universe. For a non flat universe, the angular diameter distance generalizes to

$$d_A = \frac{a}{H_0\sqrt{|\Omega_K|}} \begin{cases} \sinh[\sqrt{\Omega_K}H_0\Delta\tau] & \Omega_K > 0 \\ \sin[\sqrt{-\Omega_K}H_0\Delta\tau] & \Omega_K < 0 \end{cases} \quad (5.65)$$

Thus changing the curvature of the universe affects the angular diameter distance and subsequently the peak location. In Figure 5.25 we see how the whole CMB spectrum is shifted to

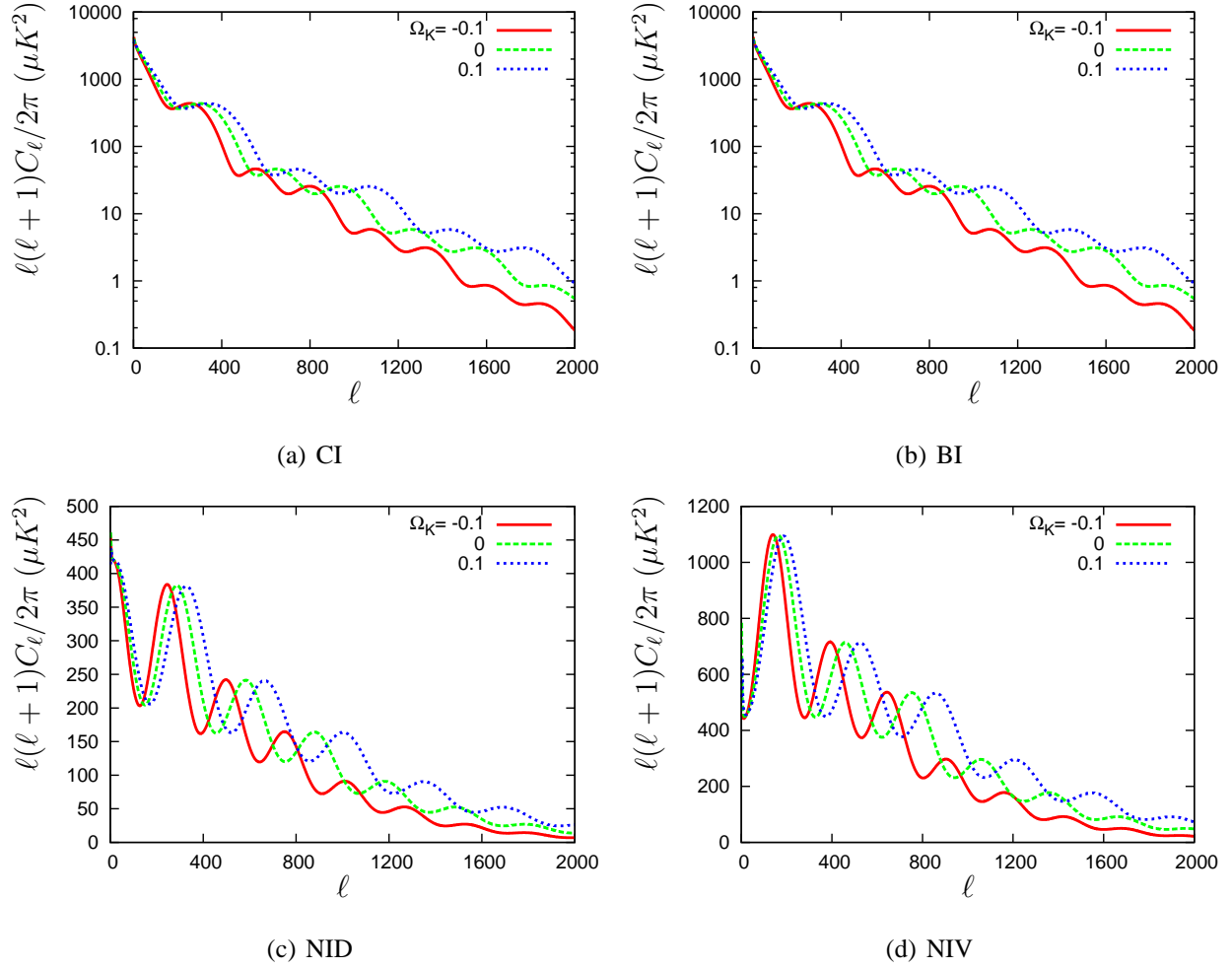


Figure 5.25: Curvature Ω_K dependence of the CMB power spectrum in isocurvature models. As we increase the curvature density, the anisotropy spectrum shifts to small scales. This is for closed ($\Omega_K = -0.1$), flat ($\Omega_K = 0$) and open ($\Omega_K = 0.1$) Λ CDM universe with $\Omega_b h^2 = 0.022$, $\Omega_c h^2 = 0.125$ and $h = 0.7$.

the higher ℓ as we go from a closed universe ($\Omega_K < 0$) to an open universe ($\Omega_K > 0$) for all isocurvature modes.

5.4.5 Optical depth τ_e

After leaving the last scattering surface, photons freestream towards us today preserving the anisotropy. This is true if we ignore the reionization of the universe at late time. In fact, as the

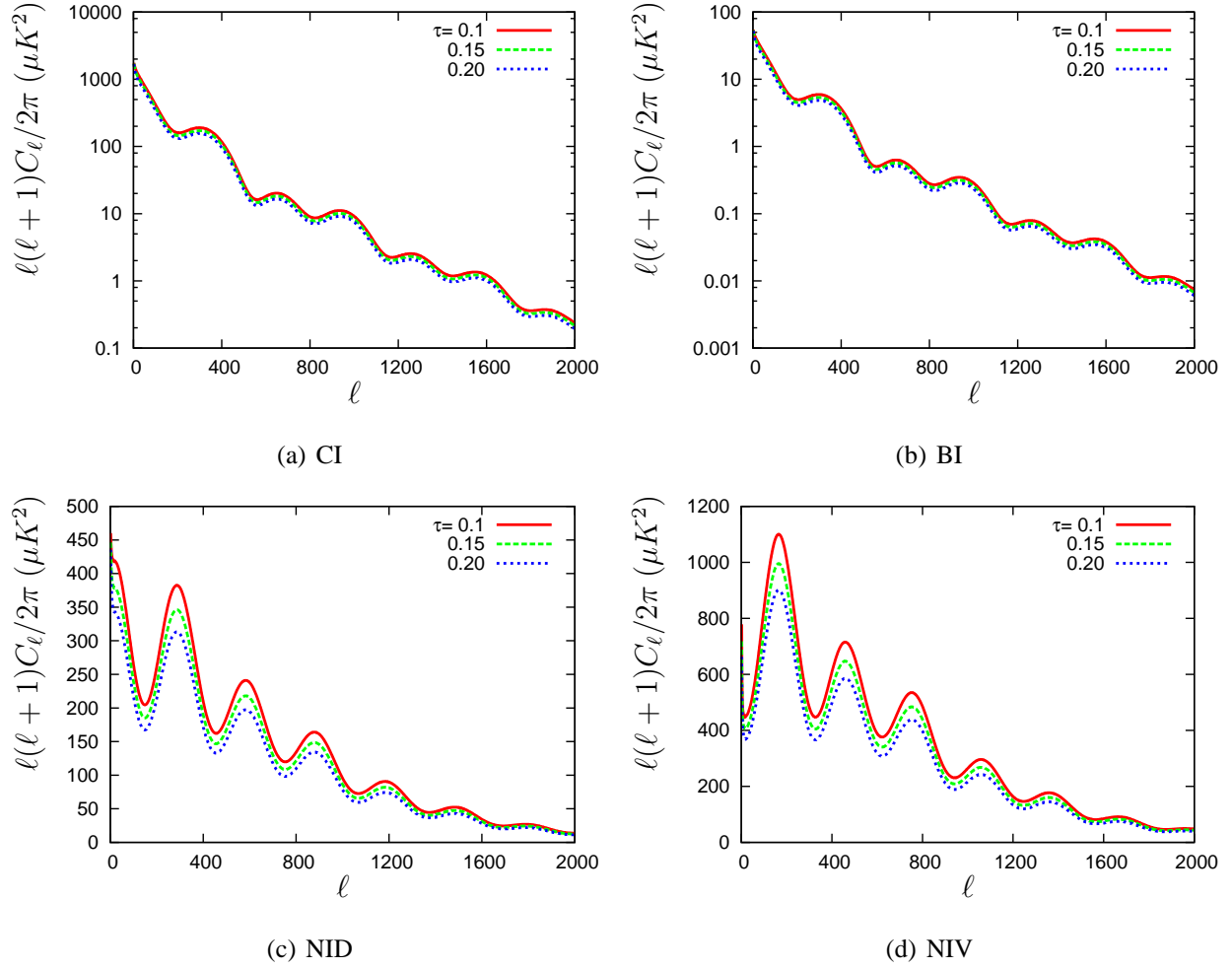


Figure 5.26: Reionization dependence of the CMB power spectrum in isocurvature modes. As the optical depth from reionization to the last scattering surface increases, anisotropies are washed out for scales inside the horizon at the reionization epoch. This is for a flat Λ CDM universe with $\Omega_b h^2 = 0.022$, $\Omega_c h^2 = 0.125$ and $h = 0.7$.

first luminous objects form their UV emission reionizes the universe. This brings photons back into contact with free electrons which erases anisotropies through Thomson scattering. Taking into account the reionization of the universe a second peak appears in the visibility function at low redshift. The CMB photons are affected by the temperature, potential, and velocity of the scattering electrons [60]. If we assume that photons have a temperature $T(1 + \Theta)$ where T is the background temperature and Θ the temperature perturbation before reionization, at reionization,

only a fraction of photons given by $e^{-\tau_e}$, will emerge without scattering. The remaining fraction $(1 - e^{-\tau_e})$ is re-emitted by the ionized region. Thus the photon temperature after reionization is

$$T(1 + \Theta)e^{-\tau_e} + T(1 - e^{-\tau_e}) = T(1 + \Theta e^{-\tau_e}). \quad (5.66)$$

This means that the CMB anisotropy after reionization is lowered by a factor $e^{-\tau_e}$ and consequently the power spectrum C_ℓ is reduced by $e^{-2\tau_e}$. Hence, all modes within the horizon ($\ell > \tau_0/\tau_{reion}$) at reionization will be affected by this process and the modes outside the horizon remain unchanged. Figure 5.26 shows that this is valid for the CI, BI, NID and NIV modes.

5.4.6 Spectral index n_s

The CMB angular power spectrum can be written as

$$C_\ell = \frac{2}{\pi} \int_0^\infty k^2 P_I(k) |\Theta_\ell(k)|^2 dk, \quad (5.67)$$

where $P_I(k)$ is the primordial power spectrum. The primordial power spectrum is proportional to k^{n_s} where k is the wavenumber and n_s the spectral density [41]. This can be written as

$$P_I(k) \propto \left(\frac{k}{k_p} \right)^{n_s}, \quad (5.68)$$

where k_p is a constant. At the wavenumber $k = k_p$, the power spectrum is independent of the spectral index. For other wavenumbers, n_s will modify the slope of the CMB power spectrum, pivoting around some multipole $\ell_p \simeq k_p \tau_0$. This effect on the CMB spectrum is clearly seen in Figure 5.27 for the CI, BI NID and NIV modes. A value of $n_s < 1$ lowers the small scale anisotropy and boosts the large scale anisotropy with the opposite effect for $n_s > 1$.

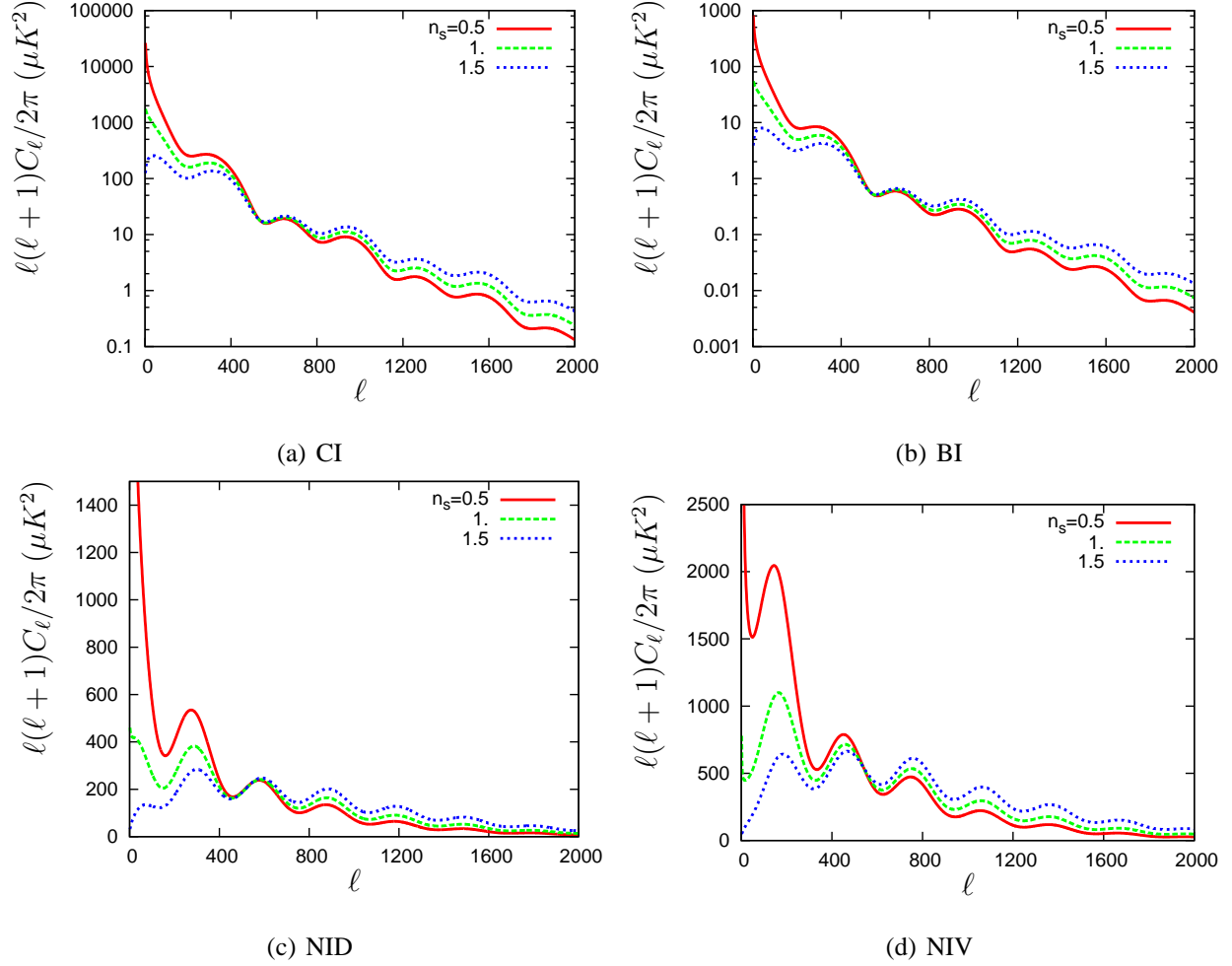


Figure 5.27: Spectral index dependence of the CMB power spectrum for isocurvature models. This is for a flat Λ CDM universe with $\Omega_b h^2 = 0.022$, $\Omega_c h^2 = 0.125$ and $h = 0.7$, pivot scale $k_p = 0.05 \text{Mpc}^{-1}$.

Fundamental Uncertainty in the BAO Scale from Isocurvature Modes

6.1 Introduction

Large galaxy surveys fall squarely in the realm of astrophysics and traditionally we think of them as living almost independently of the physics of the early Universe. In this *Letter* we show that this assumption breaks down rather dramatically in the case of Baryon Acoustic Oscillations (BAO) (for a recent review see [12]). BAO surveys are a key component of the global plan for the next two decades in cosmology because they are believed to provide a robust and powerful statistical standard ruler that can probe dark energy. They have shown to be robust to a variety of potential systematic effects which only become important at the 1% level [155, 157]. However, here we show that there is a much more significant “systematic” arising from the possibility of isocurvature modes correlated with the dominant adiabatic perturbation which may have been generated during the early Universe.

To understand this systematic, consider the standard ruler provided by the distance that sound waves can propagate in the primordial plasma. The standard picture based on adiabatic perturbations suggests that the key scale is the sound horizon:

$$r_s = \int_0^{t_{cmb}} c_s(1+z)dt = \int_{z_{cmb}}^{\infty} \frac{c_s(z')}{H(z')} dz',$$

where $c_s(z) = 1/\sqrt{3(1+R_b(1+z)^{-1})}$ and $R_b = 31500 \omega_b (T_{cmb}/2.7 \text{ K})^{-4}$. The measurement of the late-time clustering of galaxies in the transverse direction probes the angular diameter distance given by $d_A(z) = r_{\perp}(1+z)^{-1}/\Delta\Theta$ where r_{\perp} is the intrinsic size of r_s in the transverse direction and $\Delta\Theta$ is the position of the peak in the angular correlation function, while the clustering on a scale r_{\parallel} along the line of sight probes the Hubble parameter, $H(z) = \Delta z/r_{\parallel}$.

Measurements of the angular diameter distance and Hubble parameter in a series of redshift bins using the BAO technique provide an effective probe of the properties of dark energy [23, 139, 155], with prospective constraints on the equation of state of dark energy, w_0 , and its evolution w_a , as low as 0.02 and 0.04, respectively, for a future space-based spectroscopic mission (e.g., ADEPT [151]), with forecasts for current experiments (e.g., BOSS [149]) at the level of 0.03 and 0.1 respectively.

Systematic effects that affect the position and shape of the Baryon Acoustic Peak (BAP), such as nonlinearity and redshift-space distortions, have been studied and can be treated without a significant impact on dark energy constraints [155, 157]. The impact on the BAP from non-standard conditions in the early Universe such as changes in recombination, early dark energy or inhomogeneous reionization, have been studied before [40]. Here we concentrate on the possibility that the initial conditions were not purely adiabatic. Adiabatic initial conditions are described by a net density perturbation such that the relative number densities of all cosmological species remain unperturbed. There is however another possible type of perturbation, termed isocurvature, characterized by variations in the particle number ratios such that the net curvature perturbation is zero [29]. We show that isocurvature modes alter the standard picture above and deform the characteristic BAP scale which manifests in the anisotropies in the cosmic microwave background

and the clustering of matter. We investigate the extent to which an admixture of isocurvature modes, small enough to be undetectable by PLANCK, degrades constraints on dark energy parameters when allowed for, or bias the recovered values if not taken into account. Put more generally, we investigate the coupling of the primordial density perturbation to the constraints arising from our observations at late times, even with strong prior constraints on the isocurvature modes from CMB data. Constraints from WMAP 3 year data indicate that a 50% admixture of three isocurvature modes with the adiabatic mode is permitted [13], whereas forecasts for the PLANCK experiment indicate that arbitrary isocurvature mode admixtures will be constrained to below the 10% level [31].

What are the possible origins of isocurvature modes? The simplest possibility perhaps is multiple field inflation [119, 137], with the curvaton mechanism as a special case [113]. The resulting isocurvature perturbation is a leading candidate to explain any primordial non-Gaussianity and can, in certain cases, explain the observed asymmetry in the CMB [52]. While the simplest, adiabatic models of inflation are currently preferred [177], it is possible that some isocurvature contamination will be uncovered in future experiments and indeed this would be very fortuitous since it would provide new handles on the physics of the very early Universe. In this chapter we argue that allowing for the possibility of isocurvature modes is crucial in future BAO surveys and that as a reward, such surveys can provide a powerful lens on the early Universe.

6.2 The BAO peak with adiabatic and isocurvature initial conditions

The features of the BAO peak are not only sensitive to the background dynamics, but also to the evolution of the cosmic perturbations, in particular the manner in which the initial relative perturbations between the different species were established. Here we go beyond the assumption of pure adiabatic fluctuations, in which the equation of state of the universe is spatially constant and the curvature is perturbed, and allow the possibility of regular isocurvature perturbations, in

which the equation of state between the different species varies to keep the curvature constant, as well as correlations between the adiabatic and isocurvature perturbations [29]. Depending on how the different species are initially perturbed, different isocurvature modes arise, namely the cold dark matter isocurvature (CI) mode, the baryon isocurvature (BI) mode, the neutrino isocurvature density (NID) and the neutrino isocurvature velocity (NIV) mode.

Acoustic oscillations in the photon fluid in the tight-coupling regime are described by the photon density evolution equation in harmonic space

$$\ddot{\delta}_\gamma + \frac{\dot{R}}{1+R}\dot{\delta}_\gamma + k^2 c_s^2 \delta_\gamma = -\frac{2}{3} \left[\frac{\dot{R}}{1+R} \dot{h} + \ddot{h} \right] \equiv F(k, \tau), \quad (6.1)$$

where $R = \frac{R_b}{(1+z)}$ is the scaled baryon-to-photon density ratio, h is the metric field in synchronous gauge, and the dot refers to the conformal time derivative. Solving this equation prior to decoupling we find that

$$\begin{aligned} \delta_\gamma(k, \tau) = & A_S \sin kr_s(\tau) + A_C \cos kr_s(\tau) \\ & + A_I \int_0^\tau (1 + R(\tau'))^{1/2} \sin [kr_s(\tau) - kr_s(\tau')] F(k, \tau') d\tau', \end{aligned} \quad (6.2)$$

with the initial conditions that define the regular modes given by:

| | ADIA | BI | CI | NID | NIV |
|-------|----------------------|------------------------------------|------------------------------------|--------------------------------------|--|
| A_S | 0 | $-\frac{8}{\sqrt{3}k}\Omega_{c,0}$ | $-\frac{8}{\sqrt{3}k}\Omega_{b,0}$ | 0 | $\frac{4}{\sqrt{3}}\frac{R_\nu}{R_\gamma}$ |
| A_C | 0 | 0 | 0 | $-\sqrt{3}c_s\frac{R_\nu}{R_\gamma}$ | 0 |
| A_I | $\frac{\sqrt{3}}{k}$ | $\frac{\sqrt{3}}{k}$ | $\frac{\sqrt{3}}{k}$ | 0 | 0 |

where $\Omega_{c,0}$ and $\Omega_{b,0}$ are, respectively, the cold dark matter and the baryon densities today, with R_ν and R_γ the fractional energy densities of neutrinos and photons at early times, respectively. The NIV mode starts with a non-zero perturbation in the photon velocity so that it stimulates the $\sin(kr_s)$ harmonic in δ_γ , in contrast to the NID mode which has an initial non-zero perturbation in the photon density and excites the $\cos(kr_s)$ harmonic. We note that the adiabatic mode is sourced purely by the gravitational driving term $F(k, \tau)$, which is constant on large scales and at early times, so that the adiabatic solution excites a $\cos(kr_s)$ harmonic, similar to the NID mode.

At later times, though, this approximation breaks down when the mode enters the horizon, and the adiabatic solution deviates from a pure cosine mode, with the consequence that its acoustic peaks are offset in phase from the NID peaks. In the transition to matter domination, the gravitational driving term switches on as a source for the CI and BI modes, whereas its contribution to the NID and NIV modes remains negligible.

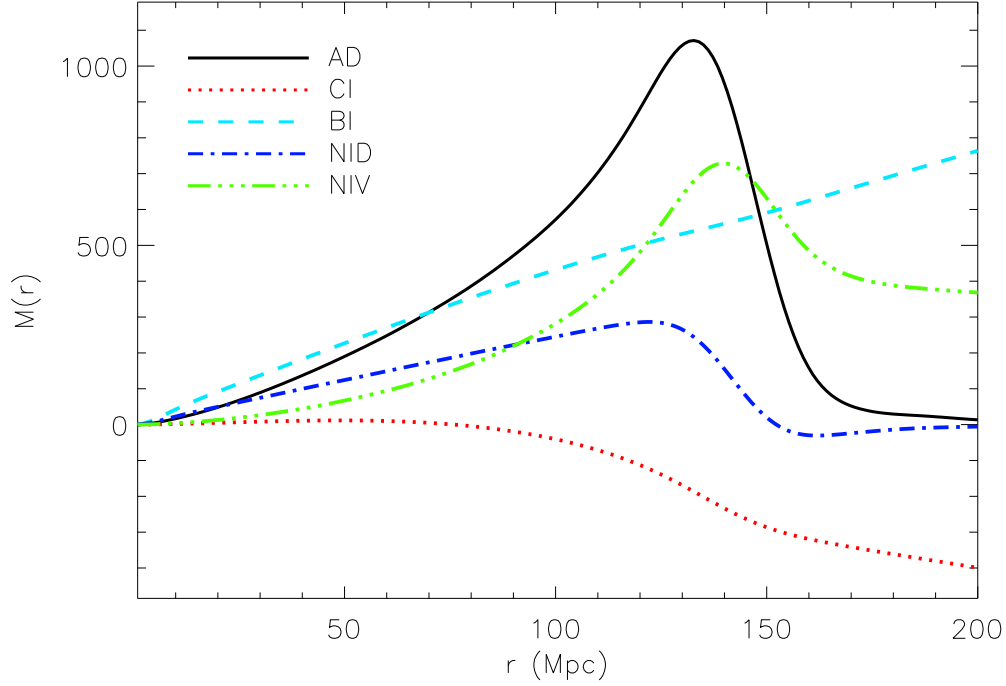


Figure 6.1: Baryon mass profile for adiabatic and isocurvature modes at decoupling, with the correct relative amplitude between the AD (black solid), NID (blue short dot-dashed line) NIV (green long dot-dashed line), BI (cyan dashed line) and CI (red dotted line) modes.

The solutions given above for the density contrasts of different modes need to be corrected for diffusion damping, by multiplying the solutions by the factor e^{-k^2/k_D^2} , where k_D is the diffusion damping wavenumber. In the absence of diffusion damping all modes have their BAO peak at the same position at all times but with differing shapes for the BAO profile due to the different initial conditions. The product of the diffusion damping factor in harmonic space acts like a

convolution in real space, smoothing the undamped BAO profile and moving baryons out of the BAO peak. The convolution over the differing BAO profile shapes thus results in a relative shift of the BAO peak position for different modes. We observe the same shift in the series of acoustic peaks exhibited in the cosmic microwave background anisotropy spectrum [43], though in this case it is recombination, as opposed to decoupling, that sets the acoustic scale. To quantify the shifts in the BAO peak of the isocurvature modes relative to the adiabatic mode, in Figure 6.1 we plot the baryon mass profile [47] of the various modes at decoupling, defined by

$$M_b(r, z) = \int T_b(k, z) \frac{\sin kr}{kr} k^2 r^2 e^{-k^2 \sigma^2/2} dk,$$

where $T_b = \delta_b/k^2$ is the baryon transfer function. Prior to decoupling and on large scales, δ_b is exactly $\frac{3}{4}\delta_\gamma$ for all modes except the BI and NID modes in which the baryon and photon density perturbations differ by a constant, respectively, 1 and R_ν/R_γ .

The mass profile captures the evolution of an initial point-like perturbation at the origin, though in practice we use a narrow gaussian, with width σ^{-1} in k space. The initial density perturbation expands out as a spherical wave at the sound speed [11] so that at decoupling there is an excess of baryons at the sound horizon scale, $r_s \approx c_s \tau_{\text{dec}}$. Note that even though the photons decouple from the baryons at $z \approx 1080$, it is only at $z \sim 500$ that the baryons stall, due to the fact that the growing mode is dominated by the velocity field on small scales, which does not decay instantaneously after decoupling. This sets the scale for the low-redshift BAO peak, which is shown in Figure 6.2. We observe that the BAO features for the isocurvature modes differ in shape and position from the adiabatic BAO peak, due to the effect of the diffusion damping on the undamped BAO profiles discussed earlier. In the case of the NID and NIV modes there is a pronounced peak which is offset from the adiabatic BAO peak due to the coupling to different harmonics, as described above. In the case of the BI and CI modes the acoustic wave has merely imprinted a ripple onto the homogeneous sea of baryons at decoupling, which evolves into a knee in the baryon mass profile at the BAO scale at late times. It is also interesting to note that the amplitude of the mass perturbation at the origin is much smaller for the isocurvature modes because the curvature, and thus the mass fluctuation, is initially unperturbed. It is clear that small admixtures of the isocurvature modes and their cross-correlations can distort the shape and location of the

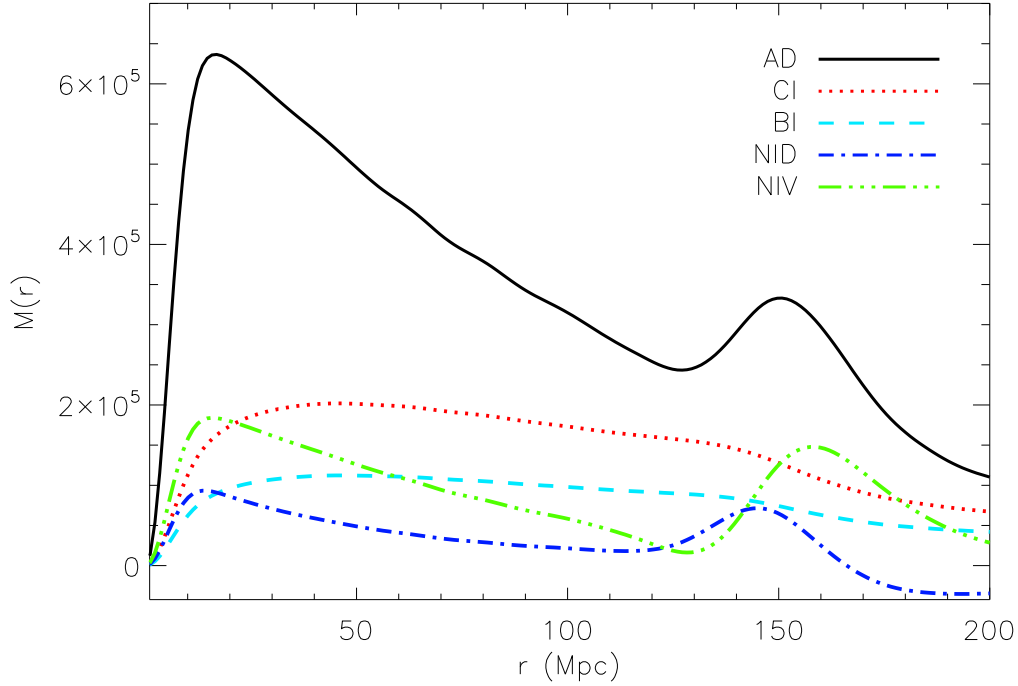


Figure 6.2: Baryon mass profile for adiabatic and isocurvature modes at $z = 0$, with the same labeling as in Figure 6.1. For clarity the NID, NIV and CI mass profiles have been multiplied by a factor of two, while the BI mass profile has been multiplied by a factor of six.

adiabatic BAO peak.

6.3 Dark energy constraints

Assuming that the variations in the cosmological parameters (including those modeling isocurvature) are small, we can model the likelihood function of a dataset as a multivariate Gaussian centered on a fiducial adiabatic Λ CDM Universe. Based on the noise estimates for the BOSS and PLANCK experiments, we can compute estimates of the errors on the cosmological parameters using a Fisher matrix formalism, by perturbing the cosmology around the fiducial model. When perturbing the dark energy model away from Λ , we allow for dynamics and parameterize

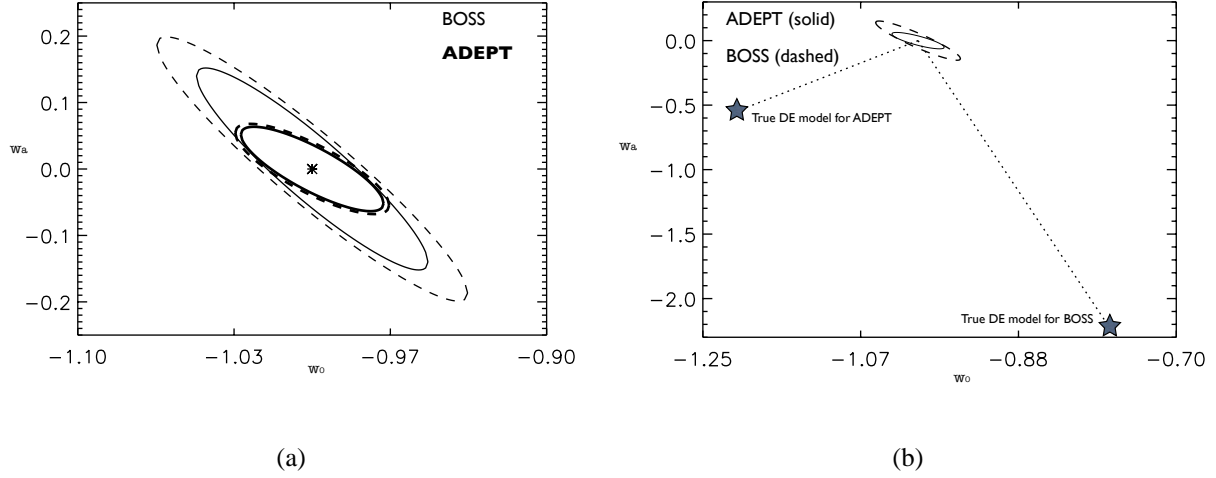


Figure 6.3: (a) 1σ error ellipses for (w_0, w_a) from the Fisher matrix calculation for the BOSS (thin lines) and ADEPT (thick lines) experiments with the PLANCK data as a prior, assuming adiabaticity (solid) and for the fully correlated isocurvature case (dashed). The fiducial dark energy model ($w_0^{fid} = -1$, $w_a^{fid} = 0$) is marked by a black star. (b) The average biases in the dark energy parameters $(\delta\bar{w}_0, \delta\bar{w}_a)$ that could potentially arise as a result of the incorrect assumption of adiabaticity are computed using equation 6.3 for a set of ϕ_i which are constructed from 10,000 linear combinations of the eigenvectors e_i . We can use the average of these biases to compute a dark energy model given by $(w_0^{fid} + \delta\bar{w}_0, w_a^{fid} + \delta\bar{w}_a)$ which, under the assumption of adiabaticity, will be indistinguishable from the fiducial model in a non-adiabatic Universe. This dark energy model is shown by the dotted lines for each of the two experiments considered. All other parameters have been marginalized over.

its equation of state using $w(a) = w_0 + (1 - a)w_a$ where $a = 1/(1 + z)$ [34, 112]. To model deviations away from adiabaticity, we adopt the isocurvature parameterization implemented in Moodley, *et al.* (2004) [121], where the different modes and their cross-correlations are described by 9 parameters, measuring the fractional contributions of the various correlations (auto and cross) to the overall total power spectrum. The relationship between this choice of isocurvature parameterization and other parameterization is described in Bean *et al.* (2006) [13]. We wish to examine the best case scenario, in which all information available from the galaxy power

spectrum is used and not just the baryon acoustic wiggles. Furthermore, we also assume perfect knowledge of the redshift-dependent bias and include the information introduced by the linear redshift distortions. Note that for the computation of the PLANCK Fisher matrix, we follow Albrecht *et al.* (2006) [3] and re-introduce the strict geometric degeneracy between the dark energy density Ω_X and w_0, w_a which may be artificially broken in the standard Fisher matrix computation, leading to under-estimates of errors. The details of the Fisher matrix implementation are given in the next chapter [124]. As a check of our numerics, we computed the Fisher matrices for the BAO experiments considered in Rassat *et al.* (2009) [139] in accordance with the details provided therein and recovered their results with reasonable agreement.

We are concerned with how well the equation of state parameters w_0 and w_a can be measured. In order to quantify the constraining power of the data, we compute the Dark Energy Task Force (DETF) figure of merit (FoM), which in practice is given by the square root of the determinant of the 2×2 Fisher matrix for the w_0 and w_a parameters and is proportional to the reciprocal of the area of the error ellipse in the $w_0 - w_a$ plane. We are concerned with the change in the FoM when isocurvature is introduced relative to the case of pure adiabaticity.

We compute the potential errors on w_0 and w_a for the case of pure adiabaticity and for the scenario where all isocurvature modes and their cross-correlations are admitted, while marginalizing over all other cosmological parameters. The results for both the BOSS and ADEPT experiments are shown in the first and last rows of table 6.1. The BOSS FoM is found to decrease by 50% when this additional freedom is introduced in the initial conditions, while the ADEPT FoM decreases by 20%. These changes are illustrated in Figure 6.3 which compares the 68% confidence regions for the adiabatic and the fully correlated isocurvature cases. Evidently, no single mode and its correlation are responsible for the change in the allowable (w_0, w_a) region, but rather a mixture of all extra degrees of freedom.

The question that we wish to ask is, what bias in the estimates of the dark energy parameters could potentially be induced by incorrectly assuming adiabaticity? For a Gaussian-distributed

| Experiment | BOSS | | ADEPT | |
|------------------|-------|-------|-------|-------|
| Modes | w_0 | w_a | w_0 | w_a |
| AD | 0.033 | 0.10 | 0.02 | 0.042 |
| AD+CI+⟨AD, CI⟩ | 0.033 | 0.10 | 0.020 | 0.042 |
| AD+NID+⟨AD, NID⟩ | 0.033 | 0.10 | 0.020 | 0.042 |
| AD+NIV+⟨AD, NIV⟩ | 0.033 | 0.10 | 0.021 | 0.042 |
| ISO (ALL) | 0.044 | 0.13 | 0.022 | 0.045 |

Table 6.1: Table summarizing the constraints on (w_0, w_a) for adiabatic and an admixtures of uncorrelated adiabatic and isocurvature modes, marginalizing other all other parameters, for the BOSS and ADEPT experiments. The fiducial model assumes adiabaticity.

likelihood function, it can be shown that the linear bias in a set of parameters that we wish to constrain, $\delta\theta_i$, due to erroneous values of a set of fixed parameters, $\delta\phi_j$, is [169]

$$\delta\theta_i = - [F^{\theta\theta}]_{ik}^{-1} F_{kj}^{\theta\phi} \delta\phi_j \quad (6.3)$$

where $F^{\theta\theta}$ is the Fisher sub-matrix for the parameters we wish to constrain and $F^{\theta\phi}$ is a Fisher sub-matrix constructed from the product of the derivatives of the power spectrum with respect to the parameters being constrained and those which are being fixed. In our case j labels the nine isocurvature mode amplitudes, incorrectly fixed to zero, k labels the eight cosmological parameters that are biased, and i labels the subset of two dark energy parameters whose bias is of interest to us. In order to set $\delta\phi_j$, we diagonalize the combined PLANCK and large-scale structure (LSS) Fisher matrix and select the eigenvector, \mathbf{e}_i with the smallest eigenvalue λ_i . This corresponds to the direction in parameter space which is least constrained by the data. We then take $\delta\phi_j = \sqrt{\frac{19.2}{\lambda_i}} \mathbf{e}_i$.

For the BOSS experiment, we find that $\delta w_0 = -0.049$ and $\delta w_a = 0.11$, while for ADEPT the biases are found to be $\delta w_0 = -0.015$ and $\delta w_a = 0.018$. However this is only one particular direction that weakly constrains all the parameters, not necessarily the dark energy parameters.

In order to explore the full range of the bias, we use a set of 10,000 random linear combinations of the eigenvectors to compute $\delta\phi_j$ and the corresponding biases. We find that the mean biases are $\mu(\delta w_0) = 0.23$ and $\mu(\delta w_a) = -2.3$ with $\sigma(\delta w_0) = 0.15$ and $\sigma(\delta w_a) = 0.73$. The implication is that if the initial conditions of our Universe are comprised of a sub-dominant contribution from isocurvature modes (within the 1σ constraints from PLANCK and the selected LSS survey), the assumption of adiabaticity could lead to an incorrect 7σ detection of $w_0 \neq -1$ or a 23σ false claim of $w_a \neq 0$. Alternatively, Λ could be found to be consistent with the data when in fact $w(z) \neq -1$. The potential bias incurred by the adiabatic assumption in the case of a more advanced BAO experiment such as ADEPT for w_0 is around 10σ with $\mu(\delta w_0) = -0.20$ and $\sigma(\delta w_0) = 0.048$, while the measurement of w_a could be inaccurate at the level of 12σ with $\mu(\delta w_a) = -0.52$ and $\sigma(\delta w_a) = 0.15$. The reduction in the bias is encouraging as one would expect that with an increase in the constraining power of the survey comes a higher risk of making false claims.

It is interesting that perhaps the most physically relevant mode, the CDM isocurvature mode, leads to no noticeable degradation of the dark energy constraints relative to the pure adiabatic model and less than a 0.5σ bias in the dark energy parameters (on average) when taken in isolation (see Table 6.1). That being said, we could be unlucky and the Universe may in fact have an isocurvature contribution from a single mode that is highly degenerate with a non- Λ dark energy model. For example, we find a particular combination of adiabatic and CDM isocurvature initial conditions can induce biases of 4σ (3σ) and 9σ (2σ) for the w_0 and w_a parameters respectively for the BOSS (ADEPT) experiment. Furthermore, even in the case of a single isocurvature mode correlated with the adiabatic mode, departures from scale invariance and a scale dependent correlation could cause further degradation of the constraints presented here. For example, it is well known [128] that scale-dependent correlations arise in realistic models of inflation with isocurvature modes since the power spectra often develop features such as bumps. Hence our results simply provide a lower-bound on the expected impact of isocurvature modes on the standard results.

| | PLANCK + BOSS | PLANCK + ADEPT |
|--|---------------|----------------|
| $\langle \text{AD}, \text{AD} \rangle$ | 0.30 (19) | 0.29 (27) |
| $\langle \text{CI}, \text{CI} \rangle$ | 0.0059 (47) | 0.0051 (54) |
| $\langle \text{NID}, \text{NID} \rangle$ | 0.014 (40) | 0.014 (40) |
| $\langle \text{NIV}, \text{NIV} \rangle$ | 0.011 (49) | 0.0085 (62) |
| $\langle \text{AD}, \text{CI} \rangle$ | 0.025 (85) | 0.023 (86) |
| $\langle \text{AD}, \text{NID} \rangle$ | 0.0011 (26) | 0.00023 (34) |
| $\langle \text{AD}, \text{NIV} \rangle$ | 8.5e-05 (99) | 7.9e-05 (99) |
| $\langle \text{CI}, \text{NID} \rangle$ | 0.013 (39) | 0.013 (39) |
| $\langle \text{CI}, \text{NIV} \rangle$ | 0.0034 (34) | 0.0029 (43) |
| $\langle \text{NID}, \text{NIV} \rangle$ | 0.013 (75) | 0.012 (76) |

Table 6.2: Forecasted uncertainties on isocurvature parameters in the fully correlated case for the PLANCK and LSS data (BOSS and ADEPT). The percentage improvement in 1σ errors when the LSS data is added to the PLANCK data is shown in brackets.

We can also turn this around and instead recognize that our results show that the combination of LSS and CMB data provide a powerful new discovery tool for exotic new early Universe physics associated with isocurvature modes. In particular, the volume of the 9-dimensional isocurvature Fisher ellipse is $2 - 4 \times 10^9$ smaller than that from PLANCK alone, showing that using CMB plus BAO data in union provides exceptionally good constraints on the early Universe relative to the CMB alone. The constraints on the isocurvature parameters from the CMB plus BAO data are summarized in table 6.2, with the percentage improvement over the CMB alone shown in brackets. We find that the error bars on the isocurvature parameters decrease by 30% to as much as 100% for certain modes when the LSS data (either BOSS or ADEPT) is added to the PLANCK data. More specifically, the parameters representing the cross-correlations between the AD and CI modes, the AD and NID modes and the NID and NIV modes show more than 75% reduction in their forecasted errors. The implication is that a combination of these parameters is strongly degenerate with the dark energy parameters and when included into the parameter

space, contributes substantially to the degradation in the forecasted w_0 and w_a constraints.

6.4 Conclusions

With forecasted constraints on dark energy from Baryon Acoustic Oscillation (BAO) experiments at the level of a few percent made possible by the large volumes probed by the most recent generation of redshift surveys, it is important to explore the full spectrum of possible BAO systematics. In this *Letter* we have found that even small isocurvature admixtures significantly alter the BAO, and by assuming adiabaticity we run the risk of incorrectly attributing a shift in the BAO away from the predicted value in a Λ CDM model, to the presence of dark energy.

In particular, ignoring isocurvature modes can bias the estimates of the dark energy parameters, leading to a 7σ (10σ) incorrect measurement of w_0 or as much as a 23σ (12σ) bias in w_a for BOSS (ADEPT) on average. Including general initial conditions removes this bias at the expense of an increase in the area of confidence intervals in the (w_0, w_a) space by 50% (20%) for the BOSS (ADEPT) survey, indicating that the assumption of adiabaticity leads to an under estimation of the errors on the dark energy parameters. On the other hand, BAO data leads to a significant improvement in the constraints on the general isocurvature mode mixture compared with those from the CMB alone, and thus opens up new windows for discovery of exotic early Universe physics.

The Sensitivity of BAO Dark Energy Constraints to General Isocurvature Perturbations

7.1 Introduction

Although the standard model of cosmology based on Λ CDM has not changed fundamentally in the last decade, there has been a remarkable refinement in our knowledge of the parameters describing the model. For example, the original supernova results gave only limits of $\Omega_m < 1.5$ at 2σ assuming a general Λ CDM model [144] while the latest results from the WiggleZ Baryon Acoustic Oscillation (BAO) survey, together with WMAP and Union2 supernova data now give $\Omega_m = 0.29 \pm 0.04$ at 2σ [22].

As a result of this progress it has become obvious that systematic errors are a key issue in pushing the frontier further. For example, in the case of supernovae there are important systematic errors related to the lightcurve fitter used which currently leads to shifts in the dark energy equation of state of about $\Delta w \sim 0.1$ [82]. There may be additional supernova systematics such as the ex-

istence of Type Ia subpopulations and correlations between absolute magnitude and host galaxy type (see e.g. [159]).

BAO have their own associated systematic errors, such as nonlinear effects which potentially bias or shift the BAO peak, although these are believed to be fairly small and possible to calibrate through theoretical modeling and N-body simulations [38]. However there is another theoretical systematic due to isocurvature perturbations that has recently received attention [185, 115]. Depending on how general one allows the primordial isocurvature admixture to be, there can be a significant impact on the ability of future BAO surveys to constrain dark energy even if one imposes the constraint that the isocurvature modes be undetectable by PLANCK alone [185]. This shows that at least in the next generation of surveys one will not be able to decouple the search for dark energy with BAO from an understanding of the early universe, a subtlety that does not affect supernovae surveys.

The key reason that even small correlated isocurvature modes cause a problem for BAO surveys is that they alter the way in which the BAO peak appears in the two-point correlation function of baryons, and hence, of galaxies. In the simple adiabatic model the BAO peak is controlled by the sound horizon, the distance that sound waves can propagate in the early universe from the time of inflation to decoupling. This characteristic scale depends only on the sound speed in the standard adiabatic picture:

$$r_s = \int_0^{t_{cmb}} c_s(1+z)dt = \int_{z_{cmb}}^{\infty} \frac{c_s(z')}{H(z')} dz' \quad (7.1)$$

where $c_s(z) = 1/\sqrt{3(1+R_b/(1+z))}$ and $R_b = 31500 \omega_b (T_{cmb}/2.7 \text{ K})^{-4}$ which can be measured accurately with the Cosmic Microwave Background (CMB). By comparing the size of this scale at the time of decoupling and its angular size at late times we can learn about the expansion history of the universe and measure cosmic distances, and hence constrain models of dark energy [12].

In [185], we found a clear degeneracy between the impact of dark energy models and non-

adiabatic initial conditions on the galaxy correlation function. In this chapter we explain in depth why small amplitude but general admixtures of correlated isocurvature modes can have such a strong impact on the cosmological constraints based on BAO surveys. We show that relaxing the assumption of adiabaticity and allowing fractions of isocurvature modes affects the development of the acoustic waves in the baryon-photon fluid. The isocurvature modes excite different harmonics which in turn, couple differently to Silk damping, and in so doing, modifies both the scale on which the sound waves imprint on the baryon distribution and the shape of the BAO peak.

This chapter is arranged as follows; in section 7.2, we study the evolution of the baryon density contrast under different initial conditions and how the structure of the BAO peak is altered. In section 7.3, a Fisher matrix formalism is implemented in order to quantify the impact of these changes on the forecasted errors on the dark energy parameters from two BAO experiments, namely BOSS [48] and ADEPT [151]. As a prior, we include the information from the high-resolution CMB temperature anisotropy and polarization spectra from the PLANCK Surveyor [136], which should provide stringent constraints on the amount of isocurvature in the initial conditions. We also conduct a study of the potential bias in our estimates of the dark energy parameters that can result from an incorrect assumption of pure adiabatic initial conditions. Lastly, we show that constraints on the isocurvature parameters can be derived from BAO surveys. We discuss our conclusions in section 7.4.

7.2 The BAO peak with adiabatic and isocurvature initial conditions

The BAO peak is sensitive not only to the matter content of the universe, but also to the character of the primordial perturbations. The features of the BAO peak such as the location, width and amplitude are mainly dictated by the time evolution of the baryon density contrast δ_b from the post-inflation period to photon-baryon decoupling. In turn, the time evolution of the

baryon density contrast during the pre-decoupling period depends on the initial configuration of the primordial perturbations in the different species at the end of inflation.

In the simplest scenario the perturbation affects all the cosmological species such that the relative ratios in the number densities remain unperturbed, exciting the adiabatic mode (AD). Although adiabatic initial conditions are a natural feature of single-field inflationary models [110], it has been shown [29] that four regular isocurvature (ISO) modes are allowed in addition to the adiabatic (AD) mode. These isocurvature modes are characterized by variations in the particle number ratios but with vanishing curvature perturbation, with different isocurvature modes excited depending on the species that are initially perturbed. These are namely the cold dark matter isocurvature (CI) mode, the baryon isocurvature (BI) mode, the neutrino isocurvature density (NID) and the neutrino isocurvature velocity (NIV) mode. While isocurvature modes are more difficult to physically motivate, the possibility of correlated isocurvature fluctuations is allowed given current cosmological data [13, 31] and should therefore be considered.

We will show that different modes of the primordial perturbations excite different harmonics and these harmonics couple differently to the Silk damping, thereby altering the characteristic scale at photon-baryon decoupling to different locations. After decoupling, baryon fluctuations on scales larger than the Jeans length λ_J slow down in the rest frame of the cold dark matter (CDM), falling into the CDM potential wells, and eventually tracing the CDM, while on scales below λ_J the fluctuations still oscillate, independently of the initial conditions. In order to study the features of the BAO peak for the different modes, we consider the time evolution of the photon-baryon fluid in the tight-coupling regime.

In this regime, photons and baryons are treated as perfect fluids. The subscripts b , c , γ and ν respectively denote the baryons, the CDM, the photons and the neutrinos. The conservation of energy-momentum leads to the following set of time evolution equations for the photon and the

baryon density contrasts δ and velocity divergences θ in the synchronous gauge [114]:

$$\dot{\delta}_\gamma = -\frac{4}{3}\theta_\gamma - \frac{2}{3}\dot{h}, \quad (7.2)$$

$$\dot{\delta}_b = -\theta_b - \frac{1}{2}\dot{h}, \quad (7.3)$$

for the density contrasts, and

$$\dot{\theta}_\gamma = k^2 \left(\frac{1}{4}\delta_\gamma - \sigma_\gamma \right) + an_e\sigma_T(\theta_b - \theta_\gamma), \quad (7.4)$$

$$\dot{\theta}_b = -\frac{\dot{a}}{a}\theta_b + c_s^2 k^2 \delta_b + \frac{4\bar{\rho}_\gamma}{3\bar{\rho}_b} an_e\sigma_T(\theta_\gamma - \theta_b), \quad (7.5)$$

for the velocity divergences. Here and throughout the chapter, σ_T is the Thomson scattering cross section, n_e is the electron number density, a is the scale factor, $\bar{\rho}$ is the background density, c_s is the sound speed given by $c_s = 1/\sqrt{3(1+R)}$, $R = \frac{3\bar{\rho}_b}{4\bar{\rho}_\gamma}$ is the baryon-to-photon density ratio, σ_γ is the photon shear, and the dot refers to the derivative with respect to the conformal time τ . The variable h is the metric field in synchronous gauge, which evolves according to [114]

$$\ddot{h} + \frac{\dot{a}}{a}h = -3 \left(\frac{\dot{a}}{a} \right)^2 \bar{\rho}_{cr} \sum_j \Omega_j \delta_j (1 + 3c_{sj}^2), \quad (7.6)$$

where $j \in \{\nu, \gamma, b, c\}$ labels the different species of the universe, $\bar{\rho}_{cr}$ is the critical density of the universe and $\Omega_j \equiv \bar{\rho}_j/\bar{\rho}_{cr}$ is the ratio of the density of the j^{th} species to the critical density.

The tight-coupling approximation allows us to set $\theta_\gamma = \theta_b = \theta_{\gamma b}$, with the photon-baryon velocity evolving as

$$(1+R)\dot{\theta}_{\gamma b} = -\dot{R}\theta_{\gamma b} + k^2 \left(\frac{1}{4}\delta_\gamma - \sigma_\gamma \right) + c_s^2 k^2 R \delta_b, \quad (7.7)$$

and the photon density contrast evolving as [74]

$$\ddot{\delta}_\gamma + \frac{\dot{R}}{1+R}\dot{\delta}_\gamma + k^2 c_s^2 \delta_\gamma = -\frac{2}{3} \left[\frac{\dot{R}}{1+R} \dot{h} + \ddot{h} \right]. \quad (7.8)$$

Here, we have neglected the photon shear (tight-coupling regime) and the pressure term in δ_b as it remains smaller than the term in δ_γ prior to decoupling. Equation (7.8) represents a driven harmonic oscillator with the competition between gravitational infall and photon pressure giving

rise to acoustic waves propagating in the photon-baryon fluid at the speed of sound.

For the associated homogeneous equation, we look for solutions of the form $\delta_\gamma \propto \exp i \int_0^\tau \omega d\tau'$ where $\omega(\tau)$ is some phase function. The two solutions to the homogeneous equation are simply $\sin kr_s$ and $\cos kr_s$, where $r_s(\tau) = \int_0^\tau c_s d\tau'$, the phase function is $\omega = kc_s$, and we have made use of the WKB approximation. On large scales, the WKB approximation breaks down, but these modes are irrelevant for the BAO treatment as they only enter the horizon well after decoupling. The particular solution is constructed by integrating the driving term weighted by the Green's function of the two homogeneous solutions [74]. Thus, the time evolution of the acoustic waves in the photon component for all initial conditions prior to decoupling is given by

$$(1 + R)^{1/2} \delta_\gamma(k, \tau) = A_S \sin kr_s(\tau) + A_C \cos kr_s(\tau) + \frac{1}{kc_s} \int_0^\tau (1 + R(\tau'))^{1/2} \sin [kr_s(\tau) - kr_s(\tau')] F(\tau') d\tau', \quad (7.9)$$

where A_S and A_C are determined by the initial conditions as described in [29], and

$$F(\tau) = -\frac{2}{3} \left(\frac{\dot{R}}{1 + R} \dot{h} + \ddot{h} \right), \quad (7.10)$$

is the gravitational driving term which evolves differently for different initial conditions. Equation (7.9) gives the time evolution of the photon density contrast in the tight-coupling regime. In this regime, the baryon density contrast is related to its photon counterpart by $\dot{\delta}_b = \frac{3}{4} \dot{\delta}_\gamma$. On small scales, a correction to the tight-coupling approximation must be applied when the Silk damping becomes important, as photons leak out of overdense regions, dragging baryons with them. This is done by multiplying the solution above by e^{-k^2/k_D^2} , where the photon diffusion scale k_D^{-1} is given by

$$k_D^{-2} = \frac{1}{6} \int \frac{1}{\dot{\tau}_e} \frac{R^2 + 4(1 + R)/5}{(1 + R)^2},$$

where $\dot{\tau}_e = an_e \sigma_T$ is the differential optical depth. The Silk damping turns out to significantly affect both the shape and the peak location of the BAO as we shall discuss later.

After decoupling, the photons free stream, while baryons fall into the CDM potential wells under gravitational instability. Here, we only consider baryon fluctuations with wavelength larger than

the Jeans scale.

The above description of the density contrast evolution in k -space can be intuitively and simply understood by looking at the evolution of the mass profile in the configuration space [47, 11].

The radial mass profile M_j of a species j , given by

$$M_j(r, z) = \int_0^\infty T_j(k, z) \frac{\sin kr}{kr} k^2 r^2 dk, \quad (7.11)$$

$$= r \int_0^\infty \delta_j(k, z) \frac{\sin kr}{k} dk, \quad (7.12)$$

where $T_j(k, z) = \delta_j(k, z)/k^2$ is the transfer function of the j^{th} species, describes the redshift evolution of a point-like overdensity initially located at the origin. The location of the mass profile peak gives the physical radius of the spherical shell of the overdensities for a given species. For numerical computations, a Gaussian overdensity of width σ^{-1} is used instead of a point-like overdensity. This is done by multiplying the integrand of equation (7.12) by $e^{-k^2\sigma^2/2}$.

Hereafter, we study the time evolution of the baryon mass profile for each mode in turn. We start from the well studied adiabatic case then move onto the isocurvature modes, since this will provide physical intuition into the effect of the isocurvature modes on the BAO.

7.2.1 AD mode

The adiabatic mode is characterized by the requirement that the densities of all species are perturbed in proportion at some initial time such that

$$\delta_{c,i} = \delta_{b,i} = \frac{3}{4}\delta_{\gamma,i} = \frac{3}{4}\delta_{\nu,i}, \quad (7.13)$$

where the subscript i labels the initial time. Or equivalently, using the relative entropy between two species x and y given by $\mathcal{S}_{xy} = \frac{\delta_x}{1+w_x} - \frac{\delta_y}{1+w_y}$, where w_x and w_y are the equation of state parameters of the species x and y respectively, we have that $\mathcal{S}_{xy} = 0$ for all pairs of species at the initial time. In addition, all velocity divergences are initially unperturbed. Therefore, using the initial conditions for the adiabatic mode [29], the photon and baryon density contrasts are

respectively given by

$$\begin{aligned}\delta_\gamma^{AD} &= \frac{\sqrt{3}}{k} e^{-k^2/k_D^2} \\ &\times \int_0^\tau (1 + R(\tau'))^{1/2} \sin[kr_s(\tau) - kr_s(\tau')] \\ &\times F^{AD}(\tau') d\tau',\end{aligned}\tag{7.14}$$

$$\begin{aligned}\delta_b^{AD} &= \frac{3}{4} \frac{\sqrt{3}}{k} e^{-k^2/k_D^2} \\ &\times \int_0^\tau (1 + R(\tau'))^{1/2} \sin[kr_s(\tau) - kr_s(\tau')] \\ &\times F^{AD}(\tau') d\tau'.\end{aligned}\tag{7.15}$$

Thus, the adiabatic mode is only sourced by the gravitational driving term F^{AD} . This driving term can be approximated by

$$F^{AD}(k, \tau) \approx 2k^2 c_s^2 j_0(kr_s)$$

on small and intermediate scales which reduces to $2k^2 c_s^2$ at early times. On very large scales the above approximation breaks down, however, this does not affect our physical description of the BAO peak as these large-scale modes are well outside the horizon at decoupling and do not substantially influence the BAO features. The lack of an exact analytic expression for the driving term makes it difficult to derive exact analytic solutions for the time evolution of the photon and baryon density contrasts. Nevertheless, good approximations for the photon and baryon density contrasts are given by

$$\delta_\gamma = \frac{4}{3} \delta_b \approx 2kr_s j_1(kr_s) \times e^{-k^2/k_D^2}.\tag{7.16}$$

Therefore, at early times ($kr_s(\tau) \ll 1$) the density contrasts for the adiabatic mode, $\delta_\gamma \propto \delta_b \propto (1 - \cos kr_s)$ couple to a $\cos kr_s$ harmonic [74].

Now, in the perfect tight-coupling approximation, that is if we omit the Silk damping correction in the density contrast equations, the baryon mass profile is given by

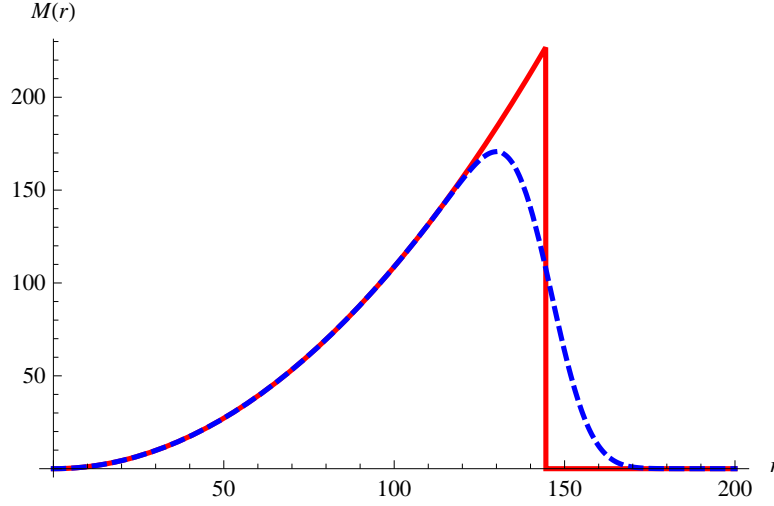


Figure 7.1: Effect of Silk damping on the baryon mass profile for the AD mode at decoupling. The solid curve represents the baryon mass profile without the Silk damping correction, while the dashed curve represents the baryon mass profile with the Silk damping factor turned on. In the absence of the damping term, the peak is located at $r = r_s = 144.5$ Mpc.

$$M_b(r) \propto (1 - H(r - r_s)) \frac{\pi r^2}{2r_s^2} \propto \begin{cases} r^2 & \text{for } r \leq r_s, \\ 0 & \text{for } r > r_s, \end{cases} \quad (7.17)$$

which is obtained by substituting the density contrast expression, without the Silk damping term, in the baryon mass profile expression. Here $H(x)$ is the Heaviside step function. We observe that in the absence of Silk damping, the baryon mass profile is quadratic at lower r and sharply peaked at a distance $r(z) = r_s(z)$. This is illustrated in Figure 7.1 where we show the effect of Silk damping on the baryon mass profile at decoupling. We see that when we include the Silk damping term, the BAO peak is smoothed, attenuated and shifted to lower r . We can understand these features as follows. As we approach decoupling, the coupling between photons and baryons weakens and the photon mean free path increases. Photons diffuse from overdensities to underdensities carrying baryons with them. Therefore, baryons leak out of the overdensity to both lower and higher r , thereby smoothing and lowering the BAO peak. Due to the shape of the undamped mass profile (with no baryons on scales larger than the sound horizon), Silk damping

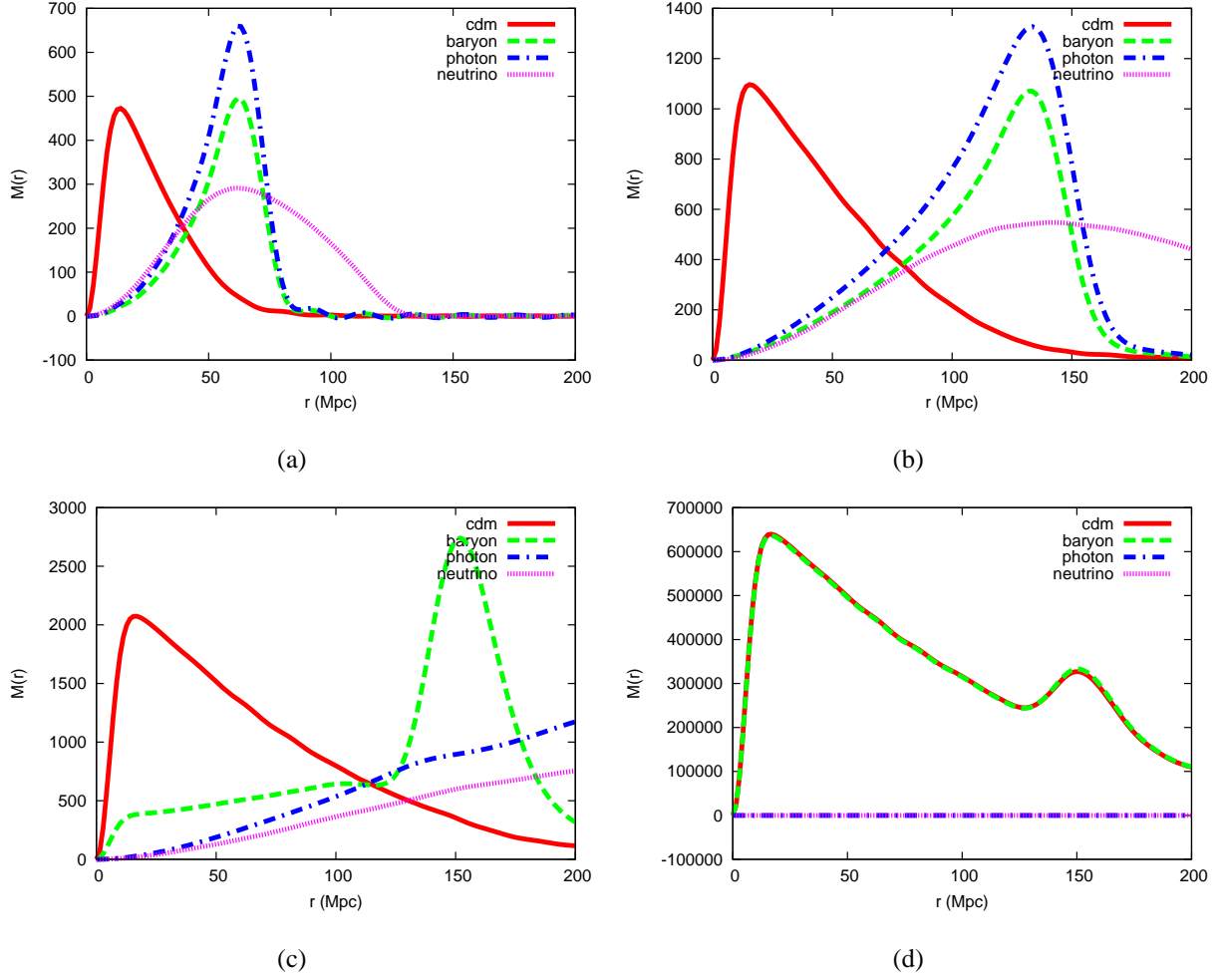


Figure 7.2: Mass profile snapshots for the AD mode at different redshifts. The red, green, blue and purple curves respectively represent the CDM, the baryon, the photon and the neutrino mass profiles. **(a)** Well before decoupling ($z = 3000$), **(b)** At decoupling ($z = 1080$), **(c)** when baryons stall ($z = 500$) and **(d)** At late times ($z = 0$). The units of the mass profile are arbitrary but correctly scaled between panels.

has the effect of moving more baryons to larger scales. As a result, the BAO peak is at a slightly smaller distance than the sound horizon. As we will see later, Silk damping changes the shape of the mass profile for the adiabatic and isocurvature modes in different ways, due to the differing shapes of the undamped mass profiles. This has important consequences for our ability to use the BAO as a standard ruler.

The redshift evolution of the mass profile for the AD mode has previously been studied in the literature [47]. Initially the overdensities of all species coincide. As time evolves, the photon pressure drives acoustic waves in the photon-baryon fluid, while neutrinos free stream at the speed of light and the CDM remains at its initial location. In Figure 7.2 we show the redshift evolution of the CDM, baryon, photon and neutrino mass profiles. Prior to decoupling, photons drag baryons at the sound speed, leaving behind a void of baryons. Thus, the initial baryon point-like overdensity evolves in a spherical shell while the CDM overdensity collapses at the origin under gravitational instability, and the neutrinos free stream.

After decoupling, photons free stream while baryons, free from the photons, collapse into the CDM potential wells. The baryon overdensity continues to collapse, pulling matter from the surrounding underdense regions to the overdense regions. As the baryon velocity divergence does not decay instantaneously at decoupling [47], the baryons only stall later at $z \sim 500$ with the consequence that the BAO peak is closer to 150 Mpc than 140 Mpc, the sound horizon size at decoupling. At $z = 0$, the baryon mass profile displays two peaks, one near the origin and a second peak at approximately 150 Mpc.

7.2.2 NID mode

The NID mode arises when the densities of the matter components are initially unperturbed while the initial perturbation in the neutrino density is balanced by its photon counterpart, keeping the curvature unperturbed. The initial perturbations are as follows:

$$\delta_{c,i} = \delta_{b,i} = 0, \quad \delta_{\gamma,i} = -\frac{R_\nu}{R_\gamma} \delta_{\nu,i}. \quad (7.18)$$

These initial conditions imply that $A_S = 0$, thus exciting the $\cos kr_s$ harmonic. The gravitational driving term contribution for this mode can be neglected without loss of accuracy, as the gravitational potential (related to \dot{h}), is initially unperturbed and only grows inside the horizon. This can also be understood by considering the right-hand side of equation (7.6). In the radiation dominated era, the photon and the neutrino density contrasts roughly cancel while the baryon and the

CDM density contrasts remain small until the matter dominated era when they grow. The time evolution of the photon and the baryon density contrasts for the NID mode are given by

$$\delta_\gamma^{NID} = -\frac{R_\nu}{R_\gamma} \sqrt{3} c_s \cos kr_s \times e^{-k^2/k_D^2}, \quad (7.19)$$

$$\delta_b^{NID} = \frac{3}{4} \frac{R_\nu}{R_\gamma} \left(1 - \sqrt{3} c_s \cos kr_s\right) \times e^{-k^2/k_D^2}, \quad (7.20)$$

where $R_\nu = \Omega_\nu/\Omega_{rad}$ and $R_\gamma = \Omega_\gamma/\Omega_{rad}$ are respectively the fractional energy densities of neutrinos and photons at early times. The pressure due to an initial localized photon overdensity creates a baryon underdensity that propagates due to its coupling to photons and perturbs, through gravitational interaction, the CDM (see Figure 7.3). In addition, isocurvature perturbations grow once they enter the horizon. It follows that the BAO peak in the case of the NID mode has smaller amplitude than in the adiabatic case. With time, the baryon and the CDM overdensities grow by pulling more matter from their surroundings, thus creating underdense regions around them. Note that the mass profile of a given species can be negative since the species can be initially perturbed positively, corresponding to an overdensity or negatively, corresponding to an underdensity, with respect to the background level. The final baryon mass profile displays a deeper trough between the two peaks compared to the adiabatic case. Most importantly, though the baryon overdensity in the NID mode evolves at earlier times like the baryon overdensity in the adiabatic mode as they both excite $\cos kr_s$ harmonics, the final locations of the NID and the AD BAO peaks differ. At late times, the adiabatic mode becomes a superposition of sine and cosine waves, departing from the NID mode and with the undamped profile being convolved differently with Silk damping.

Figure 7.4 shows the effect of Silk damping on the baryon mass profile at decoupling for the NID mode. In the absence of Silk damping, the AD and the NID BAO peak locations would coincide. The undamped baryon mass profile for the NID mode is given by

$$M_b(r) \propto (1 - H(r - r_s)) r \propto \begin{cases} r & \text{for } r \leq r_s, \\ 0 & \text{for } r > r_s. \end{cases} \quad (7.21)$$

As for the AD case, equation (7.21) is obtained by omitting the damping factor in equation (7.20) and substituting into equation (7.12) for the mass profile. The baryon mass profile for the NID

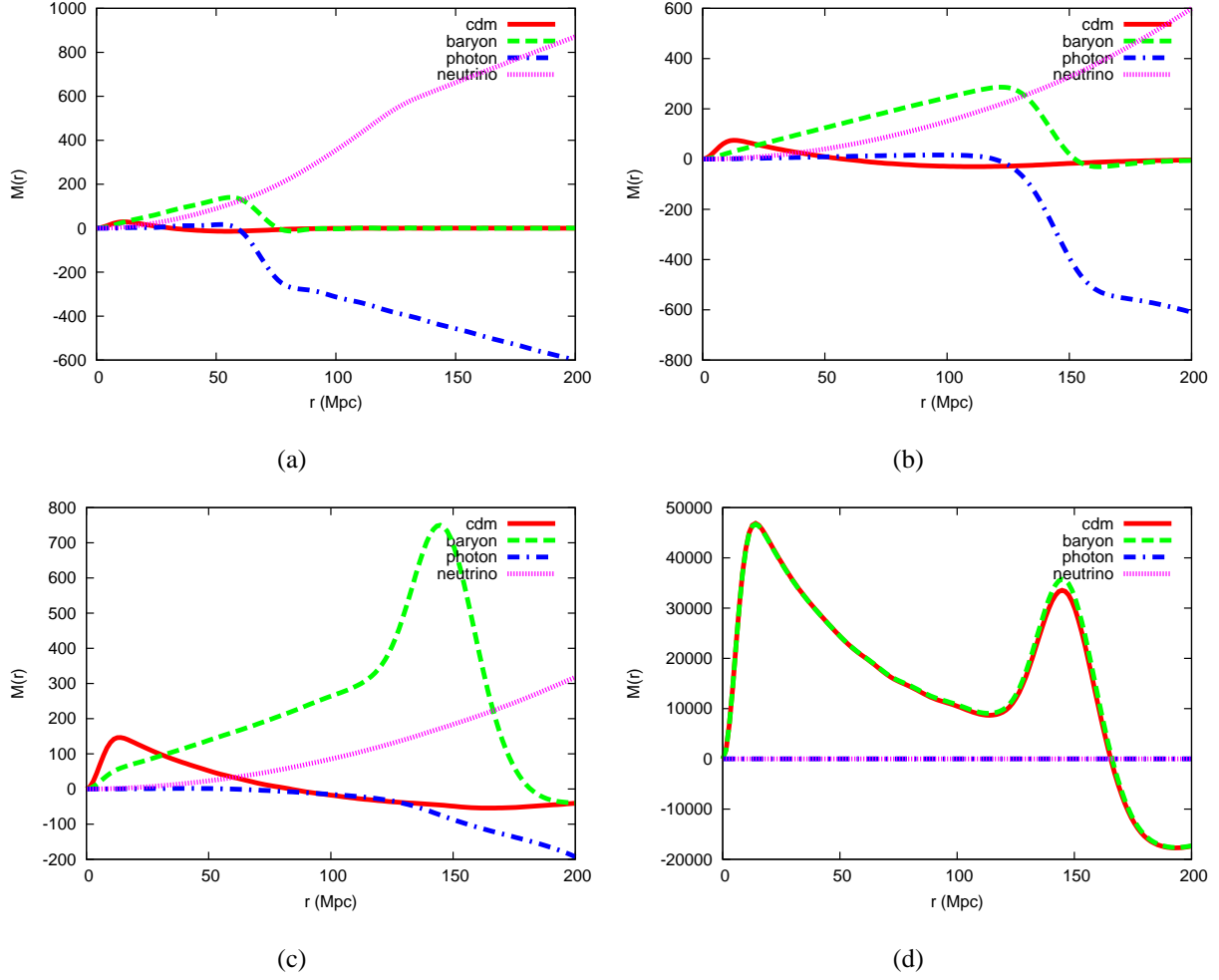


Figure 7.3: Mass profile snapshots for the NID mode at different redshifts. The red, green, blue and purple curves respectively represent the CDM, the baryon, the photon and the neutrino mass profiles. **(a)** Well before decoupling ($z = 3000$), **(b)** At decoupling ($z = 1080$), **(c)** when baryons stall ($z = 500$) and **(d)** At late times ($z = 0$). The units of the mass profile are arbitrary but correctly scaled between panels.

mode differs from the AD mode as it grows linearly with r until $r(z) = r_s(z)$ then falls to zero. For this reason, the shift in the BAO peak location due to Silk damping is larger than in the case of the AD mode for which, as previously mentioned, the undamped mass profile is quadratic in r for $r < r_s$. The difference in the shape of the undamped mass profile also sets the difference in the width of the BAO peak.

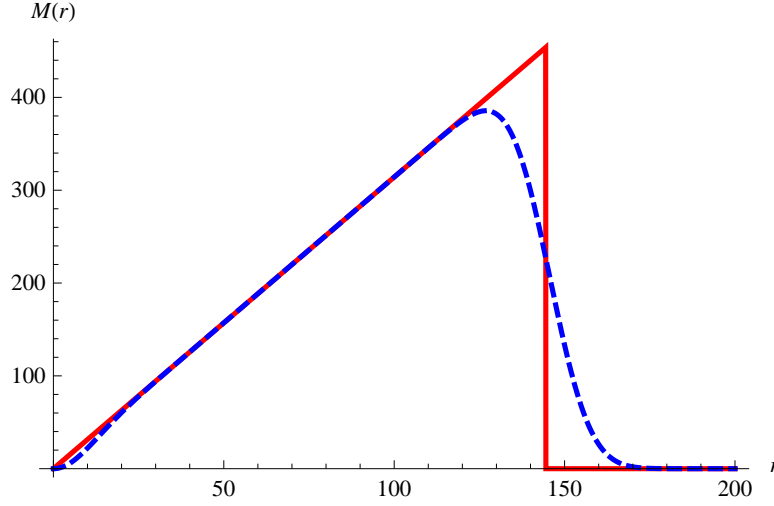


Figure 7.4: Effect of Silk damping on the baryon mass profile for the NID mode at decoupling. In the absence of the damping term (solid curve), the peak is located at $r = r_s = 144.5$ Mpc. The dashed curve takes into account the effect of Silk damping.

7.2.3 NIV mode

Unlike the other isocurvature modes, the NIV mode, like the AD mode, shows no relative entropy perturbation in the density field at some initial time. All the density perturbations are zero initially. The main difference with the AD mode is in the velocity field where the neutrino velocity divergence starts perturbed, being compensated by the photon-baryon velocity. The initial perturbations are given by:

$$\theta_{c,i} = 0, \quad \theta_{b,i} = \theta_{\gamma,i} = -\frac{R_\nu}{R_\gamma} \theta_{\nu,i}. \quad (7.22)$$

The NIV mode excites the $\sin kr_s$ harmonic, so that we can set $A_C = 0$ in equation (7.9). As for the NID mode, the gravitational driving term contribution remains irrelevant at all times as all the densities start unperturbed and the perturbations only grow in the matter dominated era. The time evolution of the photon and baryon density contrasts for the NIV mode are given by

$$\delta_\gamma^{NIV} = \frac{4}{3} \delta_b^{NIV} = \frac{R_\nu}{R_\gamma} \sqrt{3} \sin kr_s(\tau) \times e^{-k^2/k_D^2}. \quad (7.23)$$

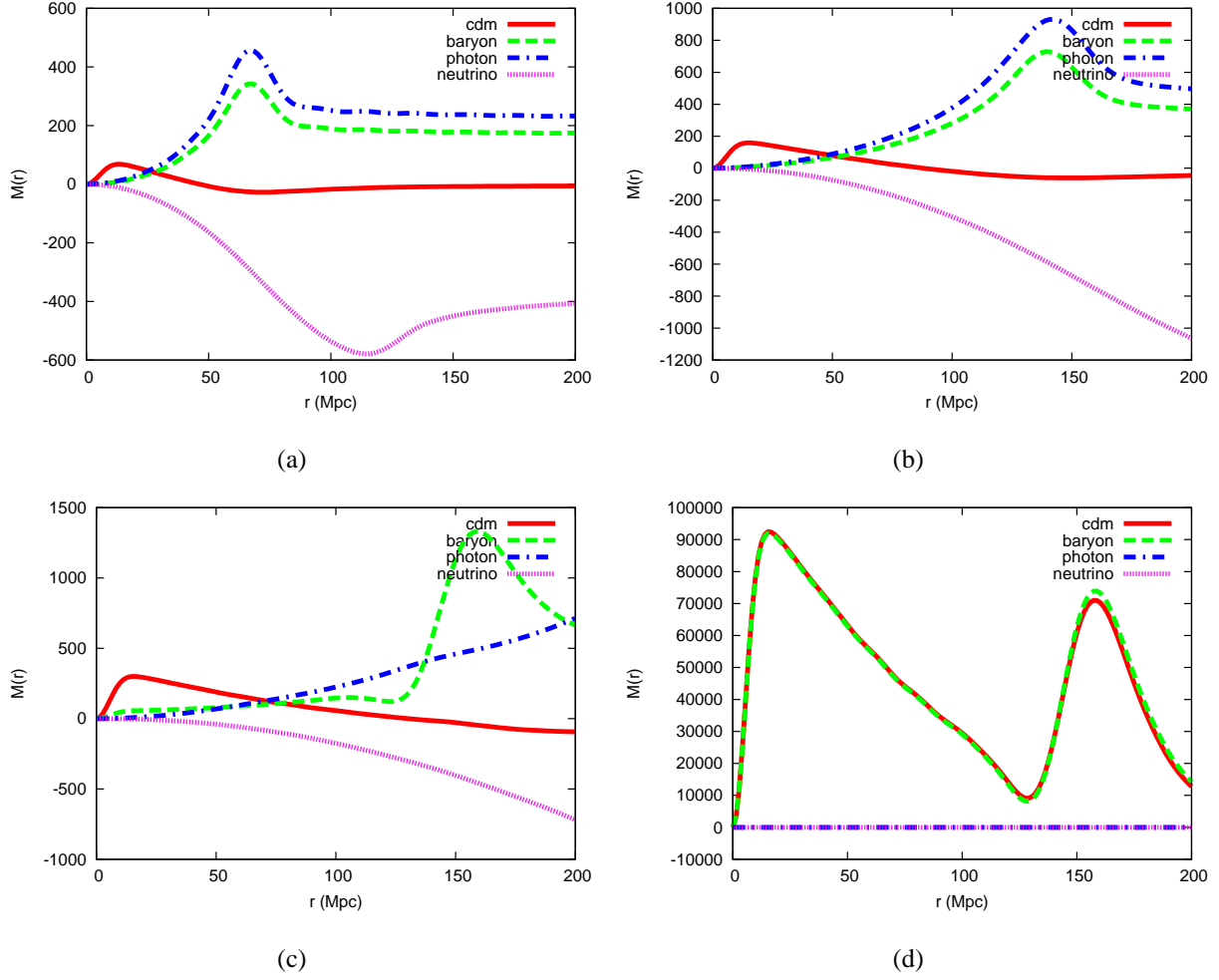


Figure 7.5: Mass profile snapshots for the NIV mode at different redshifts. The red, green, blue and purple curves respectively represent the CDM, the baryon, the photon and the neutrino mass profiles. **(a)** Well before decoupling ($z = 3000$), **(b)** At decoupling ($z = 1080$), **(c)** when baryons stall ($z = 500$) and **(d)** At late times ($z = 0$). The units of the mass profile are arbitrary but correctly scaled between panels.

The non-zero initial velocity divergence of baryons and photons pushes the baryons and photons from the origin, thus creating an overdensity at approximately the scale of the sound horizon and a plateau at larger scales, in the baryon and photon mass profiles. The redshift evolution of the baryon overdensity for the NIV mode is shown in Figure 7.5. This is similar to the NID case, except that the baryon mass profile remains positive at all times due to the initial plateau.

The BAO peak ends at a different location as the sine harmonic convolves differently with Silk damping, compared to the cosine harmonic.

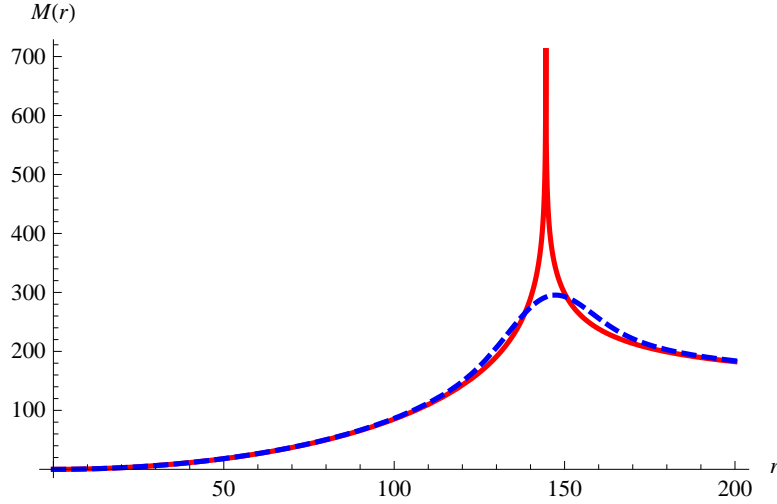


Figure 7.6: Effect of Silk damping on the baryon mass profile for the NIV mode at decoupling. In the absence of the damping term (solid curve), the peak is located at $r = r_s = 144.5$ Mpc. The dashed curve takes into account Silk damping.

In the absence of Silk damping correction, the undamped baryon mass profile for the NIV mode is given by

$$M_b(r) \propto -\frac{r}{4} \ln \frac{(r - r_s)^2}{(r + r_s)^2} \propto \begin{cases} r^2 & \text{for } r \ll r_s, \\ r^{-2} & \text{for } r \gg r_s. \end{cases} \quad (7.24)$$

The derivation of equation (7.24) is similar to the AD and NID cases. The undamped NIV mass profile grows quadratically with r for $r < r_s$ and peaks at $r = r_s$ as for the AD case. However, the shift in the BAO peak location due to Silk damping is not as significant as it is for the AD and the NID cases for the simple fact that the undamped mass profile does not abruptly fall off to zero as in the previous cases but decreases as r^{-2} before reaching a plateau of height proportional to r_s . This is due to the fact that the non-zero initial velocity of photons carries baryons beyond the sound horizon, compared to if they started from rest. Figure 7.6 shows the effect of Silk damping on the undamped baryon mass profile. In contrast to the AD and NID cases, the BAO peak is

slightly shifted to higher r . The other effects of the damping (lowering and rounding of the BAO peak) remain the same as for the AD and the NID modes.

7.2.4 CI & BI modes

The CI and the BI modes have been well studied in the literature [25, 35, 76]. The CI and BI modes are similar in that the perturbation starts in the CDM density contrast and the baryon density contrast respectively while the other species are initially unperturbed. This can be written at some initial time as

$$\delta_{c,i} = 1, \quad \delta_{b,i} = \delta_{\gamma,i} = \delta_{\nu,i} = 0, \quad (7.25)$$

for the CI mode, and as

$$\delta_{c,i} = 0, \quad \delta_{b,i} = 1, \quad \delta_{\gamma,i} = \delta_{\nu,i} = 0, \quad (7.26)$$

for the BI mode. The CI and BI initial conditions dictate that $A_S = -\frac{8}{\sqrt{3}k}\Omega_{c,0}$ for the CI mode and $A_S = -\frac{8}{\sqrt{3}k}\Omega_{b,0}$ for the BI mode, while $A_c = 0$ in both cases, thus exciting the $\sin kr_s$ harmonic [85, 29]. The constants $\Omega_{c,0}$ and $\Omega_{b,0}$ are respectively the CDM and the baryon densities today. The driving term is negligible in the radiation domination era as the photon and the neutrino densities are initially unperturbed but becomes important in the matter domination era as the matter perturbation sources the gravitational potential [73].

The time evolution of the photon and baryon density contrasts for the CI and BI modes is given by [73]

$$\begin{aligned} \delta_{\gamma}^{CI} = & -\frac{8}{3}\Omega_{c,0}\frac{\sqrt{3}}{k}\sin kr_s(\tau) \times e^{-k^2/k_D^2} \\ & + \frac{\sqrt{3}}{k} \int_0^{\tau} (1 + R(\tau'))^{1/2} \sin [kr_s(\tau) - kr_s(\tau')] \\ & \times F^{CI}(\tau') d\tau', \end{aligned} \quad (7.27)$$

$$\begin{aligned} \delta_b^{CI} = & -2\Omega_{c,0}\frac{\sqrt{3}}{k}\sin kr_s(\tau) \\ & + \frac{3}{4}\frac{\sqrt{3}}{k} \int_0^{\tau} (1 + R(\tau'))^{1/2} \sin [kr_s(\tau) - kr_s(\tau')] \\ & \times F^{CI}(\tau') d\tau' \times e^{-k^2/k_D^2}, \end{aligned} \quad (7.28)$$

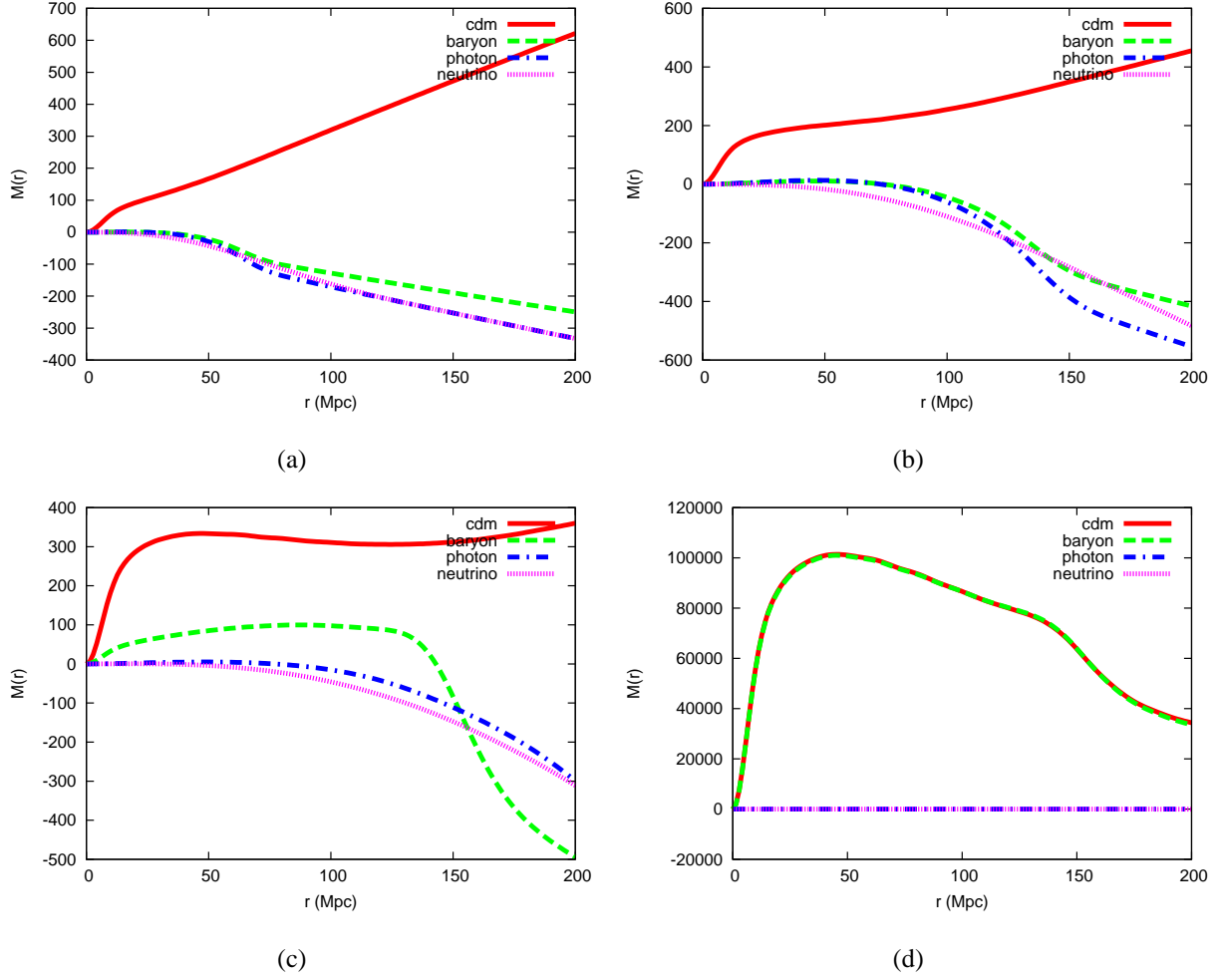


Figure 7.7: Mass profile snapshots for the CI mode at different redshifts. The red, green, blue and purple curves respectively represent the CDM, the baryon, the photon and the neutrino mass profiles. **(a)** Well before decoupling ($z = 3000$), **(b)** At decoupling ($z = 1080$), **(c)** when baryons stall ($z = 500$) and **(d)** At late times ($z = 0$). The units of the mass profile are arbitrary but correctly scaled between panels.

for the CI mode, and by

$$\begin{aligned} \delta_{\gamma}^{BI} = & -\frac{8}{3}\Omega_{b,0}\frac{\sqrt{3}}{k}\sin kr_s(\tau) \\ & + \frac{\sqrt{3}}{k}\int_0^{\tau}(1+R(\tau'))^{1/2}\sin[kr_s(\tau)-kr_s(\tau')] \\ & \times F^{BI}(\tau')d\tau' \times e^{-k^2/k_D^2}, \end{aligned} \quad (7.29)$$

$$\begin{aligned} \delta_b^{BI} = & 1 - 2\Omega_{b,0}\frac{\sqrt{3}}{k}\sin kr_s(\tau) \\ & + \frac{3\sqrt{3}}{4k}\int_0^{\tau}(1+R(\tau'))^{1/2}\sin[kr_s(\tau)-kr_s(\tau')] \\ & \times F^{BI}(\tau')d\tau' \times e^{-k^2/k_D^2}, \end{aligned} \quad (7.30)$$

for the BI mode. Equations (7.27-7.30) are exact but require a perfect knowledge of the gravitational driving term. This makes the derivation of simple explicit analytic expressions for the CI and BI modes harder as compared to the AD, NID and NIV modes. Therefore, we do not discuss the effect of Silk damping on the BAO peak for these modes. However, one thing to notice is the k^{-1} dependence of the baryon density contrast for the CI and BI modes that washes out perturbations on small scales while amplifying them on large scales. This redistribution of power results in a flattening of the baryon mass profile for these modes. On small scales, the k^{-1} and the Silk damping factors have similar effects on the BAO peak as they both suppress perturbations on these scales. However there are two main differences. Firstly, Silk damping does not act on large scales while the k^{-1} factor amplifies large scale perturbations. Secondly, Silk damping only becomes significant around recombination while the k^{-1} factor redistributes the power at all times, hindering the development of a well defined BAO peak but producing a knee instead.

For the CI mode, an overdensity in the CDM component tends to affect, through gravitational attraction, the baryon density component by gathering baryons into an overdensity but the photon pressure opposes this process until decoupling.

One should note that an initial overdensity in the photon component would easily affect the baryon component than an initial overdensity in the CDM component, the reason being the high photon pressure at earlier times. Therefore, the perturbation takes longer to imprint ripples onto the homogeneous sea of baryons. Figure 7.7 represents the time evolution of the baryon mass profile for the CI mode. Prior to decoupling, the CDM overdensity grows but does not significantly affect the baryon component. After decoupling a baryon overdensity develops through gravitational interaction with the CDM but fails to display a well defined BAO peak.

For the BI mode, an initial overdensity in the baryon component affects the CDM component through gravitational attraction, but does not significantly grow due to the photon pressure at earlier times that tends to widen and even wash out the baryon overdensity as can be seen in Figure 7.8. With a similar process as for the CI mode, the overdensity becomes a knee at late times.

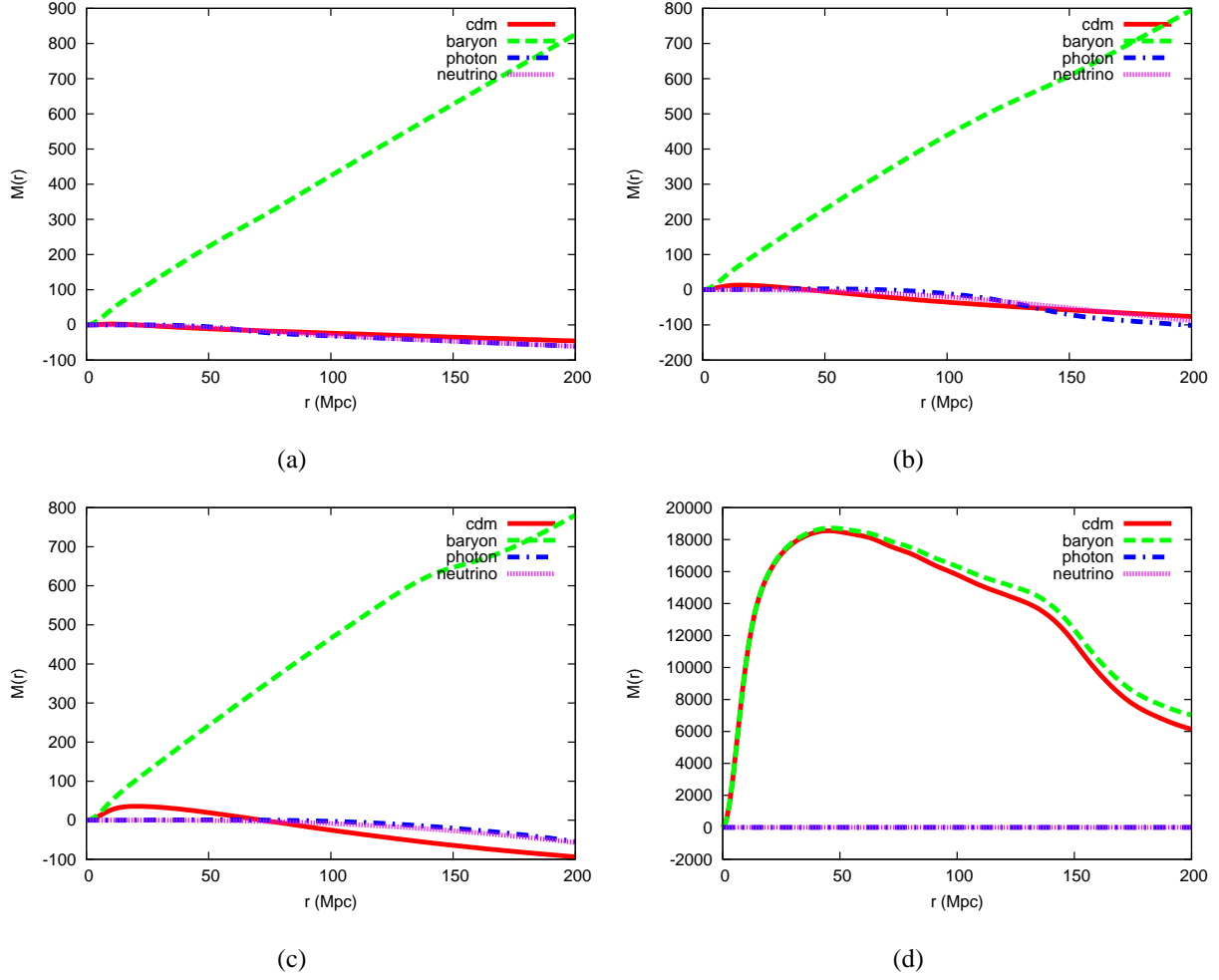


Figure 7.8: Mass profile snapshots for the BI mode at different redshifts. The red, green, blue and purple curves respectively represent the CDM, the baryon, the photon and the neutrino mass profiles. **(a)** Well before decoupling ($z = 3000$), **(b)** At decoupling ($z = 1080$), **(c)** when baryons stall ($z = 500$) and **(d)** At late times ($z = 0$). The units of the mass profile are arbitrary but correctly scaled between panels.

Although the Silk damping still affects the CI and BI modes, its effect is not as significant as in previous cases (for a discussion of this see [76, 143]). We recall that the Silk damping tends to suppress power on small scales while these modes are already significantly reduced by the k^{-1} factor for the CI and BI modes. In addition, the fact that the CI and BI modes fail to dis-

play a well defined BAO peak makes less noticeable the effect of Silk damping on the BAO peak.

7.2.4.1 Time evolution of the BAO peak position

We saw in previous subsections that in the absence of Silk damping, the BAO peak location for all the modes would coincide at all times as the acoustic wave in the photon-baryon fluid propagates at the same sound speed irrespective of the initial conditions. Here we consider the effect of Silk damping on the evolution of the BAO peak location for different modes.

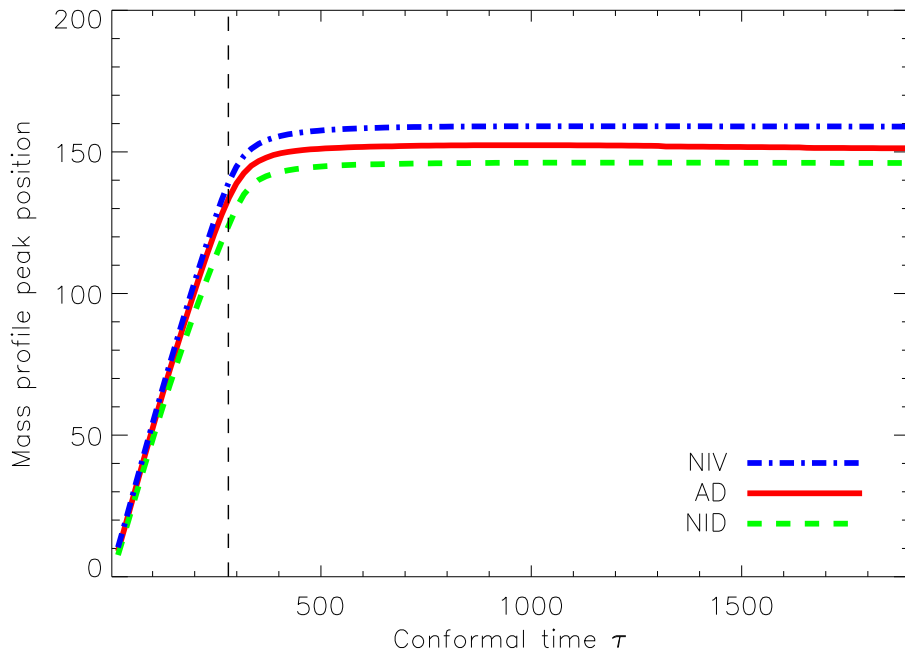


Figure 7.9: Time-evolution of the baryon mass profile peak location (see Figures 7.2, 7.3 and 7.5) for the AD, NID and NIV modes. These curves were obtained numerically from the evolution of the mass profile curves. The dashed vertical line indicates the epoch of recombination.

Figure 7.9 shows the time evolution of the BAO peak position for the AD, NID and NIV modes. We do not include the CI and BI modes as they fail to display a defined BAO peak. At early times, the BAO peak positions for the AD, NID and NIV coincide as the Silk damping

factor equals one at early times. With time, the damping scale k_D^{-1} increases as the photon-baryon coupling weakens, the three modes depart from each other and the separation increases up to decoupling. At decoupling, $k_D \approx 0.15h \text{ Mpc}^{-1}$, leading to a separation of about 15 Mpc between the NID and NIV BAO peak positions. After decoupling, though the BAO peak position still increases until $z \approx 500$ due to the bulk velocity, the separation between the modes remains constant until today.

7.3 Impact of isocurvature modes on dark energy constraints

The aim of this section is to quantify the potential impact of isocurvature modes on dark energy studies based on current- & next-generation datasets.

7.3.1 Statistical Formalism

A convenient way of quantifying the accuracy with which cosmological parameters can be measured from a given dataset is the Fisher matrix formalism (see [171] for a review). If \mathbf{x} is our observable (the CMB or the galaxy power spectrum in our case), it can be modeled as a N -dimensional random variable whose probability distribution $l(\mathbf{x}; \boldsymbol{\theta})$ depends on a vector of cosmological parameters $\boldsymbol{\theta}$ that we wish to estimate. $l(\mathbf{x}; \boldsymbol{\theta})$ is also known as the likelihood of observing a set of data given a model characterized by $\boldsymbol{\theta}$.

In this study, we consider a spatially flat cosmological model described by the following parameters: the baryon density ω_b , the CDM density ω_c , the density of the dark energy component Ω_X , the optical depth τ , the spectral index n_s and the scalar amplitude A_s . We allow for dark energy models that vary with time and parametrize the dark energy equation of state as $w(a) = w_0 + (1 - a)w_a$ [34, 112] where $a = 1/(1 + z)$ and w_0 and w_a are included in the parameter space. For the isocurvature modes, we adopt the parametrization implemented in [121], where the AD, CI, NID, NIV modes and their cross-correlations are described by 10 parameters, z_{ij} , measuring the fractional contributions of the various correlations (auto and cross) to the total

power spectrum. We do not consider the BI mode as it has the same spectra as the CI mode. In terms of these fractional parameters, the total isocurvature fraction f_{ISO} is given by

$$f_{\text{ISO}} = \frac{z_{\text{ISO}}}{z_{\text{ISO}} + z_{\langle \text{AD}, \text{AD} \rangle}}, \quad (7.31)$$

where $z_{\text{ISO}} = \sqrt{1 - z_{\langle \text{AD}, \text{AD} \rangle}^2}$ is the total isocurvature contribution.

Defining the auto- and cross-correlated primordial power spectra as follows

$$P_{ij}(k) = A_{ij} k^{n_{ij}-1}, \quad (7.32)$$

the spectral indices of the cross correlated modes are given by $n_{ij} = \frac{n_{ii} + n_{jj}}{2}$ with their amplitudes $A_{ij} \propto z_{ij}$. The constraint $\sum_{i,j=1}^{10} z_{ij}^2 = 1$ requires that the isocurvature parameters z_{ij} exist on the surface of a 9 dimensional sphere of unit radius. For further details on how this parametrization relates to others in the literature, see [13]. The parameter A_s rescales the unit power CMB temperature spectrum to its usual amplitude as, $C_\ell = 13000 \mu\text{K}^2 A_s \hat{C}_\ell$, where \hat{C}_ℓ is the fiducial CMB temperature spectrum with unit power.

| Fiducial model | | | | | | | |
|----------------|------------|------------|--------|-------|-------|-------|-------|
| ω_b | ω_c | Ω_X | τ | n_s | A_s | w_0 | w_a |
| 0.02205 | 0.12495 | 0.7 | 0.1 | 1.0 | 15.7 | -1.0 | 0.0 |

Table 7.1: Values for the parameters of the fiducial cosmological model.

The Fisher matrix is defined by

$$F_{ij} = - \left\langle \frac{\partial^2 \ln l(\mathbf{x}; \boldsymbol{\theta})}{\partial \theta_i \partial \theta_j} \right\rangle. \quad (7.33)$$

The Cramer-Rao inequality shows that F_{ii}^{-1} is the smallest variance possible for an unbiased estimator of the parameter θ_i . In this case, F^{-1} is the most optimistic covariance matrix of the dataset [171] and the forecasted error bar for θ_i is

$$\sigma_i = \sqrt{(F^{-1})_{ii}}. \quad (7.34)$$

The fiducial model θ around which the Fisher matrix is computed is chosen to be a Λ CDM universe with adiabatic initial conditions. The cosmological parameter values for the fiducial model are given in table 7.1. We use the CMB forecasts from the PLANCK experiment in addition to each LSS data set and compute the full Fisher matrix $F_{ij} = F_{ij}^{CMB} + F_{ij}^{LSS}$ for the cosmological parameter set.

7.3.1.1 Large Scale Structure (LSS) surveys

Over the next decade, the increase in the number and quality of data from LSS surveys will drive fundamental improvements in precision cosmology. As these galaxy surveys cover increasingly larger volumes, they will provide unprecedented probes of scales at which significant cosmological information is available.

The potential of the BAO method as a powerful source of cosmological information has been recognized and measuring the BAO peak at multiple redshifts is now regarded as the primary science of major future LSS surveys. We consider two such BAO experiments, one of which is the Baryon Oscillation Spectroscopy Survey (BOSS). BOSS will measure the redshifts of 1.5 million luminous red galaxies (LRGs) over a quarter of the sky to a depth of $z = 0.7$. In addition to being a redshift survey, BOSS will be the first attempt to resolve the BAO peak in the high- z density field ($2 < z < 3$), as allowed by mapping absorption lines from neutral hydrogen, in the spectra of 160 000 distant quasars [149].

The Advanced Dark Energy Physics Telescope (ADEPT) is the second proposed future LSS survey that we consider. It is a space-based experiment aiming at mapping galaxies in the redshift range $1 < z < 2$ and over 28,600 sq. deg. of the sky [151].

The BAO peak manifests as oscillations in the matter power spectrum with the size of the sound horizon determining the frequency of these oscillations. However, the matter power spectrum is a rich statistic whose features at different scales provide specific cosmological information. The

matter power spectrum is defined as

$$P(k, z) = D(z)^2 P_{\text{prim}}(k) T^2(k) \quad (7.35)$$

where $D(z)$ is the growth rate of structure, $P_{\text{prim}}(k)$ is the primordial power spectrum and $T(k)$ is the transfer function. The first source of information is the baryon acoustic oscillations, with their wavenumber $k = 2\pi/r_s$ being set by the size of the sound horizon at decoupling r_s . Since this characteristic scale is calibrated by the CMB, measuring the wavelength of these oscillations both in the radial and tangential directions delivers $D_A(z)$ and $H(z)$ respectively. The overall shape of the matter power spectrum is a second source of information. Any features which deviate from a power law, such as the turnover, provides an additional characteristic scale which is required by the Alcock-Paczynski test to be isotropic [4]. Lastly, the overall time evolution of the amplitude informs us about $D(z)$, the growth rate of structure.

In reality we measure the power spectrum as mapped by galaxies which are biased tracers of the underlying matter distribution. We can write the galaxy power spectrum as $P_g(k, z) = b(k, z)^2 P(k, z)$ where $b(z, k)$ represents this bias resulting from the effects of galaxy formation and evolution. On the scales of the BAO, the bias can be regarded as smooth, i.e., $b(z, k) = b(z)$. Any scale dependence that is not taken into account is not likely to lead to oscillations in Fourier space [156]. Furthermore, the galaxy power spectrum measured in redshift space is distorted relative to the power spectrum in real space as a result of galaxy peculiar velocities. Because galaxies moving towards an overdensity along the line of sight appear further away than equidistant galaxies moving in the tangential direction, structures appear "squeezed" in redshift space, with the amount of the distortion determined by the growth rate. On large scales this has been shown to give rise to an angle-dependent distortion which leads to a multiplicative change in the power that is a function of angle, i.e., $P_{g,\beta} = (1 + \beta(z)\mu^2)^2 P_g(k, z)$ where μ is the angle with respect to the line of sight and $\beta = f/b$ where

$$f = \frac{\partial \ln D(a)}{\partial \ln a} \simeq \Omega_m(z)^{0.6}. \quad (7.36)$$

In this article, we wish to examine the best case scenario in which all information available in the galaxy power spectrum is used. We assume perfect knowledge of a redshift-dependent bias

and include the information introduced by the redshift distortions. This amounts to the inclusion of a non-zero $\beta(z)$.

Assuming the likelihood function of the band powers of the galaxy power spectrum to be Gaussian, the Fisher matrix can be approximated as [171, 155]:

$$\begin{aligned}
F_{ij}^{LSS} &= \int_{\vec{k}_{min}}^{\vec{k}_{max}} \frac{\partial \ln P(\vec{k})}{\partial p_i} \frac{\partial \ln P(\vec{k})}{\partial p_j} V_{eff}(\vec{k}) \frac{d\vec{k}}{2(2\pi)^3} \\
&= \int_{-1}^1 \int_{k_{min}}^{k_{max}} \frac{\partial \ln P(k, \mu)}{\partial p_i} \frac{\partial \ln P(k, \mu)}{\partial p_j} \\
&\quad \times V_{eff}(k, \mu) \frac{2\pi k^2 dk d\mu}{2(2\pi)^3}
\end{aligned} \tag{7.37}$$

where,

$$V_{eff}(k, \mu) = \left[\frac{\bar{n}_g P_g(k) (1 + \beta \mu^2)^2}{\bar{n}_g P_g(k) (1 + \beta \mu^2)^2 + 1} \right]^2 V, \tag{7.38}$$

\vec{r} is the unit vector along the line of sight and \vec{k} is the wave vector with norm $k = |\vec{k}|$. Here V is the survey volume contained in a given redshift bin and $\bar{n}_g(\vec{r})$ is the selection function of the survey, dictating the a priori expectation value for the comoving number density of galaxies. We take this to be a constant. V_{eff} is the effective volume of the survey and takes into account the impact of the shot noise from undersampled regions [49]. The derivatives of the power spectrum with respect to the cosmological parameters in table 7.1 and to the isocurvature parameters are respectively shown in Figures A.1 and A.2 in the appendix.

BOSS and ADEPT survey parameters are summarized in Table 7.2. Note that the value k_{min} is always taken as the lowest possible and has been shown to have a negligible effect on the error forecasts. The smallest scale included, given by k_{max} , in the analysis does however impact on the results [23]. Following [155] we adopt conservative values for k_{max} by requiring $\sigma(R) = 0.5$ at a corresponding $R = \frac{\pi}{2k}$ where $\sigma(R)$ is defined similarly to the normalization $\sigma_8 \equiv \sigma(R = 8h^{-1}\text{Mpc})$, but for a general scale R .

| BOSS | | | | | |
|--------------------|------------------|------------------------------|------|--------------------|---------------------|
| n_g | z | $k_{max}/h \text{ Mpc}^{-1}$ | b | $V/ \text{ Gpc}^3$ | Area/deg^2 |
| 3×10^{-4} | $z < 0.35$ | 0.12 | 2.13 | 0.74 | 10,000 |
| | $0.35 < z < 0.6$ | 0.15 | 1.25 | 2.83 | 10,000 |
| | $2 < z < 3$ | 0.53 | 3.3 | 2.48 | 6000 |
| ADEPT | | | | | |
| n_g | z | $k_{max}h \text{ Mpc}^{-1}$ | b | $V/ \text{ Gpc}^3$ | Area/deg^2 |
| 3×10^{-4} | $1 < z < 1.25$ | 0.20 | 2.97 | 17.7 | 28600 |
| | $1.25 < z < 1.5$ | 0.23 | 3.21 | 19.7 | 28600 |
| | $1.5 < z < 1.75$ | 0.26 | 3.44 | 21.0 | 28600 |
| | $1.75 < z < 2$ | 0.30 | 3.67 | 21.7 | 28600 |

Table 7.2: Table summarizing the survey parameters for BOSS and ADEPT, for different redshift bins (centered at the middle of the redshift bin).

7.3.1.2 Cosmic microwave background (CMB) surveys

The CMB data primarily provides information about the initial conditions of our Universe in this analysis. Non-adiabatic initial conditions lead to very distinct features in the temperature anisotropies, with isocurvature modes producing acoustic oscillations that are out of phase with the adiabatic mode and hence a set of peaks in the temperature anisotropy power spectrum that are slightly shifted. Furthermore, CMB polarization provides a robust signature of isocurvature perturbations [31]. The latest WMAP data has confirmed that the initial perturbations were mainly of adiabatic type [88] with the possible presence of a subdominant isocurvature contribution, which could be detected in future high-precision experiments such as PLANCK [94]. The higher resolution of PLANCK over WMAP will allow for the measurement of the CMB power spectrum on much smaller scales and the use of 9 observational bands will improve the modeling of astrophysical foregrounds.

We follow the analysis in [3] and model the PLANCK dataset as CMB temperature and polarization maps of 80% of the sky measured in the two frequency bands where the CMB signal dominates. The details of the experiment are given in Table 7.3. The maps are taken to have no foreground contribution, assuming that the other frequency channels can be used to remove them. The remaining 20% of the sky is assumed to be contaminated by galactic emission. We exclude polarization data at $\ell < 30$ in order to weaken the forecasted constraint on the optical depth to $\sigma(\tau) = 0.01$ in agreement with studies that include foreground modeling [170].

| ℓ_{max}^T | ℓ_{max}^P | ν / GHz | θ_b | $\Delta_T (\mu\text{K})$ | $\Delta_P (\mu\text{K})$ |
|----------------|----------------|--------------------|------------|--------------------------|--------------------------|
| 2000 | 2500 | 143 | 8' | 5.2 | 10.8 |
| | | 217 | 5.5' | 11.7 | 24.3 |

Table 7.3: Summary of the experiment specifications for PLANCK.

For the CMB, the Fisher matrix is computed using

$$F_{ij}^{CMB} = \sum_{\ell} \sum_{X,Y} \frac{\partial C_{X\ell}}{\partial p_i} [\text{Cov}_{\ell}]_{XY}^{-1} \frac{\partial C_{X\ell}}{\partial p_j}, \quad (7.39)$$

where $C_{X\ell}$ is the power in the ℓ^{th} multipole for $X = T, E, B$ given by

$$[\text{Cov}_{\ell}]_{XX} = \frac{2}{(2\ell + 1)f_{sky}} (C_{X\ell} + N_{\ell}) \quad (7.40)$$

where N_{ℓ} , the noise level, depends on the data type. The noise is specified by the experiment.

Because there is a strict geometric degeneracy between Ω_{Λ} , w_0 and w_a , finding the derivatives of the dark energy equation of state (EOS) parameters while keeping Ω_{Λ} fixed artificially breaks this degeneracy. To this end, we follow [3] and start with computing the Fisher matrix for the CMB with the following parameters: $\mathbf{p} = \{\omega_b, \omega_c, \theta_s, \tau, n_s, A_s\}$ where θ_s is the angular size of the sound horizon. This can be written as

$$\theta_s = \pi \frac{r_s(z_{cmb})}{r(z_{cmb})}, \quad (7.41)$$

where $r_s(z_{cmb})$ is the sound horizon given in equation 7.1 and $r(z_{cmb})$ is the comoving distance to the last scattering surface

$$r(z) = c \int_0^z \frac{1}{H(z')} dz'. \quad (7.42)$$

To compute the derivative $\partial C_\ell / \partial \theta_s$, we use the transformation

$$\frac{\partial C_\ell}{\partial \theta_s} \simeq \frac{\Delta C_\ell}{\Delta \Omega_\Lambda} \frac{\Delta \Omega_\Lambda}{\Delta \theta_s}, \quad (7.43)$$

and when evaluating $\frac{\Delta \theta_s}{\Delta \Omega_\Lambda}$, ω_c and ω_b must stay fixed by compensating with h through

$$h^2 = \frac{\omega_b + \omega_c}{1 - \Omega_\Lambda}. \quad (7.44)$$

The resulting Fisher matrix F is then transformed back into \tilde{F} , corresponding to the parameters $\mathbf{p}' = \{\omega_b, \omega_c, \Omega_\Lambda, \tau, n_s, A_s, w_0, w_a\}$ using

$$\tilde{F}_{ij} = \sum_{n,m} \frac{\partial p_m}{\partial p_i} F_{mn} \frac{\partial p_n}{\partial p_j}. \quad (7.45)$$

The non-trivial expressions needed for the Jacobian are derivatives of θ_s with respect to w_0 , w_a , Ω_Λ , ω_c and ω_b .

For the calculations of the derivatives of the power spectrum with respect to the isocurvature amplitudes in equation 7.33, we have adopted the treatment in [30] where the pure isocurvature modes are normalized to have the same power in their CMB temperature spectra as the adiabatic model. This normalization is applied to both the CMB and LSS spectra.

7.3.2 The impact of isocurvature modes on dark energy

In this section we consider the impact of admitting isocurvature initial conditions on the constraints on the dark energy parameters. We follow [3] and choose not to focus on the constraints on Ω_X , given that our intuitive estimates rooted in particle physics are drastically disparate from current measurements of the dark energy density.

We compute the potential errors on w_0 and w_a for different subsets of adiabatic and isocurvature initial conditions while marginalizing over all other cosmological parameters. The results for both the BOSS and ADEPT experiments are summarized in table 7.4. We find a systematic degradation of the viable constraints on dark energy as more degrees of freedom are added. In order to quantify the constraining power of the data, we compute the Dark Energy Task Force

| Experiment | BOSS | | ADEPT | |
|------------------------------------|-------|-------|-------|-------|
| Parameters | w_0 | w_a | w_0 | w_a |
| Adiabatic mode | 0.020 | 0.061 | 0.017 | 0.041 |
| Adiabatic + 1 ISO mode | | | | |
| AD+CI+ \langle AD,CI \rangle | 0.027 | 0.070 | 0.018 | 0.042 |
| AD+NID+ \langle AD,NID \rangle | 0.022 | 0.063 | 0.018 | 0.041 |
| AD+NIV+ \langle AD,NIV \rangle | 0.021 | 0.064 | 0.017 | 0.041 |
| Adiabatic + 2 ISO modes | | | | |
| AD+CI+NID+corr | 0.031 | 0.074 | 0.020 | 0.042 |
| AD+CI+NIV+corr | 0.032 | 0.077 | 0.020 | 0.042 |
| AD+NIV+NID+corr | 0.028 | 0.075 | 0.018 | 0.043 |
| Adiabatic + all ISO modes | 0.045 | 0.097 | 0.022 | 0.044 |

Table 7.4: Table summarizing the constraints on (w_0, w_a) for adiabatic and admixtures of uncorrelated adiabatic and isocurvature modes, marginalizing over all other parameters, for the BOSS and ADEPT experiments. The fiducial model assumes adiabaticity.

(DETF) Figure of merit (FoM), which is defined as the reciprocal of the area in the $w_0 - w_a$ plane, enclosing the 95% confidence limit (CL) region [3]. We are concerned with the change in the FoM when isocurvature modes are introduced relative to the case of pure adiabaticity. The BOSS FoM is found to decrease by 60% from pure adiabaticity to the case in which all isocurvature modes are admitted in addition to the adiabatic, while the ADEPT FoM degrades by 40%. We note that the results quoted here are slightly different to those quoted in the previous chapter and in [185]. This is due to the different normalization method used in [185], which follows [121], whereas we follow [30]. However, the different normalization methods used have little impact on the results reported here, which display a similar trend to [185] but with a slightly larger relative degradation of parameter errors when isocurvature modes are included.

The results suggest that no single mode in particular and its correlation are responsible for the change in the allowable (w_0, w_a) region, but rather a mixture of all extra degrees of freedom. In order to determine the combination of parameters that is responsible for this degradation, we diagonalize the full 17x17 Fisher matrix corresponding to the PLANCK and LSS datasets separately and find the eigenvector with the smallest eigenvalue, corresponding to the direction that is least constrained by the data. Considering the PLANCK data alone and discarding the degeneracy in the $w_0 - w_a$ direction which is the main degenerate direction, four parameters, namely τ , A_s , $A_{\langle \text{AD}, \text{NIV} \rangle}$ and $A_{\langle \text{AD}, \text{NID} \rangle}$ define the most degenerate direction involving isocurvature modes, with the impact of the scalar amplitude being compensated for by a combination of the cross-correlated modes and the optical depth. The degenerate direction in the LSS data (using BOSS as an example) is more complicated and involves a combination of isocurvature parameters and dark energy parameters, namely Ω_X , A_s , w_0 , w_a , $A_{\langle \text{AD}, \text{CI} \rangle}$, $A_{\langle \text{AD}, \text{NIV} \rangle}$, $A_{\langle \text{AD}, \text{NID} \rangle}$ and $A_{\langle \text{CI}, \text{NIV} \rangle}$. Figure 7.10 shows how the perturbations in the different parameters contribute to the total change in the CMB power spectrum and the matter power spectrum.

The total derivative (shown in red) lies within the noise limits of the respective experiments, making the net change undetectable by the data.

Clearly the dark energy model is degenerate with the particular combination of isocurvature

modes in the BAO data. The implication is that the constraints on dark energy are at risk of being substantially biased if adiabaticity is incorrectly assumed. To emphasize this point, Figure 7.11 compares the correlation function, defined by

$$\xi(r) = \int_0^\infty k^2 P(k) \frac{\sin kr}{kr} dk, \quad (7.46)$$

where $P(k)$ is the matter power spectrum, that would be measured today for our fiducial Λ CDM model assuming pure adiabaticity, to a cosmological model assuming dynamical dark energy, described by $w_0 = -0.94$ and $w_a = -0.137$, and an admixture of initial conditions, 84% of which is isocurvature in nature. The correlation function is degenerate in all three redshift bins of the BOSS experiment. Note that this degeneracy is completely broken by the CMB data. We now wish to quantify this bias.

| Experiment | BOSS | | ADEPT | |
|---------------------------|------------|------------|---------------|--------------|
| Parameters | w_0 | w_a | w_0 | w_a |
| Adiabatic + 1 ISO mode | | | | |
| AD+CI+⟨AD,CI⟩ | 0.052 (3) | -0.096 (2) | 0.023 (1) | -0.019 (0.5) |
| AD+NID+⟨AD,NID⟩ | -0.031 (2) | 0.054 (1) | -0.019 (1) | -0.030 (1) |
| AD+NIV+⟨AD,NIV⟩ | -0.030 (2) | 0.076 (1) | -0.0055 (0.3) | -0.013 (0.3) |
| Adiabatic + 2 ISO modes | | | | |
| AD+CI+NID+corr | -0.065 (3) | 0.11 (2) | -0.026 (2) | -0.025 (1) |
| AD+CI+NIV+corr | -0.071 (4) | 0.12 (2) | -0.014 (1) | 0.021 (0.5) |
| AD+NIV+NID+corr | -0.049 (2) | 0.11 (2) | 0.016 (1) | -0.024 (1) |
| Adiabatic + all ISO modes | -0.15 (8) | 0.3 (4) | 0.054 (3) | -0.04 (1) |

Table 7.5: Table summarizing the biases on (w_0, w_a) that could arise from the incorrect assumption of adiabatic initial conditions, given a universe with an admixture of uncorrelated adiabatic and isocurvature modes for the BOSS and ADEPT experiments. The quantities in brackets are the biases, quoted in number of 1σ error bars corresponding to the case when pure adiabaticity is assumed.

For a Gaussian-distributed likelihood function, it can be shown that the linear bias in a set of parameters that we wish to constrain, $\delta\theta_i$, due to erroneous values of a set of fixed parameters, $\delta\phi_j$, is [169]

$$\delta\theta_i = - [F^{\theta\theta}]_{im}^{-1} F_{mj}^{\theta\phi} \delta\phi_j \quad (7.47)$$

where $F^{\theta\theta}$ is the Fisher sub-matrix for the parameters we wish to constrain and $F^{\theta\phi}$ is a Fisher sub-matrix constructed from the product of the derivatives of the power spectrum with respect to the parameters being constrained and those which are being fixed. In our case j labels the isocurvature mode amplitudes, incorrectly fixed to zero, m labels the eight cosmological parameters that are biased, and i labels the subset of two dark energy parameters whose bias is of interest to us. In order to set $\delta\phi_j$, we diagonalize the combined PLANCK and large-scale structure (LSS) Fisher matrix and select the eigenvector, \mathbf{e}_i with the smallest eigenvalue λ_i . This corresponds to the direction in parameter space which is least constrained by the data. We then take $\delta\phi_j = \sqrt{\frac{M}{\lambda_j}} \mathbf{e}_j$, where M depends on the total number of cosmological and isocurvature parameters.

We first consider the case of an admixture of the adiabatic mode and the CDM isocurvature mode. For this case we find the biases in the dark energy parameters to be $\delta w_0 = 0.052$ and $\delta w_a = -0.096$ for the BOSS experiment. Comparing the mean biases to the 1σ constraints obtained when pure adiabaticity is assumed, we find that neglecting this isocurvature contribution leads to a 3σ and 2σ error in the dark energy parameter estimates for w_0 and w_a respectively, when compared to the error forecasts assuming adiabaticity. If we repeat the calculation for the more advanced experiment ADEPT, we find $\delta w_0 = 0.023$ and $\delta w_a = -0.019$, equivalent to 1σ and 0.5σ errors in the dark energy parameters respectively when compared to the adiabatic constraints. From this result, it appears that ADEPT shows a lower risk of making false claims.

Although no theoretical models for generating the neutrino isocurvature models have thus far been proposed, we would like to conduct a comprehensive exploration of the impact of the initial conditions on the BAO constraints and therefore admit all possible isocurvature degrees of

freedom. Table 7.5 summarizes the biases for different admixtures of adiabatic and subsets of isocurvature modes. The results are consistent with the degenerate directions in parameter space identified earlier. For example, the admittance of the CI and NID isocurvature modes and their cross correlations has the potential to cause a bias in the dark energy parameters by as much as 4σ , in the case of BOSS.

For the case of an admixture of adiabatic and all isocurvature modes and their cross correlations, we find that the biases are $\delta w_0 = -0.15$ and $\delta w_a = 0.3$ for the BOSS experiment. This means that if the initial conditions of our universe are comprised of a sub-dominant contribution from all isocurvature modes (within the 1σ constraints from the PLANCK and BOSS experiments), the assumption of adiabaticity could lead to an incorrect 8σ detection of non- Λ dark energy model or a 4σ false claim of dynamics. Alternatively, Λ could be found to be consistent with the data when in fact $w(z) \neq -1$. The potential bias incurred by the adiabatic assumption in the case of the ADEPT experiment has a mean of $\delta w_0 = 0.054$ (equivalent to 3σ) while the measurement of w_a could be inaccurate at the level of only 1σ .

7.3.2.1 Constraints on isocurvature modes from the LSS data

We now consider the impact of the large scale structure information on isocurvature constraints. Although allowing for isocurvature modes degrades the dark energy constraints relative to the pure adiabatic case, this analysis has revealed a powerful positive. We find that the volume of the 9-dimensional isocurvature Fisher ellipse is roughly $2 - 4 \times 10^9$ smaller than that from PLANCK alone, showing that using the CMB and LSS data together provides exceptionally good constraints on the early universe relative to the CMB alone. The forecasted errors on the isocurvature parameters based on the CMB data alone and in conjunction with the LSS experiments are compared in tables 7.6, 7.7 and 7.8 respectively for single, double and fully correlated isocurvature modes. We find that the error bars on the isocurvature parameters decrease by 30% to as much as 100% for certain modes when the LSS data (either BOSS or ADEPT) is added to the PLANCK data. Assuming an adiabatic fiducial model, the measurement of the BAO in the first

redshift bin of the BOSS experiment and the CMB by PLANCK will reduce the allowed isocurvature fraction from 5.6% for the CMB data only to 3.6%, and to 3.1% and 2.7% when adding the information from LSS in the second and the third redshift bins.

| Adiabatic + 1 ISO mode | | |
|--|---------------|----------------|
| | PLANCK + BOSS | PLANCK + ADEPT |
| $\langle \text{AD}, \text{AD} \rangle$ | 0.29 (7) | 0.30 (3) |
| $\langle \text{CI}, \text{CI} \rangle$ | 0.013 (11) | 0.0093 (7) |
| $\langle \text{AD}, \text{CI} \rangle$ | 0.84 (97) | 0.92 (96) |
| $\langle \text{AD}, \text{AD} \rangle$ | 0.25 (18) | 0.24 (23) |
| $\langle \text{NID}, \text{NID} \rangle$ | 0.0053 (11) | 0.0053 (14) |
| $\langle \text{AD}, \text{NID} \rangle$ | 0.019 (29) | 0.019 (38) |
| $\langle \text{AD}, \text{AD} \rangle$ | 0.23 (26) | 0.22 (28) |
| $\langle \text{NIV}, \text{NIV} \rangle$ | 0.0093 (6) | 0.013 (9) |
| $\langle \text{AD}, \text{NIV} \rangle$ | 0.92 (97) | 0.84 (97) |

Table 7.6: Forecasted uncertainties on isocurvature parameters for different cases for the PLANCK and LSS data (BOSS and ADEPT) for single isocurvature modes. The percentage improvement in 1σ errors when the LSS data is added to the PLANCK data is shown in brackets.

The reason for this stems from the fact that the considered degenerate direction in parameter space for the CMB data ($\langle \text{AD}, \text{NIV} \rangle$, $\langle \text{AD}, \text{NID} \rangle$, A_s , τ_e) differs from the degenerate direction of the LSS data ($\langle \text{AD}, \text{NIV} \rangle$, $\langle \text{AD}, \text{NID} \rangle$, Ω_X , w_0 , w_a , A_s).

Figure 7.12 illustrates the different directions by showing the 1σ error ellipses for the main isocurvature contributions and w_0 . The two degenerate directions are almost orthogonal. Here, the inner straight lines represent the marginalised error bars obtained by combining both PLANCK and BOSS experiments in the case of a cosmological constant. Clearly the ability of LSS data to measure isocurvature modes is related to the information provided by the BAO about dark energy. In Figure 7.13, we compare the 1σ error ellipses for $(w_0, \langle \text{AD}, \text{NIV} \rangle)$ and $(w_0, \langle \text{AD}, \text{NID} \rangle)$

| Adiabatic + 2 ISO modes | | |
|--|---------------|----------------|
| | PLANCK + BOSS | PLANCK + ADEPT |
| $\langle \text{AD}, \text{AD} \rangle$ | 0.35 (21) | 0.33 (27) |
| $\langle \text{CI}, \text{CI} \rangle$ | 0.019 (10) | 0.019 (11) |
| $\langle \text{NID}, \text{NID} \rangle$ | 0.0071 (3) | 0.0070 (5) |
| $\langle \text{AD}, \text{CI} \rangle$ | 0.029 (97) | 0.029 (97) |
| $\langle \text{AD}, \text{NID} \rangle$ | 0.021 (32) | 0.020 (36) |
| $\langle \text{CI}, \text{NID} \rangle$ | 0.014 (5) | 0.014 (6) |
| $\langle \text{AD}, \text{AD} \rangle$ | 0.46 (21) | 0.35 (22) |
| $\langle \text{CI}, \text{CI} \rangle$ | 0.016 (15) | 0.016 (15) |
| $\langle \text{NIV}, \text{NIV} \rangle$ | 0.0093 (5) | 0.0091 (7) |
| $\langle \text{AD}, \text{CI} \rangle$ | 0.035 (96) | 0.033 (97) |
| $\langle \text{AD}, \text{NIV} \rangle$ | 0.029 (97) | 0.036 (97) |
| $\langle \text{CI}, \text{NIV} \rangle$ | 0.016 (12) | 0.015 (15) |
| $\langle \text{AD}, \text{AD} \rangle$ | 0.27 (40) | 0.25 (45) |
| $\langle \text{NID}, \text{NID} \rangle$ | 0.0082 (4) | 0.0070 (5) |
| $\langle \text{NIV}, \text{NIV} \rangle$ | 0.018 (6) | 0.017 (10) |
| $\langle \text{AD}, \text{NID} \rangle$ | 0.028 (12) | 0.020 (36) |
| $\langle \text{AD}, \text{NIV} \rangle$ | 0.037 (96) | 0.041 (96) |
| $\langle \text{NID}, \text{NIV} \rangle$ | 0.016 (6) | 0.015 (12) |

Table 7.7: Forecasted uncertainties on isocurvature parameters for different cases for the PLANCK and LSS data (BOSS and ADEPT) for double isocurvature modes. The percentage improvement in 1σ errors when the LSS data is added to the PLANCK data is shown in brackets.

that are obtained when we include the CMB dataset and add the data from the BOSS redshift bins in succession. We see that the BAO data primarily serves to reduce the phase space for w_0 with the largest improvement in the w_0 constraint coming from the second redshift bin. As the redshift increases, the contribution from dark energy diminishes until matter comes to

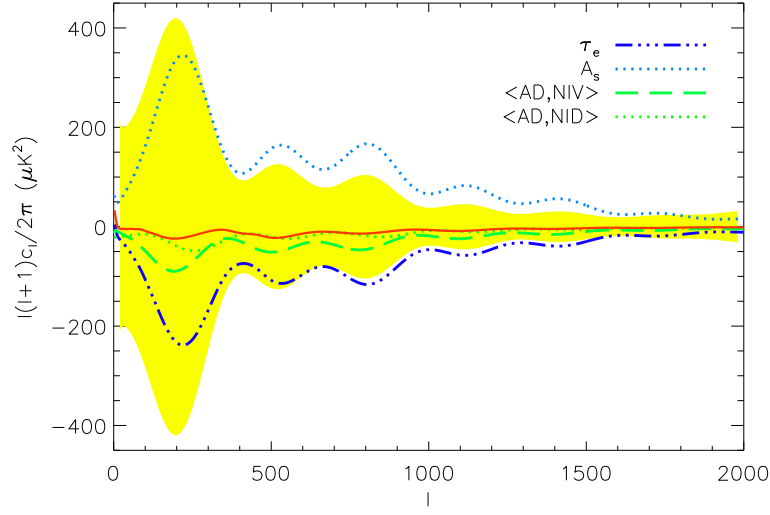
| Adiabatic + all ISO modes | | |
|--|---------------|----------------|
| | PLANCK + BOSS | PLANCK + ADEPT |
| $\langle \text{AD}, \text{AD} \rangle$ | 0.47 (21) | 0.41 (30) |
| $\langle \text{CI}, \text{CI} \rangle$ | 0.044 (23) | 0.057 (39) |
| $\langle \text{NID}, \text{NID} \rangle$ | 0.016 (16) | 0.019 (24) |
| $\langle \text{NIV}, \text{NIV} \rangle$ | 0.047 (24) | 0.047 (40) |
| $\langle \text{AD}, \text{CI} \rangle$ | 0.042 (96) | 0.042 (96) |
| $\langle \text{AD}, \text{NID} \rangle$ | 0.069 (35) | 0.038 (64) |
| $\langle \text{AD}, \text{NIV} \rangle$ | 0.072 (94) | 0.048 (96) |
| $\langle \text{CI}, \text{NID} \rangle$ | 0.057 (14) | 0.066 (20) |
| $\langle \text{CI}, \text{NIV} \rangle$ | 0.027 (34) | 0.04 (39) |
| $\langle \text{NID}, \text{NIV} \rangle$ | 0.045 (8) | 0.045 (9) |

Table 7.8: Forecasted uncertainties on isocurvature parameters for different cases for the PLANCK and LSS data (BOSS and ADEPT) for fully correlated isocurvature case. The percentage improvement in 1σ errors when the LSS data is added to the PLANCK data is shown in brackets.

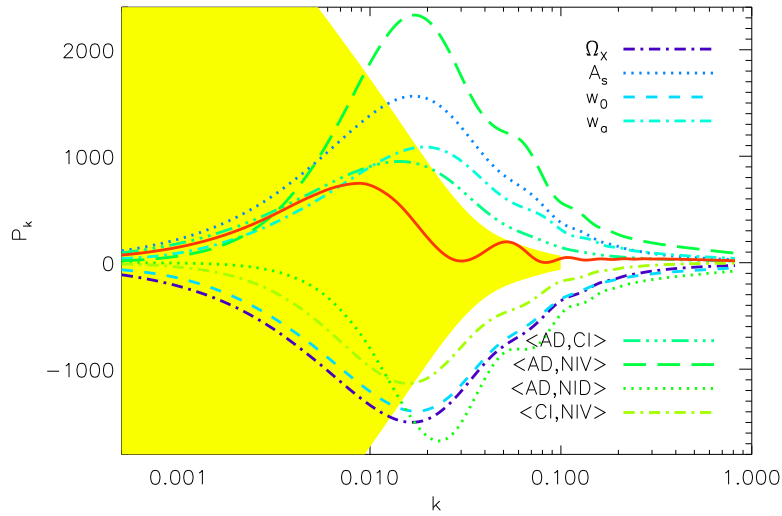
dominate, at which time the impact of dark energy on the observables is small. For this reason, the intermediate redshift bin for BOSS centered at $z = 0.6$ provides the best constraints on w_0 . In Figure 7.14 we compare the sum of the most dominant isocurvature contributions $z_{\langle \text{AD}, \text{NIV} \rangle} P^{\langle \text{AD}, \text{NIV} \rangle} + z_{\langle \text{AD}, \text{NID} \rangle} P^{\langle \text{AD}, \text{NID} \rangle}$ to the power spectrum at the different redshift bins of the BOSS experiment to their respective error bars. The area between the solid (signal) and dotted (error) curves indicates the amount of information provided by each bin. Clearly, this combination of isocurvature parameters is best constrained from the measurement of the galaxy power spectrum at $z = 0.6$ for this particular experiment. Furthermore, the differing shapes of the signal curves suggests that complementary information is available at different redshifts. Hence, the measurement of the BAO scale at different redshifts between decoupling and today helps to constrain the isocurvature modes.

We note that in this study we have assumed exact knowledge of the galaxy bias which could be a source of further degeneracy with the isocurvature parameters.

As an aside, we note that information about the initial conditions from LSS data does not stem from differences in the growth rates for different modes. Figure 7.15 shows the growth function of the perturbations on intermediate (top) and on large scales (bottom). It is clear that on very large scales, the isocurvature modes grow more slowly than the adiabatic modes. This is expected as perturbations which are isocurvature in nature only grow when they enter the horizon while adiabatic fluctuations grow at all times. However on the scales probed by the BAO signal, the isocurvature modes and adiabatic modes grow at the same rate.



(a) C_ℓ^{TT} spectrum



(b) $P(k)$ at $z = 0.35$

Figure 7.10: Main contributions to the degenerate direction with the highest isocurvature fraction **(a)** in the CMB data from PLANCK alone, **(b)** in the matter power spectrum using the BOSS dataset alone. The red solid line is the total derivative in the considered degenerate direction, which cancels to within the limits allowed by PLANCK and BOSS error bars (yellow region). For the matter power spectrum, we only plot the yellow region up to $k_{max} = 0.1h \text{ Mpc}^{-1}$ in this redshift bin.

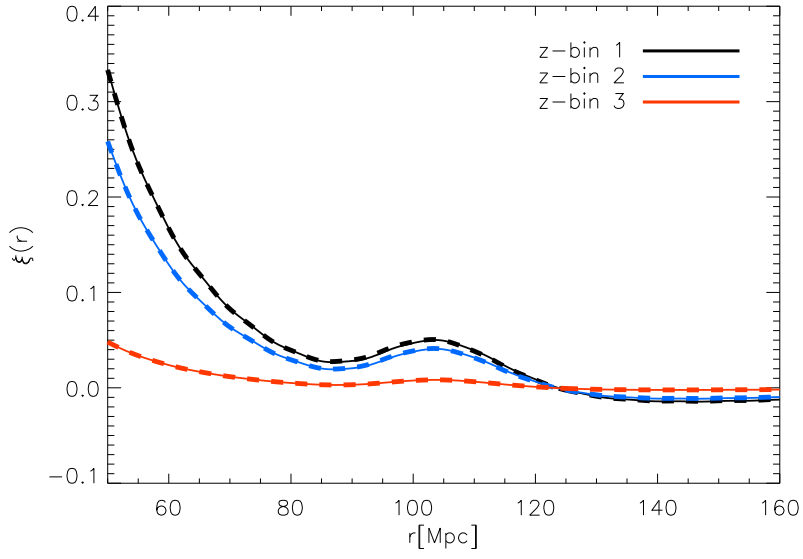
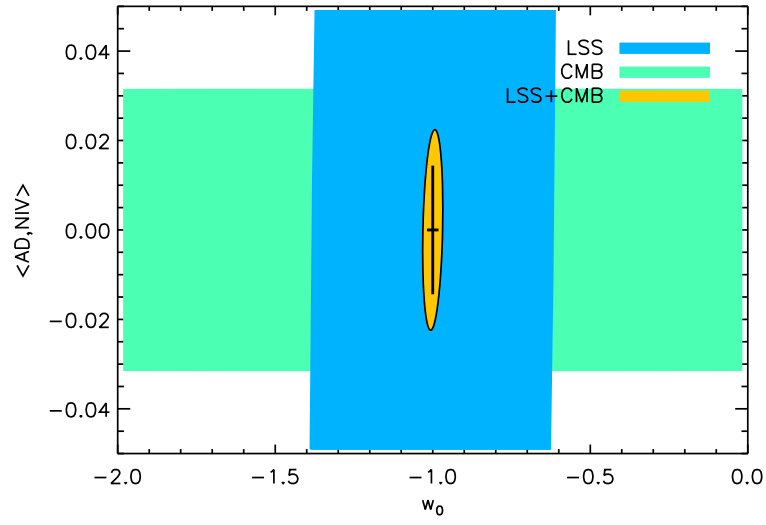
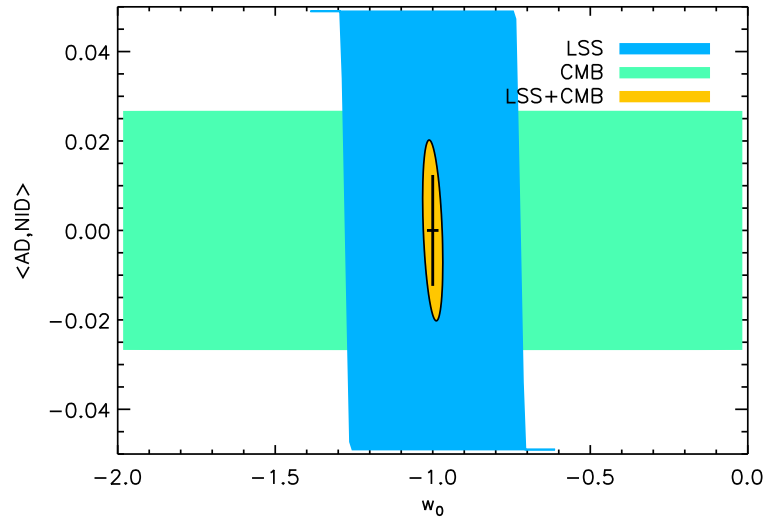


Figure 7.11: The galaxy correlation functions for the BOSS survey for different redshift bins. Solid lines represent the purely adiabatic Λ CDM fiducial model while dashed lines represent a mixed model with $f_{\text{ISO}} = 84\%$, $w_0 = -0.940$ & $w_a = -0.137$. $z = 0.35$ (black), $z = 0.6$ (blue) and $z = 3$ (red).



(a)



(b)

Figure 7.12: Effect of combining the CMB and LSS datasets on the 1σ error ellipses for isocurvature contributions and w_0 . We have only represented the isocurvature modes ($\langle\text{AD},\text{NIV}\rangle$ and $\langle\text{AD},\text{NID}\rangle$) that determine the main degenerate direction with the largest isocurvature fraction. Inner straight lines represent the error bars obtained using both CMB and LSS experiments, but assuming a cosmological constant.

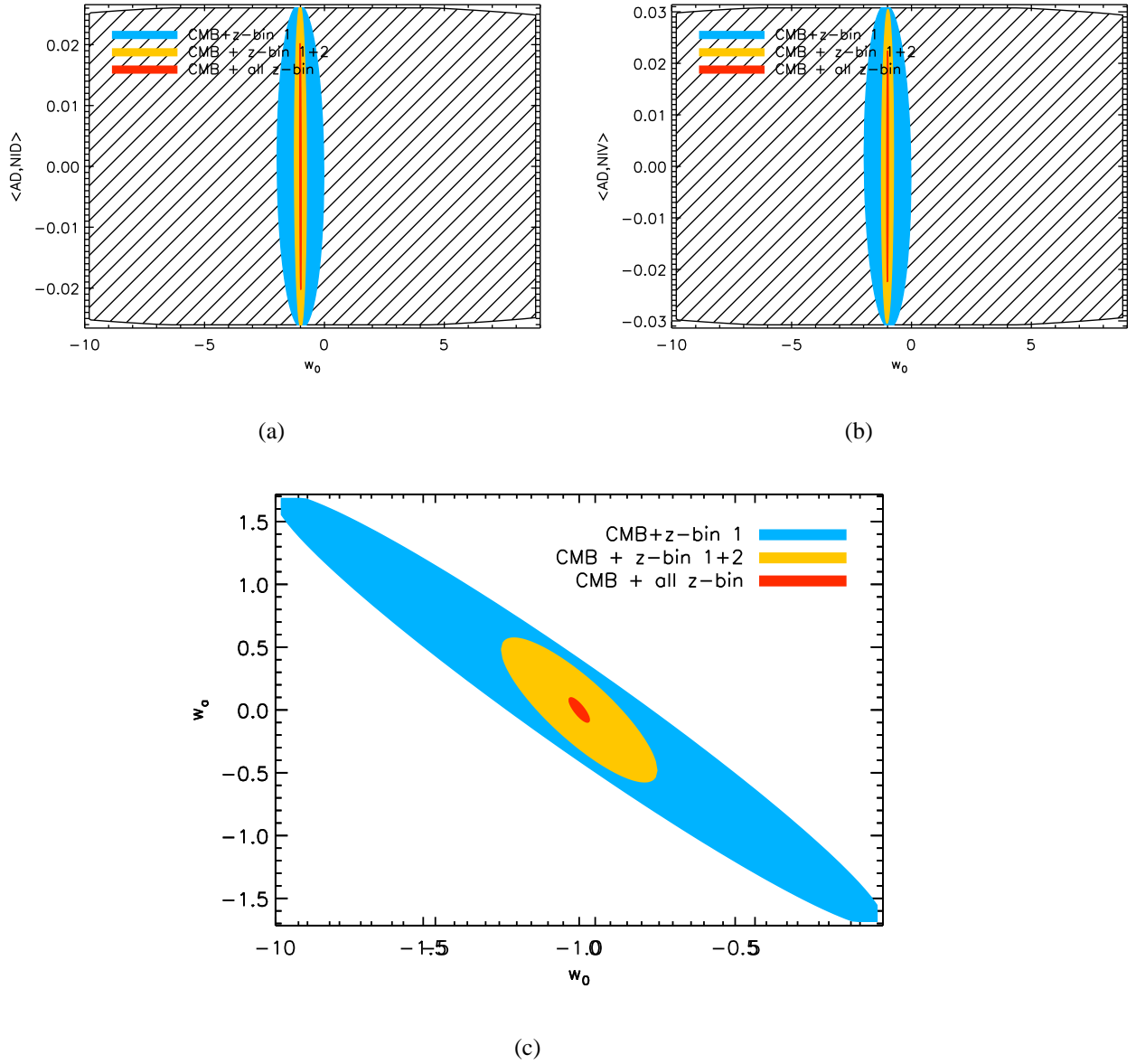


Figure 7.13: Effect of adding different redshift bin datasets on the 1σ error ellipses for $(w_0, \langle AD, NIV \rangle)$, $(w_0, \langle AD, NID \rangle)$ and (w_0, w_a) . Hatched regions on panels (a) and (b) represent the 1σ error ellipse for the CMB experiment alone.

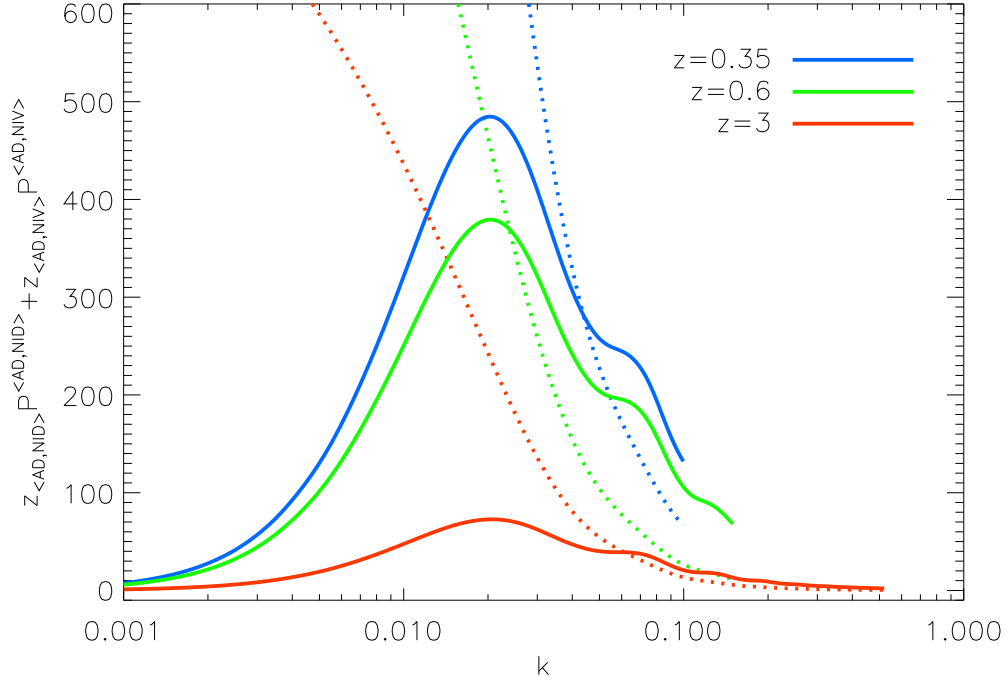


Figure 7.14: Sum of the most dominant isocurvature contributions $z_{\langle\text{AD},\text{NIV}\rangle}P^{\langle\text{AD},\text{NIV}\rangle} + z_{\langle\text{AD},\text{NID}\rangle}P^{\langle\text{AD},\text{NID}\rangle}$ to the power spectrum for different redshift bins of the BOSS experiment. The blue, green and red solid curves represents respectively the isocurvature contribution at redshift $z = 0.35$, $z = 0.6$ and $z = 3$. The dotted lines represent the BOSS error bars for different redshift bins.

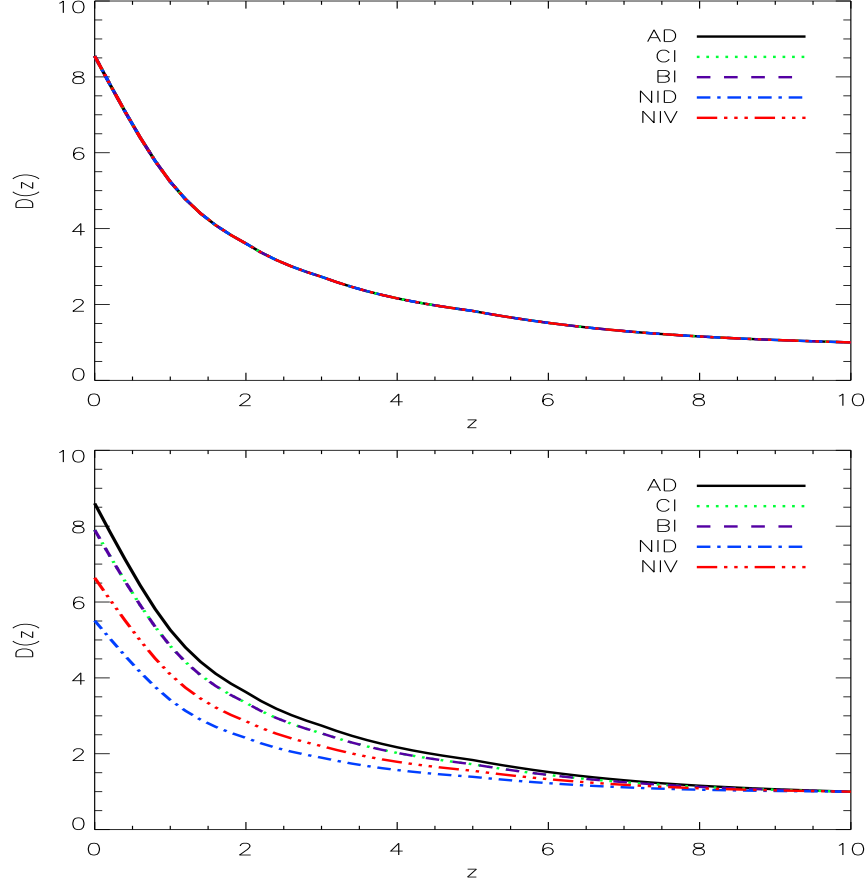


Figure 7.15: Growth function as a function of redshift for all modes. **Top:** on intermediate scales ($k = 0.01$). **Bottom:** on large scales $k = 0.0053$. On small and intermediate scales, the growth function is the same for all regular modes, while the AD mode grows faster than the isocurvature modes on large scales. We have normalized the growth to unity at $z = 10$.

7.4 Conclusions

The first detection of the BAO peak in the galaxy correlation function measured by SDSS opened the door to using the clustering of galaxies on scales of ~ 150 Mpc as a cosmic yardstick. By comparing the size of the overdensity of baryons at the epoch of recombination predicted from theory and calibrated by the CMB, with its size as it appears in the large-scale structure of galaxies today, we can study the expansion history of the universe. However, in order to succeed in making a precise measurement of the signal we will need the huge volumes probed only by the most recent generation of redshift surveys. With such precision we hope to reveal the nature of dark energy and probe its time evolution if it exists.

With claims of constraints on dark energy from BAO experiments to the level of a few percent, it becomes important to check the assumptions made in the post-observational analysis. In this chapter, we have revisited the assumption of pure adiabatic initial conditions and considered the impact of allowing isocurvature-adiabatic admixtures on the BAO peak and the implications for dark energy studies. We have shown that a combination of differences in the baryon growth profile that arises due to the presence of isocurvature modes and Silk damping change both the shape and position of the BAO peak. Non-adiabatic initial conditions leave the sound speed unchanged but instead alter the development of the acoustic waves in the baryon-photon fluid prior to decoupling which modifies the scale on which the sound waves imprint on the baryon distribution.

The degeneracy between the impact of mixed initial conditions and the effect of a dynamical dark energy model on the BAO peak weakens the potential constraints on the dark energy parameters forecasted for a combined PLANCK and LSS dataset. We found that the admission of more general initial conditions which include isocurvature modes and their cross-correlations increases the 95% confidence region in (w_0, w_a) space by 50% in the case of the BOSS experiment and thus the assumption of adiabaticity can lead to the under-estimation of the errors on the dark energy parameters. Furthermore, if we assume purely adiabatic initial conditions, we run the risk of attributing a shift in the peak away from the prediction of ~ 150 Mpc for a Λ CDM universe

to a non- Λ dark energy model. We have shown that this can lead to a bias in the estimates of the dark energy parameters, leading to a several σ incorrect confirmation of Λ or detection of non- Λ .

On a positive note, the change in the BAO peak in isocurvature models indicates that there is useful information in the galaxy correlation function on the nature of the primordial perturbations even when simultaneously measuring dark energy equation of state parameters. We find that the use of the LSS data in addition to the CMB data substantially improves our ability to measure the contributions of different modes to the initial conditions. The matter power spectrum constrains the dark energy parameters and in so doing breaks the degeneracy in the isocurvature-dark energy parameter space. Furthermore, even when assuming $w = -1$, the degenerate parameter combinations in the CMB and LSS are different.

CHAPTER 8

Conclusion

Although much progress has been made in understanding the universe, many conceptual and technical problems remain unsolved. Among them, the nature of the fluctuations which generated anisotropies in the cosmic microwave background and the large scale structure remains not well understood. Testing the nature of the primordial perturbations requires a good understanding of the different possibilities of the initial conditions. In this thesis we have investigated the signatures of isocurvature initial conditions in the CMB through the temperature anisotropies, and in the large scale structure distribution through the BAO.

In the second chapter, we briefly presented the standard cosmological model and its underlying linear cosmological perturbation theory that provides a basis for understanding the formation of the LSS of the universe and anisotropies in the CMB, and supplemented it with a discussion on the initial conditions of the primordial fluctuations.

In the third chapter, we reviewed the evolution of the perturbations in adiabatic models with a focus on the evolution of the dark matter and the photons in the tight-coupling regime as these,

with the gravitational potential, are the only quantities that are involved in the computation of the CMB spectrum through the line of sight integral. We derived semi-analytic solution of the evolution of the photon density contrast and velocity divergence prior to decoupling in synchronous gauge and found that the AD mode excites neither the pure cosine or sine harmonic, but instead, a cosine-like harmonic through the forcing term.

In the fourth chapter, we recalled how fluctuations on the last scattering surface translate into the CMB power spectrum through the line of sight integral as observed today and introduced the Hu approximation for the photon transfer function for the computation of the CMB spectrum. In this approximation, one only needs the photon density contrast and the velocity divergence evaluated at decoupling, and the evolution of the gravitational potential to compute the CMB power spectrum to about 10% accuracy. We also reviewed the effect of the cosmological parameters on the CMB temperature power spectrum in the AD mode. We focused on the impact of the baryon density and matter density on the CMB power spectrum. An increase in the baryon density enhances the odd peaks and lowers the even peaks, while an increase in the matter density lowers all acoustic peaks.

In the fifth chapter, we have investigated the features of the isocurvature CMB power spectra and studied the impact of different cosmological parameters on the CMB power spectrum. We first derived about 10% accurate semi-analytic expressions governing the evolution of the photons and baryons prior to decoupling in isocurvature models and found that non-adiabatic initial conditions leave the sound speed unchanged but instead excite different harmonics. We also found that the amplitude of the oscillations in the CI and BI modes is inversely proportional to the wavenumber, causing the suppression of the perturbations on small scales. We then studied the impact of cosmological parameters on the CMB angular power spectrum in isocurvature models and found that the effects of the physical baryon and matter densities in isocurvature models differ the most from adiabatic models. An increase in the baryon density lowers the acoustic peaks in the CI, NID and NIV, and enhances them in the BI mode. These baryon density dependence for isocurvature modes differs from the AD mode, where the odd peaks are enhanced

while even peaks are lowered, due to a gravitational potential shift. The lowering of acoustic peaks is stronger in the NIV mode and weaker in the CI. In addition, the effect of an increase in the matter density on the height of the CMB temperature acoustic peaks in the BI, NID and NIV modes is similar to the AD case where all the acoustic peaks are lowered besides being shifted to lower ℓ 's. In the CI mode, an increase in the matter density enhances the acoustic peaks as the photon density contrast is directly proportional to the matter density. We used the semi-analytic treatment to explain these cosmological parameter effects on the CMB power spectrum. The remaining four parameters have approximately the same effect in isocurvature modes as in the adiabatic mode. In this work we have only considered the primary anisotropies of the CMB. Further work will include contributions due to the polarization and to the lensing of the CMB in isocurvature models, especially since ongoing and upcoming CMB experiments such as the PLANCK mission, SPTPol and ACTPol will provide useful polarization data.

In the sixth chapter, we have explored the distortion of the standard ruler distance and the degradation of dark energy constraints due to the inclusion of isocurvature perturbations. We showed that small fractions of isocurvature perturbations correlated with the dominant adiabatic mode are a significant primordial systematic for BAO surveys which must be accounted for in future surveys. Isocurvature modes distort the standard ruler distance by broadening and shifting the peak in the galaxy correlation function. While a single isocurvature mode does not significantly degrade dark energy constraints, the general case with multiple isocurvature modes leads to biases that exceed 7σ on average in the dark energy parameters even for isocurvature amplitudes undetectable by PLANCK. Accounting for all isocurvature modes corrects for this bias but degrades the dark energy figure of merit by at least 50% in the case of the BOSS experiment. However the BAO data in turn provides significantly stronger constraints on the nature of the primordial perturbations. Future large galaxy surveys will thus be powerful probes of exotic physics in the early Universe in addition to helping pin down the nature of dark energy.

In the seventh chapter, we explored in detail the effect of allowing for small amplitude admixtures of general isocurvature perturbations in addition to the dominant adiabatic mode. We found

that non-adiabatic initial conditions leave the sound speed unchanged but instead excite different harmonics. These harmonics couple differently to Silk damping, altering the form and evolution of acoustic waves in the baryon-photon fluid prior to decoupling. This modifies not only the scale on which the sound waves imprint onto the baryon distribution, which is used as the standard ruler in BAO surveys, but also the shape, width and height of the BAO peak. We discussed these effects in detail and showed how more general initial conditions impact our interpretation of cosmological data in dark energy studies. We found that the inclusion of these additional isocurvature modes leads to an increase in the Dark Energy Task Force Figure of merit by 140% and 60% for the BOSS and ADEPT experiments respectively when considered in conjunction with PLANCK data. We also showed that the incorrect assumption of adiabaticity has the potential to bias our estimates of the dark energy parameters by 3σ (1σ) for a single correlated isocurvature mode, and up to 8σ (3σ) for three correlated isocurvature modes in the case of the BOSS (ADEPT) experiment. We found that the use of the large scale structure data in conjunction with CMB data improves our ability to measure the contributions of different modes to the initial conditions by as much as 100% for certain modes in the fully correlated case. For this work, we only made forecasts for a combination of CMB experiments and BAO surveys. Further work should widen the range of LSS probes to include the 21 cm emissions from intergalactic medium at high redshift and the Lyman alpha forest. In addition, as more galaxies are measured, the matter power spectrum surveys will give considerably more data than we presently have and will allow more stringent constraints on isocurvature modes.

On a positive note, the current rapid expansion of the dataset from both LSS surveys and CMB experiments will allow a unique probe into the physics of the early universe. For example, data from the PLANCK satellite will provide us the CMB angular power spectra for temperature and polarization in a wide range of multipoles. With the advent of the precision era in cosmology, scientists should be able to pin down the nature of the primordial perturbation in a near future.

Bibliography

- [1] B. Abroe *et al.*, *Astrophys. J.* **605**, 607 (2004)
- [2] P. Aguiar and P. Crawford, *arXiv:astro-ph/0110412* (2001)
- [3] A. Albrecht *et al.*, *arXiv:astro-ph/0609591* (2006)
- [4] C. Alcock and B. Paczynski, *Nature* **281**, 358 (1979)
- [5] R. A. Alpher *et al.*, *Phys. Rev.* **73**, 803 (1948)
- [6] R.A. Alpher and R. Herman, *Nature* **162**, 774 (1948)
- [7] L. Amendola *et al.*, *Mon. Not. Roy. Astron. Soc.* **357**, 429 (2005)
- [8] P. Astier *et al.*, *Astron. Astrophys.* **447**, 31 (2005)
- [9] N.A. Bahcall *et al.*, *Science* **284**, 1481 (1999)
- [10] N. Bartolo *et al.*, *Phys. Rev. D* **64**, 123504 (2001)
- [11] S. Bashinsky and E. Bertschinger, *Phys. Rev. D* **65**, 123008 (2002)
- [12] B.A. Bassett and R. Hlozek, *arXiv:0910.5224* (2010)

- [13] R. Bean *et al.*, Phys. Rev. D **74**, 063503 (2006)
- [14] M. Beltran *et al.*, Phys. Rev. D **72**, 103515 (2005)
- [15] M. Beltran *et al.*, Phys. Rev. D **72**, 103515 (2005)
- [16] C.L. Bennett *et al.*, Astrophys. J. Suppl. S. , (2011)
- [17] M. Bertran *et al.*, Phys. Rev. D **70**, 103530 (2004)
- [18] M. Beltran *et al.* , Phys. Rev. D **71**, 063532 (2005)
- [19] E. Bertschinger, NASA STI/Recon Technical Report N **96**, 22249 (1995)
- [20] E. Bertschinger, Ann. Rev. Astron. Astrophys. **36**, 599 (1998)
- [21] E. Bertschinger, Proceedings of Cosmology 2000, Lisbon, July (2000)
- [22] C. Blake *et al.*, arxiv:1108.2637 (2011)
- [23] C. Blake and K. Glazebrook, Astrophys. J. **594**, 665 (2003)
- [24] J.R. Bond and G. Efstathiou, Mon. Not. Roy. Astron. Soc. **218**, 103 (1986)
- [25] J.R. Bond and G. Efstathiou, Mon. Not. Roy. Astron. Soc. **22**, 33 (1987)
- [26] M.L. Brown *et al.*, Astrophys. J. **705**, 978 (2009)
- [27] M. Bucher *et al.*, Phys. Rev. Lett. **93**, 081301 (2004)
- [28] M. Bucher and D. Spergel, Phys. Rev. D **60**, 043505 (1999)
- [29] M. Bucher *et al.*, Phys. Rev. D **62**, 083508 (2000)
- [30] M. Bucher *et al.*, Phys. Rev. D **66**, 023528 (2002)
- [31] M. Bucher *et al.*, Phys. Rev. Lett **87**, 191301 (2001)
- [32] C. Carbone *et al.*, JCAP **09**, 028 (2011)

- [33] A. Challinor and A. Lasenby, *Astrophys. J.* **513**, 1 (1999)
- [34] M. Chevallier and D. Polarski, *Int. J. Mod. Phys. D* **10**, 213 (2001)
- [35] T. Chiba *et al.*, *Astrophys. J.* **429**, 427 (1994)
- [36] D. Clowe *et al.*, *Astrophys. J.* **648**, L109-L113 (2006)
- [37] S. Cole *et al.*, *Mon. Not. Roy. Astron. Soc.* **362**, 665 (2005)
- [38] M. Crocce and R. Scoccimarro, *Phys. Rev. D* **73**, 063519 (2006)
- [39] R.H. Cyburt *et al.*, *JCAP* **0811**, 012 (2008)
- [40] P. De Bernardis *et al.* *Phys. Rev. D* **79**, 043503 (2009)
- [41] S. Dodelson, *Modern Cosmology*, Academic Press (2003)”
- [42] J. Dunkley *et al.*, *Astrophys. J. Suppl.* **180**, 306 (2009)
- [43] J. Dunkley *et al.*, *Phys. Rev. Lett.* **95**, 261303 (2005)
- [44] G. Efstathiou and J.R. Bond, *Mon. Not. Roy. Astron. Soc.* **218**, 103 (1986)
- [45] G. Efstathiou, *Proceedings of the thirty-sixth Scottish Universities Summer School in Physics*, eds. J. Peacock, A. Heavens and A. Davies, Volume **36**, 361-390 (1989)”
- [46] D. J. Eisenstein *et al.*, *Astrophys. J.* **633**, 560 (2005)
- [47] D. Eisenstein *et al.*, *Astrophys. J.* **664**, 660 (2007)
- [48] D.J. Eisenstein *et al.*, *Astron. J.* **142**, 72 (2011)
- [49] D. Eisenstein *et al.*, *Astrophys. J. Lett.* **504**, L57 (1998)
- [50] K. Enqvist and H. Kurki-Suonio, *arXiv:astro-ph/9907221* (1999)
- [51] K. Enqvist *et al.*, *Phys. Rev. D* **65**, 043002 (2002)

- [52] A.L. Erickcek *et al.*, Phys. Rev. D **80**, 083507 (2009)
- [53] S.M. Faber and R.E. Jackson, Astrophys. J. **204**, 668 (1976)
- [54] R. Fadely *et al.*, arXiv:0909.1807 (2009)
- [55] A. Friedmann, General Relativity and Gravitation, **31**, 1991 (1999)
- [56] L. Fu *et al.*, Astron. Astrophys. **479**, 9 (2008)
- [57] J. Garcia-Bellido and D. Wands, Phys. Rev. D **52**, 6739 (1995)
- [58] J. Garcia-Bellido and D. Wands, Phys. Rev. D **53**, 5437 (1996)
- [59] G. Gamow, Phys. Rev. D **70**, 572 (1946)
- [60] T. Giannantonio and R. Crittenden, <http://www.arxiv.org/abs/0706.0274> (2007)”
- [61] M. Giovannini, Int. J. Mod. Phys. D **14**, 363-510 (2005)
- [62] M. Giovannini, Phys. Rev. D **70**, 103509 (2004)
- [63] N. Gouda and N. Sugiyama, Astrophys. J. **395**, L59 (1992)
- [64] C. Gordon *et al.*, Phys. Rev. D **63**, 023506 (2001)
- [65] C. Gordon and A. Lewis, Phys. Rev. D **67**, 123513 (2003)
- [66] E.R. Harrison, Phys. Rev. D **1**, 2726 (1970).
- [67] S.W. Hawking, Phys. Lett. **115B**, 295 (1982)
- [68] M. Hicken *et al.*, Astrophys. J. **700**, 1097 (2009)
- [69] G. Hinshaw *et al.*, Astrophys. J. Suppl. **180**, 225 (2009)
- [70] G. Hinshaw *et al.*, Astrophys. J. Suppl. **170**, 288-334 (2007)
- [71] W. Hu and M. White, Phys. Rev. D **56**, 596 (1997)

- [72] W. Hu and N. Sugiyama, *Astrophys. J.* **471**, 542-570 (1996)
- [73] W. Hu and N. Sugiyama, *Astrophys. J.* **436**, 456 (1994)
- [74] W. Hu and N. Sugiyama, *Astrophys. J.* **444**, 489 (1995)
- [75] W. Hu and S. Dodelson, *Ann. Rev. Astron. Astrophys.* **40**, 171 (2002)
- [76] W. Hu *et al.*, *Astrophys. J.* **447**, L59 (1995)
- [77] W. Hu, *Lect. Notes Phys.* **470**, 207 (1996)
- [78] W. Hu, Ph.D thesis, University of California, (1995)
- [79] W. Hu *et al.*, *Phys. Rev. D* **57**, 3290 (1998)
- [80] E. Hubble, *Proceedings of the National Academy of Sciences* **15**, 168 (1929)
- [81] N. Jarosik *et al.*, *Astrophys. J. Suppl.* **192**, 14 (2011).
- [82] R. Kessler *et al.*, *Astrophys. J. Suppl.* **185**, 32 (2009)
- [83] L. Knox and L. Page, *Phys. Rev. Lett.* **85**, (2000)
- [84] L. Knox, *arXiv:astro-ph/0002163v1* (2001)
- [85] H. Kodama and M Sasaki, *Int. J. Mod. Phys. A*, **1**, 265 (1986)
- [86] H. Kodama and M. Sasaki, *Prog. Theor. Phys. Suppl.* **78**, 1 (1984)
- [87] L.A. Kofman and A.D. Linde, *Nucl. Phys. B* **282**, 555 (1987)
- [88] E. Komatsu *et al.*, *Astrophys. J. Suppl. S.* **192**, 18 (2011)
- [89] M. Kunz *et al.*, *Phys. Rev. D* **74**, 023503 (2006)
- [90] H. Kurki-Suonio *et al.*, *Phys. Rev. Lett.* **71**, 131302 (2005)
- [91] H. Lampeitl *et al.*, *Astrophys. J.* **722**, 566 (2010)

- [92] D. Langlois and A. Riazuelo, Phys. Rev. D **62**, 043504 (2000)
- [93] D. Langlois and B. Tent, Class. Quantum Grav. **28**, 222001 (2011)
- [94] D. Langlois, arXiv:hep-th/0405053v1 (2004)
- [95] D. Langlois, Elsevier C.R. Phys. **4**, 953-959 (2003)
- [96] D. Langlois, Phys. Rev. D **59**, 123512 (1999)
- [97] D. Larson *et al.*, arXiv:1001.4635 (2010)
- [98] A. Lasenby and A. Challinor, Proceedings of the XL1st Rencontre de Moriond, eds. C. Magneville, R. Ansari, J. Dumarchez and J.T.T. V  n, La Thuile, Volume **40**, 15-23 (2006)
- [99] G. Lemaitre, Mon. Not. Roy. Astron. Soc. **91**, p.483 (1931)
- [100] A. Lewis and A. Challinor, CAMB (<http://camb.info/>), (2005)
- [101] A. Lewis and A. Challinor, Phys. Rept. **429**, 1 (2006)
- [102] A. Lewis *et al.*, Astrophys. J. **538**, 473 (2000)
- [103] A. Lewis, Camb notes (<http://cosmologist.info/notes/>), (2005)
- [104] A. Lewis, Ph.D. thesis, Cambridge University (2000)
- [105] A. Lewis, Phys. Rev. D **70**, 043011 (2004)
- [106] A. Liddle and D. Lyth, *Cosmological inflation and large scale structure*, Cambridge University Press (2000)
- [107] A. Liddle and D. Wolfe, Astrophys. J. **231**, 1 (1993)
- [108] A. Liddle, *An Introduction to Modern Cosmology*, John Wiley (2003)
- [109] A.D. Linde and V.F. Mukhanov, Phys. Rev. D **56**, 535 (1997)
- [110] A.D. Linde, Phys. Lett. B **108**, 389-393 (1982)

- [111] A.D. Linde, Phys. Lett. B **158**, 375 (1985)
- [112] E.V. Linder, Phys. Rev. Lett. **90**, 091301 (2003)
- [113] D.H. Lyth and D. Wands, Phys. Lett. B **524**, 5-14 (2002)
- [114] C.P. Ma and E. Bertschinger, Astrophys. J. **455** 7 (1995)
- [115] A. Mangilli *et al.*, JCAP **10**, 009 (2010)
- [116] A. Mantz *et al.*, Mon. Not. Roy. Astron. Soc. **406**, 1759 (2010)
- [117] B. Mason *et al.*, Astrophys. J. **591**, 540 (2003)
- [118] R. Massey *et al.*, Astrophys. J. Suppl. **172**, 239 (2007)
- [119] S. Mollerach and S. Matarrese, Phys. Rev. D **44**, 1670 (1991)
- [120] S. Mollerach, Phys. Lett. B **242**, 158 (1990)
- [121] K. Moodley *et al.*, Phys. Rev. D **70**, 103520 (2004)
- [122] K. Moodley, Ph.D thesis, University of Cambridge, (2002)
- [123] v. Mukhanov *et al.*, Physics Reports **215**, 203 (1992)
- [124] S. Muya Kasanda *et al.*, arXiv:1111.2572 (2011)
- [125] M. R. Nolta *et al.*, Astrophys. J. Suppl. **180**, 296 (2009)
- [126] L. Page *et al.*, Astrophys. J. Suppl. **170**, 335-376 (2007)
- [127] L. Page *et al.*, Astrophys. J. Suppl. **148**, 233 (2003)
- [128] D. Parkinson *et al.*, Phys. Rev. D **71**, 063524 (2005)
- [129] P.J.E. Peebles, Nature **327**, 210 (1987); P.J.E. Peebles, Astrophys. J. **315**, L73 (1987)
- [130] P. Peebles and B. Ratra, Rev. Mod. Phys. **75**, 559 (2003)

- [131] P.J.E. Peebles, *Astrophys. J.* **510**, 523 (1999)
- [132] A.A. Penzias and R.W. Wilson, *Astrophys. J.* **142**, 419 (1965)
- [133] S. Perlmutter *et al.*, *Astrophys. J.* **517**, 565 (1999)
- [134] E. Pierpaoli *et al.*, *JHEP* **10**, 015 (1999)
- [135] The Planck Collaboration, arXiv:1101.2022v2 (2011)
- [136] The Planck Collaboration, arXiv:astro-ph/0604069v1 (2006)
- [137] D. Polarski and A.A. Starobinsky, *Phys. Rev. D* **50**, 6123 (1994)
- [138] W. Press and E. Vishniac, *Astrophys. J.* **239**, 1 (1980)
- [139] A. Rassat *et al.*, *Phys. Rev. D* **80**, 123516 (2009)
- [140] A.K. Rebhan and D.J. Schwarz, *Phys. Rev. D* **50**, 2541 (1994)
- [141] C.L. Reichardt *et al.*, *Astrophys. J.* **694**, 1200 (2009)
- [142] B.A. Reid *et al.*, *Mon. Not. Roy. Astron. Soc.* , (2009)
- [143] J. Rich, *Fundamentals of Cosmology*. Springer. pp. 302 (2001)
- [144] A.G. Riess *et al.*, *Astron. J.* **116**, 1009 (1998)
- [145] V.C. Rubin *et al.*, *Astrophys. J.* **238**, 471 (1980)
- [146] R.K. Sachs and A.M. Wolfe, *Astrophys. J.* **147**, 73 (1967)
- [147] M. Sasaki and E.D. Stewart, *Prog. Theor. Phys.* **95**, 71 (1996)
- [148] M. Sasaki and T. Tanaka, *Prog. Theor. Phys.* **99**, 763 (1998)
- [149] D. Schlegel *et al.*, arXiv:0902.4680 (2009)
- [150] P. Schneider, arXiv:astro-ph/0509252v1 (2005)

- [151] E. Sefusatti and E. Komatsu, Phys. Rev. D **76**, 083004 (2007)
- [152] U. Seljak and M. Zaldarriaga, Astrophys.J. **469**, 437 (1996)
- [153] U. Seljak et al., Phys. Rev. D **71**, 043511 (2006)
- [154] U. Seljak et al., Phys. Rev. D **71**, 103515 (2005)
- [155] H-J. Seo and D. Eisenstein, Astrophys. J. **598**, 720 (2003)
- [156] H-J. Seo and D. Eisenstein, Astrophys. J. **633**, 575 (2005)
- [157] H-J. Seo and D. Eisenstein, Astrophys. J. **665**, 14 (2007)
- [158] B.D. Sherwin *et al.*, arXiv:1105.0419v3 (2011)
- [159] M. Smith *et al.*, arxiv:1108.4923 (2011)
- [160] R. Smith *et al.*, Phys. Rev. D **75**, 063512 (2007)
- [161] G.F. Smoot *et al.*, Astrophys. J. Lett. **396**, L1 (1992)
- [162] D. Spergel et al., Astrophys. J. Suppl. **148**, 175 (2003)
- [163] D. Spergel et al., Astrophys. J. Suppl. **170**, 377 (2007)
- [164] R. Srianand *et al.*, Nature **408**, 931 (2000)
- [165] A.J. Stompor *et al.*, Astrophys. J. **463**, 8 (1996)
- [166] N. Sugiyama *et al.*, Astrophys. J. **338** L43 (1989)
- [167] S.H. Suyu *et al.*, Astrophys. J. **711**, 201 (2010)
- [168] T. Takahashi, Front. Cosm. Grav., Yukawa Institute, 307 (2001)
- [169] A.N. Taylor *et al.*, Mon. Not. Roy. Astron. Soc. **374**, 1377 (2007)
- [170] M. Tegmark *et al.*, Astrophys. J. **530**, 133 (2000)

- [171] M. Tegmark *et al.*, *Astrophys. J.* **480**, 22 (1997)
- [172] M. Tegmark *et al.*, *Astrophys. J.* **606**, 702 (2004)
- [173] R. Trotta, *Mon. Not. Roy. Astron. Soc.* **375**, L26 (2007)
- [174] R. Trotta, *Mon. Not. Roy. Astron. Soc.*, **378**, 72 (2007)
- [175] R. Trotta, Ph.D thesis, University of Geneva, Thesis N. 3534 (2004)
- [176] S. Tsujikawa *et al.*, *Phys. Rev. D* **67**, 083516 (2003)
- [177] J. Valiviita and T. Giannantonio, *Phys. Rev. D* **80**, 123516 (2009)
- [178] A. Vikhlinin *et al.*, *Astrophys. J.* **640**, 691 (2006)
- [179] A. Vikhlinin *et al.*, *Astrophys. J.* **692**, 1060 (2009)
- [180] D. Wands *et al.*, *Phys. Rev. D* **66**, 043520 (2002)
- [181] M. White and W. Hu, *Astron. Astrophys. J.* **321**, (1997)
- [182] M. Zaldarriaga and U. Seljak, *Astrophys. J.* **129**, 431 (2000)
- [183] M. Zaldarriaga and U. Seljak, *Phys. Rev. D* **55**, 1830 (1997)
- [184] Y.B. Zeldovich, *Mon. Not. Roy. Astron. Soc.* **160**, 1 (1972)
- [185] C. Zunckel *et al.*, *Physics Letters B* **696**, 433 (2011)
- [186] F. Zwicky, *Helvetica Physica Acta* **6**, 110 (1933)
- [187] F. Zwicky, *Astrophys. J.* **86**, 217 (1937)

APPENDIX A

Matter Power Spectrum Derivatives with respect to the Isocurvature Parameters

The derivatives of the matter power spectrum with respect to the isocurvature parameters have not been presented in the literature before and we show them here for the benefit of the reader, in addition to the derivatives with respect to the cosmological parameters.

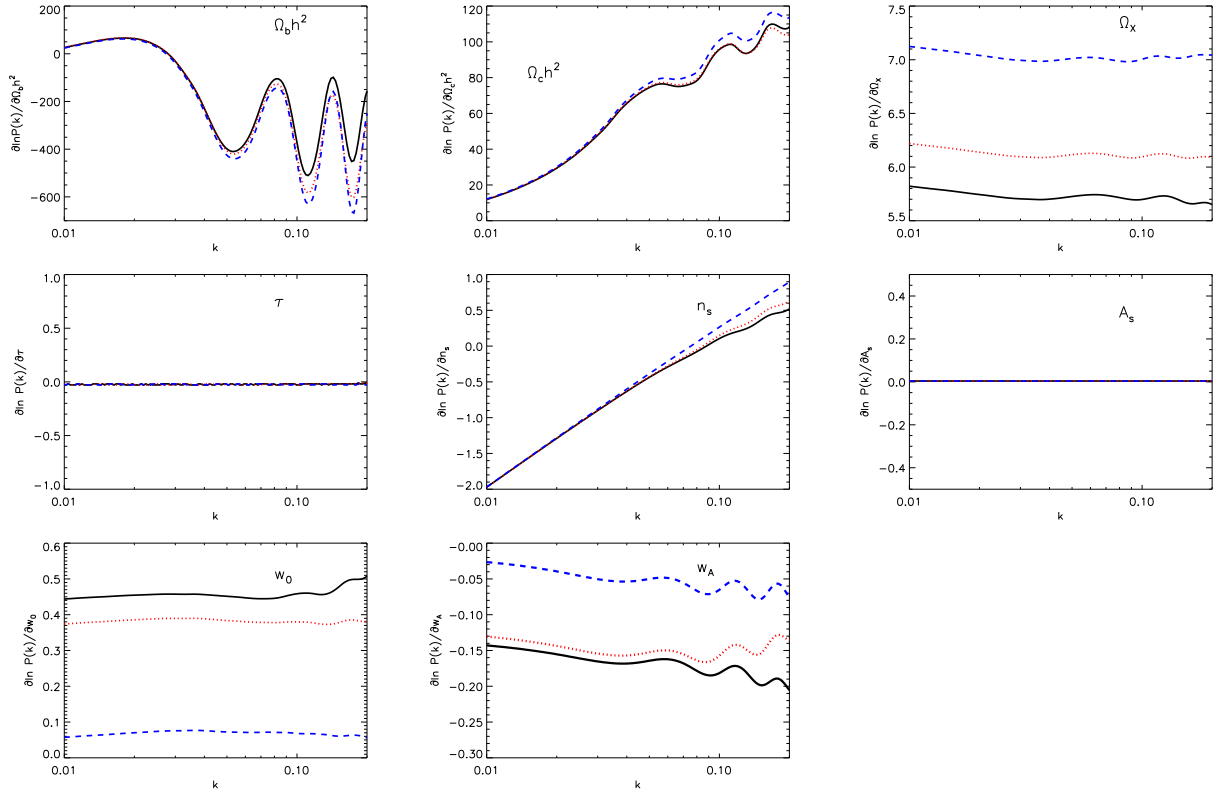


Figure A.1: Logarithmic derivatives of $P(k)$ with respect to the cosmological parameters for different redshifts: $z = 0.35$ (solid black), $z = 0.6$ (dotted red) and $z = 3$ (dashed blue). An adiabatic fiducial model is assumed.

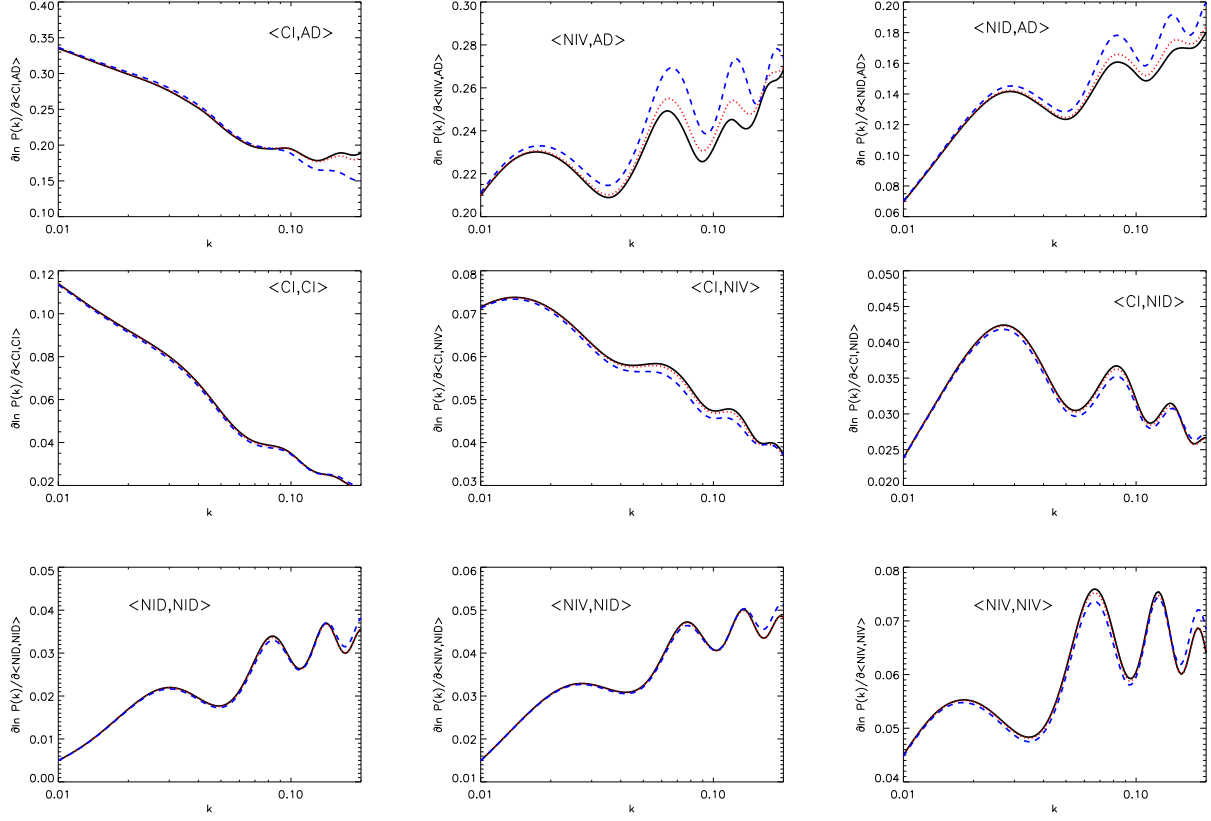


Figure A.2: Logarithmic derivatives of $P(k)$ with respect to the isocurvature parameters for different redshifts: $z = 0.35$ (solid black), $z = 0.6$ (dotted red) and $z = 3$ (dashed blue). An adiabatic fiducial model is assumed.